

SELF-MANIPULATION AND DYNAMIC TRANSITIONS FOR A LEGGED ROBOT

Aaron M. Johnson

A DISSERTATION

in

Electrical and Systems Engineering

Presented to the Faculties of the University of Pennsylvania in Partial  
Fulfillment of the Requirements for the Degree of Doctor of Philosophy

2014

Supervisor of Dissertation

---

Daniel E. Koditschek  
Professor of Electrical and Systems Engineering

Graduate Group Chairperson

---

Saswati Sarkar  
Professor of Electrical and Systems Engineering

Dissertation Committee:

George Pappas, Professor of Electrical and Systems Engineering  
Vijay Kumar, Professor of Mechanical Engineering and Applied Mechanics  
Matthew Mason, Professor of Robotics, Carnegie Mellon University

SELF-MANIPULATION AND DYNAMIC TRANSITIONS FOR A LEGGED ROBOT  
COPYRIGHT  
2014  
Aaron M. Johnson

# Acknowledgments

I would like to acknowledge the many sponsors who made this work possible, primarily the ARL/G-DRS RCTA Project under Cooperative Agreement W911NF-10-2-0016 and the DARPA Maximum Mobility and Manipulation Seedling project, with additional funding from the National Science Foundation under FIBR award 0425878 and CDI-II award 1028237, the Intelligence Community Postdoctoral Research Fellowship HM1582-08-1-0034, and the University of Pennsylvania through the Alfred Fitler Moore Chair Endowment.

I would like to thank my advisor, Dan Koditschek, for teaching me how to think clearly and communicate to the world. Thank you to my committee members, George Pappas, Vijay Kumar, and Matt Mason for many discussions and insightful suggestions. I am grateful to my undergraduate advisor Howie Choset for starting me on this journey and teaching me the value of a good demo. I have had the privilege of working closely with Clark Haynes, Deniz Ilhan, and Sam Burden who have all helped me grow as a roboticist and a researcher. In addition I would like to thank my other coauthors Goran Lynch, Avik De, Thomas Libby, Evan Chang-Siu, Robert Full, Kevin Galloway, Mackenzie White, Benjamin Plotnick, Ryan Knopf, and Matt Hale. I would like to thank Bruce Kothmann, Shai Revzen, Haldun Komsuoglu and Dan Guralnik for numerous useful consultations and stimulating discussions, and my current lab-mates especially Deniz Ilhan, Avik De, Jeff Duperret, Gavin Kenneally, and Sonia Roberts for arguing the finer points of robotics over a pint. Numerous undergraduates and visitors have helped build and run robots with me, among them Aaron Peck, Benjamin Plotnick, Matt Hale, Ryan Knopf, Albert Kwon, Jiali Sheng, Praveer Nidamaluri, David Hallac, Justin Starr, Mike Choi, Joseph Coto, Adam Farabaugh, and Pouria Sanjari. Thank you to Andrew Spence and Jonathan Clark and their students for helping us build and

make use of our robots.

Thank you to Gina Burgese and Diedra Krieger for their indispensable assistance with the logistical challenges of building robots. Thank you to Boston Dynamics, Inc., and Al Rizzi in particular, who kindly provided comparison information regarding Rugged RHex, as well as inviting me to come work with them and test robots at several points in this thesis. Thank you also to the Southwest Research Institute for help with testing in Twentynine Palms, CA, and Boston, MA. Few people have had the opportunity to work closely on an academic paper with their grandfather, and I have greatly enjoyed the experience of writing two with my own [83, 84].

Finally, I would not have been able to complete this thesis without the love and support of my family, most especially my amazing wife, Jennie, who has not bothered me about the chores I should have been doing these past few months.

## ABSTRACT

### SELF-MANIPULATION AND DYNAMIC TRANSITIONS FOR A LEGGED ROBOT

Aaron M. Johnson

Daniel E. Koditschek

How can we make a robot that can go anywhere on its own? This thesis presents several new behaviors on the RHex robot that greatly increase the variety of obstacles that it can overcome, including vertical jumps, flips, leaps onto and across ledges, aerial reorientations, and proprioceptively-aware behaviors. These behaviors inspire new tools to model and understand their transitional nature, wherein it is no longer useful to think of each step as being an equal part of a steady state gait. Legged robots will necessarily experience a variety of changing contact conditions as they locomote in complex environments epitomized by the rocky, sandy desert. Drawing on the much more mature literature of robot manipulation, this thesis presents the new modeling paradigm of “self-manipulation” that formally generates analytical equations of motion across all contact states. The framework is amenable to many ubiquitous simplifying assumptions (such as rigid bodies, plastic impact, persistent contact, Coulomb friction, and massless limbs) to reduce the complexity of these models despite the obvious physical inaccuracies that each incurs. Nevertheless the models capture enough of the physical world to represent the challenges confronting interesting behaviors in a qualitatively correct manner, including the effects of impulsive transitions between the various contact modes. More than numerical simulation, our goal is the distillation of these physically parametrized models into formal design insights (platform design, behavior design, and controller design), utilizing a variety of analytical and numerical methods. These behaviors are only possible with a robot designed to be both robust and powerful, and they make use of the unique capability of legged machines to interact with the environment in varied and, possibly, unpredictable ways. Careful actuator modeling is needed to achieve such acrobatic results, and so this thesis presents a spectrum of motor sizing tasks to ensure that the platform is up to the task. These tools are used to gain insight into various dynamic transitions for RHex, and we conjecture that their generalization will be of importance for a broad class of legged robots operating in remote and unstructured terrain.

# Contents

<b>1</b>	<b>Introduction</b>	<b>1</b>
1.1	Contributions and Organization . . . . .	3
1.2	Background . . . . .	7
1.2.1	RHex . . . . .	7
1.2.2	Behaviors . . . . .	9
1.2.3	Modeling Paradigms . . . . .	14
<b>2</b>	<b>Actuators</b>	<b>21</b>
2.1	Motor Selection . . . . .	21
2.1.1	Motor Selection for a Tail . . . . .	22
2.1.2	Motor Selection for X-RHex . . . . .	26
2.1.3	Thermal Considerations for Motor Selection . . . . .	29
2.2	Dynamic Motor Modeling . . . . .	34
2.2.1	Algorithm . . . . .	36
2.2.2	Reactive Behaviors . . . . .	41
<b>3</b>	<b>Leaping Transitions</b>	<b>45</b>
3.1	Hybrid Dynamics Over the Ground Reaction Complex . . . . .	46
3.1.1	The Ground Reaction Complex . . . . .	48
3.1.2	Hamiltonian Flows . . . . .	49
3.1.3	Hybrid Dynamics . . . . .	50

3.2	Open Loop Control of Transitions Across the Ground Reaction Complex . . . . .	52
3.2.1	Leg Strategy . . . . .	52
3.2.2	Coordination Timing . . . . .	53
3.2.3	Transition Paths . . . . .	53
3.3	Experiments . . . . .	54
3.3.1	Extensions . . . . .	57
3.4	Behaviors . . . . .	58
3.4.1	Leaping Behaviors . . . . .	58
3.4.2	Gap Crossing . . . . .	59
3.4.3	Jumping on to a Ledge . . . . .	59
3.5	Parametric Jumping Dataset . . . . .	61
<b>4</b>	<b>Self-Manipulation</b>	<b>66</b>
4.1	Self-Manipulation . . . . .	68
4.1.1	Notation . . . . .	68
4.1.2	Modeling Decisions . . . . .	71
4.1.3	Contact Conditions . . . . .	72
4.1.4	Kinematic Loop Closures . . . . .	74
4.1.5	Infinitesimal Kinematics: The Grasp Map and Hand Jacobian . . . . .	75
4.1.6	Rolling Contact . . . . .	77
4.1.7	Parameterization of the Closed-Loop Kinematics . . . . .	77
4.1.8	Quasi-static Forces and Torques . . . . .	79
4.1.9	Dynamics . . . . .	80
4.1.10	Reduced Dynamics . . . . .	82
4.1.11	Summary of Assumptions . . . . .	83
4.2	Self-Manipulation for RHex . . . . .	84
4.2.1	Model Parameters . . . . .	84
4.2.2	RHex Kinematics . . . . .	86

4.2.3	Assumptions for RHex . . . . .	87
4.3	Behaviors . . . . .	89
4.3.1	Reactive Standing . . . . .	89
4.3.2	Pitching Sensor Sweep . . . . .	96
4.3.3	Pitch Control in Leaping . . . . .	103
4.4	Appendix to Chapter 4 . . . . .	113
4.4.1	Kinematic Constraints . . . . .	113
4.4.2	Grasp Map and Hand Jacobian . . . . .	114
4.4.3	Rolling Contact . . . . .	115
4.4.4	Dynamics . . . . .	116
4.4.5	Reduced Dynamics . . . . .	118
4.4.6	Proofs of Lemmas . . . . .	119
4.4.7	Values for RHex . . . . .	121
<b>5</b>	<b>Impulses and Hybrid Systems</b>	<b>126</b>
5.1	Dynamics . . . . .	128
5.1.1	Massless Considerations . . . . .	130
5.1.2	Impact Map . . . . .	133
5.1.3	Complementarity . . . . .	134
5.1.4	Pseudo-Impulse . . . . .	139
5.1.5	Friction . . . . .	145
5.2	Hybrid Dynamical System . . . . .	146
5.2.1	The General System . . . . .	146
5.2.2	The Self-Manipulation System . . . . .	149
5.3	Appendix to Chapter 5 . . . . .	151
5.3.1	Linear Algebra . . . . .	151
5.3.2	Matrices Used in Proofs . . . . .	152
5.3.3	Proof of Lemma 5.2 . . . . .	153

5.3.4	Proof of Lemma 5.3 . . . . .	154
<b>6</b>	<b>Conclusion</b>	<b>155</b>

# List of Tables

1.1	Summary of the behavioral contributions of this thesis. . . . .	4
2.1	Motor Comparison . . . . .	28
2.2	Motor and Gearbox Combination Comparison . . . . .	29
2.3	Motor and Gearbox Thermal Comparison . . . . .	32
3.1	Apex state for the (+, +) jumps at various relative leg timings. . . . .	62
3.2	Apex state for the (-, -) jumps at various relative leg timings. . . . .	63
3.3	Apex state for the (+, -) jumps at various relative leg timings. . . . .	64
3.4	Apex state for the (-, +) jumps at various relative leg timings. . . . .	65
4.1	Key symbols used throughout this chapter. . . . .	69
4.1	Key symbols used throughout this chapter ( <i>Continued</i> ). . . . .	70
4.2	Physical quantities used in the RHex model. . . . .	86
4.3	Reactive stand power from seated position. . . . .	96
4.4	Comparison of forward leaps with toe stub. . . . .	107
5.1	Key symbols used throughout this chapter. . . . .	128

# List of Figures

1.1	X-RHex in the Mojave desert. . . . .	2
1.2	The robots used in this thesis. . . . .	8
1.3	Various models for a closed-loop kinematic chain. . . . .	15
2.1	A summary of motor selection techniques with some example domains. . . . .	22
2.2	XRL with a new tail. . . . .	23
2.3	XRL self-righting in a fall. . . . .	25
2.4	XRL surviving a run off a cliff outdoors. . . . .	25
2.5	A disassembled view of the brushless motor. . . . .	27
2.6	Torque-speed and power-speed profiles of three motor/gearbox combinations. . . . .	30
2.7	The thermal model represented as an equivalent circuit. . . . .	31
2.8	Core and Case temperature simulations for a fixed torque demand. . . . .	33
2.9	Comparison of measured and estimated case temperatures. . . . .	34
2.10	Overview of fault detection, identification, and recovery architecture. . . . .	35
2.11	Block diagram of leg observer. . . . .	36
2.12	Observer residual contrasted with controller tracking error. . . . .	38
2.13	State transition diagram for fault identification. . . . .	41
2.14	EduBot running a wall avoidance behavior inside a closed rectangular region. . . . .	42
2.15	Transitioning from walking to stair climbing. . . . .	43
2.16	Gait comparison of a robot walking with a missing sixth leg. . . . .	44
3.1	XRL leaping upward onto a 73cm high table. . . . .	46
3.2	All possible contact states, represented as a tetrahedron, showing adjacency. . . . .	50
3.3	Logical vs allowable cell transitions over the GRC. . . . .	52
3.4	Apex height, displacement, and pitch for (+, +) jumping. . . . .	55
3.5	Apex height, displacement, and pitch for (-, -), (+, -), and (-, +) jumping. . . . .	56
3.6	XRL crossing a 60cm gap. . . . .	60
4.1	Selected coordinate frames for self-manipulation of a legged robot. . . . .	67
4.2	Coordinate frames and key dimensions for RHex. . . . .	84
4.3	Quasi-static contact modes over the entire state space of joint angles. . . . .	88
4.4	Two examples of how the balancing stand works. . . . .	90
4.5	X-RHex performing a reactive stand on rocks. . . . .	95
4.6	Contour plot of pitch $\phi$ as a function of $\theta_1$ and $\theta_2$ . . . . .	98
4.7	Robot performing two pitching sensor sweeps. . . . .	101
4.8	Leg speed at takeoff. . . . .	102

4.9	Pitching velocity at apex after a forward leap. . . . .	106
4.10	Forward velocity at takeoff point of second (rear) leg. . . . .	108
4.11	Forward velocity at takeoff point of second (rear) leg for various gear ratios. . . . .	110
4.12	Forward velocity at takeoff point of second (rear) leg for various pitching velocities. . . . .	111
4.13	Robot state just prior to touchdown after two jumps. . . . .	112
4.14	Mass and Coriolis tensors. . . . .	123
5.1	Keyframes from RHex simulation leaping onto a 20cm ledge. . . . .	127
5.2	Condition number over various values of the leg mass. . . . .	133
5.3	A point sliding along ground $G$ approaches hill $H$ . . . . .	140
5.4	A rocking block settling on the ground. . . . .	142
5.5	Vertical velocity of a settling block with and without the pseudo-impulse. . . . .	143
5.6	Keyframes of impact of the second leg with and without the pseudo-impulse. . . . .	144
5.7	Ground reaction force for evaluations with and without the pseudo-impulse. . . . .	145
5.8	Keyframes from RHex simulation leaping vertically. . . . .	147
5.9	Keyframes from RHex simulation leaping onto a 73cm ledge. . . . .	148
6.1	XRL scrambling onto a ledge. . . . .	157

# Chapter 1

## Introduction

The goal of robotics is to create systems that are capable of performing tasks that aid humanity. That aid can take many forms, such as search and rescue, vacuuming, or entertainment. Whatever the task, what is desired is a behavior — we want a machine that can perform the search, clean a floor, or make us laugh. A fundamental decision in the design of a robot to accomplish some behavior is if and how it will locomote, whether that be with wheels or legs or wings. For robots that only need to interact with the world in a small area, such as on an assembly line, being bolted to the ground and reaching from there may be sufficient. For robots that operate only in flat environments, such as in an office building or on a highway, wheels (one of humanity’s greatest inventions) are an efficient and effective choice. However a robot that needs to perform a task somewhere other than in these restricted, and often engineered, environments requires more advanced locomotion capabilities. Unlike wheels, legs do not require continuous contact with the terrain, making them well suited for uneven and broken terrain such as a rocky desert, as well as the “evenly broken” terrain of an uncluttered stairwell.

One promise of legged motion is versatility, and as the size of the obstacles grow relative to the robot’s size, the robot’s controllers can change the gait parameters to better react to the terrain. However at some point the motion can no longer be usefully described as deviations about a steady state motion. The motion is inherently transitory — how can a robot, such as in Figure 1.1, transition onto the first obstacle, and then transition over second and land on the third? When every step



Figure 1.1: X-RHex in the Mojave desert.

is actually different there is little to be gained by pretending that they are the same. Unlike the maturity of steady state locomotion research [23, 125, 146, 154], dynamical transitional behaviors have not received nearly as much attention other than by formulating them in terms of compositions of existing steady state constituents [26, 169]. As new conditions arise, it is crucial to formally (and therefore automatically) generate and analyze the system dynamics, in a manner requiring as little knowledge as possible about the geometry and mechanics of the substrate.

In contrast, multi-fingered object manipulation has been well formalized for many decades [13, 119, 120, 134, 137, 162] motivating the new methods presented here to leverage this established body of work and extend it to legged robots as they manipulate themselves through the world. We exploit these “self-manipulation” modeling choices to generate the diverse constrained quasi-static and Lagrangian dynamics (as well as the impulsive transition conditions that relate them) arising from the exponentially many possible contact conditions. The framework is body centric (does not require full knowledge of the world reference frame), allows for massless limbs (does not require an invertible mass matrix), and permits underactuation (does not require an invertible kinematic Jacobian). These analytical models can be integrated numerically to simulate a certain situation,

but at best all that can be learned from that is the same thing that can be learned from running the physical robot (though possibly at a lower cost). The true value of these analytical models is their ability to provide for design insight.

There are three aspects of design a roboticist might explore: platform design, behavior design, and controller design. A capable robot requires good design in all three areas, and the field of robotics is working to collectively synthesize the best design insights to help build robots that can effectively aid humanity. One way to gain such design insight is to look to biology, but insight from biology has some limitations — the physical properties of an animal’s body can be measured and its motion and applied forces observed, however we do not yet have the tools to directly observe the controller that the animal is using. A roboticist meanwhile can gain insight in all three areas through direct observation of a robot executing some controller and performing some behavior. Beyond that, the roboticist also has direct control over the construction or selection of both the platform and the controller, and can express their design insights directly here. However the resulting behavior of the robot is a complicated function of how the robot interacts with its environment, which the roboticist can influence only indirectly through the design of the platform and controllers. This mismatch in capabilities between engineering and biology is in fact a great advantage to both fields. Biologists can observe and measure behaviors that roboticists hope to one day recreate. And roboticists can test controllers that biologists hypothesize to be a good model of the animal’s control system.

## 1.1 Contributions and Organization

This thesis explores many aspects of robot design using the hexapedal robot RHex [154]. Even after approximately 15 years of research on RHex, this thesis presents several new behaviors as well as expanding on many existing ones. These various behavioral advances are enabled by careful design of the robot and its actuators, and serve as the inspiration for new modeling and analysis tools. A summary of these behaviors, as well as the nature of their contribution, is given in Table 1.1. Some of these design insights were gained from the analysis of the behaviors: **Enumeration** behaviors that were found largely due to the systematic enumeration and exploration of the available contact

Behavior	Section	Architecture	Analysis
Leap, Table Edge	3.4.3	Actuation, Robustness	Enumeration, Hybrid-system
Leap, Vertical	3.4.1	Actuation	Enumeration, Hybrid-system
Leg Fault Recovery*	2.2.2	Proprioception	Inspiration
Reactive Standing	4.3.1	Proprioception	Self-manipulation
Scramble Onto Table	3.4.3	Actuation, Robustness	Hybrid-system, Inspiration
Tailed Reorientation*	2.1.1	Actuation, Robustness	Inspiration
Leap, Forward/Pronk	4.3.3	Actuation	Hybrid-system, Self-manipulation
Leap, Obstacles	3.4	Actuation	Hybrid-system
Sensor Sweep*	4.3.2		Self-manipulation
Wall/Stair Detection	2.2.2	Proprioception	

Table 1.1: Summary of behavioral contributions of this thesis. See Section 1.1 for explanation of the labels, and Section 1.2.2 for further details on individual behaviors and related work. The first group represents entirely new behaviors for RHex, while the second group represents existing behaviors which were either improved, or are now better understood, through the contributions listed. \* Behaviors developed in close collaboration with coauthors.

words (Chapter 3), **Hybrid-system** behaviors that take advantage of the multiple ways in which the robot can contact the world, and the impulsive transitions between them (Chapter 5), **Self-manipulation** behaviors for which the analytical dynamics models are able to provide significant design insight (Chapter 4). Other contributions pertained to the engineering of the robot architecture (both hardware and software): **Actuation** behaviors who benefited significantly from contributions in principled actuator selection (Section 2.1), **Robustness** behaviors which are made possible due to the robustness and reliability of the newest robot designs (Section 1.2.1), **Proprioception** behaviors which use proprioceptive feedback based on actuator modeling (Section 2.2). Finally there are still some behaviors where the contribution is primarily **Inspiration**, that is those which still rely primarily on the inspiration of their designer (and which inspire the need for tools beyond what is presented in this thesis).

The remainder of this chapter presents the new robot designs, X-RHex and XRL, in Section 1.2.1. Their robust construction, powerful actuators, and versatile sensor interface are crucial prerequisites for interesting dynamical behaviors. Section 1.2.2 then introduces these behaviors, as summarized in Table 1.1, and gives motivation and prior work for each. Section 1.2.3 then explores

some of the modeling principles used throughout the thesis.

Chapter 2 focuses on the question of actuator modeling and selection<sup>1</sup>. The dramatic behaviors of interest in this thesis require both careful actuator selection to ensure sufficient power is available, but also careful modeling and monitoring to ensure that the actuator is not damaged and is providing work in the desired manner. In particular a continuum of actuator selection problems is introduced, and a selection process for a simple dynamical task (tailed reorientation in flight) is given as a case study in careful motor selection. For more challenging robot design tasks, such as the construction of X-RHex, a heuristic method based on prior robot designs is used. The thermal properties of electric motors are modeled and the “heat coefficient” metric is defined to compare the thermal behavior of different motors. Once in use on a robot, continued online monitoring of the motor performance provides a proprioceptive sense. This sensor is used in three example behaviors: maze solving, stair climbing, and leg fault recovery.

Chapter 3 presents dramatic leaping transitions as a demonstration of the types of behaviors that the design and modeling results presented in this thesis are working towards understanding<sup>2</sup>. A hybrid systems framework characterizes the dynamic transitions of a planar “legged” rigid body from rest on level ground to a fully aerial state. The various contact conditions fit together to form a topologically regular structure, the “ground reaction complex”. The body’s actuated dynamics excite multifarious transitions between the cells of this complex, whose regular adjacency relations index naturally the resulting “leaps” (path sequences through the cells from rest to free flight). This chapter exhibit on a RHex robot some of the most interesting “words” formed by these achievable path sequences, documenting unprecedented levels of performance and new application possibilities that illustrate the value of understanding and expressing this vocabulary systematically.

Chapter 4 introduces self-manipulation as a new formal design methodology for legged robots with varying ground interactions<sup>3</sup>. The term denotes a set of modeling choices that permit a uniform

---

<sup>1</sup>Portions of this chapter, as well as related text and figures, previously appeared in [55, 65, 86, 87, 92]. All of these papers were written in collaboration with their respective co-authors, and only the contributions listed here are claims of this thesis.

<sup>2</sup>This chapter, as well as related text and figures, previously appeared in [89, 91].

<sup>3</sup>This chapter, as well as related text and figures, previously appeared in [90]. Additionally portions of this chapter, as well as related text and figures, also previously appeared in [88] which was written in collaboration with the listed co-authors, and only the contributions listed here are claims of this thesis.

and body-centric representation of the equations of motion — essentially a guide to the selection and configuration of coordinate frames. This chapter presents the kinematics and dynamics of a self-manipulation system in the form of a consistently structured representation that simplifies and unites the account of these otherwise bewilderingly diverse differential algebraic equations. Cleaving as closely as possible to the modeling strategies developed within the mature manipulation literature, self-manipulation models can leverage those insights and results where applicable, while clarifying the fundamental differences. Our primary motivation is not to facilitate numerical simulation but rather to promote design insight. This chapter also instantiates the abstract formalism for a simplified model of RHex, and illustrate its utility by applying a variety of analytical and computational techniques to derive new results bearing on behavior, controller, and platform design. For each example, empirical results document the specific benefits of the new insight into the robot’s transitions from standing, to moving in place, to leaping.

Chapter 5 extends the self-manipulation formalism of Chapter 4 (and similarly for manipulation [134]) to include the impulsive dynamics of the impact events that change the active contact constraints (which make up the discrete state)<sup>4</sup>. This sets up a path to specifying a formal hybrid system that is compatible with many simplifying phenomenological models, specified in Assumptions 5.1–5.9. A central claim of this chapter is the derivation of a consistent extension for Lagrangian dynamics, Newtonian impact laws, and complementarity contact conditions to systems that have certain rank deficiencies in their inertia tensor that maintains equivalence for nonsingular systems (Lemmas 5.1–5.3 and Theorems 5.5–5.6). Next, this chapter defines a new qualitatively useful *pseudo-impulse* that precludes certain *Zeno* phenomena. In addition this pseudo-impulse removes some spurious transitions by imposing an implicit bound on contact velocity below which the impact cannot impulsively remove existing contact constraints. Finally the continuous time and discrete time physics are summarized in the definition of the self-manipulation hybrid system (Definition 5.2). The closure and consistency (including if it is deterministic and non-blocking) of this system is left as an open question.

---

<sup>4</sup>This chapter, as well as related text and figures, is in preparation for submission as [85]. That paper was written in collaboration with the listed co-authors, and only the contributions listed here are claims of this thesis.

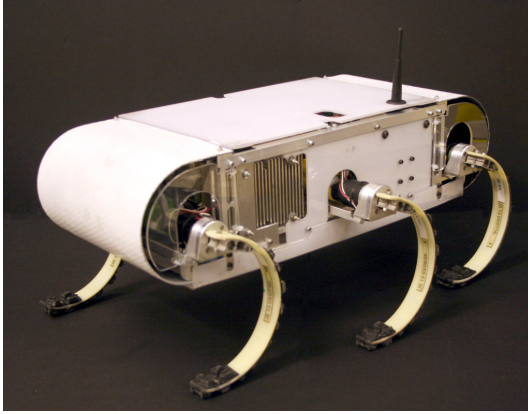
## 1.2 Background

### 1.2.1 RHex

RHex was introduced in 2001 as a “Simple and Highly Mobile Hexapod Robot” [154]. Despite its apparent age, the limits of the design are still unknown and in fact many new behaviors are demonstrated in this thesis that go beyond what was previously thought to be possible. In the process, several new RHex platforms are introduced, as shown in Figure 1.2 (see [55, Section 4] for a brief history and comparison of various versions). The physical robustness, higher ground clearance, substantially greater low end torque, modular payload system, and lighter weight (for the XRL variant) of these new robots were crucial to the success of the dynamic transitions of interest in this thesis.

The prior research versions of RHex that were available, the original Research RHex [154] and the EduBot [180] (shown in Figure 1.2b), had shown great agility but were not up to the task of high energy behaviors in the desert environments of particular interest in this thesis. This motivated the development of new platforms that would be better suited for such experiments. Initial testing in the Mojave desert used the Desert RHex upgrade to Research RHex (Figure 1.2a), In particular, it features several hardware updates: a new hard shell of carbon fiber and acrylic to survive impacts with the terrain, upgraded batteries to allow for longer experiments, a new wireless antenna to increase communication range, and added sensors (power logger, GPS) for monitoring progress.

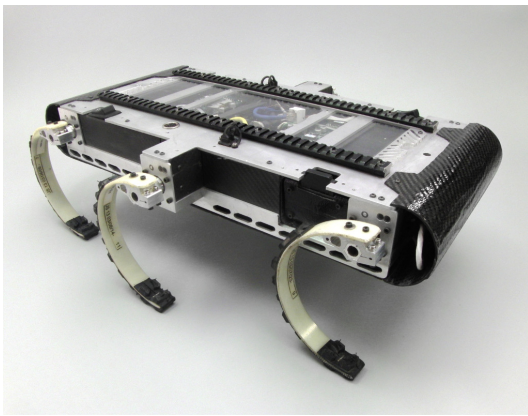
These improvements were sufficient for initial testing, but the need for a new platform was clear. The aging architecture was difficult to maintain, and the robot was not reliable especially when asked to perform high energy behaviors on rough terrain. Therefore a completely new robot was designed: X-RHex (Figure 1.2c). The design of X-RHex was a large collaborative effort led by the author and documented in [55, 65]. The dimensions of X-RHex were tightly constrained — the footprint is almost identical to Research RHex (in order to maintain the locomotion capabilities of that design, particularly on stairs) and the body height was kept to a minimum (just over half the height of Research RHex). In addition it uses commercial off the shelf (COTS) parts whenever possible, as buying replacement parts is easier than making them. Furthermore it introduced the



(a) Desert RHex, variant of [154].



(b) EduBot, variant of [180].



(c) X-RHex [55].



(d) XRL [65].

Figure 1.2: The robots used in this thesis. *These figures are included here courtesy of (a) Clark Haynes, (b) Kevin Galloway, (c) and (d) Ryan Knopf.*

*laboratory on legs* concept — a modular payload system that allows a user to rapidly develop behaviors in natural, outdoor environments as easily as on a lab bench. Subsequently a lighter version, X-RHex Lite, was designed using the same architecture (Figure 1.2d). It has a slightly smaller footprint and about 25% less mass [65], while still using the same COTS components and modular payload system as X-RHex.

One problem that is exacerbated in a desert environment is thermal considerations for motors. In the most dramatic of the behaviors presented here, the motor core temperature rises  $50^{\circ}\text{C}$  in half a second — only with a careful understanding of motor thermal properties can such behaviors be safely developed and used. These issues led to the development of a continuum of motor selection tasks [65], heuristics such as the motor heat coefficient to compare motor thermal properties (Sec-

tion 2.1.3), and a general framework for choosing a motor based on a dynamic task specification (Section 2.1), applied to a concrete example with analytical solutions (Section 2.1.1). In addition to managing the thermal budget, motor modeling is also useful as a virtual contact sensor (Section 2.2), which can be used e.g. for stair climbing [86].

## 1.2.2 Behaviors

There are many useful behaviors and behavioral components analyzed throughout the course of this text. Here we summarize and give context to these various behaviors.

### Tail Assisted Self Righting

Animals use their tails in many different ways – see the introduction to [92] for an overview. While tails can similarly provide many benefits to mobile robots, the focus here is exclusively on aerial self-righting. In general, if survivability or required performance is very sensitive to orientation, an inertial tail will be beneficial. Designing a robot with a tail, or adding one to an existing design, has many costs, including the extra mass, volume and extended body envelope as well as the added complexity and new opportunities for failure. Weighing the penalties associated with these multifaceted disadvantages against the benefits of increased maneuverability lies far beyond the scope of this behavioral study whose contribution is to address the much narrower question of how to parametrize the design space and then how to select within it an actuator for a self-righting tail.

### Disturbance Detection

A robot operating in an interesting environment will encounter many obstacles that will disrupt its steady state locomotion, whether it is an insurmountable obstacle like a wall or simply something that requires a different locomotion strategy, such as a staircase. These behaviors are intended to demonstrate the value of adding into a leg contact detector an internal state model patterned on the decades-long tradition of industrial online fault detection [50] (translated more recently into the setting of robot execution monitoring [142] and hybrid systems diagnosis [126]), without the need for an exteroceptive sensor such as a laser scanner. The first behavior is a maze exploration

behavior with the simple obstacle avoidance rule of “turn right”. The second is a stair climbing behavior where the transition to the stair climbing gait is triggered and executed in stride.

In contrast to the methods used here, prior work has relied upon memoryless contact detectors, for example, examining directly the discrepancy between commanded and actual motor shaft output [100, 179] and the difficulty in getting these schemes to function robustly serves as a strong motivation for the present work, and Section 2.2.1 documents the comparative benefit of this internal model approach to diagnostics relative to the memoryless alternatives.

Such difficulties have motivated prior work to undertake the significant effort of instrumenting a direct physical contact sensor [109], but this is a particularly challenging exercise on the continually circulating legs of RHex-style machines<sup>5</sup>. With non-recirculating legs the more modest cost and complexity of leg contact hardware can be justified by the documented benefits — e.g., in climbing unknown vertical substrates [165] or highly irregular level ground surfaces [38] (albeit, note these authors described the physical touchdown sensors as not “adequate”). Even in these settings, running a model based observer will provide a good reference for accurately determining what is an expected disturbance and what is an unexpected disturbance. The broader virtues proposed in the industrial fault detection literature [50] for “analytical redundancy” will likely make the state-based software contact sensor explored here a useful adjunct to such hardware solutions.

### **Leg Fault Recovery**

The most compelling case for legged locomotion arises from the promise of robust adaptation and graceful degradation of mobility performance in mechanically complex and highly varied environments and under conditions of changing or compromised self-health. To date most of the locomotion literature has addressed operation in the extremes: either fixed, consistent terrain wherein a specific gait can be tuned over repeated trials and accumulating experience [36, 98, 154, 165, 181, 188] or wildly varied footing conditions [28, 62, 143, 173] wherein it is not at all clear that the notion of

---

<sup>5</sup> Bringing the sensor signals across the unconstrained rotating legs necessitates some non-contact communications channel. Prior work used a wireless scheme in [109] but this has proven very challenging to maintain in robust operating form. Additional work has also experimented with infra-red (unpublished) and even slip-ring [54] communications bridges between body and legs. All of these hardware approaches can be coaxed into functional operating form, but — as long argued in the “sensor-minimal robotics” literature [31, 118] — each incurs its own additional fragilities and operational complexity.

a gait is even appropriate. We are aware of only two investigations of adaptive legged locomotion in the presumably far more common middle-ground setting of challenging but “modestly” varying terrain: online deterministic gait parameter feedback [179]; and tuned robustness against stochastic perturbation of an open loop stride-map as an alternative to deterministic gaits [29]. In contrast, although the promise of redundancy against individual joint or limb failure ought to be one of the major advantages of legged mobility, with few exceptions [17, 49, 101, 184] there is little legged robotics literature on gait adaptation in the face of compromised self-health.

Inevitably, the question of how to respond to various alterations in the condition of the environment and state of self-repair hinges upon the issue of what sort of sensing is available. One way to detect the changed circumstances that may require an altered locomotion strategy is to instrument the legs with contact, force, strain, or other sensors that measure directly what is happening to them or their environment. However, instrumenting a leg may not be easy and will always have a cost both in terms of money and design constraints. This behavior further pursues the long-standing theme of sensor-minimal robotics [31, 118] applied to reactive locomotion in [100] and continued in [179]. Specifically, Section 2.2 introduces and studies empirically an algorithm that can acquire the relevant information using an estimator driven only by a motor mounted encoder that would typically be included in any actuator package. Other work on loss of limb [49] and reduced limb functionality [184] shows interesting gait strategies, but differs from these results as the presented behaviors make use of no sensory information other than actuators, and employ a robot with a minimal number of actuators for locomotion.

### **Reactive Standing**

Reactive standing (Section 4.3.1) seeks to find a reduction in the power needed for stand-in-place tasks on unmodeled rough terrain [88]. The controller developed is quite simple and implements the intuitive notion that all actuators must resist external load while relaxing any relative imbalances between their individual efforts. However it is not immediately apparent under what circumstances this scheme is correct, nor even that it converges in all application situations. The analytical expression for internal and external torques facilitates the identification of the appropriate operating

conditions and a proof of convergence assuming they prevail. As this proof covers both round and stick legs, the design choice makes no real difference for this behavior. The controller provides up to a 90% reduction in power use compared to an open-loop stand.

Why worry about the power used when the robot is idle? In one urban search and rescue study researchers discovered that for 49% of the robot’s deployment it remained stationary, as the operators needed that time to gain situational awareness [25]. This is corroborated by RHex tests in the Mojave desert, where in at least one specific instance during a trial in March of 2010, the operator paused the robot in a standing posture while deciding how to proceed, causing a motor to burn out after less than a minute. Robots operating on challenging terrain, especially in the heat of a desert, need a low-energy standing posture for health and mission runtime.

### **Pitching Sensor Sweep**

For almost any exteroceptive task, perceptual capability can be increased by extending a sensor’s field of view by moving it. Rather than (or in addition to) adding dedicated “neck” actuators, Section 4.3.2 documents how RHex’s legs can be used to provide a change in pitch, increasing the vertical field of view of any payload. Here the formal setup of the constraints in different contact modes determines analytically both the pitching range as well as the pitching velocity in any mode. Furthermore the dynamical liftoff conditions provide a speed bound for safe execution.

Our empirical example of this general idea features a horizontal (Dorsal) planar laser scanner, a sensor that has no vertical extent and so the only way to build a two dimensional depth map is to move it out of the plane. Prior work on this behavior used an ad-hoc geometric model of the half circle legs to numerically compute an operable scanning range of about  $10^\circ$  [155]. Without an analytical form, the geometry would have to be re-generated in each contact state. It turns out that this behavior benefits from a different contact mode (with the body sliding on the ground). Furthermore while both round and stick legs can reach this same peak pitch, the rounded legs require less torque to do so. Since the kinematics and dynamics are analytically derived with this formalism across all contact states, the pitching velocity can be controlled, and the maximal velocity the behavior can execute without breaking ground contact is found to be higher in the sliding contact mode. The

final behavior has a range of  $\pm 17^\circ$  that can be used for example to more easily detect stairwells and cliffs [86].

## Leaping

Leaping is a key transition from rest to a variety of high energy behaviors. It allows us to engage in nearly pure form one of the foundational questions of robotics: how can we program the transfer of energy in a robot's battery or fuel tank to its mechanical state?

When jumping onto a ledge or across a gap, sometimes a single leap is all that is needed. However the leap can also be used to setup a second step, as exemplified by the behaviors documented in Section 3.4. In that section, the second step will be essentially governed by the dynamics of the SLIP template (i.e., the spring-mass hopper literally instantiated by Raibert [146], and empirically used by all running animals [14]), wherein the state of the SLIP system (height, forward velocity, etc) at apex before a hop determines the reachable set after the hop [6, 72]. Naturally the second hop can lead to a third, and thus the leap can be a quick transition into a high kinetic energy running gait from a seated position.

Beyond its value in reaching across obstacles and setting up other behaviors, there are a number of tasks that may entail a leap as an intrinsic goal. The robot may need to flip over if it is not completely symmetric or if there are payloads only available on one side [152]. It also may need to reach a certain height to gain a better vantage point for its sensors.

## Pitch Control

In addition to considering leaps designed to cross a gap, jump onto an obstacle, or continuing into another leap, this behavior studies a finer use of the actuators over the course of a prescribed leap through the contact modes (notionally motivated by gap crossing or pronking [4, 128]) wherein the robot must at some point engage all its legs on the ground and reach an aerial state with large forward but low pitching kinetic energy.

Section 4.3.3 analyzes three aspects of pitch control for such leaps in — the behavior design (focusing on the splay or the asymmetry in leg angle), the controller design (focusing on stubbing

the toes and using the legs as tails), and the robot design (focusing on the shape and the mass of the legs). The underlying dynamics of a splayed posture is beneficial in several ways. While pushing with both legs equally maintains a level pitch at first, the front leg provably break its ground contact first, and so the robot pitches upwards. A splayed leap (as used before and adjusted via hand tuning [128], touchdown plane control [4], or exhaustive search as in Chapter 3) minimizes this liftoff imbalance. Furthermore a splayed pronk has the added benefit of a higher possible velocity.

The best results for pronking on RHex have all resorted to decelerating or stubbing the rear legs near the end of stance [4, 127]. We show analytically that this negative work does cut down the pitch of the robot, though at the same time bleeding off some of the forward kinetic energy, as demonstrated experimentally in an extreme case.

Next, to illustrate the role of leg design in leaping, the dynamics are combined with the takeoff conditions in single support to derive a bound on maximum forward velocity. This bound suggests that the rounded leg design of RHex enables a higher maximum speed than an equivalent stick leg. Furthermore we consider the inertial effects of the nearly massless legs [7], which in the air act as “tails,” [92, 108], that are able to generate a non-trivial body rotation.

### 1.2.3 Modeling Paradigms

In addition to developing new platforms and behaviors for those platforms, this thesis advances several modeling paradigms summarized as “self-manipulation” models. This section gives a brief background on these models.

#### Self-Manipulation and Manipulation

*Self-manipulation* is the process of using one’s limbs to rearrange one’s body (to follow the opening line of [119]) [99, 115, 153], broadly including any activity that alters a robot’s configuration, whether or not it affects the center of mass frame. Figure 1.3 suggests how the self-manipulation problem (Fig. 1.3f) relates to more traditional manipulation (Fig. 1.3a) and locomotion (Fig. 1.3d) problems. Joining these perspectives motivates our exploration of the long noted more general

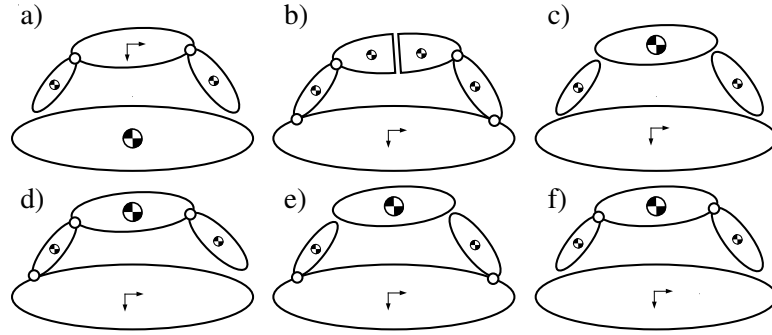


Figure 1.3: Various models for a closed-loop kinematic chain: a) manipulating the world with your feet, b) “broken back” – symmetric robots that meet in the middle, c) free body diagram, d) “walking model” – single open chain, e) being manipulated by the world, f) self-manipulation (used here).

duality between locomotion and manipulation<sup>6</sup> [10, 115, 186, 187], leading to dual-use actuators that can locomote and manipulate [11, 111, 121, 122, 140, 166, 174], as well as lending insight into locomotion through manipulation [10, 160] or the reverse [21, 73].

Following that tradition, the self-manipulation methodology appeals to the key formulation of the manipulation literature, the “grasp map” or “grip transformation”,  $\mathbf{G}$  [120], which relates wrenches at the contact points to wrenches on the object.<sup>7</sup> Specifically, in Section 4.1.2, we adopt the same modeling choices that lead to this map in the traditional setting. However in self-manipulation, the robot must itself move relative to the inertial world, and we focus attention on the consequences of this departure from the manipulation framework.

Of course such modeling decisions are not required to arrive at accurate kinematics or dynamics. Consider the robot in Fig. 1.3, a single kinematic chain similar to a 4 bar mechanism. The robot could be “cut” in many ways, in order to determine the identical e-DOF (degrees of freedom, here  $e = 1$ ) from various  $q$ -dimensional open-loop dynamics and  $c$  constraint forces. For example, one might make: one cut, at a toe ( $q=3$ ,  $c=2$ , Fig. 1.3d, common in walking analysis [37], [162, Ch. 16]) or at the robot center ( $q=4$ ,  $c=3$ , Fig. 1.3b, producing strong symmetries); two cuts at the hips ( $q=5$ ,  $c=4$ , Fig. 1.3e, akin to parts feeding [187]) or at the toes ( $q=5$ ,  $c=4$ , Fig. 1.3a, direct instantiation

<sup>6</sup> E.g., “a different way to view a person walking on a globe is to say the person is manipulating the globe with his feet,” [186].

<sup>7</sup>We will adopt the specific notation introduced in [134], though these ideas coincide with the formulation in [13, 119, 120, 137, 162] — and, indeed, most works on the subject make similar modeling decisions.

of manipulation [10, 160], as well as Fig. 1.3f, sometimes called a “floating-base” [48]); four cuts, at the joints ( $q=9$ ,  $c=8$ , Fig. 1.3c, a free body diagram). Each variation of this example results the same one-DOF mechanics model, however cutting at the toes (Fig. 1.3f) admits simple expressions for friction at each toe (as opposed to at the hip or body, Fig. 1.3b,e), generalizes across all contact conditions (as opposed to the walking model which must be separately instantiated in each mode, Fig. 1.3d), and with far fewer states and constraints than the more general problem (Fig. 1.3c).

Contrary to the oft encountered adage, locomotion is not the *same* as manipulation. To any reasonable level of precision, a legged robot is not moving the world with its feet (i.e. the “object” is Earth,<sup>8</sup> Fig. 1.3a, [10, 160]), nor is the world moving the robot (i.e. grounded legs reaching up and manipulating the robot Fig. 1.3e, [187]). In particular there are three main differences between the usual manipulation formulation and the self-manipulation setting: the robot is the object (and so the “Palm” and “Object” frames are coincident, as in Fig. 4.1); we are concerned with motion of the robot and not what the robot is touching (and so the grasp map must be composed with an appropriate reflection); and the dynamics of the legs and body are not decoupled (so in particular the mass matrix is no longer block diagonal, complicating the dynamics). Why bother following a manipulation formulation if the problems are actually different? While not every result carries over exactly, the problems are similar enough that matching as closely as possible the modeling decisions that have emerged from this very successful and mature body of work facilitates the reuse, or slightly modified extension, of several valuable ideas and results (e.g. rolling contact [30, 97, 131, 147, 151], Section 4.1.6).

## Physical Assumptions

This section gives a brief introduction to the physics problems and models used in this thesis, and list a few key references. For a much more complete bibliography of such issues see e.g. [19, 56].

This thesis models self-manipulation systems (and, by analogy, manipulation) using a hybrid systems paradigm, detailed in Section 5.2, which will assume instantaneous transitions (as opposed to a continuous contact or compliant contact model [56]). The class of hybrid systems considered

---

<sup>8</sup>“The planet Earth’s radius and mass are  $R_0$  and  $M_0$ ,” [10].

in Section 5.2 are formally a specialization of the *hybrid automaton* of [113, Definition II.1]. In the dynamics of self-manipulation, the dimension of distinct domains varies depending on the number of active constraints (and hence generally varies between domains), and the codimension of a *guarded* event corresponds to the number of distinct mechanical contacts established or broken through its activation (and hence generally can be arbitrary depending on the number of independent constraints in the system).

The hybrid system uses the active contact constraints to define the discrete state [19, 78, 112]. Note that persistence of contact is merely a modeling assumption that usefully describes the intuitive notion of bodies touching for some finite amount of time. However even when starting with a simple Lagrangian hybrid system without persistent contact states it appears to be useful to add such states to allow executions to continue beyond a Zeno equilibrium [1, 138]. In contrast to the formulation presented here, it is possible (and can be computationally efficient) to instead use a “time-stepping” or “impulse-based” method which accounts for contact interactions only using impulses by integrating applied forces over small time-steps [3, 130, 168]. These methods allow contact constraints to be added or removed at any time-step, but only once per time-step. This is an advantage as it is one way to avoid both Zeno phenomena as well as other apparent contradictions between forces and impulses that can arise (as described below), but at the cost of persistence of contact, one of the simplifying modeling assumptions of interest in this thesis.

Any formulation that allows for persistent contact must decide which contacts to make active and which to remove<sup>9</sup>. When there is no impulse (i.e. no constraint to add, but one or more constraints have violated the unilateral constraint cone), the removal process has been commonly modeled by a complementarity problem on the contact force and separating acceleration, where in the simplest case of a single contact point with zero or negative contact force it is simply removed. This complementarity problem is well formed for rigid bodies, though it does raise certain paradoxical consequences for deformable bodies [33]. When there is an impulse induced from one or more contact constraint becoming active, other constraints might have to be removed if they would require

---

<sup>9</sup>The removal ends up being the harder question, as “there is no problem in deciding when and which constraint to add to the active set since there is a constraint function to base the decision on. The problem of dropping constraints is more delicate...” [112, p. 283].

a negative impulse to remain. When invoked as a modeling principle, complementarity precludes the pairing of contact induced impulses with separation velocities. The complementarity conditions lead to a unique solution for plastic frictionless impact [41, 42, 71, 80, 172]. Unfortunately further generalizations can lead to inconsistencies and ambiguities [33, 78, 157]. The existence and uniqueness of a solution will therefore have to be separately established by each physical circumstance that brings friction into play in a plastic impact model — or merely be assumed. For instance, for the physical circumstances assumed in Sections 4.1.11 and 5.1.5, there is no conflict, as all contact points with friction are attached only to massless links. However, massless legs introduce new problems into the complementarity problem.

The massless leg condition in general, as introduced in Section 4.1.9 and 5.1.1, and also used in countless prior works (e.g. [15, 57, 95]), allows for the neglect of certain states deemed inconsequential to the dynamics of interest when unconstrained (of course, the appropriateness of this neglect is task dependent rather than in any way intrinsic to the underlying physics, c.f. Section 4.3.3 or [7]). Indeed a massless leg that is not touching the ground is unconstrained and its position can be taken as arbitrary (or regarded as evolving according to dynamics sufficiently decoupled as to be considered independent), as used in the behavior analysis in Section 4.3.3. However the complementarity condition as listed in e.g. [172] is ill-posed in the absence of mass since there is no well-defined separation velocity (and therefore nothing precluding all massless contact points from always separating). In Section 5.1.3 we propose the alternate condition that were it to maintain contact it would have had a negative force, and prove in Theorems 5.5–5.6 that this is equivalent to the usual complementarity condition when the inertia tensor is non-singular.

The usual Newtonian impact law (as in [35, Eqn. 3], [48, Eqn. 11.65] and many others) involves inversion of the inertia tensor, which would preclude the possibility of massless limbs. Therefore in Section 5.1.2 we rework the usual law to use the mass-weighted left inverse (defined in Section 5.1.1) which simplifies and generalizes the impact law definition for singular mass matrices. Even if there are no truly massless links, a nearly massless body segment will yield a poorly-conditioned inertia tensor (leading to similar formulations for continuous time dynamics used in e.g. [72, Sec. 4.3] [48, Eqn. 3.17]). We prove in Theorem 5.3 that the impulse we compute is con-

sistent with the result obtained from the usual formula in the limiting case as some subset of segment masses tend to zero. This plastic impact law can be thought of as a mass-orthogonal projection onto the constraint manifold as used in e.g. augmented Lagrangian techniques [9, Eqn. 25].

In this thesis we will restrict our attention to systems modeled as exhibiting only perfectly plastic impact. This avoids certain inconsistencies, but more importantly we claim plastic impact provides a more useful model of the robotic systems of interest. Elastic impact is clearly needed in some robotics applications such as juggling [22, 156], tapping [76] or ping-pong [2], but plastic impact, where there is no restitution and therefore no separation velocity after impact, is a more desirable model for most forms of locomotion (when it is important to keep ones feet on the ground) [34, 182] and manipulation (when it is important to keep one’s fingers on the object) [34, 177].

Impulses arising from impacts (both plastic and elastic) generally break existing contacts. For example an impulse imparted to the underside of a rigid block resting on the ground in a gravitational field must cause it to leave the ground for a small time interval no matter how weak the impulse or how massive the block. In truth the block is not rigid and the impulse is temporally distributed; modeling the resulting subtle deflections would greatly complicate the model. Instead we propose in Section 5.1.4 an additive *pseudo*-impulse that approximates the work performed by gravity and other continuous-time forces over a short time interval, used only in determining which contacts to break. The pseudo-impulse eliminates certain Zeno executions by allowing the system to transition to a constrained mode after finitely many transitions, as in [1, 138]. In addition the pseudo-impulse eliminates other other evidently unwanted transitions, such as the example of the simple block that lifts off the ground. It allows the system to seamlessly transition from what might be considered *quasi-static* to *dynamic* operating regime. In the example of the rigid block, with this pseudo-impulse there is now a minimum threshold on impulse magnitude below which the system may be considered quasi-static and the block remains on the ground, but above which the system dynamics are important and the block detaches from the substrate. A different approach to considering such forces has been to determine a variable coefficient of restitution [145] (while here there is no restitution at all and the pseudo-impulse will not be actually applied to the system). A similar effect is also seen for impulse-based simulations [3, 130, 168], which always consider forces over

small but finite time-steps. Under these time-stepping schemes the magnitude of this effect is not an independent parameter as it will be proportional to the small duration of a single time-step. Furthermore we believe the explicit introduction of the pseudo-impulse here will afford a much clearer hybrid systems formalism.

While Section 5.1 focuses on the impact problem, which friction greatly complicates [96, 136, 170, 176, 177], even simulating the continuous-time dynamics of rigid bodies with friction can be difficult (formally  $NP$ -hard [8]) due to the possibility of “jamming” events [47, 123], first attributed to Painlevé [141]. In this thesis strong assumptions about frictional contact enable integration of the dynamics as a DAE (as opposed to the implicit time-stepping approach pursued in [3, 130, 168]). Though we have maintained those assumptions through most of the thesis, in Section 5.1.5 we show examples where this assumption is a poor model of the physics and propose an extension that allow the toes to slip while still avoiding these jamming problems. The hybrid system defined in Section 5.2 is written so as to allow for contact points that can stick or slip. For more general systems (in particular those that are not well modeled by the assumptions of Section 5.1.5) this problem can be solved by allowing impulses at times without collisions, with such jamming events considered an extension of the guards and reset maps presented here; see also “Is Painlevé a real obstacle?” [19, Sec. 8.1].

## Chapter 2

# Actuators

### 2.1 Motor Selection

Motor sizing for legged robots poses challenges distinct from those presented in most other systems that perform mechanical work. Traditional methods [94], involve selecting an actuator with an appropriate power rating geared to work on a load specified at one or a very few fixed operating setpoints (paired speed torque operating values). For example in order to select a motor for an industrial robot arm, the maximum weight of the payload will dictate the required torque, which when combined with the desired speed of operation will provide a set operating point, whereupon the choice of a motor (and gearbox) that can meet this demand is straightforward.

As suggested by Figure 2.1, systems required to deliver multiple or more complex work loops will not present the designer a single operating setpoint. For example, the robotic tail task [92], to be discussed further in Section 2.1.1, does not entail any particular minimum torque specification (e.g. as might be required were there a need to work against gravity), but, instead, imposes an overall completion time for repositioning a specified inertial load, in a manner most succinctly expressed by a dynamical control problem whose solution imposes a non-trivial functional constraint on the motor parameters. In the somewhat more complex problem setting of vertical running [44, 171], the imposition of a target task dynamics conferred by an identified template [52] provides a dynamical work-loop specification. It can be shown that these dynamics offer a precise enough task specifica-

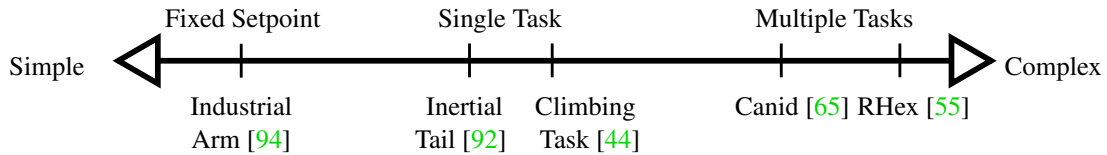


Figure 2.1: A summary of motor selection techniques with some example domains.

tion as to imply the necessity of additional passive dynamical elements in the power train mitigating peak power requirements otherwise unachievable by any COTS actuator [114]. In such settings, task specification via target dynamics (typically along with various problem-specific constraints) still yields a tractable design problem, affording direct comparison of the relative performance on some task metric of very different motors by relaxing the requirement that they all complete the task in the same way (i.e., via some artificially imposed trajectory on the speed-torque plane) [44].

However versatile robots such as RHex are from their very inception intended to perform different tasks at different times. Balancing the performance requirements and constraints of multiple tasks performed in a variety of operational environments precludes using either the fixed setpoint or single dynamical task specification methods. RHex [154] must actuate its limbs over an unusually wide operational range, including slow speed activities requiring large leg torques, such as clambering over rocks and climbing stairs, as well as high speed activities with moderate torques, like running at high speeds or walking with high duty factor gaits, all without overheating [44, 55, 88, 129]. There are few non-robotics applications in which a motor operates at both its stall torque and its no-load speed within a short period of time. This spectrum of motor selection tasks is summarized in Figure 2.1. The next two subsections will work through the motor selection process for both a single task domain, adding a tail, and then for a multiple-task domain, the leg motors in X-RHex.

### 2.1.1 Motor Selection for a Tail

Adding an inertial tail to RHex could enable a variety of new behaviors, however here the focus will be on reorientation in free-fall. The tail created for RHex [92] is an appropriately scaled approximation to that of Tailbot [32], both comprising an approximate point-mass made of brass at about



Figure 2.2: XRL [65] with a new tail, and with approximately sized image of Tailbot [32, 108]. *This figure originally appeared in [92] is included here courtesy of Tom Libby and Ryan Knopf.*

1/10th body mass, attached to a carbon fiber tube of about one body length, as seen in Figure 2.2. While Tailbot was a special-built machine, the tail for RHex must be added to an existing platform as a modular payload [65], and as such the range of motion is significantly lower than Tailbot’s, especially given a safety margin to avoid collision with the body. To compensate, the RHex tail design targets a slightly higher effectiveness  $\varepsilon = 1.29$  (this is the ratio of tail to body rotation [92]) so as to afford the same  $90^\circ$  body correction capability as Tailbot.

To mitigate the integration task, both Tailbot’s and XRLs tail actuators were for simplicity chosen to be the same as their wheel/leg motors. But to maximize the performance of the tail, a more careful study is warranted. In the spirit of [44], we can define a single dynamical task and a number of performance metrics, and then calculate the optimal performance of all available motors [124]. In that paper, the optimal gear ratio was calculated via numerical optimization on one performance metric — here we find an analytical solution<sup>1</sup>. The power,  $P$ , is given for each motor and we now

<sup>1</sup>Anecdotally, having this analytical solution to the gear ratio reduced the simulation time for all 1,546 motors considered from 171s to 0.175s.

seek to determine the minimal completion time,  $t$ , (parametrized by morphology) for a rotation  $\theta_0$  as a function of power rather than the inverse (to find the minimum power needed to complete a rotation in a fixed time). The optimal no load speed,  $\omega_m$ , (a proxy for gear ratio) and resulting completion time,  $t$ , functions are (see [93] for full derivation),

$$\omega_m = \left( \frac{k_\omega \theta_0 P}{I_b} \left( 1 + \frac{1}{\varepsilon} \right)^2 \right)^{1/3}; \quad t = \left( \frac{k_t \theta_0^2 I_b}{P} \left( 1 + \frac{1}{\varepsilon} \right) \right)^{1/3}. \quad (1)$$

where  $I_b$  is the body inertia, and the constants  $k_\omega \approx 3.156$ ,  $k_t \approx 1.547$ . Other metrics to consider are physical (size, mass), electrical (current and voltage available), and thermal. The thermal cost of a tail for inertial self-righting is in general small due to the very small time scales, however some motors may still overheat (see below for more detailed thermal modeling). Now, following [44], whose numerical optimization step does not require the restriction to the linear dynamics used to derive (1) and which can incorporate these additional metrics, the performance of all commercial motors [124] can be compared. Out of the 1,546 motors considered, 82 of them met the length ( $< 30\text{mm}$ ), weight ( $< 200\text{g}$ ), and minimum completion time ( $< 0.5\text{s}$ ) constraints. Of those, the chosen motor was the third fastest, only 22% slower than what would be the optimal motor. The optimal gear ratio for our motor would be 27:1, the 28:1 gear ratio used is the closest commercially available<sup>2</sup>.

As an empirical validation of design (including the motor selection), we conducted a series of initial tests (Figure 2.3) to see how large a body rotation can be achieved by a relative tail rotation of about  $155^\circ$ , which is limited by geometry. The robot was dropped nose first from a height of 1.36m (over 8 times the standing height and 2.7 times the body length). The body angle was measured from an IMU and regulated to horizontal by a simple PD controller. The motor was able to rotate the tail, and the robot, in 0.35 seconds to within  $5^\circ$  of level, or just more than one body length of fall, and maintain that with no more than  $4^\circ$  overshoot. This test used the entire  $155^\circ$  range of relative tail motion, rotating the body a maximum of  $89.7^\circ$  before hitting the hard stop. From these two final positions we can calculate an average  $\varepsilon_n = 1.38$ , which matches our approximate estimate

---

<sup>2</sup>This analysis could be made more accurate by considering a current limit and more complicated controller.

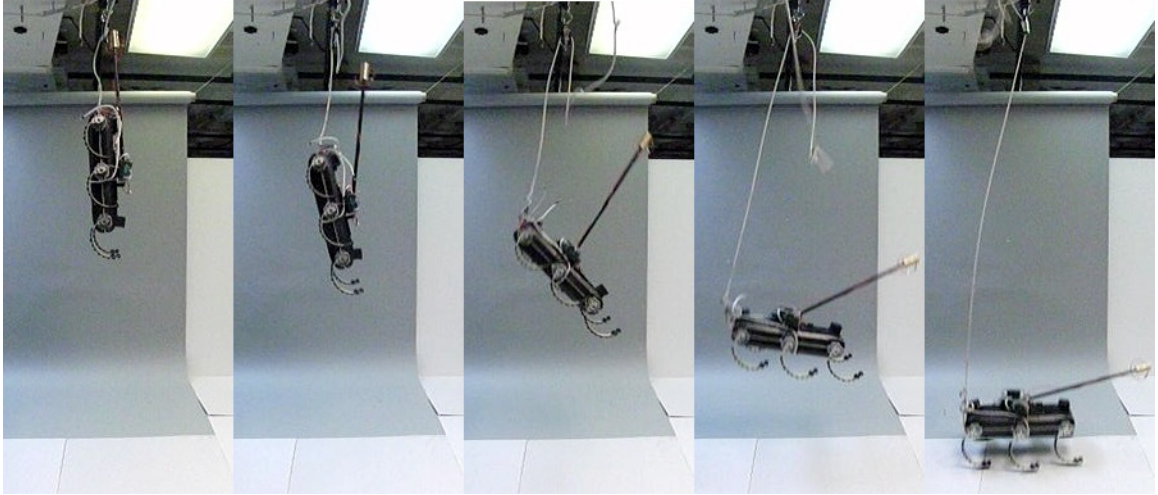


Figure 2.3: XRL self-righting in a fall.



Figure 2.4: XRL surviving a run off a cliff outdoors.

of  $\varepsilon = 1.29$  to within 7% and is reasonable considering the errors involved in measuring inertia [148] and manufacturing. As a comparison, the robot was also dropped with no tail activation, causing the front two legs to snap as well as some minor internal damage. Thus if the robot tasks requires a fall from this height, it is definitely survivable assuming it successfully reorients to land within about  $5^\circ$  of level<sup>3</sup>.

To demonstrate this new ability for XRL in a practical task, the second set of experiments was conducted outdoors, running along and then away from a 62 cm (3.8 times the hip height or 1.2 body-length) cliff. The robot's inertial sensors detect the cliff upon initial body pitch, then actuate the tail according to the previously described closed loop control policy, and the robot lands on its feet (Figure 2.4). Another test with XRL running from a cliff with a *passive* tail confirmed that it would land nose first.

<sup>3</sup>This is an empirical bound still subject to further tests.

### 2.1.2 Motor Selection for X-RHex

Our most reliable understanding of a RHex-like machine’s motor operating regime comes from Research RHex data. While our ongoing research entails the development of more advanced simulation and analytical tools for motor sizing in these multiple-task applications, we have chosen motors for X-RHex based on empirical data from Research RHex.

Our first significant design decision was to support brushless motors. The principal downside to brushless technology is the complexity of controlling these motors [117]. The commercial motor controller boards described in [55], however, manage most aspects of brushless motor commutation and control, and provide an extensive API, trading the cost of design effort and hardware complexity for the effort of learning how to effectively use the manufacturer’s motor control interface. While the efficiency and service life benefits of brushless motors are often touted [117], the primary advantage, for our application, is the option to use high-torque, flat “pancake-style” brushless motors offered by Maxon Motors<sup>4</sup>, as seen in Figure 2.5. Inverting the design of most “pencil” motors, these pancake motors consist of an internal stator containing the windings, surrounded by a rotor containing a permanent magnet ring. The rotor is part of the back of the motor and is exposed while spinning. Because of the large rotor diameter, the motors are very short and light (110g, less than half the mass of an equivalently powerful pencil motor), though with a slower mechanical time constant due to the increased rotor inertia. The small footprint and tiny mass of these motors is overwhelmingly appealing in a mobile robotics application, and, following team experience with RiSE V3 [63], provided us with perhaps the strongest incentive to support brushless technology.

Within the pancake form factor, there are a number of motor options. We limited our choice to those nominally specified to deliver 50W, exceeding the Research RHex motor power specification (20W) by more than a factor of 2. In the computation of motor parameters, care was taken on a number of points: first, given parameters for each motor were compensated based on our battery voltage, as each motor is specified relative to a given nominal voltage, while X-RHex’s electrical system was designed around a 37V battery. Therefore, we recompute relevant motor parameters

---

<sup>4</sup>Maxon provides a collection of motors in finely grained size and power increments; we have not encountered other manufacturers with similarly comprehensive options at the scales and quality of interest to us.

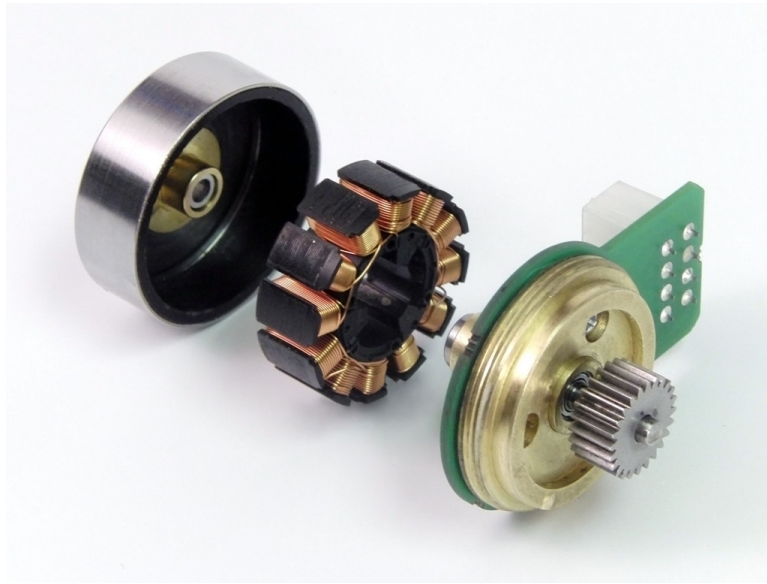


Figure 2.5: A disassembled view of the brushless motor. *This figure originally appeared in [55] is included here courtesy of Ryan Knopf.*

using a voltage of 37V, using the standard linear motor model as presented in [144]. Using a voltage different from the nominal voltage specified by Maxon in their product line documentation affects the computation of a motor’s apparent stall torque and no-load speed, though not the motor’s maximum continuous torque, which is governed purely by the thermal influence of current running through the motor. Second, our motor controllers limit peak instantaneous motor current to 20A. However, with the 37V supply on X-RHex, some motors are capable of drawing more than 20A at low speeds. Thus, we also denote an “Achievable Stall Torque,” the torque that corresponds to the controller’s maximum current output. Our chosen motor dramatically exceeds the Research RHex motor in its achievable stall torque (670mNm vs 257mNm) and maximum continuous torque (83.1mNm vs 26.7mNm), though it has a slightly lower no-load speed (10314rpm vs 13600rpm). In principle, the X-RHex motor is capable of much higher power output than its predecessor. However, motor thermal constraints pose real operational limitations and are harder to assess without a specification of the target task domain. We discuss thermal behavior in greater detail in Section 2.1.3. The parameters for our chosen motor are shown next to those of Research RHex in Table 2.1.

Nearly as important as the selection of the motor is the selection of a gearbox to accompany it.

Attribute	Research RHex Motor	X-RHex Motor
Type	Brushed DC	Brushless
Maxon Part Number	118752	251601
Battery voltage (V)	24	37
No load speed (rpm)	13600	10314
Achievable stall torque (mNm)	245	670
Continuously sustainable torque (mNm)	23.1	83.1
Mechanical Time Constant (ms)	4.28	11.8
Length (mm)	54.5	20.9
Width (mm)	25	45
Mass (g)	130	110

Table 2.1: Motor Comparison

We initially chose an 18:1 gearbox as this results in dramatic, across-the-board improvements to the speed and torque capabilities of the motor/gearbox combination in X-RHex when compared to those used in Research RHex, despite boasting a slightly lower total mass (see Table 2.2 and Figure 2.6a). However, when tested in X-RHex, we found that we had to restrict motor current to each motor to 9A for thermal safety (see Section 2.1.3 for a further discussion of thermal considerations). This resulted in the torque and power characteristics in Figure 2.6b. Notably, restricting the X-RHex motor to 9A results in substantially lower torque and power output capacity than Research RHex at low operating speeds. This handicap manifested itself during high-torque, slow speed maneuvers such as standing up or turning in place. In order to boost torque and shift peak power output to lower speeds, we switched to a 28:1 gearbox with an identical form factor. The properties of the same motor with this gearbox are also depicted in Figure 2.6. The increased gear ratio ensures that we are able to supply about the same amount of torque as Research RHex at low speeds and significantly more torque than Research RHex at moderate speeds, with top speed suffering slightly. We suspect, owing to the fact that X-RHex can generate larger torques than Research RHex until very near its no-load speed, that X-RHex will have little trouble matching Research RHex in gait speed during actual, loaded operational regimes.

The final consideration in choosing a gearbox was ensuring that the mechanical device was physically capable of withstanding the high-torques generated by X-RHex. Unlike high speed mo-

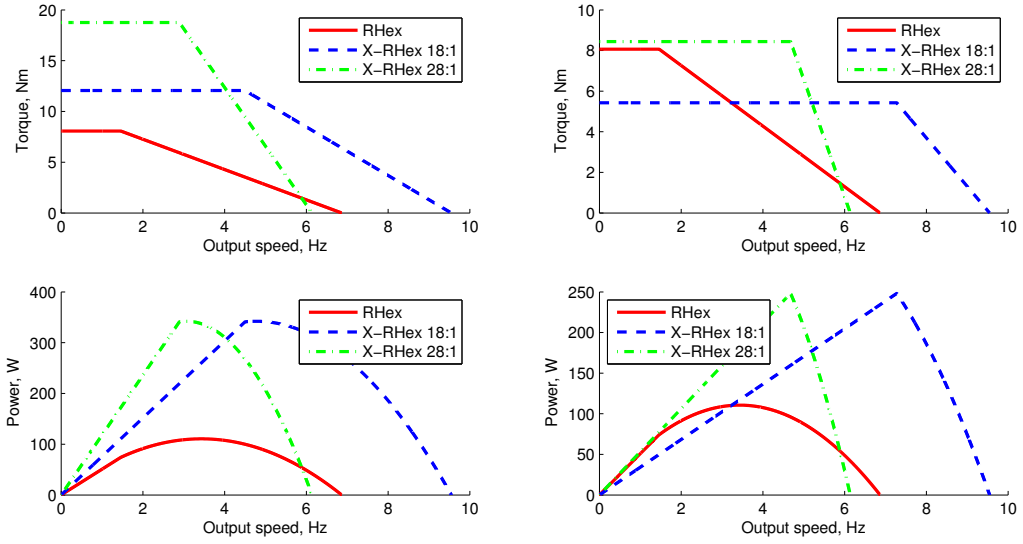
Attribute	Research RHex	X-RHex 18:1	X-RHex 28:1
Gearbox Type	Planetary	Planetary	Planetary
Maxon Gearbox Part Number	166163	326659	326662
Gear reduction	33:1	18:1	28:1
Peak permissible torque (Nm)	3.4	6	6
Continuously permissible torque (Nm)	2.25	4	4
No load output speed (rpm)	412	557.5	358.39
No load output speed (Hz)	6.86	9.25	5.94
Achievable output stall torque (Nm)	8.1	9.9	15.4
Continuous output torque (Nm)	.76	1.2	1.9
Gearbox Mass (g)	162	178	178
Combination Mass (g)	292	288	288

Table 2.2: Motor and Gearbox Combination Comparison

tor applications in which stall torque is rarely reached, we expect X-RHex to be approaching stall torque with regularity, demanding very large torques from each gearbox. Thus, we chose a “high-power” gearbox from Maxon’s line. When compared to its ceramic alternative, the high-power gearbox increased the peak permissible torque output from 3.4Nm to 6Nm and continuously permissible torque from 2.25Nm to 4Nm. While our motor, after the gear reduction, is capable of supplying almost 16Nm of torque in stall (greatly exceeding the 6Nm limit imposed by the gearbox), our expectation is that, with a modicum of care in current limiting, we may prevent extended operation at stall and that Maxon’s thresholds will never be thoroughly tested. Indeed, Research RHex has a similar conundrum: its 8.5Nm stall torque is more than double the 3.4Nm peak torque output capacity of its gearbox, yet gearboxes are damaged only very infrequently. The design specifications for the motor and gearbox combinations of Research RHex and X-RHex (with both gearbox iterations) are given in Table 2.2.

### 2.1.3 Thermal Considerations for Motor Selection

Power density is one of the most important determinants of dynamic legged locomotive performance. Accordingly, we are strongly motivated to extract maximum power output from whichever motors we choose. The large amount of electrical power these motors consume causes heat to build up and



(a) X-RHex restricted to 20A, Research RHex to 15A. These values correspond to the current limits imposed by the respective motors' controllers. (b) X-RHex restricted to 9A, Research RHex to 15A. The 9A limit placed upon X-RHex is empirically derived; above this limit we find that, in normal operation, the motors tend to heat up too quickly.

Figure 2.6: The output torque-speed and power-speed profiles of the three motor/gearbox combinations, for two different current limits. *This figure originally appeared in [55] is included here courtesy of Goran Lynch.*

can, if left unchecked, cause the motor coils to overheat and become damaged. However, the core motor temperature can not be measured directly: to estimate it, we build an observer in the form of a second-order lumped-element thermal model [45] using parameters given by Maxon [124]. This model is used both offline, to predict the thermal impact of a given behavior, and online, to monitor motor temperature as the robot is operating. The model is most easily visualized as a circuit consisting of two capacitors and two resistors, a current source, and a voltage source, as pictured in Figure 2.7. The capacitors are referred to as “thermal masses” ( $C_{th1}$  and  $C_{th2}$ ), while the resistors are “thermal resistances” ( $R_{th1}$  and  $R_{th2}$ )<sup>5</sup>. Voltages represent temperatures, while currents denote the flow of thermal energy. Thermal resistances characterize the impediment to heat transferring between adjacent thermal masses (in this case, different parts of the motor), while thermal masses

<sup>5</sup>Maxon specifies two “thermal time constants” ( $\tau_{th1}$  and  $\tau_{th2}$ ) instead of thermal masses; these are just the thermal resistances multiplied by the thermal masses.

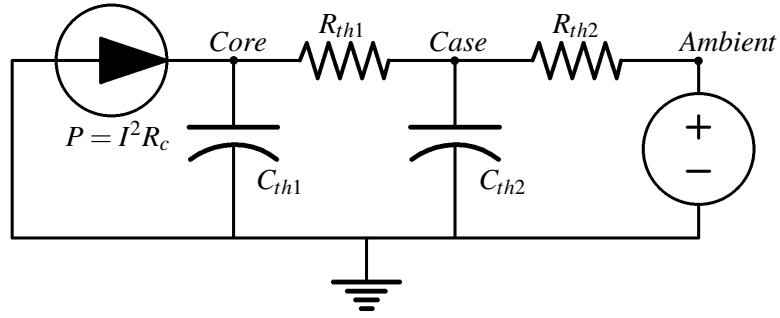


Figure 2.7: The thermal model represented as an equivalent circuit.

indicate the amount of energy that is required to heat up a given motor element. The voltage source represents the ambient temperature around the motor, which is different from the unchanging reference temperature represented by ground.

The amount of power lost over the motor coils' resistance is  $I^2 R_c$ , where  $I$  is the motor current and  $R_c$  is the terminal resistance. This heat source is the “input current” to our thermal circuit model. The continuous current limit given in the datasheet is derived from this model and the maximum winding temperature of  $125^\circ\text{C}$ .

Combining the thermal resistances with a motor torque constant  $k_M$  and selected gear ratio  $G$ , we can compute two derived value constants for each motor that we refer to as the “heat coefficient” for the core and case:

$$H_{core} = \frac{R_c R_{th1}}{k_M^2 G^2}$$

$$H_{case} = \frac{R_c R_{th2}}{k_M^2 G^2}$$

Both of these values have units of  $\frac{^\circ\text{C}}{(\text{mNm})^2}$ , and can be thought of as the relative steady-state temperature rise for a given (squared) torque demand at the output of the gearbox. The first measures the temperature rise of the motor core relative to the case temperature, while the second is the temperature rise of the motor case relative to the ambient temperature — to get the temperature rise of the motor core relative to the ambient simply add the values together. These values along with the two thermal time constants completely describe the thermal properties of a given motor, and are

Attribute	Research RHex	X-RHex 18:1	X-RHex 28:1
Thermal Time Constant Core (s)	12.4	16.7	16.7
Listed Thermal Time Constant Case (s)	910	212	212
Measured Thermal Time Constant Case (s)	551	710	710
Heat Coefficient Core $\frac{^{\circ}\text{C}}{(\text{mNm})^2}$	9.9	9.4	3.9
Listed Heat Coefficient Case $\frac{^{\circ}\text{C}}{(\text{mNm})^2}$	44.8	8.9	3.7
Measured Heat Coefficient Case $\frac{^{\circ}\text{C}}{(\text{mNm})^2}$	17.2	10.2	4.2

Table 2.3: Motor and Gearbox Thermal Comparison

summarized in Table 2.3.

The thermal model can be used to run a simulation of what we expect the motor’s core temperature to be given a certain torque demand. As shown in Figure 2.8, we see that the Research RHex and X-RHex motors with 18:1 gearbox perform about equally well in the short term, with the X-RHex motor running a little cooler in the long run. This is due to the fact that they have similar core thermal constants, and Research RHex has both a higher case heat coefficient and case time constant. The X-RHex motor with 28:1 gearbox performs significantly better than either. The efficiencies of the brushless motor in the 18:1 case are almost balanced out by the better thermal characteristics of a brushed motor. Additionally, the low gear ratio means that the motor needs to generate more torque (and correspondingly more current) than an identical motor with a larger gear ratio.

The parameters supplied by Maxon are for a bare motor, and do not take into account the thermal effect of a gearbox. Since the gearbox is mostly metal and attached directly to the motor’s case, it acts as a heat sink. To account for this, we conducted a controlled experiment to measure the thermal mass of the case and thermal resistance between the case and the air, thus assuming that the gearbox acts as an addition to the case. The gearbox could be represented separately using an additional thermal mass and thermal resistances, but we chose to employ the simple second order system as it delivered accurate empirical results during testing. We calculated an estimate for the thermal mass and resistance and used those parameters for our model. See Figure 2.9 for a comparison of the

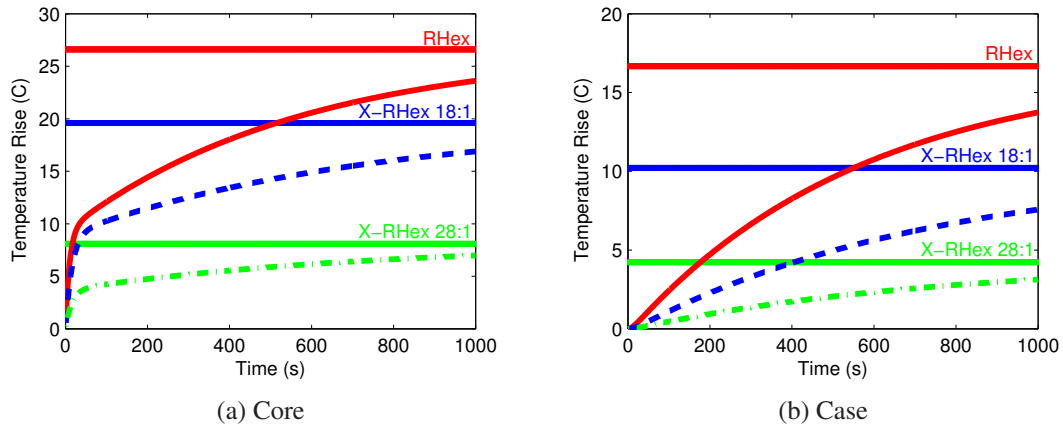


Figure 2.8: Core and Case temperature simulations for a fixed torque demand. Horizontal lines represent steady state temperature. Note that in the short run, X-RHex with the 18:1 gearbox runs at approximately the same temperature as Research RHex

experimental and simulation results, and Table 2.3 for the numerical values<sup>6</sup>. The model fits the data with an RMS case temperature error of about 1°C.

There is a significant difference in the way the gearbox attaches to the motor on the brushed Research RHex motors and brushless X-RHex motors, resulting in substantially divergent thermal performance. The brushed motor coils are physically connected to the case/gearbox via bearings, brushes, and output shaft; each of these connections facilitates heat transfer between coils and gearbox. In contrast, the brushless motor coils on X-RHex are stationary, attached only to a fiberglass circuit board which acts as a thermal insulator, partially isolating the coils from the gearbox, as seen in Figure 2.5. As a result, while the gearbox on a brushless motor does act as a heatsink, the thermal performance improvement is substantially more pronounced when using brushed motors. Indeed, anecdotally, the gearboxes on Research RHex become much warmer than the gearboxes on X-RHex, suggesting that they are doing a better job of sinking the heat generated in the coils. The calculated thermal resistance between the case and ambient for a Research RHex motor is less than half the thermal resistance listed for a stock motor with no gearbox, while the X-RHex motor had no improvement because of the poor physical connection to the gearbox. In both cases the calculated thermal mass of the case was much more than the listed thermal mass of a stock motor. This leads

<sup>6</sup>Note that the “List” values are for a bare motor as reported by Maxon, while “Measured” were calculated by the authors and there is a slight discrepancy in some values that can be attributed to differences in methodology

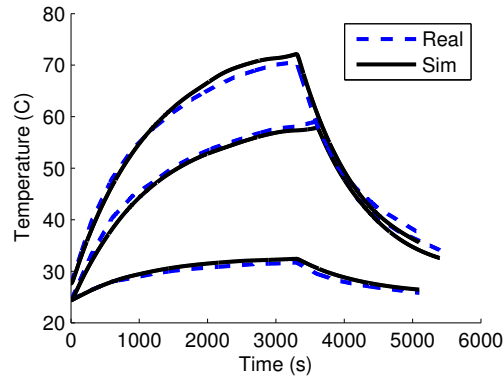


Figure 2.9: Comparison of measured and estimated case temperatures for three different fixed current demands followed by a cooling period (at 3300 seconds).

to the modified  $\tau_{ih2}$  for Research RHex being lower than stock, while for X-RHex it is higher than stock. These measured parameters were used when generating Figure 2.8.

While X-RHex motors with 18:1 gearboxes operate at slightly lower temperatures than Research RHex motors when tested on the bench (normalized for a given torque output), they run at higher temperatures on the robot. This lead us to limit the current to no more than 9A during normal operations. We are investigating multiple causes of this discrepancy, but the increase in gear ratio has substantially reduced the temperature of X-RHex motors in normal operation. Our switch from from an 18:1 to a 28:1 gearbox reduces the rise in motor temperature to achieve a given torque by 60% (as seen by taking the ratio of heat coefficients in the last two columns of Table 2.3).

## 2.2 Dynamic Motor Modeling

This section describes a software contact-event sensor designed to trigger a legged gait recovery transition. There are two principal contributions in this section: first, we adapt the traditional control theoretic framework of deterministic dynamical fault detection and recovery [50] to identify the need for a transition (as summarized in Figure 2.10); second, we apply topologically informed gait control policies to achieve a smooth transition to desired gait timings that produce stable locomotion. In doing so, we take a small but important, novel step toward developing an operational framework for guarded autonomous legged locomotion in general terrain.

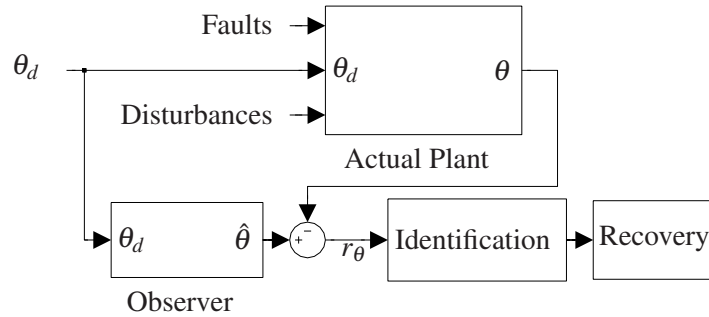


Figure 2.10: Overview of fault detection, identification, and recovery architecture for a single state system. See [50]

To achieve this, the measured output (leg position) is compared with estimates generated by an independent dynamical observer to form a “residual” (error signal) containing clues about how the physical plant’s behavior departs from modeled expectations to be processed by downstream diagnostics. These estimates could also have been generated via a dynamic bayes network (as in [106]), or a particle filter method (as in [102]), or other estimation technique. However the targeted application domain presents very starkly and characteristically distinctive dynamics that seem well captured by the simple, deterministic models and well classified by the modest, deterministic finite state automaton we introduce. Very likely, in settings requiring the classification of many different terrains the more complex stochastic methods will justify their significantly greater calibration effort (e.g., selection of priors) and lengthier transients. Such an inquiry lies considerably beyond the scope of the present study.

In concert with the overall framework of [50] (echoed in [142]), our detector’s residual signal is passed through a decision logic block for purposes of disturbance identification. For these behaviors, the decision block takes the form of a hand-designed and hand-coded finite state machine, depicted in Fig. 2.13. In the longer term, as the range of possible environments broadens and the diversity of potential fault sources increases, we suspect that automated methods of [150] will be required for the reliable and robust generation of such decision blocks, and, as mentioned above, it seems likely that a stochastic formulation may be required [102, 106].

The problem of fault recovery represents a vast, important domain in its own right that is still relatively unexplored in robotics. Bongard et al [17] compare the sensor-motor signatures of their

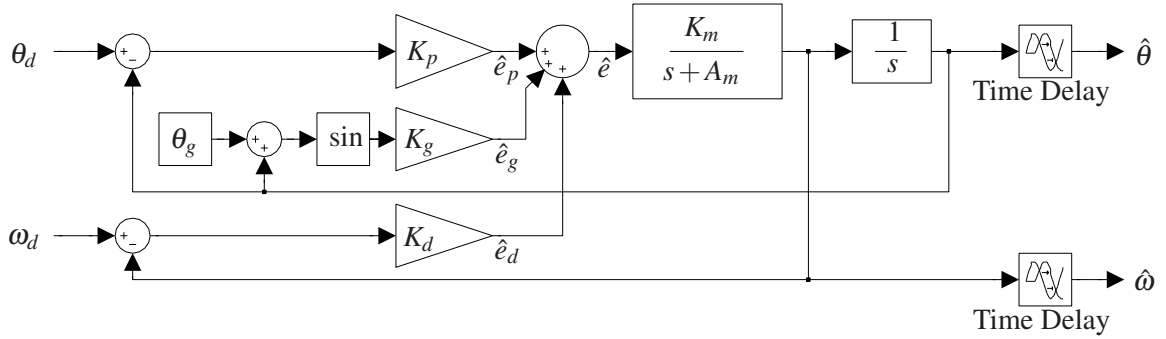


Figure 2.11: Block diagram of leg observer. The estimated angle  $\hat{\theta}$  and angular velocity  $\hat{\omega}$  are generated from the same reference angle  $\theta_d$  and velocity  $\omega_d$  as the actual leg using a simple model of the motor and controller.

robot with a physics simulation based upon generated self-models, for purpose of detecting the design configuration of the robot mechanism. While similar in purpose to our methods, we are focused upon models in which the implicit physics are simple, rather than making use of accurate full-body simulation.

### 2.2.1 Algorithm

A key factor underlying the success of our observer-based sensor is that the dynamical properties of a RHex leg in flight are extremely simple to model: it is essentially a one degree of freedom proportional-derivative reference tracking loop, decoupled from all the other degrees of freedom. In contrast, it is well understood that modeling contact is hard: characterizing a leg's interaction with complex substrates lies at the cutting edge of contemporary applied physics research [107], and, even on simple substrates, modeling the complex Lagrangian mechanics characterizing a robot's joints while contacting a surface remains challenging. Thus, our problem formulation establishes a leg's swing phase as its nominal operational state to be contrasted with "disturbances" caused by either ground or obstacle collision, which the subsequent fault logic can then readily classify as either expected, unexpected, or missing contacts.

## Disturbance Detection

The leg flight model in RHex-style machines takes the particularly simple form<sup>7</sup> of a single, decoupled, servo motor with estimated state (shaft position,  $\hat{\theta}$ , and velocity,  $\hat{\omega}$ ) driven by a linear estimated error,  $\hat{e}$ ,

$$\hat{\omega} = \frac{K_m}{s + A_m} \hat{e}; \quad \hat{\theta} = \frac{1}{s} \hat{\omega} \quad (2)$$

arising from a proportional-derivative (PD) tracker,<sup>8</sup>

$$\hat{e} = \hat{e}_p + \hat{e}_d; \quad \hat{e}_p = K_p \cdot (\theta_d - \hat{\theta}); \quad \hat{e}_d = K_d \cdot (\omega_d - \hat{\omega}) \quad (3)$$

excited by the desired reference position,  $\theta_d$ , and velocity,  $\omega_d$ , signals issued from the “Buehler clock” that defines a RHex gait [154]. In addition, as our legs operate in the vertical plane, they are affected by gravity which we model (instead of trying to cancel actively) by adjoining a third known “reference error” term,  $\hat{e}_g$ , to the tracking controller’s input. Equation 3 is thus replaced by:

$$\hat{e} = \hat{e}_p + \hat{e}_d + \hat{e}_g; \quad \hat{e}_g = K_g \cdot \sin(\hat{\theta} + \theta_g) \quad (4)$$

where  $K_g$  is the magnitude of the effect and  $\theta_g$  is the angular offset. Finally, there is a time delay  $T_{del}$  at the end to synchronize the observer with the physical plant<sup>9</sup>. Figure 2.11 depicts the model just described.

The unknown parameters ( $K_m$ ,  $A_m$ ,  $K_g$ ,  $\theta_g$ ,  $K_d$ , and  $T_{del}$ ) are calibrated via the Nelder-Mead algorithm [135] using a hand-tuned starting simplex. The final parameter,  $K_p$ , is taken to be the

<sup>7</sup>The more advanced motor controllers available on X-RHex permit measurement of motor current, and so a slightly different motor model is used for the stair climbing behavior on X-RHex that includes estimated current as well as a current residual.

<sup>8</sup>Note that since  $\theta_d$  and  $\hat{\theta}$  lie on the circle ( $\mathbb{S}^1$ ), their difference in Equation 3 is taken to be in the range  $(-\pi, \pi]$ , and computed by a standard modulus function. Also note that the physical interpretation of the parameters is standard and not essential to this section’s central contribution. We discuss how to calibrate these parameters in the following paragraphs.

<sup>9</sup>The robot’s distributed control architecture and bus structure incurs a time delay from motherboard (where  $\theta_d$  and  $\omega_d$  are generated) through the network to the local hip controller and then back up to the motherboard where the residuals are calculated. Since our system is time invariant, we can combine these delays into an overall delay of twice the average one way network transport time. Our observer outputs are thus held in a buffer for a total of  $T_{del}$ .

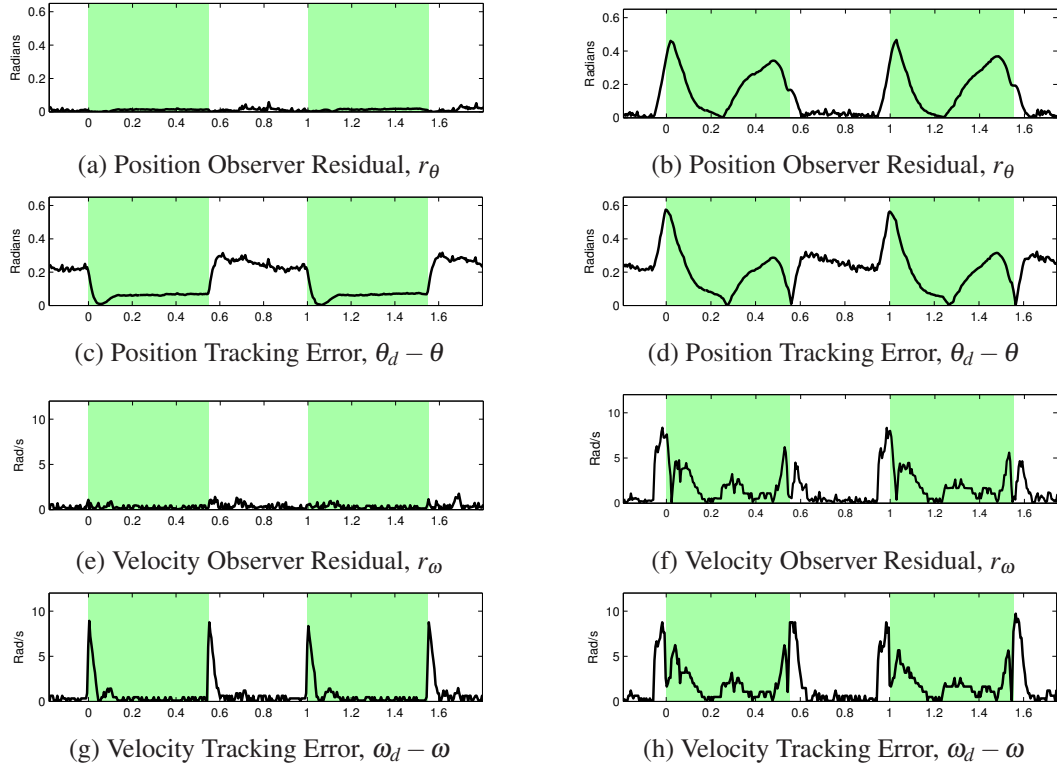


Figure 2.12: Observer residual contrasted with controller tracking error in both position and velocity under conditions of *Left*: free leg swing (no “disturbance” from any ground contact); *Right*: cyclic ground contact (one of the disturbances of interest). The abscissas display time in seconds. Green shading indicates the expected stance phase of the gait.

value used by the higher level controller<sup>10</sup>. Furthermore,  $T_{del}$  is taken to be constant across all legs. For all experiments listed in Section 2.2.2, these parameters were trained on a dataset collected when the robot was allowed to spin all legs freely and with a standard alternating tripod gait. The speed of the gait was ramped up over time from approximately 0.6 to 2.5 strides per second.

The outputs of this observer,  $\hat{\theta}$  and  $\hat{\omega}$ , are compared with the actual achieved angle  $\theta$  and angular velocity  $\omega$ , as reported by the motor-mounted encoder, to form the observer residual vector<sup>11</sup>:

$$\begin{bmatrix} r_\theta \\ r_\omega \end{bmatrix} = \begin{bmatrix} \hat{\theta} - \theta \\ \hat{\omega} - \omega \end{bmatrix} \quad (5)$$

To test the accuracy of the observer, we collected a second dataset at a moderate speed of one

<sup>10</sup> Due to the implementation of the derivative feedback in our controller,  $K_d$  had to be calculated

<sup>11</sup> As with Equation 3, the value  $\hat{\theta} - \theta$  is taken to lie in the range  $(-\pi, \pi]$ .

stride per second for 15 seconds. This yielded a median position residual of  $r_\theta = 0.0271$  radians (1.59 degrees) and a median velocity residual of  $r_\omega = 0.4267$  rad/s (4.075 rpm) over all six legs. The maximum residuals were  $r_\theta = 0.1038$  radians (5.95 degrees) and  $r_\omega = 3.8857$  (37.11 rpm). A section of this raw data from the first leg is shown in Figure 2.12 for the robot both in the air and making ground contact. In both figures parts (a) and (b) we plot  $r_\theta$  and in parts (e) and (f) we plot  $r_\omega$ . For comparison, errors calculated from the position and velocity tracking ( $\theta_d - \theta$  and  $\omega_d - \omega$ ) are plotted in parts (b) and (d), respectively. The green shaded portion indicates the nominal stance phase of the gait.

These plots suggest the significantly greater utility of observer residuals relative to mere controller tracking errors in assessing a leg’s relationship to the ground. Whereas the simple tracking errors exhibit sizable and varying excursions even when the leg has no load, the observer residuals account for the predictable causes of such variation, and only exhibit excursions when contact conditions change. More specifically, during normal operation, due to the nature of the proportional-derivative controller, velocity tracking cannot account for abrupt changes in reference velocity (which the motor cannot perfectly follow), and position tracking must lag as a function of the commanded and actual speeds. These structural features of the PD error signals are particularly onerous because they are strongest just at the moments of the putative ground interaction of true interest. The change in gait phase to slow the leg down for stance by definition should happen around the same time as the touchdown event we are trying to detect. In contrast, these expected dynamical variations in the normal tracking error are accounted for in the observer, as is evidenced by the low level of error for both  $r_\theta$  and  $r_\omega$  in Figure 2.12a and 2.12e. While both estimated states,  $\hat{\theta}$  and  $\hat{\omega}$ , provide useful information, we have found that using only  $\hat{\theta}$  is sufficient for disturbance identification.

### **Disturbance Identification**

Given an informative disturbance signal,  $r_\theta$ , we introduce a simple output logic stage to classify the conditions of interest with respect to an intuitively developed partition of the signal space as follows. The circle,  $\mathbb{S}^1$ , of leg phase angles is partitioned into four intervals labeled “ground” (G)

— leg angles that the Buehler clock associates with ground contact by commanding lower  $\omega_d$  — and “air” (A) — leg angles that the clock associates with free flight by commanding higher  $\omega_d$  — together with two intermediating phase angles labeled “takeoff” (T) — an interval over which the transition from low to high  $\omega_d$  is expected to occur — and “landing” (L) — an interval over which the transition from high to low  $\omega_d$  is expected to occur. Similarly, the circle,  $\mathbb{S}^1$ , of residual position angle errors is partitioned into three intervals labeled “high” (H) — large residual values that experience suggests should be expected only in conjunction with stance — “low” (L) — small residuals associated with typical free flight conditions — and “medium” (M) — a pair of disconnected intervals that separate the “low” and “high” intervals. We use these symbols to trigger the transition of a simple hand-designed FSM with four normal states — stance, possible takeoff, flight, or possible landing. The FSM includes two additional error states — unexpected disturbance and missing ground. An unexpected disturbance occurs when  $r_\theta$  increases but the leg is not in a phase of the gait where it could hit the ground. Missing ground is when  $r_\theta$  does not increase but the leg is in a phase of the gait where it should have contacted the ground. There is also a minimum lingering time in each state of the FSM to avoid quick transitions due to noise spikes. The state transition diagram is depicted in Figure 2.13.

The possible takeoff and possible landing states were added to improve accuracy over a wider range of gait speeds. For instance the leg may be in a state with  $\theta \in T$  and  $r_\theta \in M$  but it should not be construed as having taken off unless at some point in the near future  $r_\theta$  continues to decrease. In contrast, if  $r_\theta$  goes back up then we should treat the leg as if it is still on the ground. The possible landing state allows our ground detector to trigger at the medium error level but not declare a confirmed ground contact unless  $r_\theta$  continues to rise up to the high level.

The ad hoc construction of this diagnostic state machine could surely be improved by recourse to the more formal methods of supervisory control [150]. However, for this application, we believe the details of its cell structure and transition logic are less important than the broader design insight that a sound decision about the nature of the current disturbance must be based on the available information:  $\theta$ ,  $\omega$ ,  $r_\theta$ ,  $r_\omega$ , and their evolution in time.

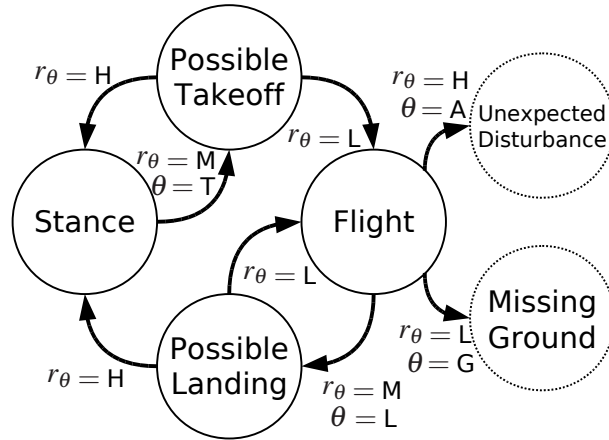


Figure 2.13: State transition diagram for fault identification.

### Disturbance Recovery

Reacting to and recovering from disturbances or damage to limbs during locomotion should be a strength of multi-legged platforms, given the intuitive understanding that a multitude of legs confers redundancy. In planning and executing the gait recovery mechanism used here, we build upon prior work in topological gait classification, analysis, and control [68]. In the stair climbing scenario, the robot transitions to a different six legged gait that is better suited for climbing stairs, as introduced in [67]. When the robot accidentally breaks a leg, we signal a gait recovery transition using an asymmetric five-legged gait for a hexapedal machine, see [87, Section II.C] for more details.

### 2.2.2 Reactive Behaviors

#### Wall Avoidance

The first behavior that we have implemented using this software contact detector and disturbance classifier is a simple wall avoidance algorithm. Instead of whiskers or antennae [43], the robot must touch the wall with its leg and, upon unexpected disturbance (see Section 2.2.1), back up to turn away. While not necessarily an efficient solution to any sort of maze problem, this simple, useful behavior illustrates the reliability of our contact detector for disturbance detection and identification.

In this case disturbance recovery is quite simple. Once the robot knows there is an obstacle in

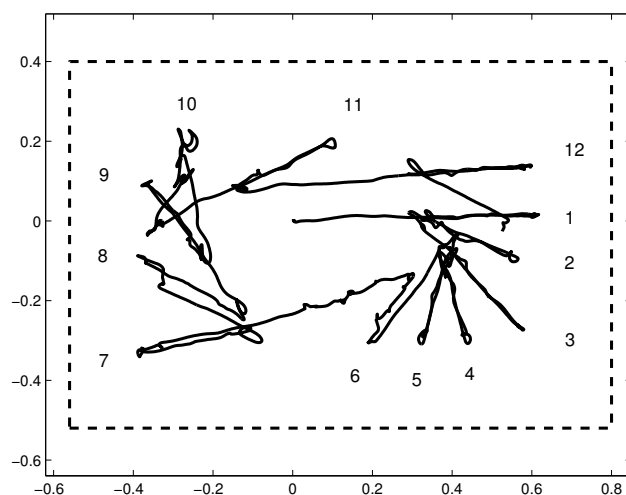


Figure 2.14: Overhead plot, in meters, of the center of mass of an EduBot running a wall avoidance behavior inside a closed rectangular region, using the described method as the only sensing strategy. The twelve contact points are labeled.

front of it, it must immediately move backwards, turn, and continue on its way. For simplicity of solution, here the robot always turns right. An overhead plot of this behavior within an enclosed rectangle seen in Fig. 2.14, recorded using a Vicon motion capture system<sup>12</sup>. A second experiment with an available exit is shown in the video attachment to [87].

### Stair Climbing

In addition to triggering a maze solving behavior, detecting a disturbance in flight can be used to aid autonomous stair climbing [86]. In this scenario, the robot uses a laser scanner and a self-manipulation behavior (analyzed in Section 4.3.2) that varies the pitch of the platform to produce a 2D depth map, which it uses to detect that there is a nearby staircase. As the robot walks towards it, the exact number of steps before impact is not known as there will always be some odometry error. Therefore when the robot gets close it uses the disturbance detection to trigger the transition to the stair climbing gait. Stair climbing is different from the normal walking gait, and so a transition is needed to the stair climbing gait, as first described in [67]. With the stair disturbance detected and

<sup>12</sup><http://www.vicon.com/>

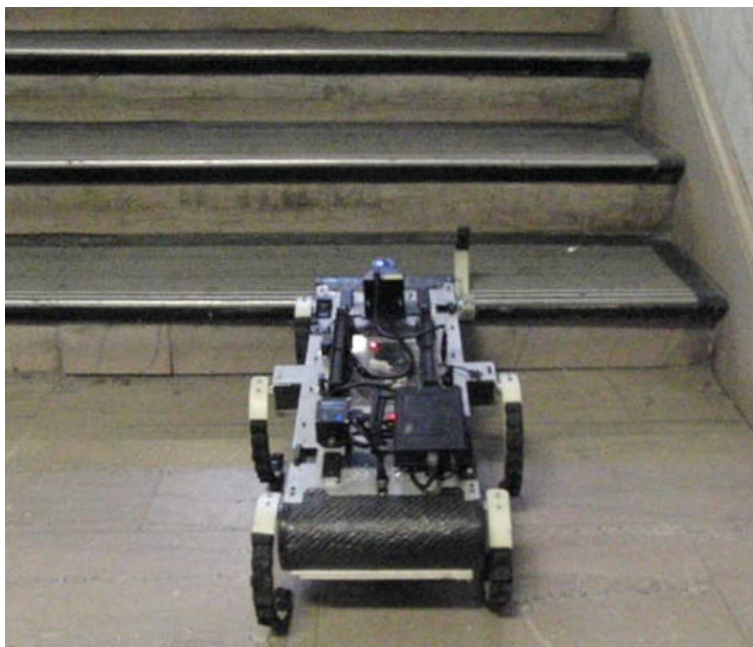


Figure 2.15: Transitioning from walking to stair climbing.

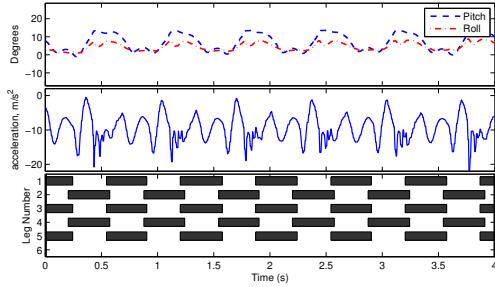
identified, the robot is able to recover by using this gait transition in stride and smoothly switch to climbing the stairwell.

The details on the rest of the autonomous behavior can be found in [86], as well as a full account of the results. The stair transition using this framework was quite reliable, failing 4 times on the 61 flights of stairs (93% success rate). Some of the failures were in detection and identification, while others were in the recovery behavior itself (which sometimes failed when the robot was far from being perpendicular to the stairs).

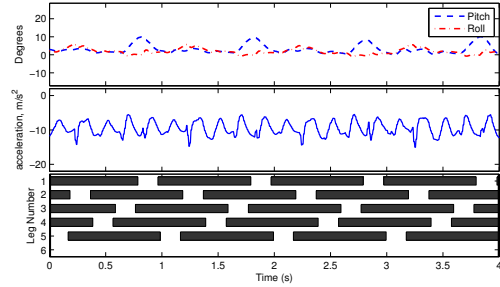
### **Leg Fault Recovery**

To test the effectiveness of our detection of and recovery from disturbances, we now exhibit behavioral strategies on the EduBot machine in which the robot must quickly adapt to dramatically changed locomotion capabilities.

The robot was rigged with purposefully weakened legs designed to fracture and fall off after only a few steps. Without disturbance detection, the now five-legged machine naïvely continues to make use of the alternating tripod gait, but does so with dramatically reduced stability. As shown in



(a) Alternating Tripod Gait with 5 Legs



(b) Five-legged Crawl Gait

Figure 2.16: Gait comparison using inertial measurements of a robot walking with a missing sixth leg. For the bottom plot of each, black regions indicate stance. On five legs, the tripod gait loses stability and impacts the ground, seen by strong impacts in the vertical acceleration. The crawl gait retains stability, reduces roll, and induces only small pitching moments. *This figure originally appeared in [87] is included here courtesy of Clark Haynes.*

Fig. 2.16a, the machine impacts the ground (chattering in vertical acceleration) during each stride due to loss of stability, greatly decreasing its locomotive quality.

Upon execution of a transition to a five-legged crawl gait triggered by a missing ground event using strategies outlined in Sections 2.2.1, the robot is still handicapped with just five legs, seen in Fig. 2.16b at steady-state behavior, but maintains stability and does not impact the ground. An example of both the reactive and non-reactive cases is included in the video attachment to [87].

## Chapter 3

# Leaping Transitions

In this chapter we explore the intrinsic vocabulary of a particularly simple transition: the legged leap on a solid level substrate from a motionless state to some desired aerial apex condition in a high energy regime, such as the leap onto a ledge in Fig. 3.1.

In Section 3.1, we review some preliminary formal ideas concerning the central object of study, a two legged sagittal plane hopper, and exhibit the topological space — the “ground reaction complex” (in this case a simplicial tetrathedron) — over whose variously dimensioned cells the Hamiltonian flows of its constrained body evolve as directed by the ground reaction forces. This cellular construction indexes in a computationally effective (“grammatical”) manner the realizable sequences of continuous dynamics that are physically available, providing crucial intuition for hand-designed behaviors (as suggested by the new capabilities we document) as well as parameterizing the various sequences of constraints that would be required for any automated method of behavior generation (i.e. a learning or optimization based approach).

The value of working out the cell adjacency relations in the ground reaction complex is the resulting catalog it affords of all possible leaps (transitions from the rest state to the fully aerial state). Presented in Section 3.2, this is shown to take the form of variously triggered hybrid dynamic transitions between adjacent cells. These cell-labeled sequences of gradually ascending dimensional flows comprise this hopper’s vocabulary of leaps. In Section 3.3 we document empirically a variety of the very different terminal aerial phase conditions that can result from these various leaps through

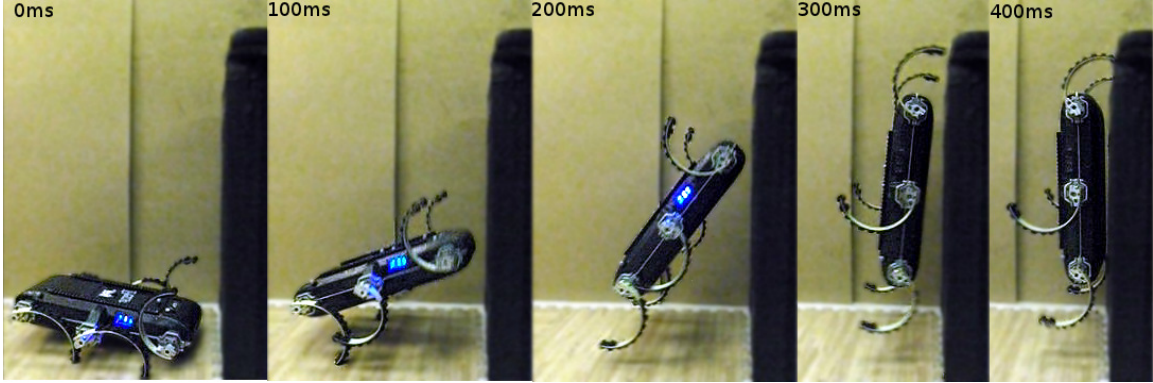


Figure 3.1: XRL [65] leaping upward onto a 73cm high table, nearly 1.5 times its bodylength. Frames taken every 100ms from a high speed video.

appropriately coordinated open loop maneuvers implemented on XRL. In Section 3.4 we show how two different instances of these leaps lead to evidently useful behaviors heretofore unachieved by a general purpose legged robot<sup>1</sup>: a two hop vault across a gap 20% wider than the robot’s body length; and a high jump onto a ledge almost 50% taller than the robot is long.

### 3.1 Hybrid Dynamics Over the Ground Reaction Complex

A complete model of the dynamics for a robot such as RHex is given in Chapters 4 and 5, and here we present only that which is needed to motivate the analysis of the leaping behaviors used in this chapter. We are concerned with a planar rigid body,  $x \in \text{SE}(2)$ , possessed of two massless limbs whose revolute joints  $\theta_i \in \Theta_i := \mathbb{S}^1, i \in \{1, 2\}$ , relative to the body are actuated by the motors. The resulting five degree of freedom kinematic system,  $q := (\theta_1, \theta_2, x) \in \mathcal{Q} := \Theta_1 \times \Theta_2 \times \text{SE}(2)$ , is further subject to a set of unilateral constraints,  $a_j(q) \geq 0, j \in \mathcal{I}$ , specified by smooth maps,  $a_j : \mathcal{Q} \rightarrow \mathbb{R}$  (and an index set,  $\mathcal{I}$ , that we introduce below), that define the base topological space and thereby comprise in part the “guard” or “boundary” conditions on the dynamical flows over the base cells. We will simplify the body contact by assuming two contact points (“front” and “rear” along the bottom), reducing the possible contact conditions to an enumeration of constraint

<sup>1</sup>By which we mean a power-autonomous robot without specialized jumping (e.g. [103]) or climbing (e.g. [165]) mechanisms.

equations over the powerset of  $\mathcal{P}$ ,

$$\mathcal{P} := \{p_{k,l} \in \mathbb{R} : (k,l) \in \mathcal{I} := \{F,R\} \times \{B,L\}\}$$

where  $\{F,R\}$  indexes the “front” or “rear” location and  $\{B,L\}$  indexes the “body” or “leg” terminal. It now follows that there are  $2^{|\mathcal{I}|} = 16$  different logically possible contact conditions yielding 16 different Lagrangian dynamical systems whose physical features we will specify below.

While compliance in the legs almost certainly helps achieve some of the behaviors documented here, for the most part the body will follow the rigid linkage path with the springs acting to force the robot onto that trajectory, and so we will assume rigid legs<sup>2</sup>. We will assume that the actuators can deliver the greatest amount of work to the body when they are individually doing the most work they can on their individual motor shafts. The infinitesimal kinematics of rigid closed kinematic chains generically accord unequally weighted contribution to the net body wrench (see Section 4.3.1 for one example). However, none of the closed chains relevant to leaps against the simple level substrate encounter sign changes in these weights, so actuators might “waste” energy generating internal forces but will not impart negative work to the body when they are asserting their maximum torque in the direction of shaft travel<sup>3</sup>.

We further assume that the actuators are each capable of and are restricted to delivering a constant torque (in either direction) throughout their operation, which is saturated by the motor controller current limit. This, of course, does fly in the face of physical reality [51, 77], and power limitations are well understood to play a critical role in fast moving legged robot limbs [60, 114]. Fortunately, here much of the action takes place at relatively low limb speeds, and so there is relatively little back EMF to substantially reduce the output torque. For similar reasons, we neglect damping in the joints and limbs and ignore any other source of energy loss throughout this thesis.

---

<sup>2</sup>Though compliance can easily be added back, as in [149] and others.

<sup>3</sup>As a motivating extension beyond the scope of this thesis, we do document one instance in Section 3.3.1 where the compliance in the legs allow for a novel trajectory, where this maximal torque assumption fails.

### 3.1.1 The Ground Reaction Complex

In [68] a cell complex [61] was used to index all possible abstract coordination schemes that a legged machine might undertake and in [70] this cell complex was used to organize the possible gait transitions and recovery strategies of a quasistatic vertical climbing robot, treating the varying ground contact conditions experienced along the way as mere “noise” shown to be robustly rejected by a proper feedback implementation of the coordination controller. Here we explore what is in some sense the opposite extreme case: we are only interested in characterizing the possible direction and magnitude of ground reaction forces in consequence of different limb configurations; we are only interested in the high energy dynamical regime; and we wish to factor out all the inessential details of interlimb coordination.

Hence, although the kinematic system just introduced has as many as five degrees of freedom, we now exploit the assumption of massless limbs to introduce a coordination assumption that will cut away the inessential dimensions with no loss of generality regarding the ground reaction force interactions of central focus. Namely, we will assume when either limb is free of ground contact that there is some “mirror law” [20], of the form  $\theta_i = m_i(q)$ ,  $i = 1, 2$  that the joint actuators track exactly.

Denote by  $\pi_z$  the projection onto the second coordinate of some world frame representation of the body and leg contact points<sup>4</sup>. Consider the family of constraint equations,

$$\pi_z p_{k,l} = 0 \quad (k,l) \in \mathcal{I}_j \subset 2^{\mathcal{I}}$$

where the subscript,  $j$ , on the active-constraint set,  $\mathcal{I}_j$ , indexes each subset of  $\mathcal{I}$  through a Boolean string denoting membership (or its absence) respecting the lexicographic ordering of  $\mathcal{I}$ ,  $(FB, FL, RB, RL)$  so that, for example  $\mathcal{I}_{0111} = \{FL, RB, RL\}$ .

With this nomenclature in place we now enumerate all of the 16 possible ground contact conditions that form the base space on which our hybrid system is defined, grouping them into the following categories according to their common dynamics as follows:

- One state where the body has three degrees of freedom (3-DOF): the aerial state with no

---

<sup>4</sup> We must cut off the “north pole” of the bodys rotational component by always requiring  $\pi_z p_{FB} < \ell$ , where  $\ell$  is the robot’s bodylength (to ensure each cell is truly contractible as formally required).

contact  $\mathcal{I}_{0000} := \{\}$ .

- Two 2-DOF states have one end of the robot on the ground sliding  $\mathcal{I}_{1000}, \mathcal{I}_{0010}$ .
- Two 2-DOF states have only one leg is down and there is a 2-link open kinematic chain  $\mathcal{I}_{0100}, \mathcal{I}_{0001}$ .
- Two 1-DOF states have a leg and the opposite side of the body down in a crank-slider configuration  $\mathcal{I}_{0110}, \mathcal{I}_{1001}$ .
- Two 1-DOF states have a leg and the body on the same side down like a single link chain  $\mathcal{I}_{1100}, \mathcal{I}_{0011}$ .
- One 1-DOF state has both legs down in a four bar linkage  $\mathcal{I}_{0101}$ .
- One 1-DOF state has the body completely on the ground but still able to slide  $\mathcal{I}_{1010}$ .
- Four completely constrained states that in general the robot will spend no time in,  $\mathcal{I}_{1110}, \mathcal{I}_{1101}, \mathcal{I}_{1011}, \mathcal{I}_{0111}$ .
- One degenerate case that is over-constrained with all possible contacts simultaneously on the ground,  $\mathcal{I}_{1111}$ .

These states are illustrated in Fig. 3.2 arranged as a simplicial tetrahedron, with the aerial state in the interior, the 2-DOF states as the faces, and the 1-DOF states as the edges. The 0-DOF states are not illustrated but are the vertex points, and the over-constrained system is not depicted as it represents a degenerate case. Space and time constraints preclude our formal demonstration that the definitions just introduced yield the topological tetrahedron depicted, but it will suffice for the reader to merely keep track of the adjacency relations the figure implies.

### 3.1.2 Hamiltonian Flows

See Chapter 4 for our preferred method of populating (by formal symbolic manipulation) the exact terms in appropriate local coordinates arising in each of the 16 different Lagrangian dynamical

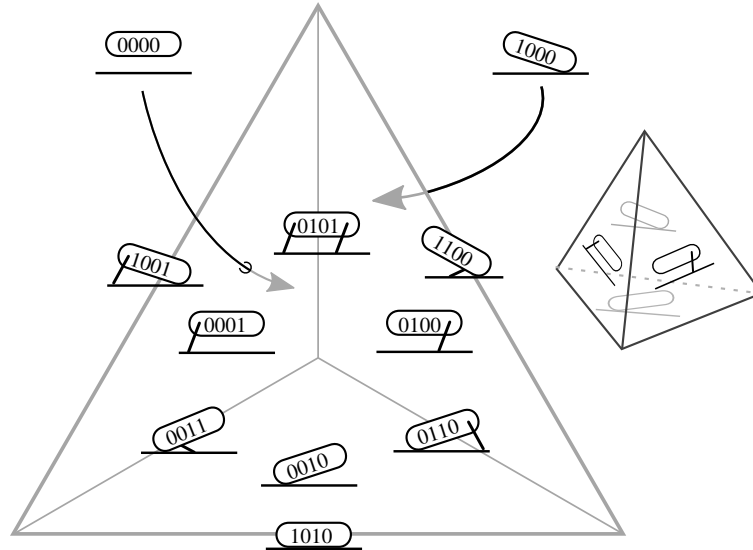


Figure 3.2: All possible contact states, represented as a tetrahedron, showing adjacency. The interior volume and bottom face are indicated with arrows.

systems describing the distinctly different contact mechanics associated with each GRC cell. We simply exhibit here the formal abstract expression from which each specific instance can be systematically derived. Define the Lagrangian free variable(s) as  $y \in \mathcal{Y}$  (related by  $h : \mathcal{Y} \rightarrow \mathcal{Q}$  to the state), and so the dynamics of  $\dot{y}$  are an unconstrained function of state. For this analysis we will assume that the body of the robot can slide along the ground with minimal friction, while the leg toes have enough friction to act as if it were pinned until it reaches the guard condition<sup>5</sup>.

### 3.1.3 Hybrid Dynamics

A unified formalism for the representation of hybrid dynamical systems was worked out roughly two decades ago [18], and a full hybrid system account for RHex is given in Section 5.2. While the general framework allows for transitions between arbitrary (piecewise) smooth “patches” of state space, our physical setting restricts transitions to occur only between patches that bear a topological “incidence” relationship. For this reason, our major focus of effort concerns mapping out and

<sup>5</sup>There is one exception: where the legs are fighting against each other — in these cases the large internal force does not necessarily break this friction assumption (as in Section 4.3.1), however in this regime of maximal torque output it will. Therefore when the motors are commanded with opposite directions, the toes will be assumed to be in sliding friction.

systematically exploiting these incidence patterns, and the more general, knotty issues associated with hybrid systems recedes to the background.

There is a growing literature on hybrid dynamical systems over stratified sets [58, 178], of the kind we study here that arise from the changing degrees of freedom intrinsic to “regrasped” rigid body manipulation by limbs or fingers of limited physical extent. Although switches across strata can be understood and planned at non-zero velocity [79], in this chapter we are concerned with the truly dynamical regime wherein the *timing* of actuation is crucial to shepherding effectively a body’s accumulating kinetic energy through the various transitions. As far as we can determine, the recent literature concerned with (self-) regrasping in a high kinetic energy regime has focused on planning, sensing and control of the object capture [53] or self-landing [59, 183] rather than exploring the many routes from rest toward the high energy aerial phase as we do here. Some exceptions include consideration of one or a few most common routes [5, 158, 161], and one paper [163] that formulates the space of hybrid system states into a structure, though not a simplicial complex.

In general the robot can transition between any adjacent states. Adjacent states can be found by either adding a contact (resulting in a loss of one degree of freedom) or removing a contact (resulting in the addition of one degree of freedom) from the current state contact set. The full set of all possible transitions can be thought of as the Hasse diagram of  $\mathcal{I}$ , with generically  $|\mathcal{I}| \cdot 2^{|\mathcal{I}|}$  directed edges, in this case 64 possible transitions.

These transitions can be categorized as: *Control Triggered*, by touching a leg to the ground, as in  $\mathcal{I}_{1010} \rightarrow \mathcal{I}_{1101}$  where the guard condition is the zero of  $a_{1010,1101} = \theta_1 - \theta_g$  for some  $\theta_g$ ; *Sometimes Control Triggered*, for example  $\mathcal{I}_{0000} \rightarrow \mathcal{I}_{0100}$ , where the guard condition is a function of height and pitch and may be positive for all  $\theta$  (i.e. the set  $g_{j,k}^{-1}(0)$  does not include any configurations at the point  $x$ ); *State Triggered*, but possible based on the dynamics and initial conditions of the system, such as the takeoff condition  $\mathcal{I}_{0101} \rightarrow \mathcal{I}_{0001}$  and explored in more detail in Section 4.3.3; *Impossible*, the transition where the body lifts off the ground with no action as in  $\mathcal{I}_{1010} \rightarrow \mathcal{I}_{1000}$ ; and *Undesirable*, while the robot is certainly capable of a hard landing  $\mathcal{I}_{0000} \rightarrow \mathcal{I}_{1000}$ , a behavior designer may wish to avoid it (and furthermore such transitions may not advance the goal of this chapter, leaping). Thus the set of transitions which we will consider (i.e. those that are both possible

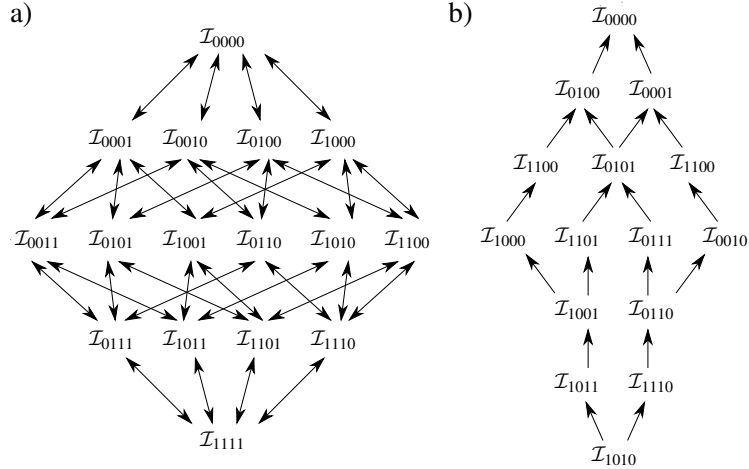


Figure 3.3: Logical vs allowable cell transitions over the GRC.

and desirable) is reduced from 64 to only 18, which are shown in Fig. 3.3. Note that 15 of the 16 contact conditions remain (only  $\mathcal{I}_{1111}$ , the overconstrained case, has been eliminated), but the graph of possible transitions is not nearly as dense. Note that the resulting directed graph in Fig. 3.3.b does indeed specify a formal grammar comprising all paths initiated at the root (rest state) which reach the terminus (flight state) — a vocabulary of legged leaps.

## 3.2 Open Loop Control of Transitions Across the Ground Reaction Complex

Here we limit the discussion to leaping transitions, namely transitions that take the robot from  $\mathcal{I}_{1010} = \{FB, RB\}$  to  $\mathcal{I}_{0000} = \{\}$ . The transitions directly to the two 2-DOF systems adjacent to the start ( $\mathcal{I}_{1000}$  and  $\mathcal{I}_{0010}$ ) are impossible, so a path through one of the ends of this edge is required, namely the robot must put down either the front or rear leg.

### 3.2.1 Leg Strategy

The saturated torque assumption yields a binary control input for each leg, pushing forwards + or backwards −, and the combined leg strategy  $S \in [+,-] \times [+,-]$  on the robot is then specified by an

ordered pair such as  $(+, +)$ .

These four distinct control inputs are each capable of exciting a multitude of pathways through the directed graph of Fig. 3.3, yielding the large variety of leaps we explore empirically in Section 3.3. Furthermore, the half circle legs imply that, for the most part,  $(+, +)$  produces a forward lunge, while  $(-, -)$  produces a flip. The rest of this section will focus on  $(+, +)$  as an example of the insight afforded by the grammar of leaps enumerated in (2) – (7), however all four basic strategies (and a representative selection of the varied leaps achievable by suitably coordinating their relative timing) are documented in the experimental section.

### 3.2.2 Coordination Timing

Choose as a reference time the touchdown of the front leg, and consider the relative timings of the other transitions. The second leg will touch down at  $t_2$ , which is a coordination time,  $C$ , that can be chosen arbitrarily. More complicated leg strategies that depart from the assumptions of Section 4.1 may have a higher dimension coordination timing, and might well explore a slightly richer subgraph of Fig. 3.3.a than the more restricted leaping grammar we focus on in this chapter. The time of transition to the air for each leg,  $t_{1a}$  and  $t_{2a}$ , are implicitly defined based on the Hamiltonian flow and the liftoff guard condition on the hybrid dynamics,  $a(f(t)) = 0$ , which in a deterministic world are fixed by the choice of jumping strategy  $S$  and are a smooth function  $T : \mathbb{R} \rightarrow \mathbb{R}$  of the coordination timing  $C$ ,

$$t_{1a} = T_{1a}^S(C); \quad t_{2a} = T_{2a}^S(C) \quad (1)$$

where in this example  $t_{1a} = T_{1a}^{(+,+)}(t_2)$ . A closed form for  $T$  is not explicitly needed, but even without it some basic properties will trivially be true, such as  $0 < T_{1a}$  and  $t_2 < T_{2a}$ .

### 3.2.3 Transition Paths

Now we can write out all of the possible state transitions for a jump, based on the set of possible cell transitions described above. The transition path, i.e., the “leap-word”, is an ordered list, and the

set of words that are possible are thus (with the zero time transition states suppressed, as well as the always present initial  $\mathcal{I}_{1010}$  and final  $\mathcal{I}_{0000}$  states),

$$(\mathcal{I}_{0110}, \mathcal{I}_{0010}, \mathcal{I}_{0001}) \Leftrightarrow t_{1a}^* < t_2 \quad (2)$$

$$(\mathcal{I}_{0110}, \mathcal{I}_{0101}, \mathcal{I}_{0001}) \Leftrightarrow 0 < t_2 < t_{1a}^*, t_{1a} < t_{2a} \quad (3)$$

$$(\mathcal{I}_{0110}, \mathcal{I}_{0101}, \mathcal{I}_{0100}) \Leftrightarrow 0 < t_2 < t_{1a}^*, t_{2a} < t_{1a} \quad (4)$$

$$(\mathcal{I}_{1001}, \mathcal{I}_{0101}, \mathcal{I}_{0001}) \Leftrightarrow t_{2a}^* < t_2 < 0, t_{1a} < t_{2a} \quad (5)$$

$$(\mathcal{I}_{1001}, \mathcal{I}_{0101}, \mathcal{I}_{0100}) \Leftrightarrow t_{2a}^* < t_2 < 0, t_{2a} < t_{1a} \quad (6)$$

$$(\mathcal{I}_{1001}, \mathcal{I}_{1000}, \mathcal{I}_{0001}) \Leftrightarrow t_2 < t_{2a}^* \quad (7)$$

as shown in Fig. 3.3.b. Specific physical parameters may well make some words impossible. For RHex the front leg tends to lift off the ground first, and so the (4) word is not realizable.

Additionally there can be degenerate “double” transitions that are quite interesting, such as the basic jump when  $t_2 = 0$ . The restriction that  $T_{1a}$  is strictly greater than zero, and  $T_{2a}$  is strictly greater than  $t_2$ , along with the fact that for RHex  $T_{1a}^S(0) \neq T_{2a}^S(0) \forall S$ , eliminates all higher order degeneracies.

### 3.3 Experiments

In order to explore various regions of the space of jumping controllers,  $(S, C)$ , and to test the claim that the underlying topological construction predicts interesting behavioral consequences, we have run over 100 trials sampling the space<sup>6</sup>. Each of the four leg strategies was tested with a sampling of coordination timing parameter values. As RHex actually has 3 legs in the plane, in these experiments the “leading” leg was disabled, i.e. the front leg for  $(+, +)$ , middle leg for  $(+, -)$  and  $(-, +)$ , and rear leg for  $(-, -)$ , but we will relax this requirement later.

Here we report on the height, displacement, and pitch at apex<sup>7</sup>, with the  $(+, +)$  case highlighted in Fig. 3.4, and the remaining cases shown in Fig. 3.5. Full data tables, including additional measurements are available at the end of this chapter in Section 3.5, and the video attachment to [91]

<sup>6</sup>In order to minimize the effect of battery charge level and other time varying effects, the trial order was randomized and the batteries were never allowed to fall below 75% of full.

<sup>7</sup>Recorded with a Vicon Motion System, <http://www.vicon.com/>

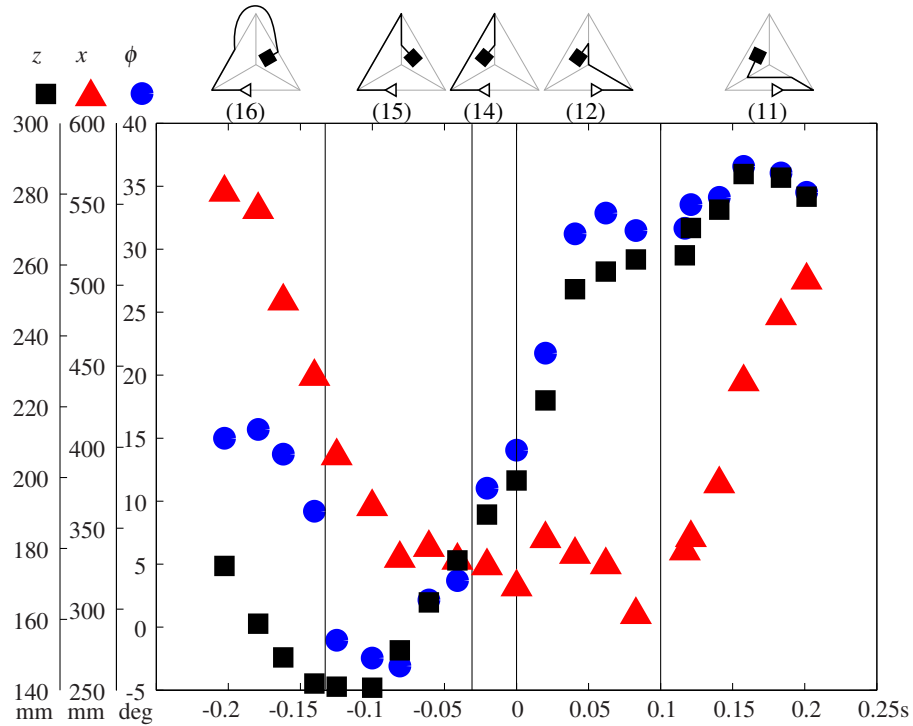


Figure 3.4: Apex height (black square), displacement (red triangle), and pitch (blue circle) for (+, +) jumping strategy at various relative leg timings.

shows a selection of behaviors. The top of Fig. 3.4 lists the coordination “word”, (2) – (7), and depicts in a graphical cartoon the different paths through the cell complex, with vertical lines marking approximate transition points<sup>8</sup>. It is clear that depending on what combinations of these metrics the task requires, several different regions in this space could be useful.

The repeatability can be quantified by comparing the results of 20 additional (+, +) jumps (listed in Table 3.1) to a linearly interpolated estimate based on Fig. 3.4. This shows an RMS error of 4.3 mm in  $z$ , 12.4 mm in  $x$ , and  $1.4^\circ$  in  $\phi$ .

But beyond demonstrating which control strategies result in what kinds of jumps, this data clearly shows notable changes near the boundaries between transition paths through the cell complex. For example, the height achieved by the (+, +) strategy has a nearly discontinuous jump just

<sup>8</sup>Paths start at the triangle, end at the square where they transition to the interior (aerial state), and paths outside the triangle represent the bottom face. This data was coded by hand from high speed video of each trial. Takeoff ambiguity is the main reason these transitions are approximate.

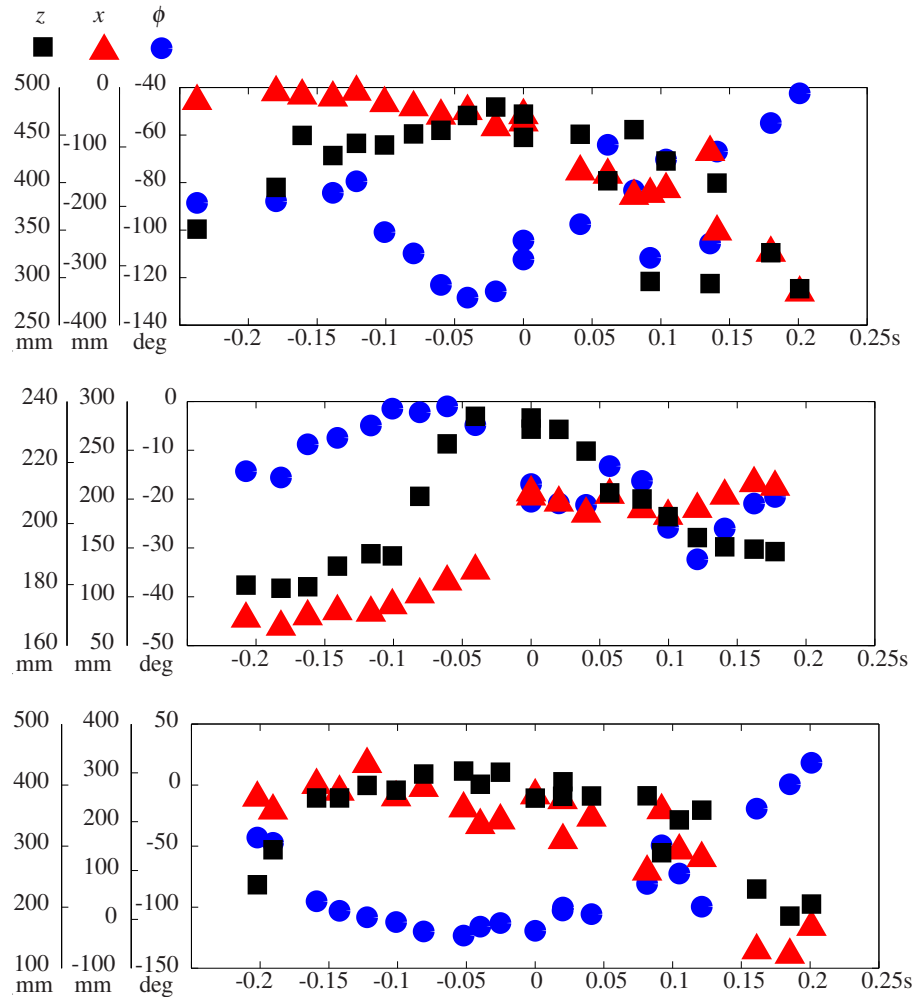


Figure 3.5: Apex height (black square), displacement (red triangle), and pitch (blue circle) for  $(-, -)$ , top,  $(+, -)$ , middle, and  $(-, +)$ , bottom, jumping strategies at various relative leg timings.

after  $t_2 = 0$  — there is a noteworthy advantage in height to letting the front leg start before the rear leg. A similar jump is also present in the pitch however, which may or may not be a good thing depending on the task.

Qualitatively, the leaping strategies are quite different. The  $(+, +)$  strategy yields mostly a forward leap, while the  $(-, -)$  strategy yields largely a flipping behavior, though for  $t_2 > 0$  the robot does not quite complete the flip and instead lands on its nose. The  $(+, -)$  strategy causes the robot to jump more or less vertically into the air. The  $(-, +)$  strategy is mostly a flip, but had trouble for positive values of  $t_2$ . In those trials (as well as a couple for  $(-, -)$ ) the front leg, which

is pushing backwards, stretched back along the ground until it hit the middle leg support. Since the motor was at full torque, the leg stuck to the corner of the frame for a short time. Therefore the front leg leading jumps in this strategy would benefit from a more subtle controller to avoid this.

### 3.3.1 Extensions

Here we present some anecdotal results that lie outside the scope of this thesis, however can still be informed by the methods presented here.

#### Three Legged Jumps

RHex actually has six legs, and not two. While it is easy to anchor the dynamics to the sagittal plane by keeping pairs of legs together, that still leaves three legs. Formally, the third leg will increase the number of hybrid states though not the dimension of the ground reaction complex (which is fixed by body dynamics). However in rigid, non-singular cases only two legs can actually maintain contact on the ground at a time.

However with compliance, and when operating near a singularity (such as  $t_2 = 0$ , a common occurrence on RHex) it is possible for the three legs to be used, but it may or may not be useful. Initial tests have shown that in the  $(+, +)$  case the third leg can only add about 1cm to the final height. In contrast, for the  $(+, -)$  case including the middle leg (in the  $-$  direction) added 7cm to the apex height, or about a 30% gain in potential energy.

#### Reversing Strategies

In a rigid system, reversing the direction of force applied by a motor will simply bleed off some of the energy that is already in the system. However for the compliant half circle legs of RHex, when the leg is moving forward and therefore on the round half of the leg, reversing the torque<sup>9</sup> will sometimes cause the leg to jam and unfold, producing a novel motion. The reverse is not true — if the leg is pushing backwards it will be on the point of the toe, and reversing the direction will

---

<sup>9</sup>A rapid reversal of motor torque requires well hardened electronics with adequate flyback protection, however the electronics in RHex were designed with this in mind [65].

usually just lift the leg off of the ground early, or if it did jam simply curl the leg up and slow down the robot. A less extreme reversal has been used in the past [128] to correct the pitch instability of pronk, though the role of the compliant legs was not fully understood. Note that this strategy is taking advantage of the shape change that the compliance allows, but does not recover any energy stored in the unfolded spring.

Since the principle motivation for leg reversal is pitch stabilization, we have tested a hand tuned reversing strategy on the  $(+, +)$  jump with  $t_2 = 0$ , as this may be the most used jump on RHex but does have about  $15^\circ$  of unwanted pitch at apex (more by the time the robot lands). In these initial tests, we have found that in fact stubbing the toe at the end of stroke causes about  $20^\circ$  of pitch correction, albeit at the cost of forward velocity which dropped by 18%. Surprisingly though the stubbed toe experiments did show a slight (2cm) gain in maximum height, which we attribute in part the compliant leg being stretched by this behavior, pushing the robot upwards. Overall the reversing jump had less total energy, but the change in pitch and slight height benefit make it a useful strategy in certain situations.

## 3.4 Behaviors

This section applies the preceding catalogue of open loop controllers to the generation of several useful behaviors.

### 3.4.1 Leaping Behaviors

There are many cases where the apex state after a jumping transition is inherently useful. In order to cross a small gap, RHex has previously been shown (but not published) to be capable of crossing a 40cm gap (using the middle and rear legs only). This has been extended to 50.5cm (1 body length) using the  $(+, +)$  strategy and  $t_2 = 0.02$ , a 26% increase. The backflip has been better studied as a way to recover a preferred orientation [152], but has always been completed by rolling on the nose (i.e. never leaving the  $\mathcal{I}_{1000} = \{FB\}$  state), implying an apex height of 27cm (though this work did not explicitly optimize for apex height). Fig. 3.5 documents the  $(-, -)$  leap with  $t_2 = -.02$  achieving

a 48cm apex height (300% of standing height). Because both of these behaviors entail leap-words virtually identical to that past work, we attribute most of the gains to the substantially improved hardware of the current generation robot [65].

While the backflips achieve the highest apex, they are pitched nearly vertical at that state. Fig. 3.5 reveals a new leap excited by the  $(+, -)$  strategy achieving a 23cm apex (143% of standing height) at less than  $5^\circ$  pitch. Adding the third pair of legs yields a 30cm apex (nearly 200% of standing height) at  $17^\circ$  pitch. To the best of our knowledge such a near-level vertical leap has never before been elicited from RHex and represents an immediately beneficial consequence of enumerating the entire space of dynamic transitions.

### 3.4.2 Gap Crossing

A variety of compound jumping behaviors benefit significantly from the ability to select a specific initial leap. For example, several high kinetic energy RHex gaits have relatively small basins which can be very effectively “prepared” [27] by selecting the apex state from rest via a leap. However, here, we focus on compound jumps across bigger obstacles than any single leap can afford. Specifically, a leap-step behavior initiated by a 3 legged  $(+, +)$  leap with  $t_2 = 0$ , achieves a high, near-zero pitch apex with significant forward velocity when a reversing strategy is used. Followed by a simple spring-mass stride (with the SLIP parameters adjusted by hand) [72], this leap-step crosses a gap of 60cm (almost 120% of body length), as shown in Fig. 3.6, representing to the best of our knowledge a 20% gain over the farthest gap jump previously achieved by any general purpose legged robot [23].

### 3.4.3 Jumping on to a Ledge

Another useful application of jumping is to gain access to a high step or ledge. Past quasi-static work on a similar robot has allowed the robot to access an incredible 53% of the body length<sup>10</sup> [39], the equivalent of a 27cm step up for XRL. By inspecting the results in Fig. 3.4, it appears that a  $(+, +)$  leaping strategy with a large  $t_2$  may be advantageous (i.e. push with the front legs well

---

<sup>10</sup>This work used leg length as the scale, however we feel that under these strategies the robot is gaining much more of an advantage from body length than from leg length.

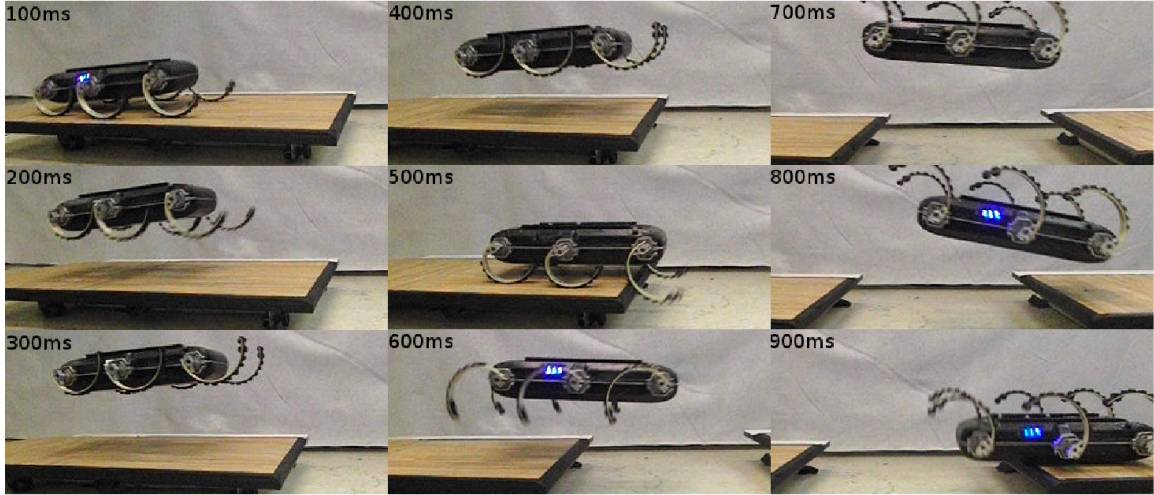


Figure 3.6: XRL crossing a 60cm gap. Frames taken every 100ms from a high speed video.

before the rear legs), as it reaches a significant height with some forward velocity and a moderate pitch. A timing parameter of about  $t_2 = 0.18$  was found to be the best, and was capable of lifting the robot onto a 27cm ledge with either a two or three legged strategy, about the same as the best quasi-static behavior.

For a compound jump onto a ledge, a leap-step similar to the gap crossing behavior reached a ledge of 29cm, a slight improvement. However the previous section reveals far higher leaps are possible, though with significant pitching. This suggests a different compound jump whose initial leap terminates at a vertically pitched apex that vault the legs above a far higher ledge, with the hope of grabbing and pulling the robot up onto it during the second stride. A  $(-, -)$  leap with  $t_2 = 0.06$  achieves such a (nearly vertical) high apex with some net horizontal displacement. This leap-grab, with no modification, is indeed capable of hooking the robots legs onto a 73cm high table, or 145% of the body length (450% of leg length), as shown in Fig. 3.1.

The second stride in this compound jump, intended to pull the robot up onto the ledge, is not easy to achieve in the present open loop setting (see also Figure 6.1 and discussion in Chapter 6). Absent specialized climbing feet [165], the robot will typically slip off even a coarse-sandpaper-surfaced ledge, as it tries to gain purchase. Extensive tuning (requiring well over 400 attempts) finally achieved a successful stride whose properties lie beyond the scope of this thesis (requiring

leg compliance in extension — the rear legs are nearly completely uncurled — and subtle sliding interaction), yet likely is encompassed within the more general self-manipulation framework (Chapter 4). To the best of our knowledge, this compound jump enables the robot to climb onto a ledge higher than that achieved by any previous general purpose legged robot, nearly doubling the best reported prior effort (53% of body length, or 230% of leg length [39]).

### 3.5 Parametric Jumping Dataset

This section contains Tables 3.1–3.4 documenting the apex state achieved after performing the leaps shown in Figure 3.4 and 3.5. The forward leap, (+, +), has been featured in the above analysis and so additional test data was collected to provide a more careful sampling of the leg coordination timing. The reverse jump, (−, −), is typically a backflip and since the robot was often more than half way through a flip at apex, the motion capture system was unable to continue tracking the robot. Therefore some velocity entries are missing, and the corresponding apex states should be taken to be “highest observed.” Also note that the  $t_2 = -0.161$  jump pitch reading is erroneous, a review of the high speed video puts the true pitch at about  $-90^\circ$ . Finally, the  $t_2 = 0.092$  and  $t_2 = 0.136$  appear to be outliers, which upon review of the high speed video reveals that one of the front legs (which are pushing before the rear legs, as  $t_2 > 0$ ) got stuck on the frame, as noted above for the (−, +) strategy. The (−, +) results have similar issues to (−, −), with regards to measurement during inversion and front legs contacting the frame.

$t_2$ (s)	$z$ (mm)	$x$ (mm)	$\phi$ (deg)	$\dot{x}$ (mm/s)	$\dot{\phi}$ (deg/s)
-0.203	175.1	557.4	15.0	1313.6	-77.3
-0.192	168.6	552.6	16.3	1419.9	-67.6
-0.179	158.8	546.6	15.7	1378.1	-14.7
-0.171	154.7	517.2	15.7	1876.2	32.8
-0.162	149.3	490.2	13.7	1780.0	94.1
-0.152	146.5	489.2	14.1	1788.4	84.0
-0.140	141.9	443.6	9.2	2441.7	222.4
-0.128	141.9	430.7	4.6	2049.0	190.7
-0.125	141.0	394.6	-1.0	2112.7	196.3
-0.112	143.7	392.6	-1.2	2088.6	186.5
-0.111	141.4	373.2	-2.5	2086.0	177.8
-0.100	140.7	363.2	-2.5	2085.6	176.9
-0.091	148.4	347.6	-3.1	2007.6	138.1
-0.081	151.3	331.4	-3.1	1981.9	126.1
-0.071	158.0	330.3	-1.3	1941.4	109.2
-0.071	159.1	334.6	-1.9	1945.8	100.6
-0.061	164.8	338.0	2.2	1934.7	107.7
-0.055	170.2	312.2	1.7	1864.6	87.5
-0.041	176.6	330.1	3.7	1856.4	80.6
-0.031	178.5	320.1	6.6	1821.5	79.8
-0.021	189.6	326.7	11.0	1870.2	90.3
-0.010	189.8	311.2	11.7	2402.4	108.4
0.000	199.2	313.7	14.1	1749.4	82.4
0.010	199.5	305.4	16.1	2055.2	106.7
0.020	221.8	343.4	21.8	1803.2	67.8
0.030	250.4	355.1	29.2	1635.0	61.6
0.041	253.2	333.8	31.2	1492.9	41.2
0.051	254.2	334.0	32.0	1423.4	37.3
0.062	258.1	327.3	32.9	1356.1	15.1
0.071	258.6	303.2	32.0	1398.4	69.8
0.081	258.2	311.1	31.2	1338.6	54.7
0.083	261.6	296.6	31.5	1355.4	73.7
0.091	259.9	311.9	31.3	1555.7	61.2
0.111	263.2	322.9	31.6	1346.0	25.9
0.117	262.7	335.9	31.7	1335.7	22.2
0.121	270.5	344.1	33.5	947.2	11.8
0.131	268.4	363.8	32.8	1395.9	4.2
0.141	275.6	377.3	34.1	1441.4	-2.5
0.153	284.8	418.2	36.8	1308.3	0.0
0.158	285.7	440.4	36.6	1550.5	-1.9
0.184	284.7	481.1	36.1	1384.9	-11.4
0.191	280.8	481.1	35.1	1676.0	-28.8
0.201	279.3	503.1	34.5	1703.3	-26.6
0.208	272.5	500.6	32.9	1739.4	-33.1
0.212	272.6	503.4	32.9	1741.6	-33.8

Table 3.1: Apex state for the (+, +) jumps at various relative leg timings, including additional trials not show in Figure 3.4.

$t_2$ (s)	$z$ (mm)	$x$ (mm)	$\phi$ (deg)	$\dot{x}$ (mm/s)	$\dot{\phi}$ (deg/s)
-0.237	351.0	-23.0	-88.6	114.3	-40.5
-0.180	394.8	-8.2	-87.9	61.3	-106.6
-0.161	449.6	-13.7	-219.5	108.9	16.2
-0.139	428.3	-17.2	-84.3	109.1	-203.5
-0.121	441.3	-7.4	-79.4	37.5	-204.2
-0.101	439.5	-26.5	-100.9	145.6	331.6
-0.080	451.2	-33.4	-109.8	117.6	365.6
-0.060	455.0	-47.6	-123.1	*	*
-0.041	470.5	-39.7	-128.4	*	*
-0.020	479.4	-67.1	-125.8	*	*
0.000	471.9	-46.8	-112.4	158.5	254.2
0.000	447.5	-59.1	-104.4	231.0	284.2
0.041	450.8	-141.6	-97.6	409.4	-44.0
0.061	401.9	-147.1	-64.1	553.1	-60.8
0.081	455.6	-182.8	-83.3	653.6	-159.5
0.092	295.9	-179.2	-111.7	868.7	32.2
0.104	422.6	-171.2	-70.3	589.2	-123.1
0.136	293.7	-108.7	-105.6	574.6	14.5
0.141	399.4	-242.7	-67.0	898.1	-221.6
0.180	326.1	-278.5	-55.0	1038.8	-178.0
0.201	288.3	-345.5	-42.4	1547.7	-241.8

Table 3.2: Apex state for the  $(-, -)$  jumps at various relative leg timings.

$t_2$ (s)	$z$ (mm)	$x$ (mm)	$\phi$ (deg)	$\dot{x}$ (mm/s)	$\dot{\phi}$ (deg/s)
-0.207	179.8	77.5	-14.3	751.5	392.3
-0.182	178.8	69.1	-15.6	844.7	347.6
-0.162	179.3	79.8	-8.8	853.5	314.5
-0.141	186.1	85.1	-7.4	952.8	318.6
-0.117	190.1	83.6	-4.9	751.3	210.4
-0.101	189.4	91.2	-1.5	682.3	152.3
-0.081	208.9	102.3	-2.2	660.9	102.2
-0.061	226.1	115.5	-1.0	670.1	99.1
-0.041	235.1	126.6	-4.8	668.6	51.8
0.000	234.6	206.8	-20.5	679.4	-74.4
0.000	230.9	202.5	-16.9	944.4	-72.3
0.020	230.9	196.4	-20.9	883.9	-108.6
0.040	223.8	185.1	-21.2	848.6	-100.8
0.057	210.0	204.2	-13.2	1067.7	-4.5
0.081	208.1	189.5	-16.3	803.6	-27.8
0.100	202.3	182.7	-25.9	874.4	-69.7
0.121	195.4	189.8	-32.3	969.8	-67.5
0.141	192.4	203.5	-26.0	959.3	-30.5
0.162	191.6	216.2	-20.9	926.0	-11.3
0.177	190.8	212.5	-19.5	854.4	-23.5
0.266	188.7	279.6	-41.5	656.9	2.8

Table 3.3: Apex state for the (+, -) jumps at various relative leg timings.

$t_2$ (s)	$z$ (mm)	$x$ (mm)	$\phi$ (deg)	$\dot{x}$ (mm/s)	$\dot{\phi}$ (deg/s)
-0.202	236.7	249.0	-43.0	382.6	-89.9
-0.191	294.0	222.7	-47.3	396.4	-92.1
-0.159	378.9	274.9	-95.1	*	*
-0.142	378.8	261.2	-103.0	*	*
-0.122	399.4	318.1	-108.3	*	*
-0.101	391.8	249.8	-112.2	*	*
-0.081	418.2	269.1	-119.9	*	*
-0.052	422.9	227.2	-123.3	*	*
-0.040	401.5	192.8	-116.0	*	*
-0.025	421.3	202.5	-113.0	*	*
0.000	378.8	253.9	-119.4	705.1	275.7
0.020	381.8	243.9	-102.7	*	*
0.020	405.5	162.1	-100.3	414.6	264.2
0.041	382.2	208.0	-105.8	458.8	258.4
0.081	382.5	97.6	-81.0	282.1	-136.5
0.092	289.1	223.2	-49.4	634.0	39.6
0.105	343.1	141.0	-72.4	546.6	-113.4
0.121	358.9	125.4	-99.6	310.0	130.8
0.161	229.7	-63.5	-19.3	592.9	-134.7
0.185	185.2	-72.9	0.8	389.3	-63.4
0.201	205.1	-15.7	18.3	542.4	-35.6

Table 3.4: Apex state for the  $(-, +)$  jumps at various relative leg timings.

## Chapter 4

# Self-Manipulation

The central contribution of this chapter is summarized in a single “master equation” (33), in addition to the equations and modeling decisions that lead up to it, expressing a rigid robot’s Lagrangian dynamics together with the constraint forces required to sustain them for any combination of legs and other body parts contacting rigid ground, such as the notional mechanism in Fig. 4.1. From the perspective of electromechanical platform design, this model elucidates the role of morphology and actuator characteristics in promoting or precluding certain desired motions of the body. From the perspective of behavior design, the model comprises a compact, uniform representation of the hybrid dynamical control system — the family of state spaces, controlled dynamics over them, and guard conditions and reset maps determining their adjacency — that must be exercised to achieve those motions.

The use of this formalism is illustrated with reference to a succession of tasks executed on the RHex robot wherein the interplay of controlled joint torques, leg contact conditions, and body reactions is particularly heightened by that machine’s very limited actuation. But the model is applicable to any legged machine, and we are convinced that specific power (W/kg) limitations exhibited by every available actuation scheme [46, 77, 116] will incur very similar, complex tradeoffs between various limb strategies for imparting work upon the body. We believe that the body-centric self-manipulation framework will reveal deeper, more formal results concerning the adjacency relations between a legged machine’s hybrid dynamics cells with strong behavioral implications, but these

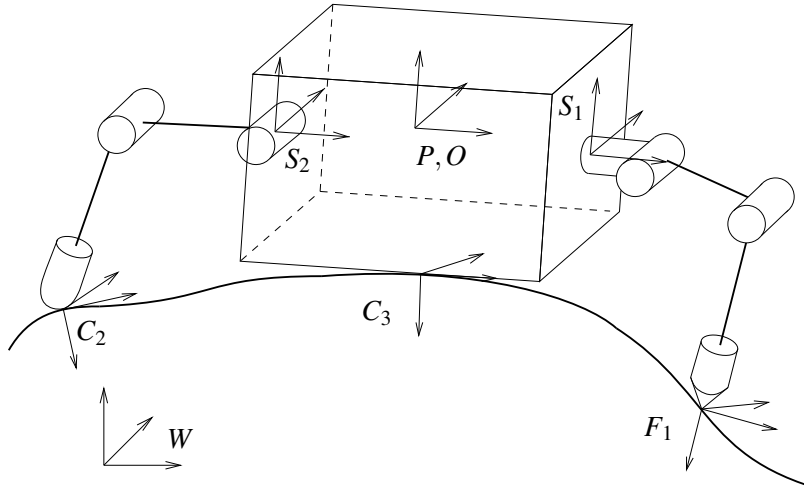


Figure 4.1: Selected coordinate frames for self-manipulation of a legged robot, where the object frame  $O$  is connected to the world but co-located with the palm frame  $P$  on the robot. Figure adapted from [134, Fig. 5.14]

ideas go beyond the scope of the present chapter and are merely hinted at in the conclusion through speculative remarks concerning further work presently in progress.

We intend the chapter to be readily accessible to readers acquainted with modern texts on robot manipulation and control [13, 119, 120, 134, 137, 162]. The modeling principles underlying self-manipulation are quite general, and as such are presented first in tutorial form. We believe their value and coherence is best conveyed in the context of a specific robot presented with a variety of specific tasks, spanning the energetic range from static to quasi-static to dynamic. The RHex robot is required to first stand in place (with the least possible energy on unknown terrain [88]), then manipulate itself in that place (while acting as a “tilt-scanning” sensor platform [86, 155]) and finally leap dynamically from that place (to “prepare” [27] various behaviors such as pronking [128] or gap crossing presented in Chapter 3). The value of this formal method becomes quite apparent when the great multiplicity, diversity and dynamically varying nature of the contact modes is considered across these seemingly disparate tasks. The framework generates automatically the equations of motion for all of them, whose consistent structure differs only in one term (the matrix  $\mathbf{A}$  in Eqn. (32)) facilitating not only computational analysis but also formal proofs of the validity or optimality of behavioral choices, controller design, and robot morphology.

We illustrate the utility of the self-manipulation formalism through a succession of increasingly energetic tasks implemented on RHex. The selected behaviors hopefully strike the reader as a plausible and coherent short “episode” of a kind likely to arise within an autonomous missions: the robot comes to a halt at some location of interest; once there, it actively engages its sensory payload; this new information provokes the sudden determination to leap up and escape that location. Notwithstanding the intuitively straightforward, even mundane nature of this simple vignette, in the absence of a systematic formalism along the lines this chapter develops, such a succession of tasks would present the behavior designer with a diverse (and combinatorially numerous) array of seemingly unrelated mechatronic and sensorimotor control problems whose common implementation offers no unifying insight into what properties of the platform might help or hinder the mission. In contrast, we point out how this general methodology informs and simplifies the analysis of each of these constituent tasks regarded separately, and affords a unifying framework for analyzing the performance as a function of platform design parameters (here focused on leg shape [132, 133], but the formalism makes explicit the role of the various other morphological parameters (e.g., Table 4.2) in the behavioral consequences).

This chapter is structured as follows: Section 4.1 formalizes the modeling decisions and then review the quasi-static and dynamic equations of motion. The abstract formalism is instantiated in Section 4.2 for RHex, providing a concrete example. This model is put to task in Section 4.3, where the various behaviors are instantiated and analyzed, with specific new design results called out. Section 4.4 contains additional details and analysis.

## 4.1 Self-Manipulation

### 4.1.1 Notation

Table 4.1 summarizes the notation in this section, chosen where possible to match [134]. Denote a rigid frame  $B$ , expressed in the coordinates of rigid frame  $A$  (or, equivalently, a rigid transformation that takes frame  $A$  into frame  $B$ )  $\mathbf{g}_{ab} \in \mathcal{G}_a := SE(d)$ , where  $d=2$  for a planar model and  $d=3$  for a spatial model. In local coordinates a rigid transformation will be written as a vector, for

$\mathbf{a} :=  \mathbf{n} - \mathbf{e}  \in \mathbb{Z}^+$	Internal or uncontrolled DOF (4.1.8)
$\mathbf{a} : \mathcal{Q} \rightarrow \mathcal{C}$	Base Constraint Function (9)
$\mathbf{A} : T\mathcal{Q} \rightarrow T\mathcal{C}$	Velocity Constraint Function (11)
$\mathbf{Ad}_{\mathcal{G}_{ab}} : T\mathcal{G}_a \rightarrow T\mathcal{G}_b$	Adjoint transformation from $a$ to $b$ (4.1.1)
$\mathbf{B}_{c,k} : T^*\mathcal{C}_k \rightarrow T^*\mathcal{G}_{c_k}$	Wrench basis at contact (3)
$c = \dim(\mathcal{C}) \in \mathbb{Z}^+$	Number of active contact wrenches (4.1.3)
$\mathbf{C} : T\mathcal{Q}^2 \rightarrow T^2\mathcal{Q}$	Coriolis matrix (30)
$\mathcal{C}_k \in \mathcal{G}_c$	Contact frames (ground aligned) (4.1.3)
$\mathcal{C}_k \subset \mathcal{G}_{c_k}, \mathcal{C} = \prod_k \mathcal{C}_k$	Space of contact positions (4.1.3)
$d \in \{2, 3\}$	Dimension of model (planar or spatial) (4.1.1)
$\mathbf{D} : T\mathcal{Q} \rightarrow T^2\mathcal{Q}$	Coriolis & internal dynamics (33)
$\mathbf{E} : T^*\mathcal{Q} \rightarrow T^2\mathcal{Q}$	Applied & external dynamics (33)
$e = \mathbf{q} - \mathbf{c} \in \mathbb{Z}^+$	Unconstrained DOF (4.1.7)
$\mathbf{f} \in T^*\mathcal{C}$	Contact wrench magnitudes (6)
$\mathbf{F}_a \in T^*\mathcal{G}_a$	Generalized force (wrench) (4.1.1)
$F_k \in \mathcal{G}_f$	Finger frames (leg aligned) (4.1.3)
$\mathbf{g}_{ab} \in \mathcal{G}_a := SE(d)$	Rigid transformation from $A$ to $B$ (4.1.1)
$\mathbf{G}_s : T^*\mathcal{C} \rightarrow T^*\mathcal{G}_p$	Self-manipulation grasp map (15)
$\mathbf{h} : \mathcal{Y} \rightarrow \mathcal{Q}, \mathbf{H} := D\mathbf{h}$	Implicit kinematic mobility function (18), (19)
$\mathbf{J}_h : T\Theta \rightarrow T\mathcal{C}$	Hand Jacobian (16)
$\mathbf{J}_{sf}^s : T\Theta \rightarrow T\mathcal{G}_c$	Finger Jacobians (4.1.5)
$\mathcal{K} \subseteq \mathbb{Z}^+, k =  \mathcal{K} $	Set of active contact points (1)
$L : T\mathcal{Q} \rightarrow \mathbb{R}$	Lagrangian (28)
$L_k \in \mathcal{G}_l$	Leg segment frame (leg aligned) (4.1.3)
$\mathbf{M}_a : T^2\mathcal{G}_a \rightarrow T^*\mathcal{G}_a$	Mass matrix (25)–(26)
$M_k \in \mathcal{G}_m$	Motor frames (leg aligned) (4.1.2)
$n = \dim(\Theta) \in \mathbb{Z}^+$	Number of joints (4.1.2)

Table 4.1: Key symbols used throughout this chapter, with Section or Equation of introduction noted. (Continued on next page)

$\mathbf{N} : \mathcal{Q} \rightarrow T^*\mathcal{Q}$	Nonlinear forces (gravity) (31)
$O \in \mathcal{G}_o,$	Object frame (coincident with $P$ ) (4.1.2)
$P \in \mathcal{G}_p$	Palm frame (body aligned) (4.1.2)
$q = n + d(d+1)/2 \in \mathbb{Z}^+$	Dimension of the combined state (4.1.2)
$\mathbf{q} \in \mathcal{Q} := \Theta \times \mathcal{G}_o$	Combined system state (4.1.2)
$\mathbf{R} \in SO(d)$	Rotation Matrix (4.1.1)
$S_k \in \mathcal{G}_s$	Leg attachment frames (body aligned) (4.1.2)
$T : T\mathcal{Q} \rightarrow \mathbb{R}^+$	Kinetic Energy (24)
$\mathbf{U} : T^*\mathcal{C} \rightarrow \mathbb{R}^k$	Friction cone (4)
$\mathcal{U} \subseteq \mathbb{S}^1$	Range of angles considered (4.1.2)
$v \in T\pi\mathcal{G}$	Linear velocity (4.1.1)
$V : \mathcal{Q} \rightarrow \mathbb{R}^+$	Potential energy (27)
$\mathbf{V}_{ab}^s \in T\mathcal{G}_a, \mathbf{V}_{ab}^b \in T\mathcal{G}_b$	Generalized velocity (twist) (4.1.1)
$W \in \mathcal{G}_w$	World inertial frame (4.1.2)
$\mathbf{x} \in \mathcal{G}$	Body position and orientation (4.1.2)
$\mathbf{x}_c \in \mathcal{C}$	Contact location in the contact basis (5)
$\mathbf{y} := \boldsymbol{\psi}(\mathbf{q}) \in \mathcal{Y}$	Lagrangian free variables (4.1.7)
$\alpha \in \mathbb{R}^a$	Internal force magnitude (22)
$\zeta \in \mathbb{R}$	Height function (4.1.9)
$\boldsymbol{\theta} \in \Theta := \mathcal{U}^n$	Joint angle vector (4.1.2)
$\lambda \in T^*\mathcal{C}$	Lagrange multipliers (constraint forces) (29)
$\pi : SE(d) \rightarrow \mathbb{R}^d$	Projection down to linear components (4.1.1)
$\boldsymbol{\tau} \in T^*\Theta$	Torque (4.1.1)
$\Upsilon \in T^*\mathcal{Q}$	External forces (including torques) (31)
$\phi \in SO(d)$	Body Orientation (4.1.2)
$\boldsymbol{\psi} : \mathcal{Q} \rightarrow \mathcal{Y}, \mathbf{Y} := D\boldsymbol{\psi}$	Lagrangian free variable map (4.1.7)
$\boldsymbol{\omega} \in TSO(d)$	Angular velocity (4.1.1)

Table 4.1: Key symbols used throughout this chapter, with Section or Equation of introduction noted. (Continued from previous page)

example  $\mathbf{x} = [x, y, z, \phi_y, \phi_p, \phi_r]^T$ , where the Euler angles may be chosen as convenient but here will be ZYX — Yaw, Pitch, Roll. The group product will be denoted as  $\mathbf{g}_{ab} \cdot \mathbf{g}_{bc}$ . The velocity of frame  $B$  relative to frame  $A$  as seen by  $A$  is  $\mathbf{V}_{ab}^s = \dot{\mathbf{g}}_{ab} \cdot \mathbf{g}_{ab}^{-1}$ , or in twist coordinates  $\begin{bmatrix} v_{ab}^s \\ \omega_{ab}^s \end{bmatrix}$  (the “spatial” velocity), while the same velocity written in the coordinates of frame  $B$  is  $\mathbf{V}_{ab}^b = \mathbf{g}_{ab}^{-1} \cdot \dot{\mathbf{g}}_{ab}$  (the “body” velocity) [134, Section 2.4.2]. A body wrench (generalized force),  $\mathbf{F}_b := \begin{bmatrix} f \\ \tau \end{bmatrix}$ , is defined such that work is  $\mathbf{V}_{a,b}^b \cdot \mathbf{F}_b$ . An adjoint transformation matrix,  $\mathbf{Ad}_{g_{ab}} : T\mathcal{G}_a \rightarrow T\mathcal{G}_b$ , relates the two expressions of velocity,  $\mathbf{V}_{ab}^s = \mathbf{Ad}_{g_{ab}} \mathbf{V}_{ab}^b$  [134, Chapter 2].

Denoting by  $\pi_x$  a projection down to the  $x$  component,  $\pi_{c_k}$  a projection to some collection of components to be defined by the friction conditions as specified below, and the non-subscripted  $\pi$  the projection from an element of  $SE(d)$  (position and orientation) to  $\mathbb{R}^d$  (position only), we express the origin of a frame,  $\mathbf{g}$ , as (e.g. when  $d=2$ )  $(x, z) = \pi(\mathbf{g}) \in \pi(\mathcal{G}) \approx \mathbb{R}^2$ . Similarly let  $\mathbf{R}_{ab} = \pi_R \mathbf{g}_{ab}$  be the rotational component of the rigid transformation, in matrix form. To convert between local coordinates and twist coordinates, define (e.g. when  $d=2$ ),  $\mathbf{R} := \begin{bmatrix} R & 0 \\ 0 & 1 \end{bmatrix}$ , so that  $\mathbf{V}_{ab}^b = \mathbf{R}_{ab}^T \dot{\mathbf{x}}$ .

### 4.1.2 Modeling Decisions

This self-manipulation model follows the usual conventions from manipulation [13, 119, 120, 134, 137, 162]: the hand and object are separated at the fingertips; the wrench bases at the fingers (i.e. the motions that the contact resists) are considered in unison; and (through the separated velocity constraints of the grasp map and hand Jacobian) dictate the forces and torques on the object and robot. However since the robot is the object, we set the “Object” frame,  $O$ , to be coincident with the robot’s “Palm” frame,  $P$ .

Define the following coordinate frames, as shown in Fig. 4.1 (and corresponding to [134, Fig. 5.14]). Let  $P$  be attached to the COM of the robot body segment, and the object frame,  $O$  be co-located at  $P$ , but attached to the world. The usual manipulation problem takes the palm frame as fixed, and so from the robot’s perspective it appears that the gravitational force is applied to the movable Earth (the object), and not the other way around. Co-locating the object and palm coordinate frames allows for wrenches and twists that are referenced to that point in the world, and the robot’s actual motion is simply be the opposite sign (from a ground based observation), as explored

below. The true world inertial frame,  $W$ , is at some unknown but fixed location relative to the ground, and aligned with gravity. The position of the robot,  $\mathbf{g}_{wp} \in SE(d)$ , or  $\mathbf{x}$  when written in local coordinates, is part of our state but we strive to not necessarily need to know anything other than the robot orientation relative to gravity,  $\phi \in SO(d)$ .

Each leg attaches at a frame fixed on the robot body,  $S_i$  for leg  $i$ , and for each joint of that leg  $j$  a rotating frame that moves with the motor,  $M_{i,j}$ , at the center of the joint but rotated by  $\theta_{i,j} \in \mathbb{S}^1$  about some joint axis (although it may be convenient to restrict the available angles to  $\theta_{i,j} \in \mathcal{U}$ , for example  $\mathcal{U} := [-30^\circ, 30^\circ]$ ). Denote by  $\mathbf{g}_{s_i m_{i,j}}(\theta_{i,1}, \dots, \theta_{i,j})$  this open-chain kinematic mapping from  $\mathbb{T}^j$  into the appropriate rigid group. Define a “leg” frame,  $L_{i,j}$ , at the center of mass of link and a “finger” frame,  $F_i$ , at the toe and fixed relative to the final leg segment. The collection of  $n$  total joint angles,  $\theta \in \Theta$ , combined with the COM position define our overall state,  $\mathbf{q} = [\theta \quad \mathbf{x}] \in \mathcal{Q} := \Theta \times \mathcal{G}_o \equiv \mathbb{T}^n \times SE(d)$ , having dimension  $q := n + d(d+1)/2$ .

### 4.1.3 Contact Conditions

In order to determine which parts of the robot are in contact with the ground we first define a contact frame,  $C_i$ , at each potential contact point (toe or other body part, and located at  $F_i$  in the case of a toe). The contact frame is typically oriented with the  $\mathbf{z}$  axis pointing into the object, however here the object being manipulated is the robot. We choose to keep the definition consistent with respect to the legs, and so the  $\mathbf{z}$  axis points into the ground (which on flat terrain aligns  $C_i$  with  $W$ ). Note that body contact under this system simply involves a zero jointed “leg” with an appropriate contact frame. Section 4.1.6 extends these ideas to rolling contact.

Which contact points are active can be determined by checking the distance to the surface of the local world, with contact of some sort occurring when that distance is zero [162, Section 27.2] (the type of contact is specified below). This condition can be reduced to checking the contact point height,  $\zeta_{c_i}(\mathbf{q}) := \pi_z(\mathbf{g}_{c_i w}) - \hat{\zeta}_{c_i}$ , for some local terrain height  $\hat{\zeta}_{c_i}$  (where  $\hat{\zeta}_{c_i} := 0$  for flat level ground). Call the set of  $k$  active contact point indices  $\mathcal{K}$ , such that,

$$\mathcal{K} := \{k | \zeta_{c_k}(\mathbf{q}) \equiv 0\}. \quad (1)$$

The set can be updated based on the current contact conditions by checking the unilateral constraint conditions (defined below) on all active contact points and the touchdown conditions on all non-active contact points, see Chapter 5 for more details on the impulsive switching this entails. The set of contact conditions for a quasi-static RHex is needed in the analysis of Section 4.3.2 (see Fig. 4.3 — and these boundary conditions are used throughout) however it is important to note that none of the control algorithms we develop in this chapter require that the robot actually know anything about their location.

There are a number of different types of contact possible once a contact point is known, for example RHex has both sliding and non-sliding point contacts (see [120, Table 2-3], [134, Table 5.2] for a full list of examples). In each contact frame define a subspace consisting of only the degrees of freedom that friction keeps fixed,  $\mathcal{C}_k \subseteq \mathcal{G}_{c_k}, k \in \mathcal{K}$ , with a projection (whose expression in coordinates is a sub-block of the identity matrix),  $\mathbf{x}_{c_k} := \pi_{c_k}(\mathbf{g}_{c_k w})$ . However the standard grasping analysis instead focuses on the wrenches that the contact can resist (as is required for the non-holonomic constraints of rolling contact), and so in that spirit define the *wrench basis* as the image of the pullback of  $\pi_{c_k}$  from the allowable contact wrenches to all possible contact wrenches at a contact point point [134, Section 5.2.1],  $\mathbf{B}_{c_k} : T^*\mathcal{C}_k \rightarrow T^*\mathcal{G}_{c_k}$ , (written in coordinates,  $\mathbf{B}_{c_k}^T := D\pi_{c_k}$ ). The contact conditions enforce zero motion in these directions as well — giving rise to the familiar dual pairing,

$$\dot{\mathbf{x}}_{c_k} = \mathbf{B}_{c_k}^T \mathbf{V}_{w, c_k}^b, \quad \dot{\mathbf{x}}_{c_k} \in T\mathcal{C}_k, \quad (2)$$

$$\mathbf{F}_{c_k} = \mathbf{B}_{c_k} \mathbf{f}_{c_k}, \quad \mathbf{f}_{c_k} \in T^*\mathcal{C}_k. \quad (3)$$

This contact constraint holds only when the contact forces are in some Coulomb friction cone relating the normal and tangential forces,<sup>1</sup>

$$\mathbf{U}_k(\mathbf{f}_{c_k}) \geq \mathbf{0}, \quad \mathbf{U}_k : T^*\mathcal{C}_k \rightarrow \mathbb{R}^{c_k}, \quad (4)$$

---

<sup>1</sup>The given frame convention for the  $\mathbf{z}$  axis of  $\mathcal{C}_k$  means that the normal forces are negative in general, see Appendix (76), (78).

[134, Section 5.2.1], [162, Section 27.3], satisfying,

$$\mathbf{U}_k(\mathbf{f}_a) \geq 0, \quad \mathbf{U}_k(\mathbf{f}_b) \geq 0 \Rightarrow \mathbf{U}_k(\alpha\mathbf{f}_a + \beta\mathbf{f}_b) \geq 0 \quad \forall \alpha, \beta \in \mathbb{R}^+,$$

which in the planar case (d=2) is simply a matrix multiplication,  $\mathbf{U}_k\mathbf{f}_{c_k} \geq 0$ .

For multi-finger robots, and now multi-legged robots, it is often convenient to deal with the collection of contact positions (and similarly for twists and wrenches) among all contact points,

$$\mathbf{x}_c := (\mathbf{x}_{c_1}, \dots, \mathbf{x}_{c_n}) \in \mathcal{C} := \prod_{k \in \mathcal{K}} \mathcal{C}_k, \quad (5)$$

$$\mathbf{f}_c := (\mathbf{f}_{c_1}, \dots, \mathbf{f}_{c_n}) \in T^*\mathcal{C}, \quad (6)$$

$$\mathbf{U}(\mathbf{f}_c) := (\mathbf{U}_1(\mathbf{f}_{c_1}), \dots, \mathbf{U}_n(\mathbf{f}_{c_n})) \geq \mathbf{0}, \quad (7)$$

where  $c := \dim(\mathcal{C}) = \sum_{k \in \mathcal{K}} \dim(\mathcal{C}_k)$  is the total number of constraints on the system.

#### 4.1.4 Kinematic Loop Closures

The friction holding the contact points in place along some dimensions sets up the following constraint functions, expressing the  $k^{\text{th}}$  contact condition by the equality,

$$\mathbf{x}_{c_k} = \pi_{c_k}(\mathbf{g}_{c_k w}(\mathbf{q})) = \pi_{c_k}(\mathbf{g}_{c_k s_k}(\mathbf{q}) \cdot \mathbf{g}_{s_k w}(\mathbf{x})), \quad (8)$$

(see further discussion in the Appendix Section 4.4.1), motivating the definition of the constraint function

$$\mathbf{a}_k(\mathbf{q}) := \pi_{c_k}(\mathbf{g}_{c_k w}(\mathbf{q})) - \hat{\mathbf{x}}_{c_k}, \quad (9)$$

whose zeros,  $\mathbf{a}_k^{-1}[0]$ , comprise the constraint set for some initial contact position  $\hat{\mathbf{x}}_{c_k}$ . Collectively, the  $c$  kinematic constraints are,

$$0 \equiv \mathbf{a}(\mathbf{q}). \quad (10)$$

This constraint sets up the initial pitching sensor behavior presented in Section 4.3.2, though this is quickly extended to include rolling contact as described in Section 4.1.6.

#### 4.1.5 Infinitesimal Kinematics: The Grasp Map and Hand Jacobian

The infinitesimal kinematics over the base constraint (10), relates wrenches and twists between the body and joints and contacts, through induced tangent constraints. Given a constrained motion,  $\mathbf{q}_a(t) : \mathbb{R} \rightarrow \mathcal{Q}$ , satisfying (10),  $\mathbf{a} \circ \mathbf{q}_a \equiv 0$ , these induced constraints can be given coordinate expression by differentiating the constraint equation, however by using the fact that the constraint equation must be true no matter where the world frame is, some of the interdependence is removed. Therefore we claim that,

$$\frac{d}{dt} \mathbf{a}_k \circ \mathbf{q}_a \equiv 0 \Rightarrow \mathbf{A}_k(\mathbf{q}) \dot{\mathbf{q}} := [-\mathbf{B}_{c_k}^T \mathbf{Ad}_{g_{c_k f_k}} \mathbf{J}_{s_k f_k}^b \quad -\mathbf{B}_{c_k}^T \mathbf{Ad}_{g_{c_k p}} \mathbf{R}_{wp}^T] \dot{\mathbf{q}} \equiv 0, \quad (11)$$

where the leg Jacobian  $\mathbf{J}_{s_k f_k}^b$  is defined such that,  $\mathbf{V}_{s_k f_k}^b = \mathbf{J}_{s_k f_k}^b(\theta) \dot{\theta}$ . The proof of this claim may be written out using either a homogeneous representation or a twist representation, as shown in the Appendix Section 4.4.1. Here instead we show that this equality (11) is equivalent to the standard manipulation constraint,

$$\mathbf{J}_h \dot{\theta} = \mathbf{G}^T \mathbf{V}_{p_o}^b, \quad (12)$$

[134, Eqn. 5.15], typically derived directly in terms of twists by defining the grasp map and hand Jacobian, and not by differentiating a base constraint (10).

In manipulation literature, the *grasp map*,  $\mathbf{G} : T^* \mathcal{C} \rightarrow T^* \mathcal{G}_o$ , takes wrenches at the contact points (i.e., forces at the contact points),  $\mathbf{f}_c \in T^* \mathcal{C}$  to wrenches on the object,  $\mathbf{F}_o \in T^* \mathcal{G}_o$ , and its dual,  $\mathbf{G}^T$ , acts covariantly, taking body twists of the object,  $\mathbf{V}_o \in T \mathcal{G}_o$ , to twists at the contact point,  $\dot{\mathbf{x}}_c \in T \mathcal{C}$ , all expressed in coordinates as,

$$\mathbf{G}\mathbf{f}_c = \mathbf{F}_o \quad \mathbf{G}^T \mathbf{V}_{po}^b = \dot{\mathbf{x}}_c, \quad (13)$$

$$\mathbf{G} := \left[ \mathbf{A}_{g_{c_1o}}^T \mathbf{B}_{c_1} \quad \dots \quad \mathbf{A}_{g_{c_no}}^T \mathbf{B}_{c_n} \right], \quad (14)$$

[134, Section 5.2.2, Fig. 5.15], where  $\mathbf{G} \in \mathbb{R}^{3 \times c}$  if  $d=2$ , and  $\mathbf{G} \in \mathbb{R}^{6 \times c}$  if  $d=3$ . As this is a self-manipulation,  $\mathbf{V}_{po}^b$  is the opposite of the body velocity one would normally consider, as it is the velocity of  $O$ , attached to the world. This opposite direction comes from the more general identity,  $\mathbf{V}_{po}^b = -\mathbf{Ad}_{g_{op}} \mathbf{V}_{op}^b$ , [134, Lemma 2.16] (see Appendix Section 4.4.6 for proof), but in this case the adjoint matrix is simply identity. Therefore a self-manipulation “grasp” map is defined as,

$$\mathbf{G}_s := -\mathbf{G}, \quad \mathbf{G}_s^T \mathbf{V}_{op}^b = \dot{\mathbf{x}}_c, \quad \mathbf{G}_s \mathbf{f}_c = \mathbf{F}_p \quad (15)$$

where recall that  $\mathbf{V}_{op}^b = \mathbf{V}_{wp}^b$  is the body velocity of  $P$  relative to any world coordinate frame, and  $\mathbf{F}_p$  is the body wrench.

Next, the *hand Jacobian*,  $\mathbf{J}_h$  relates infinitesimal motion at the joints,  $\dot{\boldsymbol{\theta}} \in T\Theta$  to twists at the contact points,  $\dot{\mathbf{x}}_c \in T\mathcal{C}$ , and has a dual, the pullback from contact wrenches,  $\mathbf{f}_c \in T^*\mathcal{C}$  to hip torques,  $\boldsymbol{\tau} \in T^*\mathcal{C}$ , all expressed as,

$$\mathbf{J}_h \dot{\boldsymbol{\theta}} = \dot{\mathbf{x}}_c \quad \mathbf{J}_h^T \mathbf{f}_c = \boldsymbol{\tau}, \quad (16)$$

[134, Section 5.5.1, Fig. 5.15], where  $\mathbf{J}_h \in \mathbb{R}^{n \times c}$ . The hand Jacobian definition carries over directly from manipulation,

$$\mathbf{J}_h := \begin{bmatrix} \mathbf{B}_{c_1}^T \mathbf{Ad}_{g_{sc_1}}^{-1} \mathbf{J}_{sf_1}^s & 0 & 0 \\ 0 & \ddots & 0 \\ 0 & 0 & \mathbf{B}_{c_n}^T \mathbf{Ad}_{g_{sc_n}}^{-1} \mathbf{J}_{sf_n}^s \end{bmatrix}.$$

Note that in the case of body contact, the hand Jacobian has a column of all zeros, that is contact wrenches at that point have no direct projection onto the joint torques (see Appendix Section 4.4.2 for further discussion).

Combining (13) and (16), and recalling that  $\mathbf{V}_{op}^b = \mathbf{R}_{wp}^T \dot{\mathbf{x}}$ , we see that as claimed in (11),

$$\mathbf{A}(\mathbf{q})\dot{\mathbf{q}} = [-\mathbf{J}_h \quad \mathbf{G}_s^T \mathbf{R}_{pw}^T] \begin{bmatrix} \dot{\boldsymbol{\theta}} \\ \dot{\mathbf{x}} \end{bmatrix} = [-\mathbf{J}_h \quad \mathbf{G}_s^T] \begin{bmatrix} \dot{\boldsymbol{\theta}} \\ \mathbf{V}_{op}^b \end{bmatrix} = \mathbf{0}, \quad (17)$$

asserting that the motion of the contact frames as seen from the robot and the world agree (so long as the friction constraints hold (7)).

#### 4.1.6 Rolling Contact

Rolling contact, when the contact frame  $C_k$  is not fixed relative to either the body or object, can be treated as a simple extension to the above analysis. At each instant the velocity of the body and joints is as if the leg was a simple stick leg, with a toe at the point of contact,<sup>2</sup> however the evolution of the contact location is dictated by the relative geometry. The underlying contact velocity constraint is still correct, as the contact instantaneously cannot move in the constrained direction, however in general this constraint is non-holonomic [97] (i.e. there is no corresponding base constraint (8)).

Therefore in general the velocity constraint components  $\mathbf{G}_s$  and  $\mathbf{J}_h$  also depend on parameterized contact coordinates,  $\eta$ , which update as some function of the local geometry [131]. For RHex, the geometry is simple enough that no extra  $\eta$  parameters are needed (the rolling contact frames can be described fully by elements of  $\mathbf{q}$ ), and so in the interest of space we direct the reader to [134, Chapter 5.6] for a full derivation (with similar notation) as well as [30, 97, 131]. In addition see [147, 151] for higher order considerations — for now it is sufficient to note that while the constraint,  $\mathbf{A}$  (11), is the same for rolling contact as an equivalent stick leg,  $\dot{\mathbf{A}}$  may not be, and so while quasi-statically both follow the same trajectory, the dynamics are different in order to account for the changing constraints. This fact is used for example in Result C.4.

#### 4.1.7 Parameterization of the Closed-Loop Kinematics

In most of the applications settings considered below, given the  $c$  constraints (10), it is convenient to work with a local parameterization of the  $e = q - c$  dimensional manifold of remaining mobility. This

---

<sup>2</sup>See the Appendix Section 4.4.3 for simple proof for RHex like circular legs.

amounts to the choice of an implicit function,  $h : \mathcal{Y} \rightarrow \mathcal{Q}$ , where  $\mathcal{Y}$  is some convenient open subset of  $\mathbb{R}^e$ . To simply answer certain questions about the robot motion in terms of particular components of  $\mathbf{q}$ , it is convenient to identify  $\mathcal{Y}$  with a problem-specific Euclidean submanifold of our generalized coordinates, i.e.  $\mathcal{Y} := \psi(\mathcal{Q})$ , where, in coordinates,  $\psi$  is some fixed linear combination of the components of  $\mathbf{q}$  corresponding to the directions of interest in the problem (and often a projection whose matrix representation is a subcollection of columns from the identify matrix). The tangent map,  $\mathbf{Y} := D\psi$ ,  $\mathbf{Y} \in \mathbb{R}^{q \times e}$ , results in a combined constraint equation,

$$\begin{bmatrix} \mathbf{A} & 0 \\ \mathbf{Y} & -\mathbf{Id}_e \end{bmatrix} \begin{bmatrix} \dot{\mathbf{q}} \\ \dot{\mathbf{y}} \end{bmatrix} = 0,$$

such that the associated implicit function (split into hand and object components),

$$\mathbf{h}_h(\mathbf{y}) = \boldsymbol{\theta}, \quad \mathbf{h}_o(\mathbf{y}) = \mathbf{x}, \quad \mathbf{h} = (\mathbf{h}_h, \mathbf{h}_o) : \mathcal{Y} \rightarrow \mathcal{Q}, \quad (18)$$

is a local immersion — i.e., its Jacobian maps,

$$\dot{\boldsymbol{\theta}} = \mathbf{H}_h \dot{\mathbf{y}}, \quad \dot{\mathbf{x}} = \mathbf{H}_o \dot{\mathbf{y}}, \quad \mathbf{H} := D_{\mathbf{y}} \mathbf{h}, \quad (19)$$

$$\mathbf{H} = \begin{bmatrix} \mathbf{A} \\ \mathbf{Y} \end{bmatrix}^{-1} \begin{bmatrix} 0 \\ \mathbf{Id}_e \end{bmatrix}, \quad (20)$$

is full rank (never passing through the origin) in both tangent spaces (for some local region in  $\mathcal{Y}$ ). In this chapter we assume that such a parameterization exists. The matrix inverted in (20) is dimension  $q \times q$ , and invertible except at singularities in the kinematics or parameterization. Note that  $\mathbf{H}_h$  can be thought of as the instantaneous gear ratios for  $n$  independent motor shafts coupled rigidly to an external output load with  $e$  DOF.

This implicit function is used to show that the change of basis in Section 4.3.1 is a good approximation, and again in Section 4.3.2 that  $\mathbf{H}_o$  can be used to control the pitching rate of the robot.

### 4.1.8 Quasi-static Forces and Torques

The wrench due to the gravitational potential field,  $\mathbf{F}_g$ , is derived from the height  $\zeta : \mathcal{G}_p \rightarrow \mathbb{R}$  in that potential field and, at static equilibrium, it is exactly balanced by the contact forces through the grasp map (13),

$$\mathbf{G}_s \mathbf{f}_c = -\mathbf{F}_g. \quad (21)$$

If the number of DOF in the closed-chain analysis,  $e$ , is less than the number of motors,  $n$ , there is some “internal” force components, which lies in the subspace [134, Definition 5.3],

$$\ker(\mathbf{G}_s) = \text{Im}(\mathbf{f}_N) := \left\{ \sum_{i=1}^a \alpha_i \mathbf{f}_{Ni} \mid \alpha_i \in \mathbb{R} \right\}, \quad (22)$$

that forms the homogeneous solution, i.e. contact wrenches that are *internal* in that they can perform no work on the object, where  $a := n - e$ .

To invert (21) and determine the contact forces required to balance the external wrench, torque constraints<sup>3</sup> of the form  $\mathbf{t}_i^T \boldsymbol{\tau} = 0, i \leq a$  must be imposed upon the hip joint torque vector,  $\boldsymbol{\tau} \in T^* \Theta$ , (16). Pulling back through the infinitesimal kinematics, this now constrains the contact wrench magnitude vector  $\mathbf{f}_c \in T^* \mathcal{C}$  leading to a unique solution of the full rank augmented version of (21) taking the form,

$$\mathbf{t}^T \mathbf{J}_h^T \mathbf{f}_c = 0, \quad \mathbf{f}_p := - \begin{bmatrix} \mathbf{G}_s \\ \mathbf{t}^T \mathbf{J}_h^T \end{bmatrix}^{-1} \begin{bmatrix} \mathbf{F}_g \\ 0 \end{bmatrix}, \quad (23)$$

Thus the overall vector of contact wrench magnitudes is,

$$\mathbf{f}_c = \mathbf{f}_p + \sum_i \alpha_i \mathbf{f}_{Ni},$$

and the internal and external components may be projected back into motor torques through (16).

---

<sup>3</sup> Alternatively a “no internal force” constraint may be encoded as  $\mathbf{f}_N^T \mathbf{f}_c = 0$  [120], however in general we allow some internal force to achieve some other goal, such as no internal torque.

These quasi-static internal and external forces are the key to the reactive standing behavior in Section 4.3.1, and calculating the torque requirement in the pitching sensor sweep (Section 4.3.2).

#### 4.1.9 Dynamics

This section derives a Lagrangian formulation for the robot dynamics in terms of some local coordinates, arriving at a relationship between  $\mathbf{q}$ ,  $\dot{\mathbf{q}}$ , and  $\ddot{\mathbf{q}}$  in (33). We allow for the option of having massless legs, and so expressions of the dynamics cannot involve directly inverting the mass matrix.

If the body of the robot has mass  $m_b$  and inertia  $I_b$ , and each leg segment may have mass  $m_{l_i}$  and inertia  $I_{l_i}$ , then observe that the total kinetic energy is,<sup>4</sup>

$$T = \frac{1}{2} \begin{bmatrix} \dot{\boldsymbol{\theta}}^T & \mathbf{V}_{op}^{bT} \end{bmatrix} \widehat{\mathbf{M}} \begin{bmatrix} \dot{\boldsymbol{\theta}} \\ \mathbf{V}_{op}^b \end{bmatrix} = \frac{1}{2} \dot{\mathbf{q}}^T \overline{\mathbf{M}} \dot{\mathbf{q}}, \quad (24)$$

$$\widehat{\mathbf{M}} := \begin{bmatrix} \sum_i \mathbf{J}_{pl_i}^{bT} \mathbf{M}_{l_i} \mathbf{J}_{pl_i}^b & \sum_i \mathbf{J}_{pl_i}^{bT} \mathbf{M}_{l_i} \mathbf{A} \mathbf{d}_{g_{pl_i}}^{-1} \\ \sum_i \mathbf{A} \mathbf{d}_{g_{pl_i}}^{-1T} \mathbf{M}_{l_i} \mathbf{J}_{pl_i}^b & \mathbf{M}_b + \sum_i \mathbf{A} \mathbf{d}_{g_{pl_i}}^{-1T} \mathbf{M}_{l_i} \mathbf{A} \mathbf{d}_{g_{pl_i}}^{-1} \end{bmatrix}, \quad (25)$$

$$\mathbf{M}_{l_i} := \begin{bmatrix} m_{l_i} \mathbf{I}_d & 0 \\ 0 & I_{l_i} \end{bmatrix}, \quad \overline{\mathbf{M}} := \begin{bmatrix} \mathbf{I}_d & 0 \\ 0 & \mathbf{R}_{wp} \end{bmatrix} \widehat{\mathbf{M}} \begin{bmatrix} \mathbf{I}_d & 0 \\ 0 & \mathbf{R}_{wp}^T \end{bmatrix} \quad (26)$$

(see Appendix Section 4.4.4 for full derivation) where recall that  $\mathbf{J}_{pl_i}^b \dot{\boldsymbol{\theta}} = \mathbf{V}_{pl_i}^b$ .

The potential energy depends on the world-referenced height of the body in the gravitational field,  $\zeta_o(\mathbf{x})$ , and the configuration-dependent height of each link relative to the body,  $\zeta_l(\boldsymbol{\theta}, \boldsymbol{\phi})$ ,

$$V(\mathbf{q}) = m_b g \zeta_o(\mathbf{x}) + \sum_{l=1}^n m_l g (\zeta_o(\mathbf{x}) + \zeta_l(\boldsymbol{\theta}, \boldsymbol{\phi})). \quad (27)$$

Using these statements of the kinetic and potential energy, and applying Lagrange's equations [134, Eqn. 6.4], [16, Sec. 5.1],

<sup>4</sup>This “self-manipulation” inertia tensor (25) is much simpler when the legs are taken to be massless,  $\mathbf{M}_{l_i} = 0 \Rightarrow \widehat{\mathbf{M}} = \begin{bmatrix} 0 & 0 \\ 0 & \mathbf{M}_b \end{bmatrix}$ , and quite different than in manipulation,  $\widehat{\mathbf{M}} = \begin{bmatrix} \sum \mathbf{J}^T \mathbf{M}_i \mathbf{J} & 0 \\ 0 & \mathbf{M}_b \end{bmatrix}$ , (as in [134, Eqn. 6.24]), where the extra terms in (25) arise from the coupling inherent in self-manipulation.

$$L(\mathbf{q}, \dot{\mathbf{q}}) = \frac{1}{2} \dot{\mathbf{q}}^T \bar{\mathbf{M}}(\theta, \phi) \dot{\mathbf{q}} - V(\mathbf{q}) = \frac{1}{2} \sum_{i,j=1}^q \bar{M}_{ij} \dot{q}_i \dot{q}_j - V(\mathbf{q}), \quad (28)$$

$$0 = \frac{d}{dt} \frac{\partial L}{\partial \dot{q}_i} - \frac{\partial L}{\partial q_i} + \mathbf{A}^T \lambda - \Upsilon, \quad (29)$$

$$\frac{d}{dt} \frac{\partial L}{\partial \dot{q}_i} = \frac{d}{dt} \left( \sum_{i,j=1}^q \bar{M}_{ij} \dot{q}_j \right) = \sum_{i,j=1}^q \left( \bar{M}_{ij} \ddot{q}_j + \dot{\bar{M}}_{ij} \dot{q}_j \right),$$

$$\frac{\partial L}{\partial q_i} = \frac{1}{2} \sum_{j,k=1}^q \frac{\partial \bar{M}_{kj}}{\partial q_i} \dot{q}_k \dot{q}_j - \frac{\partial V}{\partial q_i}.$$

The Coriolis terms may be grouped in the usual way,<sup>5</sup>

$$\bar{C}_{ij} = \frac{1}{2} \sum_{k=1}^q \left( \frac{\partial \bar{M}_{ij}}{\partial q_k} + \frac{\partial \bar{M}_{ik}}{\partial q_j} - \frac{\partial \bar{M}_{kj}}{\partial q_i} \right) \dot{q}_k, \quad (30)$$

and the nonlinear (gravitational) and applied forces are,

$$\bar{N}_i(\theta, \phi) = \frac{\partial V}{\partial q_i}, \quad \Upsilon(\boldsymbol{\tau}) = \begin{bmatrix} \boldsymbol{\tau} \\ \mathbf{0} \end{bmatrix}, \quad (31)$$

where  $\bar{\mathbf{N}}$  depends only on  $\theta$  and  $\phi$  as the force due to gravity is position independent. Note that damping may also be modeled with  $\bar{\mathbf{N}}$ , in which case it depends on  $\dot{\mathbf{q}}$ .

The constraint forces,  $\mathbf{A}^T \lambda$ , arise from the closed-loop constraint (11), and the contact force magnitudes must satisfy the friction constraint (7),  $\mathbf{U}(\lambda) \geq 0$ .

Rearranging (29) into the familiar form, where note that  $\mathbf{A}$  is the only term that varies with contact mode,

$$\bar{\mathbf{M}}(\theta, \phi) \ddot{\mathbf{q}} + \bar{\mathbf{C}}(\theta, \phi, \dot{\mathbf{q}}) \dot{\mathbf{q}} + \bar{\mathbf{N}}(\theta, \phi) + \mathbf{A}^T(\mathbf{q}) \lambda = \Upsilon(\boldsymbol{\tau}), \quad (32)$$

the dynamics and the constraints may be combined in a few different ways to solve for  $\ddot{\mathbf{q}}$  and  $\lambda$ , here we choose,

<sup>5</sup> The  $\bar{\mathbf{C}}$  matrix does not have any particular block diagonal structure as was the case in a manipulation problem [134, Eqn. 6.24]. If the legs are considered massless then  $\bar{\mathbf{C}}$  may all be zeros, depending on parameterization.

$$\begin{bmatrix} \ddot{\mathbf{q}} \\ \lambda \end{bmatrix} = \underbrace{\begin{bmatrix} \bar{\mathbf{M}} & \mathbf{A}^T \\ \mathbf{A} & 0 \end{bmatrix}^{-1} \begin{bmatrix} \Upsilon - \bar{\mathbf{N}} \\ 0 \end{bmatrix}}_{\mathbf{E}(\theta, \phi, \tau)} - \underbrace{\begin{bmatrix} \bar{\mathbf{M}} & \mathbf{A}^T \\ \mathbf{A} & 0 \end{bmatrix}^{-1} \begin{bmatrix} \bar{\mathbf{C}} \\ \dot{\mathbf{A}} \end{bmatrix}}_{\mathbf{D}(\theta, \phi, \dot{\mathbf{q}})} \dot{\mathbf{q}}, \quad (33)$$

where we assume that the inverted matrix in (33) is nonsingular even if  $\bar{\mathbf{M}}$  is not (see Appendix Section 4.4.4).

This formulation of the dynamics is sufficient to determine, for example, that the front leg always lifts off the ground before the rear leg in a symmetric leap (Section 4.3.3). However it is convenient to use the parameterization of Section 4.1.7 to separate the free dynamics from the constraint forces, as shown in the next section.

#### 4.1.10 Reduced Dynamics

Instead of working with the complete dynamics we can instead consider only the  $e$  free Lagrangian variables in  $\mathbf{y}$ , as introduced above. In this case the dynamics are,

$$\tilde{\mathbf{M}}(\mathbf{q})\ddot{\mathbf{y}} + \tilde{\mathbf{C}}(\mathbf{q}, \mathbf{H}(\mathbf{q})\dot{\mathbf{y}})\dot{\mathbf{y}} + \tilde{\mathbf{N}}(\mathbf{q}) = \tilde{\Upsilon}, \quad (34)$$

$$\ddot{\mathbf{y}} = \underbrace{\tilde{\mathbf{M}}^{-1}(\mathbf{q}) (\tilde{\Upsilon} - \tilde{\mathbf{N}}(\mathbf{q}))}_{\tilde{\mathbf{E}}(\mathbf{q})} - \underbrace{\tilde{\mathbf{M}}^{-1}(\mathbf{q}) \tilde{\mathbf{C}}(\mathbf{q}, \mathbf{H}(\mathbf{q})\dot{\mathbf{y}})\dot{\mathbf{y}}}_{\tilde{\mathbf{D}}(\mathbf{q}, \dot{\mathbf{y}})}, \quad (35)$$

where,

$$\tilde{\mathbf{M}} := \mathbf{H}^T \bar{\mathbf{M}} \mathbf{H}, \quad \tilde{\mathbf{C}} := \mathbf{H}^T \bar{\mathbf{C}} \mathbf{H} + \mathbf{H}^T \bar{\mathbf{M}} \dot{\mathbf{H}}, \quad (36)$$

$$\tilde{\mathbf{N}} := \mathbf{H}^T \bar{\mathbf{N}}, \quad \tilde{\Upsilon} := \mathbf{H}^T \Upsilon, \quad (37)$$

(see Appendix Section 4.4.5 for derivation). Note that while the base constraint is a function of the initial conditions ( $\hat{\mathbf{x}}_c$ ), the Jacobian constraint is not, and so any analysis that holds across any initial conditions needs the full  $\mathbf{q}$ . Furthermore in general rolling contact requires non-holonomic constraints, and so  $\mathbf{h}$  may not exist. Therefore we have left  $\mathbf{q}$  in explicitly in (35) and write out the reduced dynamics in terms of both the reduced variables,  $\mathbf{y}$ , and original variables,  $\mathbf{q}$ , (although  $\mathbf{h}(\mathbf{y})$  may be substituted for  $\mathbf{q}$  when possible).

To recover the original configuration space accelerations and Lagrange multipliers,

$$\ddot{\mathbf{q}} = \mathbf{H}\ddot{\mathbf{y}} + \dot{\mathbf{H}}\dot{\mathbf{y}}. \quad (38)$$

$$\lambda = \underbrace{\mathbf{A}^*(\Upsilon - \bar{\mathbf{N}})}_{\tilde{\mathbf{E}}_\lambda(\mathbf{q})} - \underbrace{\mathbf{A}^*(\bar{\mathbf{M}}\dot{\mathbf{H}} + \bar{\mathbf{C}}\mathbf{H})\dot{\mathbf{y}}}_{\tilde{\mathbf{D}}_\lambda(\mathbf{q}, \dot{\mathbf{y}})}, \quad (39)$$

where  $\mathbf{A}^*$ , a left inverse of  $\mathbf{A}$ , is chosen to also satisfy  $\mathbf{A}^*\bar{\mathbf{M}}\mathbf{H} = \mathbf{0}$ , that is,

$$\begin{bmatrix} \mathbf{A}^* \\ (\bar{\mathbf{M}}\mathbf{H})^* \end{bmatrix} := \begin{bmatrix} \mathbf{A}^T & \bar{\mathbf{M}}\mathbf{H} \end{bmatrix}^{-1} \Rightarrow \mathbf{A}^*\mathbf{A}^T = \mathbf{Id}_c, \quad \mathbf{A}^*\bar{\mathbf{M}}\mathbf{H} = \mathbf{0}, \quad (40)$$

(see Appendix Section 4.4.5 for derivation).

These reduced dynamics lead to, for example, a simple proof that stubbing the toe at the end of stance in pronk is beneficial to the robot's pitch, as described in Section 4.3.3.

#### 4.1.11 Summary of Assumptions

For convenience, the assumptions made by the self-manipulation framework just presented are summarized as follows:

- A.1. There is a distinguished (pre-selected) rigid body on the robot with a frame,  $P$ , attached at the COM.
- A.2. There is an inertial world frame,  $W$ , at some (possibly unknown) fixed location, and at each instant is rigidly connected to a frame,  $O$ , co-located at  $P$ .
- A.3. The robot is in contact with the world at some finite number of points,  $C_k$ , and the set of all possible contact points is known (albeit, in general, not their location).
- A.4. The combined mass matrix  $\bar{\mathbf{M}}$  does not need to be full rank (i.e. there may be massless limbs), however the reduced mass matrix,  $\tilde{\mathbf{M}}$ , is (i.e. any massless links are constrained such that the overall system motion is well defined).
- A.5. Some choice of generalized coordinates, i.e., a non-singular minimal parameterization of the free motion,  $\mathbf{y}$ , is available in any mode of interest.

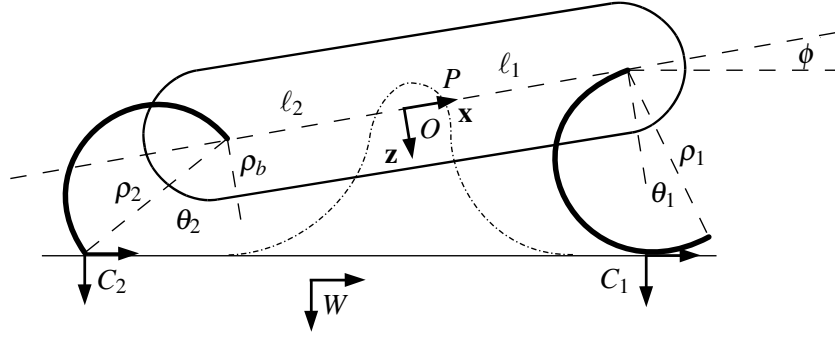


Figure 4.2: Coordinate frames and key dimensions for RHex under the self-manipulation formulation.

Furthermore the following assumptions are made in this chapter, but not fundamental to the structure of the framework,

- B.1. There are no elastic or compliant components.
- B.2. Any damping or air resistance is negligible.

Some additional assumptions are made when this general framework is instantiated in the next section.

## 4.2 Self-Manipulation for RHex

### 4.2.1 Model Parameters

When RHex uses pairs of contralateral legs in phase on level ground, it is very effectively anchored to the sagittal plane, and so here we develop a planar model for RHex ( $d:= 2$ ), with only two legs modeled, each with one joint ( $n:= 2, q= 5$ ), as shown in Fig. 4.2. In addition the body is allowed to contact the ground at up to two locations (front and rear), so that  $k \leq 4$ . The rubber treads on the toes have a relatively high coefficient of friction (especially on rough outdoor terrain) that we assume always resists tangential (sliding) motion, while the hard shell of RHex's body has a very low coefficient of friction and so we assume that the body always is able to slide. There are thus 2 contact wrenches at each toe and 1 at the front and rear of the robot, implying that  $c \leq 6$ . We do not

assume that the robot is endowed with any exteroceptive sensors, and as such must assume instead that the robot is on flat level ground, and so the contact normals are aligned with gravity.

The location and orientation of the various frames are shown in Fig. 4.2. In the palm frame, let the  $+x$  axis be aligned with the robot,  $+z$  in the “downward” direction from the robot, and thus  $+y$  exiting the page (this is a standard “North, East, Down” orientation). Hip  $i$  ( $S_i$ ) is located  $\ell_i$  away from the  $P$  frame along the positive  $x$  direction, and the leg length is  $\rho_i$  putting the  $F_i$  frame at  $\rho_i$  along the positive  $z$  direction from  $M_i$ , thus,

$$\begin{aligned}\mathbf{g}_{pc_1}(\boldsymbol{\theta}, \phi) &:= [\ell_1 - \rho_1 \sin \theta_1, \rho_1 \cos \theta_1, -\phi]^T, \\ \mathbf{g}_{pc_2}(\boldsymbol{\theta}, \phi) &:= [-\ell_2 - \rho_2 \sin \theta_2, \rho_2 \cos \theta_2, -\phi]^T,\end{aligned}$$

when the leg is supported on its toe ( $0 \leq \theta_i - \phi < \pi$ , as with leg 2 in Fig. 4.2). While the leg is in rolling contact (as with leg 1 in Fig. 4.2),

$$\begin{aligned}\mathbf{g}_{pc_1}(\boldsymbol{\theta}, \phi) &:= [\ell_1 - \frac{\rho_1}{2}(\sin \theta_1 + \sin \phi), \frac{\rho_1}{2}(\cos \theta_1 + \cos \phi), -\phi]^T, \\ \mathbf{g}_{pc_2}(\boldsymbol{\theta}, \phi) &:= [-\ell_2 - \frac{\rho_2}{2}(\sin \theta_2 + \sin \phi), \frac{\rho_2}{2}(\cos \theta_2 + \cos \phi), -\phi]^T.\end{aligned}$$

The body has semi-circular ends with radius  $\rho_b$  about the hips and so the two potential body contact points are,

$$\begin{aligned}\mathbf{g}_{pc_3}(\boldsymbol{\theta}, \phi) &:= [\ell_1 - \rho_b \sin \phi, \rho_b \cos \phi, -\phi]^T, \\ \mathbf{g}_{pc_4}(\boldsymbol{\theta}, \phi) &:= [-\ell_2 - \rho_b \sin \phi, \rho_b \cos \phi, -\phi]^T.\end{aligned}$$

The body pitch is  $\phi = 0$  when the robot is horizontal and a positive pitch when hip 1 is higher than hip 2. The leg angles are measured as  $\theta_1$  and  $\theta_2$  in the clockwise direction from the body  $+z$  direction. In Fig. 4.2,  $\theta_1 < 0, \theta_2 > 0, \phi > 0$ . Physical values used, including lengths and masses, are summarized in Table 4.2.

Symbol	Value	Definition
$m_b$	7.15 kg	Body Mass
$I_b$	0.15 kg·m <sup>2</sup>	Body Inertia
$m_l$	0.063 kg	Leg Mass
$I_l$	0.00046 kg·m <sup>2</sup>	Leg Inertia
$\ell_1, \ell_2$	20.5 cm	Body-Hip Length
$\rho_1, \rho_2$	17 cm	Leg Length
$\rho_b$	5 cm	Body Radius
$\tau_s$	15 N·m	Saturated Maximum Torque

Table 4.2: Physical quantities used in the RHex model. Note that  $m_l$ ,  $I_l$ , and  $\tau_s$  are doubled in practice as contra-lateral legs are used in parallel in this chapter, though all but the last behavior assume massless legs.

## 4.2.2 RHex Kinematics

The definitions of the previous subsection completely describe the kinematics and dynamics of the robot in any contact configuration. A full list of the resulting matrix formulation of the kinematics and dynamics is included in the Appendix Section 4.4.7, while here we only look at the base constraint and explore the quasi-static state space.

From Section 4.1.4, the base kinematic constraint is defined by composing the inverse of the specified maps for  $\mathbf{g}_{pc_k}$  with the body coordinates,  $\mathbf{x}$ , which for stick legs ( $0 \leq \theta_i - \phi < \pi$ ),

$$\mathbf{a}_k(\mathbf{q}) = \pi(\mathbf{g}_{c_k w}(\mathbf{q})) - \hat{\mathbf{x}}_{c_k} = \begin{bmatrix} -x - \ell_k \cos(\phi) + \rho_k \sin(\theta_k - \phi) \\ -z + \ell_k \sin(\phi) - \rho_k \cos(\theta_k - \phi) \end{bmatrix} - \begin{bmatrix} \hat{x}_{c_k} \\ \hat{z}_{c_k} \end{bmatrix}, \quad k \in \{1, 2\} \quad (41)$$

while for rolling contact ( $-\pi \leq \theta_i - \phi < 0$ ),

$$\mathbf{a}_k(\mathbf{q}) = \pi(\mathbf{g}_{c_k w}(\mathbf{q})) - \hat{\mathbf{x}}_{c_k} = \begin{bmatrix} -x - \ell_k \cos(\phi) + \frac{\rho_k}{2} \sin(\theta_k - \phi) \\ -z + \ell_k \sin(\phi) - \frac{\rho_k}{2} (1 - \cos(\theta_k - \phi)) \end{bmatrix} - \begin{bmatrix} \hat{x}_{c_k} \\ \hat{z}_{c_k} \end{bmatrix}, \quad k \in \{1, 2\}. \quad (42)$$

Similarly for the body contact, the base kinematic map is,

$$\mathbf{a}_k(\mathbf{q}) = \pi_z(\mathbf{g}_{c_k w}(\mathbf{q})) - \hat{\mathbf{x}}_{c_k} = \begin{bmatrix} -z + \ell_k \sin(\phi) - \rho_b \end{bmatrix} - \begin{bmatrix} \hat{z}_{c_k} \end{bmatrix}, \quad k \in \{3, 4\} \quad (43)$$

which is the equivalent of setting  $\theta_k = \phi$ .

As introduced in Section 4.1.3, the active contact constraints can be found by checking the height of each potential contact frame,  $\zeta_{c_k}(\mathbf{x})$ . If however the robot does not know its exact place in the world ( $\pi(\mathbf{x})$ ), the contact condition can still be found by relying on the assumptions of flat level ground and quasi-static operation. First since the robot is quasi-static, choose the world reference frame to be  $W \equiv O$ , and so  $\pi(\mathbf{x}) = 0$ . In this case the active contact points are simply those that are farthest from the body in their  $\mathbf{z}$  direction, which recall is always non-positive by convention,

$$\pi_z(\mathbf{g}_{c_{k0}}) < \pi_z(\mathbf{g}_{c_{i0}}), \quad \forall k \in \mathcal{K}, i \notin \mathcal{K}.$$

To consider the difference between rolling contact (on the rounded part of the half circle leg) and point contact (on the toe of the leg) a further condition is needed that specifies which part of the leg are rounded. In particular, the leg presents the rounded half of its shape when  $-\pi < \theta_i - \phi < 0$  (as opposed to e.g. [74] which is rounded on the other half).

Once contact mode is determined, pitch is an implicit function of the equality of the constraint (10),  $0 \equiv \mathbf{a}_{c_k}(\mathbf{q})$ . As before, take  $\pi(\mathbf{x}) \equiv 0$ , and so,

$$\begin{aligned} \pi_z(\mathbf{a}_{c_i}) - \pi_z(\mathbf{a}_{c_j}) &\equiv 0, \quad \forall i, j \in \mathcal{K}, \\ \pi_z(\mathbf{g}_{c_{i0}}) &\equiv \pi_z(\mathbf{g}_{c_{j0}}), \end{aligned} \tag{44}$$

from which we can locally derive the body pitch as an implicit function of the joint angles. These conditions are combined to create Fig. 4.3, which shows the various quasi-static contact conditions across the entire joint space,  $\Theta$ .

### 4.2.3 Assumptions for RHex

As a summary, the following assumptions, in addition to those listed in Section 4.1.11, are made about the RHex model,

- C.1. RHex is anchored to the sagittal plane by using contralateral legs together, and so  $d=2$ .
- C.2. The middle legs are not used, and so  $n=2$ .

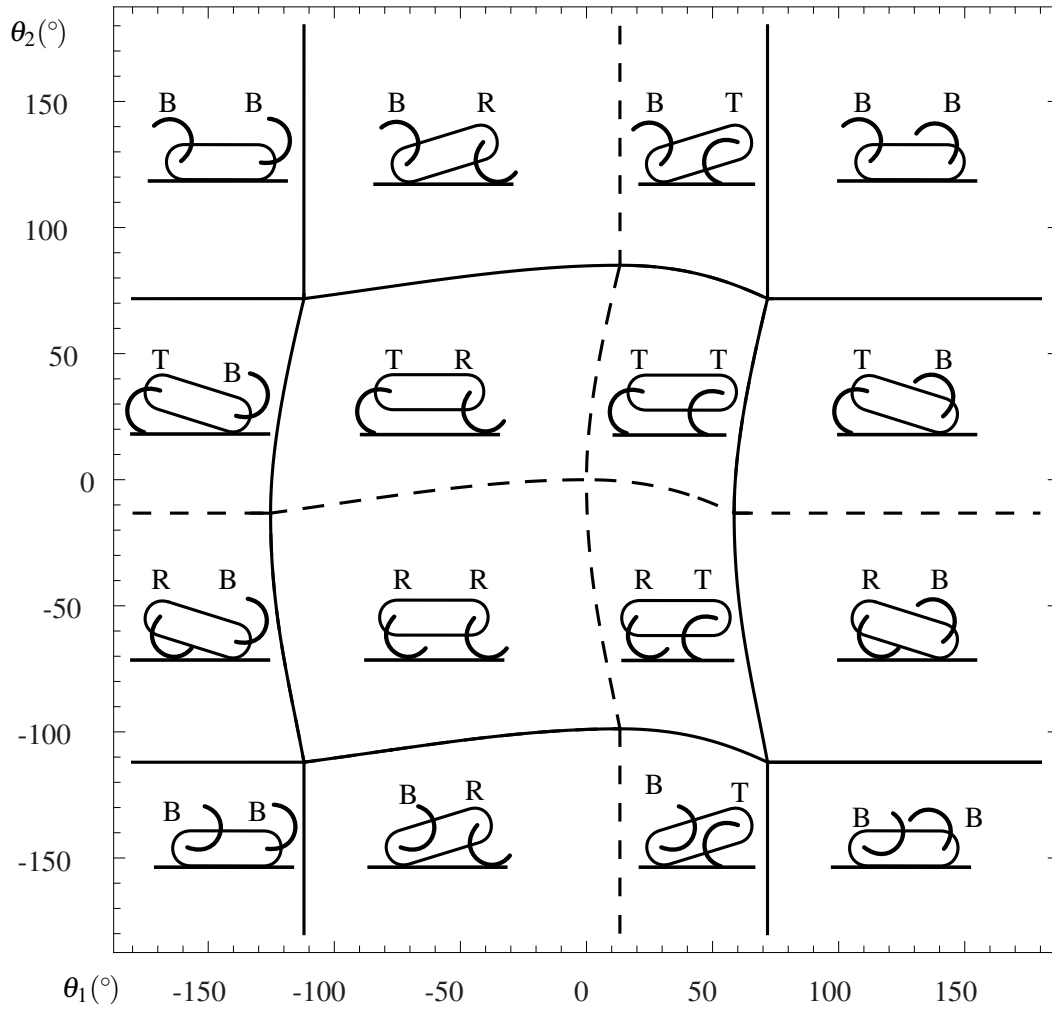


Figure 4.3: Quasi-static contact modes over the entire state space of joint angles ( $\Theta \approx \mathbb{T}^2$ ). Each region is distinguished by front and rear contact conditions that can be Body, Rolling, or Toe contact, as indicated by the respective letter.

- C.3. The body can contact in up to two locations but has a low coefficient of friction that never resists tangential friction forces.
- C.4. The rubber toes have a high coefficient of friction and therefore always resist tangential forces (as the surface normal and frictional coefficients for novel terrain is unknown — if they are assumed to be known then the friction cone could be checked with (7)).
- C.5. The robot is on flat level ground ( $C_k$  aligned with  $W$ , assumed everywhere except Section 4.3.1).
- C.6. The legs are massless ( $m_l \equiv 0, I_l \equiv 0$ , assumed everywhere except Section 4.3.3).

Furthermore the following simplifying assumptions are made in some of the following behaviors as marked,

- D.1. The robot is near a nominally standing posture, i.e. the legs are “under” the robot,  $\theta_k \in \mathcal{U} := [-30^\circ, 30^\circ]$ , and the robot is close to level,  $\phi \in [-10^\circ, 10^\circ]$ .
- D.2. The robot is symmetric ( $\ell_1 \equiv \ell_2 := \ell, \rho_1 \equiv \rho_2 := \rho$ , implicitly assumed for numerical calculations based on Table 4.2).
- D.3. The robot is a point mass ( $I_b \equiv 0$ ).

## 4.3 Behaviors

### 4.3.1 Reactive Standing

In this section we document a quasi-static RHex standing controller that delivers up to a 90% reduction in power use relative to an open-loop stand on unmodeled rough terrain [88]. The scheme is extraordinarily simple: the controller seeks simultaneously to reduce the variance of joint torques around their mean (right side of Fig. 4.4), while fighting to “lean up” against the mean load (left side of Fig. 4.4). The self-manipulation model is needed to formalize these insights and establish the correctness of the controller.

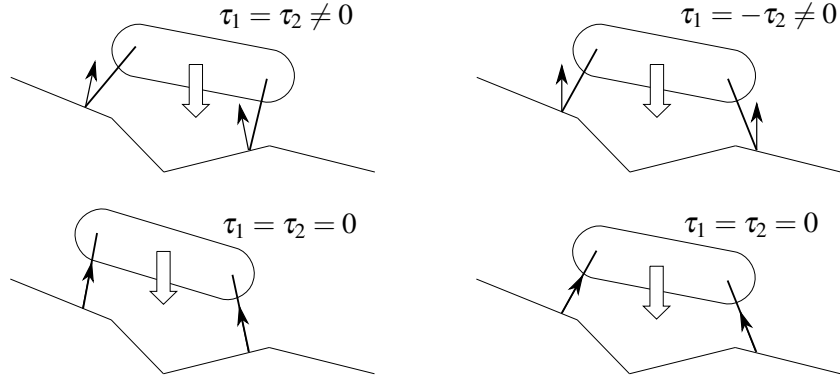


Figure 4.4: Two examples of how the balancing stand works, noting the relationship between motor torques. On the left, start and end conditions for fighting an external force, on the right start and end conditions for relaxing an internal force.

This notion of fighting an external force and relaxing the internal force has been used before on legged robots, usually without stating it in this way. For example, prior work on RHex pushes the body uphill to be centered over the legs while climbing steep terrain [64], and separately regulate individual leg torques such that no one leg pushes harder than the rest [179]. These ideas were further developed on RiSE [66, 69] whose reactive gait phase adjustments were designed to balance forces within and between the sides. Similar internal force management strategies have been suggested on quadrupeds [164] and highly articulated bipeds [159], though without a proof of convergence.

To analyze this behavior, Section 4.3.1 decomposes the motor cost into average and difference terms,  $\varepsilon$  and  $\delta$ , and derive the quasi-static torques necessary to fight external (gravity) and any internal (legs fighting) wrenches. The key to this decomposition is to apply the closed-loop constraint to find the internal and external forces at the toes (Section 4.1.8), and projecting that back into motor torques (Section 4.1.5). Section 4.3.1 sets up the controller summarized in Fig. 4.4, in part by using an approximation to the closed-loop velocity constraint (Section 4.1.7). Section 4.3.1 brings these parts all together and show convergence of the controller. This entire behavior is analyzed using stick legs with point contact, but as Section 4.1.6 has shown, the free motion of rolling contact is the same as that of a stick leg with appropriate radius, and so by showing Lyapunov convergence for any angle and any leg lengths (within appropriate bounds), the rolling contact can be ignored. Note that this proof does not rely on Assumption C.5 but instead simply uses Assumptions C.4 and D.1.

Finally Section 4.3.1 tests this controller on a variety of indoor and outdoor terrain, with results documented in Table 4.3.

### Problem Setup

For this problem we are trying to minimize the thermal cost needed to stand, which is proportional to the square of current (which in turn is proportional to torque). A natural goal to set is  $\Pi := \frac{1}{2}(\tau_1^2 + \tau_2^2)$ . A key insight is to break apart the functional form of  $\Pi = \varepsilon(\tau_1, \tau_2) + \delta(\tau_1, \tau_2)$ , where  $\varepsilon(\tau_1, \tau_2) := \tau_m^2$  is the squared mean torque, and  $\delta(\tau_1, \tau_2) := \tau_d^2$ , is the squared difference in torques,

$$\begin{bmatrix} \tau_m \\ \tau_d \end{bmatrix} := \mathbf{T}\boldsymbol{\tau} \quad \mathbf{T} := \begin{bmatrix} \mathbf{t}_m^T \\ \mathbf{t}_d^T \end{bmatrix} = \frac{1}{2} \begin{bmatrix} 1 & 1 \\ 1 & -1 \end{bmatrix}, \quad (45)$$

and analogously  $[\theta_m \quad \theta_d]^T := \mathbf{T}\boldsymbol{\theta}$ . Section 4.3.1 shows that  $\varepsilon$  captures the cost due to gravity while  $\delta$  captures the cost due to internal forces, and more importantly the proposed controller drives both costs to zero.

Similarly we may choose to parameterize the implicit function associated with the closed-loop constraint by the average velocity, with  $y \equiv \theta_m = \mathbf{t}_m^T \boldsymbol{\theta}$ , i.e.  $\dot{y} = \mathbf{Y}\dot{\mathbf{q}} := \frac{1}{2}[1 \ 1 \ 0 \ 0 \ 0]\dot{\mathbf{q}}$ . This choice is motivated by the observation that motion has equal cost in both motors, though selection of  $y \equiv \theta_1$  or  $y \equiv \theta_2$  also works well. The Jacobian of the associated implicit function (19) on some open neighborhood of the origin,  $\mathcal{U} \subset \mathbb{R}$ , is,

$$\mathbf{H}_h := D_{\theta_m} \mathbf{h}_h = \frac{2}{\gamma_1 + \gamma_2} \begin{bmatrix} \gamma_1 \\ \gamma_2 \end{bmatrix}, \quad (46)$$

$$\gamma_i := (\ell_1 + \ell_2)\rho_j \cos \theta_j + \rho_1 \rho_2 \sin(\theta_2 - \theta_1), \quad j = 3 - i, \quad (47)$$

and is full rank (never passing through the origin) in both tangent spaces as the ‘‘gear ratios,’’  $\gamma_k$ , are always positive and nearly equal (bounded numerically by  $0.83 \leq \gamma_1/\gamma_2 \leq 1.19$  under Assumption D.1 in [88]).

The ‘‘internal’’ component of the forces at the toes lies in the subspace defined by (22), which form the homogeneous solution, i.e. toe forces that are *internal* in that they can perform no work

on the object. To specify a particular solution, apply (23) with  $\mathbf{t}^T \equiv \mathbf{t}_d^T$ . This choice of particular solution, depicted in the lower sketches of Fig. 4.4, corresponds to toe forces that cancel gravity with the “right amount” of internal force, here defined by the difference condition.

The torque produced by these toe forces is given by the hand Jacobian,  $\mathbf{J}_h^T$ , as in (16). It is convenient to work in a new basis for the joint-space torques,  $\boldsymbol{\tau} \in T^*\Theta$ , given by the scaled rotational transformation  $\mathbf{T}$  into the mean and difference of the torques as defined in (45). The torque implication of the particular solution ( $\alpha = 0$ ) is,

$$\begin{bmatrix} \tau_m \\ \tau_d \end{bmatrix}_p := \mathbf{T}\mathbf{J}_h^T \mathbf{f}_p = -m_b g \rho_1 \rho_2 \frac{\ell_1 \cos \theta_1 \sin(\theta_2 - \phi) + \ell_2 \cos \theta_2 \sin(\theta_1 - \phi)}{\gamma_1 + \gamma_2} \begin{bmatrix} 1 \\ 0 \end{bmatrix}, \quad (48)$$

where  $\tau_{d,p} = 0$  because the particular solution has no component in the  $\mathbf{t}_d^T$  direction (23). Therefore all of the virtual work against gravity must show up in  $\tau_{m,p}$ , so that  $\tau_{m,p} = \frac{1}{2} \mathbf{F}_g^T \mathbf{H}_o = \frac{1}{2} m_b g D\zeta \circ D\mathbf{h}_o$  (see [88] for proof).

The torque projection of the homogeneous solution is,

$$\begin{bmatrix} \tau_m \\ \tau_d \end{bmatrix}_h := \alpha \mathbf{T}\mathbf{J}_h^T \mathbf{f}_N = \frac{\alpha}{2} \begin{bmatrix} \gamma_2 - \gamma_1 \\ \gamma_2 + \gamma_1 \end{bmatrix}. \quad (49)$$

Here there is not an exact decomposition — we would like  $\tau_{m,h}$  to be zero so that  $\tau_m$  is exactly  $\tau_{m,p}$ . However we have observed (in (47) and related discussion) that  $\gamma_1 \approx \gamma_2$ , and in any case if our controller is successful we can achieve this by simply canceling the internal force magnitude,  $\alpha$ . Having derived an expression for the various torque components in (48)–(49), we can now apply a controller to this system and observe the effect on the component cost functions,  $\varepsilon$  and  $\delta$ .

## Controller Design

In this section, we show how direct current readings at the hips yield intrinsic sensors that approximate the gradient of two costs,  $\varepsilon$  and  $\delta$ , eliminating all need to know or compute the exact kinematics online. The change of basis in torque space,  $\mathbf{T}$ , allows the robot to use these sum and difference torque measurements to closely approximate the gradient of its power-use cost function.

Because the motor controller is highly overdamped and rate limited we adopt “generalized damper” mechanics and model the motor as velocity controlled in general,  $\dot{\theta} = \kappa_p \tilde{\theta}$ , for some command  $\tilde{\theta} \in T\Theta$ . To guarantee that the system remains quasi-static, this command is rate limited to ensure  $\tilde{\theta} \leq \kappa_\sigma$ . However the motion is constrained by the closed-loop condition (12), and so the constrained motion is approximately,

$$\dot{\theta}_m = \kappa_p \tilde{\theta}_m, \quad (50)$$

$$\dot{\theta}_d = 0, \quad (51)$$

since the system can move freely in approximately the  $\theta_m$  direction (exactly, in the  $\mathbf{H}_h$  (46) direction). In contrast, in the approximate  $\theta_d$  direction (exactly, along infinitesimal motions orthogonal to  $\mathbf{H}_h$ ), motion is locked, hence generated torque must increase as,

$$\dot{\tau}_d = \kappa_t \tilde{\theta}_d, \quad (52)$$

i.e. any differentially applied command increases the torque as the system cannot move in that direction.

Again, we emphasize that this locked leg assumption is merely an approximation (as  $\partial\theta_d/\partial\theta_m$  is small), but no matter how large the shift, so long as  $\gamma > 0$  for all angles, i.e. the sign of the direction of motion is correct, we can simply allow the internal force controller to compensate for this “disturbance” in  $\theta_d$  as the robot moves.<sup>6</sup> Moreover this misalignment between the approximate and true parameterization of the free motion does not affect the zero point — in either case the zero has  $\tau_1 = \tau_2 = 0$  and so the controller converges to the correct place, even if it does not take the “most direct” route.

### Internal and External Cost

Note that the internal cost,  $\delta = \tau_d^2 = \alpha^2(\gamma_1 + \gamma_2)^2/4$  (49), vanishes if  $\alpha = 0$ . Therefore since the particular solution makes no contribution to  $\tau_d$  (48), based on our actuator model (51)–(52), it is

<sup>6</sup>Without this dependence, the two controllers could be run sequentially.

straightforward to reduce  $\delta$  by asserting a control policy,  $\tilde{\theta}_d := -\kappa_d \tau_d$ , resulting in,

$$\dot{\delta} = 2\tau_d \dot{\tau}_d = \begin{cases} -2\kappa_d \kappa_i \tau_d^2 & |\tilde{\theta}_d| \leq \kappa_\sigma \\ -2\kappa_d \kappa_i \kappa_\sigma |\tau_d| & |\tilde{\theta}_d| > \kappa_\sigma \end{cases}. \quad (53)$$

Thus the positive definite function,  $\delta$ , has a negative definite derivative along the motions of (52) under the specified control and, thus, as a Lyapunov function,

*Result A.1.* Relaxing the difference in torque (53) assures that  $\tau_d$ , and therefore the internal cost  $\delta$ , decays to zero from any nominally standing posture (Assumption D.1).

The exponential decay of the homogeneous (internal) torque solution leaves the second term of the cost function,  $\varepsilon = \tau_m^2 = (\tau_{m,p} + \tau_{m,h})^2$ , determined by the gravitational torque field through  $\tau_{m,p}$  (48), which can be minimized by bringing  $\theta_m$  to a critical point of  $\zeta_o$ . For  $\phi \in \mathcal{U}$ , the closest critical point is a local maximum. Therefore, we consider minimizing the function  $-\zeta_o$ , and implement the quasi-static dynamics  $\tilde{\theta}_m := \kappa_m \tau_m$ , since this implies,<sup>7</sup>

$$-\dot{\zeta}_o = -D\zeta_o \cdot \dot{\theta}_m = \begin{cases} -m_b g \kappa_m \kappa_p |D\zeta_o|^2 & |\tilde{\theta}_m| \leq \kappa_\sigma \\ -\kappa_p \kappa_\sigma |D\zeta_o| & |\tilde{\theta}_m| > \kappa_\sigma \end{cases}, \quad (54)$$

i.e.,  $-\zeta_o$  (a smooth positive definite function in the neighborhood of a maximum), has a negative definite derivative under the control input as it enters the dynamics (50), and therefore,

*Result A.2.* Fighting the mean torque (54) assures that  $\theta_m$  converges to the local minimum of  $-\zeta_o$ , the local maximum of  $\zeta_o$ , and therefore the external cost  $\varepsilon$ , decays to zero from any nominally standing posture (Assumption D.1).

Furthermore, as discussed in Section 4.1.6, since quasi-statically rolling is the same as an equivalent stick leg, and the above proof holds for any leg angle and length so long as  $\gamma_i > 0$ , we find that,

*Result A.3.* The convergence of (53)–(54) holds even under rolling contact, and so either leg shape converges to near-zero cost.

---

<sup>7</sup>The coupling of  $\tau_{m,h}$  adds a sign indefinite term to the top line,  $-\alpha \kappa_m \kappa_p \frac{\gamma_i - \gamma_h}{2} D\zeta_o$ , but  $\alpha$  is exponentially driven to zero by (53).



Figure 4.5: X-RHex performing a reactive stand on rocks.

Thus for this first behavior, either leg shape is acceptable.

### Experimental Results

We implement this controller on the robot by straightforward generalization of the difference torque controller (53), for each leg individually, and the mean torque controller (54), now applied to the mean of all six legs [88, Section III.D]. The controller was tested on a variety of terrains by having the robot execute a reactive stand from either a sitting or walking posture. Fig. 4.5 shows a test on a pile of rocks, and Table 4.3 summarizes the results.

Note that regardless of the initial conditions, the reactive power was reduced to around 4 W. In fact every trial except for one on the rocks reduced the power to below 5 W. In that outlier, with a final power usage of 21.2 W, the robot slipped partway through execution of the smart stand, and, as the current behavior executes for a fixed time, the robot did not have time to completely recover. Anecdotally, the entire robot can typically be turned off after this behavior runs and the robot remains standing (implying that the remaining 4 W may have come from the control electronics or noise). Furthermore since the experiments that started from a walk contained a mixture of leg

Terrain	Slope	Normal Power	Reactive Power	Change
Asphalt	None	6.02 W	3.64 W	39.6%
Rocks	Various	6.32 W	3.73 W	40.1%
Grass	-14.0° pitch, 11.1° roll	5.89 W	4.12 W	30.0%
Grass	1.2° pitch, 5.5° roll	11.43 W	4.34 W	62.0%
Dirt	18.8-19.9° pitch	22.50 W	4.01 W	82.2%
Carpet	None	36.63 W	3.97 W	89.2%
Smooth	10.6° pitch	15.55 W	3.98 W	74.4%
Rocks	Various	31.25 W	7.30 W	76.6%

Table 4.3: Reactive stand power from seated position. Each row is an average of five trials, and idle (“hotel”) power has been removed. First group started from a sitting posture, second group started from walking posture.

contact conditions (some legs on the rounded half and some on the toe), these results supports the claim that both round and stick legs converge to near-zero power under this controller.

### 4.3.2 Pitching Sensor Sweep

The behavior developed in this section allows the robot to actuate around the pitch component of its body frame. While prior work has posed the problem and initiated an analysis [155] and empirical application [86] of such behaviors, both efforts introduced point solutions that focused on a single contact mode with ad-hoc geometry. Here the formal derivation of an expression for the pitch as an implicit function of the leg state,  $\mathbf{h}_\phi(\theta)$ , allows analytical solutions in any contact condition, with consequent formal insight into the implications of leg shape.

Section 4.3.2 uses the domains of the various quasi-static contact conditions for RHex (Section 4.1.3, Fig. 4.3) and the implicit function for pitch based on the base kinematic constraint (Section 4.1.4) as in (44) in order to evaluate across all contact conditions to find the maximum range (as shown in Fig. 4.6). This range is extended from about 10° of pitch when both legs are in rolling contact (as first discovered in [155]), to about 35° when all modes are considered, greatly increasing the view of the world afforded to any payload sensors. Furthermore Section 4.3.2 compares the torque (Section 4.1.8) needed to hold a pitched pose with different leg shapes, finding that the rounded leg uses less power than the stick leg. Section 4.3.2 shows that the pitching rate is exactly

controlled by the analytical expression (59), based on the closed-loop constraint (Section 4.1.7), eliminating the need for a numerical solution to guarantee constant pitching velocity [155]. Finally, Section 4.3.2 checks the dynamic effects (Section 4.1.10) to maintain the integrity of the sensory behavior by ensuring that the platform maintains frictional contact with the ground.

### Scanning Range

Within a given quasi-static contact mode (Fig. 4.3), pitch is an implicit function of the equality constraint (44), which for example in rolling contact on both legs (for simplicity written here for a symmetric robot, Assumption D.2),<sup>8</sup>

$$\mathbf{h}_\phi(\boldsymbol{\theta}) = \arctan\left(\frac{4\ell + \rho(\sin(\theta_2) - \sin(\theta_1))}{\rho(\cos(\theta_2) - \cos(\theta_1))}\right), \quad (55)$$

The value for  $\phi$  for all quasi-static contact modes is shown in the contour plot of Fig. 4.6, as well as flow lines showing the constrained motion as a pushforward of a vector field over  $\mathcal{Y}$  through (19).

The behavioral design problem is then to find the extrema of this pitch, formally set up as either a constrained optimization in each contact mode, or an unconstrained optimization over the combined implicit value for  $\phi$ . This combined function is continuous as the active constraints in two neighboring contact conditions are subsets of the constraints on the boundary. The easiest way to solve this analytically is to choose  $y = \theta_1 - \phi$ , the global leg angle, and then parameterize the implicit function (55) in terms of  $y$ , (here shown for the case of a stick leg in front and body contact in the rear),<sup>9</sup>

$$\mathbf{h}_\phi(y) = \arcsin\frac{\rho_1 \cos(y) - \rho_b}{\ell_1 + \ell_2}, \quad (56)$$

which is maximized at  $\phi = \arcsin\frac{\rho_1 - \rho_b}{\ell_1 + \ell_2} \approx 17^\circ$ . It is clear from Fig. 4.6 that this maximal upward pitch of  $\phi \approx 17^\circ$  is achieved at  $\theta_1 = 17^\circ$  and  $\theta_2 < -100^\circ$ , and from sitting ( $\theta_1 = \theta_2 = -180^\circ$ ) this pitch is only reachable when the rear body is sliding along the ground. Similarly the maximal

<sup>8</sup>Calculated by solving (44) for  $\phi$  with the appropriate  $\mathbf{a}$  (i.e. a concatenation of (42) for each leg).

<sup>9</sup>Calculated by solving (44) for  $\phi$  with the appropriate  $\mathbf{a}$  (i.e. a concatenation of (41) for the front and (43) in the rear) and replacing  $\theta_1$  with  $y + \phi$ .

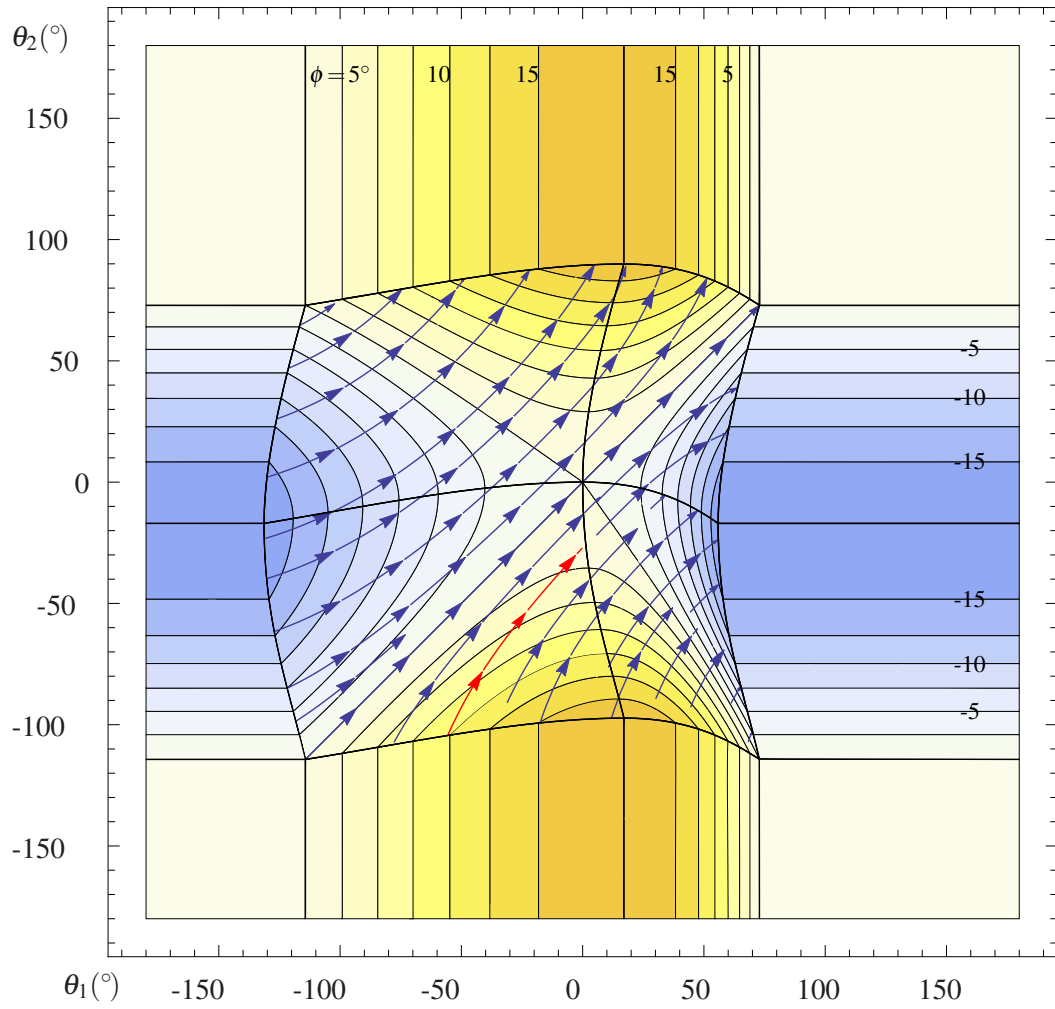


Figure 4.6: Contour plot of pitch  $\phi$  as a function of  $\theta_1$  and  $\theta_2$ , (55) over entire quasi-static configuration space (Fig. 4.3). Flow lines show constrained motion of the joints during double support (19). The red highlighted flow is solution from [155].

downward pitch of  $\phi \approx -17^\circ$  is achieved at  $\theta_2 = -17^\circ$  and  $\theta_1 < -130^\circ$ , i.e. when the front body is on the ground. This proves that,

*Result B.1.* The maximal pitching sensor sweep reaches  $\phi = \pm \arcsin \frac{\rho_1 - \rho_b}{\ell_1 + \ell_2} \approx \pm 17^\circ$  by using the sliding contact modes (56).

Such behaviors are shown in Fig. 4.7, where the robot is using a planar laser scanner to detect a stairwell and check for cliffs, as in [86]. However depending on the exact task a path through the double stance region may be useful in order to smoothly access both positive and negative pitches. If restricted to only rolling contact, then the maximal pitch is about  $10^\circ$ , as found in [155], and shown in Fig. 4.6.

### Torque Requirement

While both round and stick legs reach these same extrema in pitch, the torque required is not the same. Under quasi-static operation the leg torque required to resist gravity is dictated by (16) and (23), however in these sliding contact modes  $n=e=1$ , and so there are no internal forces, and  $\mathbf{G}_s$  is directly invertible. Thus,

$$\tau_1 = -\mathbf{J}_h^T \mathbf{G}_s^{-1} \mathbf{F}_g,$$

which can be compared for different leg shapes. Evaluating for round legs,<sup>10</sup>

$$\tau_1 = -\frac{\ell_2 \rho_1 m_b g \cos(\phi) \sin(\theta_1 - \phi)}{2(\ell_1 + \ell_2) \cos(\phi) - \rho_1 \sin(\theta_1 - \phi)}, \quad (57)$$

while for stick legs,<sup>11</sup>

$$\tau_1 = -\frac{\ell_2 \rho_1 m_b g \cos(\phi) \sin(\theta_1 - \phi)}{(\ell_1 + \ell_2) \cos(\phi) - \rho_1 \sin(\theta_1 - \phi)}. \quad (58)$$

---

<sup>10</sup>Calculated with the appropriate  $\mathbf{G}_s$  (i.e. a concatenation (84) of (82) for the front and (83) for the rear) and  $\mathbf{J}_h$  (i.e. simply (86) for the front).

<sup>11</sup>Calculated with the appropriate  $\mathbf{G}_s$  (i.e. a concatenation (84) of (81) for the front and (83) for the rear) and  $\mathbf{J}_h$  (i.e. simply (85) for the front).

While both leg shapes have the same zero torque point (when the leg is vertical, as found for the previous behavior), in general,<sup>12</sup>

*Result B.2.* A round leg (57) requires less torque to hold a pitched position than a stick leg (58) at the same angle.

This is easy to see intuitively, as the rounded leg has a shorter effective lever arm.

### Velocity Control

As the robot is pitching its sensor, the data can be correlated by recording the pitch as measured or calculated at each instant. However it may be necessary to sweep the sensor with some constant pitching speed. In [155] this was achieved by numerically inverting the forward kinematics to choose a leg angle velocity that produced the desired pitch velocity.

Here we take advantage of the analytical expression of  $\mathbf{H}_\phi$  (19), the velocity Jacobian that arises from the closed-loop constraint. Take for example rolling contact for the front leg and body contact in the rear, and let  $y := \theta_1$ , then a desired pitch velocity of  $\dot{\phi}_d$  can be achieved by setting the leg velocity,<sup>13</sup>

$$\dot{\phi} = \mathbf{H}_\phi \dot{\theta}_1 := \pi_\phi \mathbf{H} \dot{\theta}_1 \iff \dot{\theta}_1 = (\mathbf{H}_\phi)^{-1} \dot{\phi}, \quad (59)$$

$$\text{where } (\mathbf{H}_\phi)^{-1} = \frac{\rho_1 \sin(\theta_1 - \phi) - 2(\ell_1 + \ell_2) \cos(\phi)}{\rho_1 \sin(\theta_1 - \phi)},$$

which can be implemented as an online feedback controller based on local measurements of  $\theta_1$  and  $\phi$ , or can be calculated in advance numerically by using (18), (19), and thus,

*Result B.3.* A desired sensor pitch rate,  $\dot{\phi}_d$  can be exactly achieved by joint velocity tracking control around the reference signal (59) as derived from the velocity Jacobian (19).

Note that the denominator of (19) goes to zero when  $\theta_1 - \phi = 0$ , i.e. when the leg is vertical, as in fact the maximal pitch has been reached and the velocity control can no longer be applied.

<sup>12</sup>Recall that these different contact conditions have different implicit relationships between  $\phi$  and  $\theta_1$ , however the factor of 2 in the denominator of (57) is the dominant factor.

<sup>13</sup>Calculated from (20) with  $y$  as given and the appropriate  $\mathbf{A}$  (i.e. (17) with  $\mathbf{G}_s$  and  $\mathbf{J}_h$  as in (57)).



Figure 4.7: Robot performing two pitching sensor sweeps with a planar laser scanner: (Left) upward ( $\phi > 0$ ) to scan a staircase, (Right) downward ( $\phi < 0$ ) to check for a cliff.

### Dynamics

The maximum speed at which the scanning behavior can be executed is limited by the takeoff condition,  $\mathbf{U}\lambda \geq 0$ , (7), based on the dynamics, (39) i.e. above a certain speed ( $\dot{y} := \dot{\theta}_1$ ) one of the contact points may lift off the ground. The maximum joint speed that avoids liftoff of either leg (with no torque, i.e. when the behavior reverses) is,

$$\begin{aligned} \max \quad & \dot{y}, \\ \text{s.t.} \quad & \mathbf{U}\lambda \geq 0, \\ & \lambda = -\tilde{\mathbf{D}}_\lambda \dot{y} + \tilde{\mathbf{E}}_\lambda, \\ & \tau = 0. \end{aligned}$$

This speed is shown in Fig. 4.8 for a subset of the configuration space, along with a trace of the solution from [155]. Now we can bound the speed of the system to be below the minimum over this range, which is about  $300^\circ/s$  for the entire rolling contact range, or a little higher for most specific trajectories. In the rear body sliding contact case there is no solution to  $\lambda_{2,n} = 0$ , i.e. the front leg acting alone cannot lift the body off of the ground. However at high speeds the front leg loses contact, but those speeds are about twice that of the rolling contact case, and so, the maximum speed still consistent with full frictional contact is found numerically to be higher in the sliding modes (Fig. 4.8).

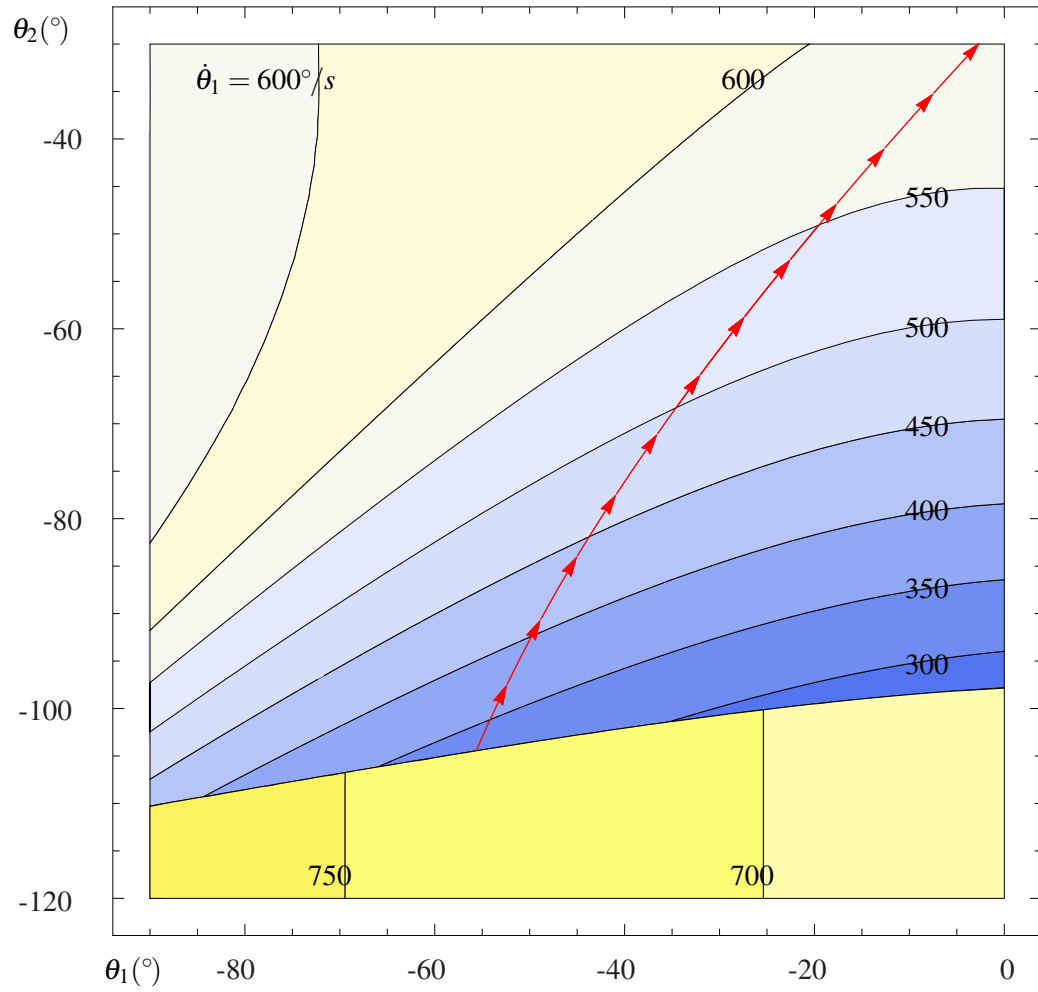


Figure 4.8: Leg speed ( $\dot{y} := \dot{\theta}_1$ , in  $^\circ/s$ ) at takeoff. The discontinuity at around  $\theta_2 = -110^\circ$  occurs when the rear leg engages the ground. The red highlighted flow is solution from [155], but any behavior that engages only the front leg ( $\theta_2 < -110$ ) may be run faster.

### 4.3.3 Pitch Control in Leaping

Leaping with a low pitching velocity but high forward velocity is very challenging for RHex because it entails in the high energy regime the delicate interaction of dynamics (Section 4.1.9) with contact conditions (Section 4.1.3) that we have already found to play a critical role in the quasi-static setting. For example, the pronk gait is known to have “severe pitch instability” on RHex [4], and as such several methods of pronking pitch control have been suggested<sup>14</sup> — modifying torques during stance, adjusting the leg angles before touchdown, and rear leg stubbing (rapid leg deceleration at the end of stance). The first strategy applies a differential torque between the motors [128], but under rigid assumptions the robot motion is constrained to a single DOF (as noted in the standing behavior). Even assuming leg compliance, this control authority is near-singular for typical leg angles for pronking [4].

The second strategy considers the plane generated by the toes when landing, as the robot quickly pitches until all toes are on the ground [128]. This effect can be canceled by setting the toes to be parallel to the ground [4], or exploited by adjusting it to a desired pitch [128]. This had limited success, as it, “appeared to disturb the robot’s touchdown angles enough to cause skidding” [127]. However the partial success of such strategies suggests that it may be beneficial in other ways, as it results in a splayed posture. The intuitive motivation to enforce symmetry between the legs does, at first, appear to control the pitch of the robot in stance as the parameterized free motion (19) has zero pitch. However when the friction constraints are considered (7), Section 4.3.3 proves that the front leg lifts off the ground first due to an unavoidable imbalance in toe normal forces (60), resulting in a positive pitch velocity. The same is not true when a fixed splay between the legs is applied, and Section 4.3.3 proves that a leap that uses such a splay inherently lowers the difference between front and rear normal forces, resulting in a lower pitch velocity (Fig. 4.9).

The dynamics of the resulting rear leg support mode are higher dimensional and underactuated, but by following Section 4.1.10 we show in Section 4.3.3 that the faster the rear leg is moving, the more the robot pitches upwards (63). This effect explains the “stubbing” strategy used by some

---

<sup>14</sup>Of the first two, [127] notes, “Unfortunately ... neither method could be used successfully to control pitch during pronking.”

pronk controllers [4, 127], and is shown in an extreme case in Table 4.4 (based on the leaping behaviors presented in Chapter 3), where over 20° of pitch correction is generated by a last minute reversal in leg torque. Furthermore the liftoff conditions in this mode bound the possible forward velocity, which can be used to answer both leg and behavioral design questions (Section 4.3.3). This bound is lower for stick legs than rounded legs, and lower for level jumps than for pitched jumps, further supporting the need for a splayed leap.

Finally Section 4.3.3 tests the inertial effects of the nearly-massless legs, as derived from the robot dynamics. Leaping experiments verify that the legs can generate about 14° of body rotation (Fig. 4.13).

### Symmetric Liftoff Conditions

Before the undesirable pitching velocity can be corrected, it is necessary to determine the source of the instability. Consider a symmetric robot (Assumption D.2) engaged in a “perfect” symmetric leap, i.e. with two stick legs locked in parallel ( $\theta_1 \equiv \theta_2 \Rightarrow \phi \equiv 0$ ). This would at first glance appear to be a desirable target for stable pronking (as was used, e.g. in [4]), since there is no pitch and the pitch velocity is zeroed out by the infinitesimal kinematics,<sup>15</sup>

$$\mathbf{H}_\phi := \frac{\partial \phi}{\partial \theta_m} = \frac{2\rho^2 \sin(\theta_2 - \theta_1)}{\gamma_1 + \gamma_2} = 0,$$

implying the same condition holds for the pitch acceleration,  $\ddot{\phi}$ . Why then does this gait fail? The answer lies in the liftoff conditions,  $U\lambda \geq 0$ ,<sup>16</sup>

$$\lambda = -\mathbf{D}_\lambda \dot{\mathbf{q}} + \mathbf{E}_\lambda = \begin{bmatrix} -\frac{\tau \tan(\theta_2)}{\ell} + \frac{\tau \cos(\theta_2)}{\rho} - \frac{1}{4}m_b g \sin(2\theta_2) - \frac{1}{2}m_b \rho \sin(\theta_2) \dot{\theta}_2^2 \\ \frac{\tau}{\ell} + \frac{m_b g}{4} + \frac{\tau \sin(\theta_2)}{\rho} + \frac{1}{4}m_b g \cos(2\theta_2) + \frac{1}{2}m_b \rho \cos(\theta_2) \dot{\theta}_2^2 \\ \frac{\tau \tan(\theta_2)}{\ell} + \frac{\tau \cos(\theta_2)}{\rho} - \frac{1}{4}m_b g \sin(2\theta_2) - \frac{1}{2}m_b \rho \sin(\theta_2) \dot{\theta}_2^2 \\ -\frac{\tau}{\ell} + \frac{m_b g}{4} + \frac{\tau \sin(\theta_2)}{\rho} + \frac{1}{4}m_b g \cos(2\theta_2) + \frac{1}{2}m_b \rho \cos(\theta_2) \dot{\theta}_2^2 \end{bmatrix}.$$

<sup>15</sup>Calculated from (20) with  $\mathbf{y} \equiv \theta_m$  (as in (47)) and the appropriate  $\mathbf{A}$  (i.e. (17) where  $\mathbf{G}_s$  is a concatenation (84) of (82) for each leg and  $\mathbf{J}_h$  is block diagonal (87) with (86) for each leg), under Assumption D.2.

<sup>16</sup>Calculated from (33), using (88)–(92) and the same  $\mathbf{A}$ , or equivalently (39), under Assumption D.2.

Thus the difference between the rear toe normal force (4th row, denoted “2n”) and front toe normal force (2nd row, denoted “1n”) is (note that in the normal force direction,  $\mathbf{U} = -1$ , as in (76)),

$$(\mathbf{U}\lambda)_{2n} - (\mathbf{U}\lambda)_{1n} = \frac{2\tau}{\ell}, \quad (60)$$

i.e. the rear normal force is always larger than the front normal force, and so,

*Result C.1.* In a symmetric jump ( $\theta_1 = \theta_2$ ), the front leg lifts off the ground first (60) as an unavoidable consequence of the dynamics (19) and contact constraint (7) (under Assumption D.2).

If this were a bilateral constraint (e.g. pin joint), the front leg would continue to pull down on the robot to maintain the neutral pitch that the closed-loop constraint suggests.

### Splayed Liftoff Conditions

For the non-symmetric jumping case ( $\theta_1 \neq \theta_2$ ), the analytical solution to  $\lambda$  is complicated enough to obviate any benefit of direct visual inspection. However we can look at how the imbalance of (60) changes with the splay angle,  $\theta_d := \mathbf{t}_d^T \boldsymbol{\theta}$  (45) (under Assumptions D.2 and D.3),

$$\left. \frac{\partial ((\mathbf{U}\lambda)_{2n} - (\mathbf{U}\lambda)_{1n})}{\partial \theta_d} \right|_{\theta_d=0} = -\frac{2\rho\tau \sin^2(\theta_m)}{\ell^2 \cos(\theta_m)} < 0, \quad (61)$$

(and numerically true even for  $I_b$  in Table 4.2), thus with otherwise equivalent conditions,

*Result C.2.* A positive splay angle ( $\theta_d$ ) reduces the imbalance between the front and rear normal forces (61) for RHex performing a forward leap (under Assumptions D.2 and D.3).

This splayed posture result is supported by the leaping dataset in Section 3.5. In those experiments, the robot performed a family of forward leaps while applying maximally available motor shaft torque with variations only in the relative timing of torque onset,  $t_2$ , which can be seen in that dataset to be well correlated with  $\theta_d$ . Looking at the pitching moment at apex, as listed in Table 3.1 and plotted in Fig. 4.9, it is clear that the pitching moment generated from a single leap decreases with increasing splay. Therefore a leap or pronk with a higher pitch ( $\theta_d > 0$ , i.e. below the main

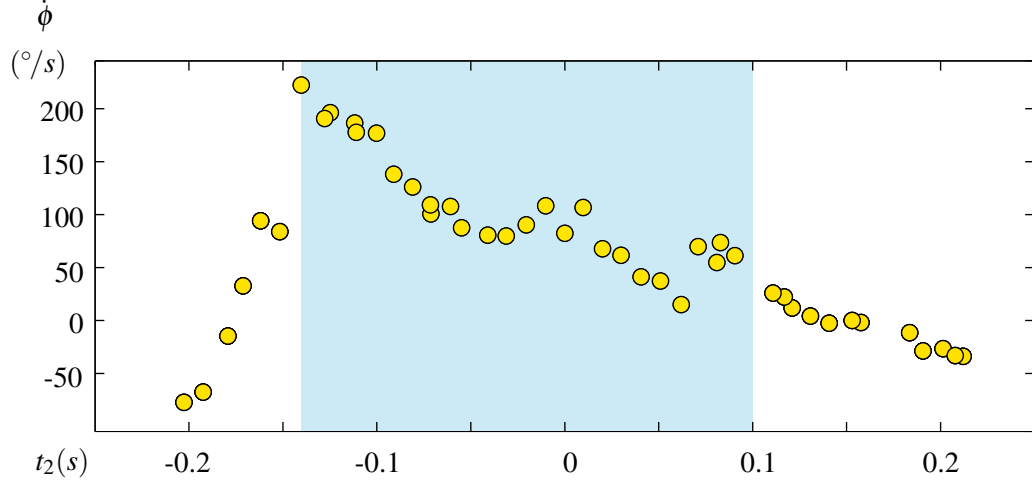


Figure 4.9: Pitching velocity ( $\dot{\phi}$ , in  $^{\circ}/s$ ) at apex after a forward leap vs relative timing ( $t_2$  in s). Highlighted region are leaps that included a double stance period.

diagonal in the double rolling contact region of Fig. 4.6) on average incurs less deviation from that initial pitch during this first phase of the leap.

### Single Leg Dynamics

Once the front leg has lifted off the ground, the hybrid dynamics admit two degrees of freedom, and so we drop  $\theta_1$  from the state as under Assumption C.6, the massless front leg can have arbitrary position in the air, which would otherwise violate Assumption A.4. Note that this contact mode is not accessible quasi-statically, and as such is not shown in Fig. 4.3. Choosing  $\mathbf{y} = [\theta_2, \phi]^T$ , the constrained motion of (19) evaluated with  $\mathbf{A}$  for a stick leg in the rear and no contact in the front,<sup>17</sup>

$$\dot{\mathbf{q}} = \mathbf{H}\dot{\mathbf{y}} = \begin{bmatrix} \dot{\theta}_2 \\ \rho_2 \cos(\theta_2 - \phi)(\dot{\theta}_2 - \dot{\phi}) - l_2 \sin(\phi) \dot{\phi} \\ \rho_2 \sin(\theta_2 - \phi)(\dot{\theta}_2 - \dot{\phi}) - l_2 \cos(\phi) \dot{\phi} \\ \dot{\phi} \end{bmatrix}, \quad (62)$$

leading to the reduced dynamics of (35) for pitch,<sup>18</sup>

<sup>17</sup>Calculated from (20) with  $\mathbf{Y} = [1, 0, 0, 1]$  as given and the appropriate  $\mathbf{A}$  (i.e. (17) where  $\mathbf{G}_s$  is simply (81) and  $\mathbf{J}_h$  is simply (85).

<sup>18</sup>Calculated from (35)–(37) with (88)–(92) and  $\mathbf{H}$  as shown in (62).

$$\ddot{\phi} = -\tilde{\mathbf{D}}_{\phi} \dot{\mathbf{q}} + \tilde{\mathbf{E}}_{\phi} = \frac{\ell_2 m_b \cos(\theta_2) \left( \rho_2 (\dot{\theta}_2 - \dot{\phi})^2 + \ell_2 \sin(\theta_2) \dot{\phi}^2 \right)}{I_b + \ell_2^2 m_b \cos^2(\theta_2)} + \frac{\tau_2 \left( 1 + \frac{\ell_2}{\rho_2} \sin(\theta_2) \right) - \ell_2 m_b g \cos(\theta_2) \cos(\theta_2 - \phi)}{I_b + \ell_2^2 m_b \cos^2(\theta_2)}, \quad (63)$$

where it is clear that,

*Result C.3.* Once the front leg has lifted off the ground, the harder the rear motor is pushing ( $\tau_2$ ), and the faster the rear leg is moving ( $\dot{\theta}_2$ , when  $|\dot{\phi}| < |\dot{\theta}_2|$ ), the more the robot accelerates counter-clockwise in pitch (i.e. “upwards”, in the positive  $\phi$  direction) (63).

Thus the controller design problem for a pronk-like leap becomes a balancing act between the conflicting criteria to both move quickly and maintain pitch control. Some pronk implementations on RHex reconcile this conflict by significantly reducing the torque at the end of stance, rapidly decelerating the leg [4, 127], essentially stubbing the toe in order to quickly correct the pitch. This toe stubbing effect is also anecdotally demonstrated as a leaping task in Chapter 3 — here we present additional data from that experiment. To show the possibilities of this strategy in an extreme case, the apex state for two leaps, one with a strong toe stub and one without, are included in Table 4.4. This confirms that rapidly slowing down the rear leg at the end of a jump can induce a large pitch correction, greatly affecting the pitch velocity, though at the cost of 17% of the forward velocity.

Toe Stub?	$\phi$	$\dot{\phi}$	$ \dot{x} $	$T$
Without	10.4°	57°/s	1704 mm/s	11.4 J
With	-13.5°	-145°/s	1414 mm/s	8.3 J

Table 4.4: Comparison of forward leaps: the toe stub (Result C.3) has significant control authority over body pitch, in this extreme example changing the pitch by 24°.

### Implications of the Takeoff Condition

As in the prior subsection, consider the case where the front leg has taken off and only the rear leg remains in contact. The friction cone (7) sets up an implicit bound on torque based on the contact

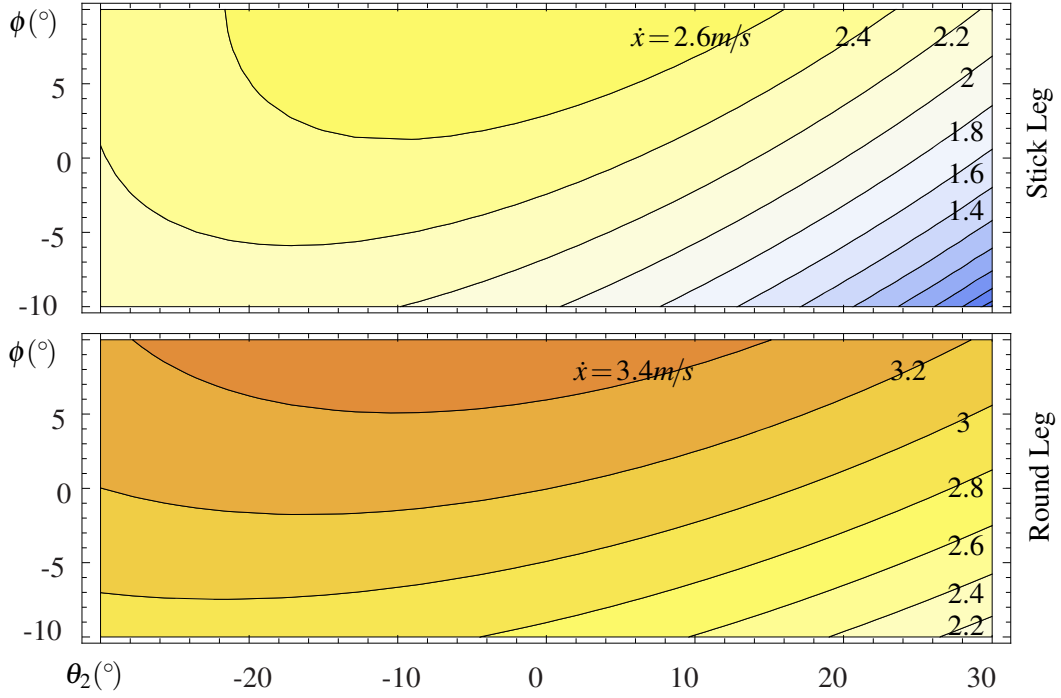


Figure 4.10: Forward velocity ( $|\dot{x}|$ , in  $m/s$ ) at takeoff point of second (rear) leg for various leg angle  $\theta_2$  and pitch  $\phi$ , assuming  $\dot{\phi} = 0$ , and gear ratio  $G = 23$ . On top, takeoff based on a stick leg, while on bottom takeoff based on a round leg.

forces (39),<sup>19</sup>

$$(\mathbf{U}\lambda)_{2n} \geq 0 \Rightarrow \tau \geq \frac{I_b m_b \rho_2 \cos(\theta_2 - \phi) (\rho_2 (\dot{\theta}_2 - \dot{\phi})^2 + \ell_2 \sin(\theta_2) \dot{\phi} - g \cos(\theta_2 - \phi))}{\ell_2 m_b \cos \theta_2 (\rho_2 \cos(\theta_2 - \phi) + \ell_2 \sin \phi) - I_b \sin(\theta_2 - \phi)}, \quad (64)$$

(here shown for a stick leg). Thus the faster the robot is moving ( $\dot{\theta}_2$ ), the more torque is required to maintain contact, and so with any limited-torque actuator, the system speed exhibits a corresponding upper bound. However in general the faster an actuator is moving, the less torque it can produce. Applying a motor model of  $\tau \leq \kappa_P \kappa_G (1 - \kappa_G \dot{\theta})$  [129] (where  $\kappa_P$  is proportional to peak motor power and  $\kappa_G$  is proportional to gear ratio), we can substitute for  $\tau$  in (64) to get an equality that imposes a necessary condition for liftoff on the robot's state. This equality constraint can now be solved with a variety of different implicit functions to gain insight into the manner in which different

<sup>19</sup>Calculated from (39)–(40) with (88)–(92) and  $\mathbf{H}$  as shown in (62). Note that the denominator of (64) is positive under Assumption D.1, i.e. normal standing/running ranges, for values listed in Table 4.2.

design choices — either entailing physical parameters, or various behaviors entailing controllers which aim for different state space trajectories — can potentially influence the resulting conditions at liftoff. The simplest of these obtains by considering the equality to be a quadratic form in  $\dot{\theta}$ , so that the resulting root functions can be passed through the infinitesimal kinematics (62) yielding a closed-form expression for the maximum forward velocity at liftoff, here shown for mid-stance ( $\theta_2 = 0$  and  $\phi = 0$ ) with stick legs,

$$\dot{x} = \frac{-\kappa_b + \sqrt{\kappa_b^2 + 4I_b \kappa_c}}{2I_b}, \quad (65)$$

$$\kappa_b := \ell_2 \kappa_G^2 \kappa_P, \quad \kappa_c := \kappa_b \rho_2 \left( \frac{1}{\kappa_G} - \dot{\phi} \right) + \rho_2 g I_b.$$

For rounded legs, the same maximum forward velocity is,

$$\dot{x} = \frac{-\kappa_b + \sqrt{\kappa_b^2 + 4\frac{I_b}{2} \kappa_c}}{2\frac{I_b}{2}}. \quad (66)$$

Fig. 4.10 shows this forward velocity bound for a robot with a stick leg and for a rounded leg across a range of leg and body angles typically found for stance. We conclude that,

*Result C.4.* The dynamical bound on the forward speed is higher for rounded legs (66) than for stick legs (65).

as is true analytically for mid-stance<sup>20</sup> and therefore by smoothness for some neighborhood around that point, and is numerically shown to be at least  $0.6m/s$  faster over the entire range of Fig. 4.10 (all assuming  $\dot{\phi} \approx 0$ ).

This bound is very rough as it does not consider compliance or damping (or in this figure, pitching velocity), but does shed considerable light on the new considerations that emerge in the dynamical regime whereby the rounded legs of RHex when running forward afford a higher speed limit, even at the point of mid-stance whereas, in contrast, quasi-statically the two morphological

<sup>20</sup>Compare (65)–(66) with the quadratic formula and note that the factor of 2 in the inertia ( $x^2$  term when written out in quadratic form) makes (65) smaller than (66) for any set of positive parameter values and  $\dot{\phi} < 1/\kappa_G$ , i.e. the motor no-load speed.

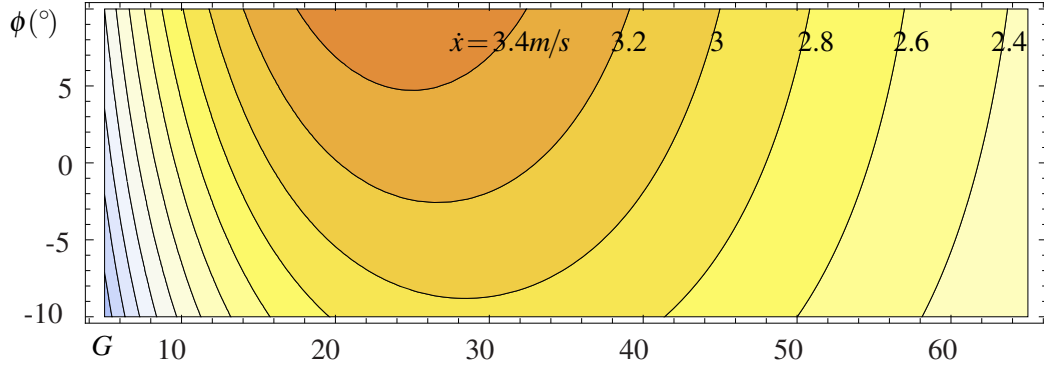


Figure 4.11: Forward velocity ( $\dot{x}$ , in  $m/s$ ) at takeoff point of second (rear) leg under rolling contact for various gear ratios  $G$  and pitch  $\phi$ , shown for  $\dot{\phi} = 0$ , and optimal  $\theta_2$ . Gear ratio for XRL is typically 23:1, just below the optimal of between 25–30.

variants are equivalent (as described in Section 4.1.6).

In contrast, the liftoff constraint (64) can be used in a more conventional numerical manner, for example determining the

$$\begin{aligned}
 \max \quad & \dot{x}, \\
 \text{s.t.} \quad & (\mathbf{U}\boldsymbol{\lambda})_{2n} \geq 0, \\
 & \boldsymbol{\lambda} = -\tilde{\mathbf{D}}_{\lambda}\dot{\mathbf{y}} + \tilde{\mathbf{E}}_{\lambda}, \\
 & \boldsymbol{\tau} \leq \kappa_P \kappa_G (1 - \kappa_G \dot{\boldsymbol{\theta}})
 \end{aligned}$$

allowing  $\dot{\mathbf{y}}$  to vary. Specifically, note that for each  $\phi$  in Fig. 4.10, there is a unique  $\theta_2$  that maximizes  $\dot{x}$ . As shown in Fig. 4.11 (shown for  $\dot{\phi} \approx 0$ ), the optimal gear ratio lies somewhere around 25:1 depending on the pitch at take off, only slightly above the actual value of 23:1 for this robot.

Similarly, using this maximal takeoff point to eliminate  $\theta_2$  from (64) we can now test the desirability of  $\dot{\phi} \approx 0$ . Calculated numerically and shown in Fig. 4.12, we see that a positive pitch  $\phi$  but small pitching velocity  $\dot{\phi}$  (as results from a splayed posture) results in the highest maximum forward speed (numerically calculated based on Table 4.2).

These maximal speed points are specific positions and velocities  $(\mathbf{y}, \dot{\mathbf{y}})$  that may or may not be reachable – in fact as shown in Fig. 4.9 all of the jumps with double support in this way still had a non-zero positive pitching moment (see Table 3.1).

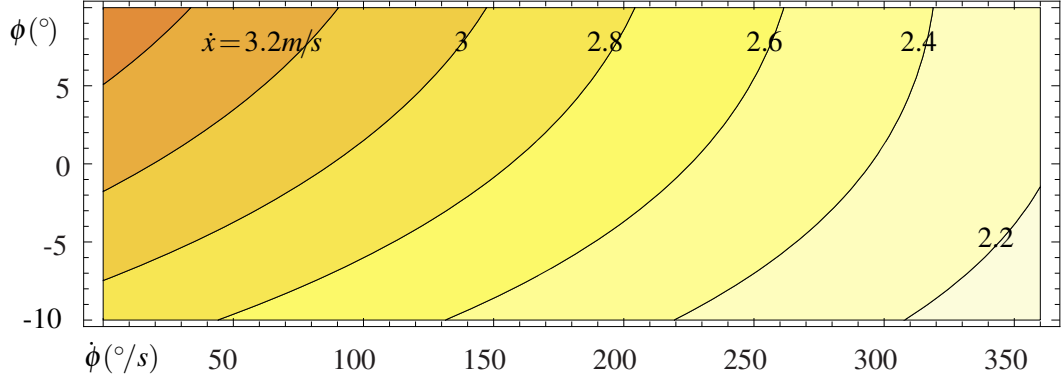


Figure 4.12: Forward velocity ( $|\dot{x}|$ , in  $m/s$ ) at takeoff point of second (rear) leg under rolling contact for various pitching velocities  $\dot{\phi}$  (in  $^\circ/s$ ) and pitches  $\phi$  (in  $^\circ$ ), for optimal  $\theta_2$ , and gear ratio  $G = 23$ .

### Inertial Leg Effects

In the air, the dynamics of the robot are not restricted by the closed-loop constraint (12), as there are no contact forces, however conservation of angular momentum in the absence of external forces now imposes a nonholonomic constraint. Solving the dynamics as in Section 4.1.9 takes these conservation laws into account, ensuring that the time derivative of momentum is equal to the applied force, which here is zero. Recall that up until this point under Assumption C.6 we have used massless legs (as  $m_l/m_b < 1\%$ ), but here we drop that assumption to test what effect the very light legs do have. The leg effectiveness [92] is defined as the body velocity per differential leg velocity, which can be calculated by placing the world reference frame,  $W$ , at the system center of mass and solving the conservation of angular momentum equation as follows (for a single leg),<sup>21</sup>

$$\begin{aligned} \pi_\phi \left( \frac{\partial L}{\partial \dot{q}} \right) &= \pi_\phi \left( \mathbf{Ad}_{g_{pw}}^T \widehat{\mathbf{M}} \begin{bmatrix} \dot{\theta} \\ \mathbf{v}_{op}^b \end{bmatrix} \right) = 0 \Rightarrow \\ \varepsilon_n &:= \frac{\dot{\phi}}{\dot{\theta}_1} = - \frac{I_l + m_r \left( \left( \frac{\rho_1}{2} \right)^2 - \ell_1 \frac{\rho_1}{2} \sin \theta_1 \right)}{I_b + I_t + m_r \left( \ell_1^2 + \left( \frac{\rho_1}{2} \right)^2 - 2\ell_1 \left( \frac{\rho_1}{2} \right) \sin \theta_1 \right)}, \\ m_r &:= \frac{m_b m_l}{m_b + m_l}, \end{aligned} \quad (67)$$

<sup>21</sup>Calculated with  $\pi_{\mathbf{g}_{pw}} := \frac{m_l}{m_l + m_b} \pi_{\mathbf{g}_{pl_1}}$ . Note that the conservation of momentum laws apply only to body velocities at the center of mass, as used here.

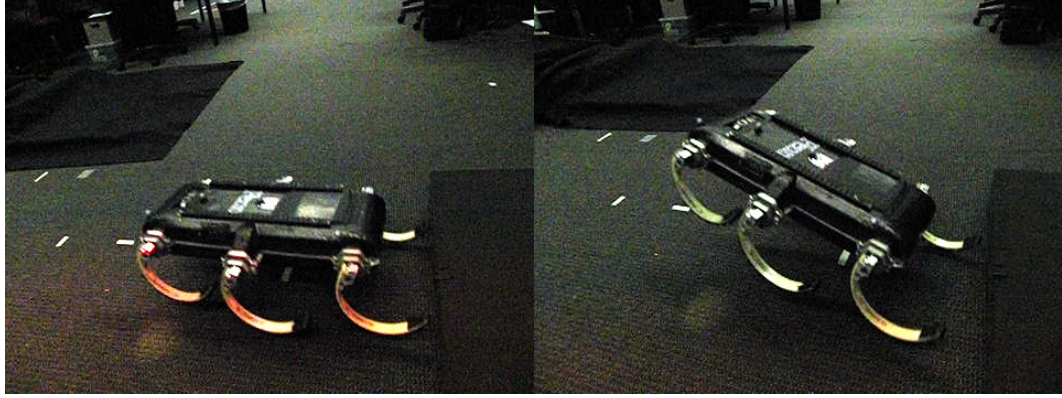


Figure 4.13: Robot state just prior to touchdown after two jumps: (Left) the legs completely recirculated clockwise, (Right) the legs went directly to the final angle counterclockwise.

which is the same as [92], up to notation. Note that the effectiveness is shape dependent — the relationship between leg velocity and body velocity is not constant over all  $\theta$ . However an interesting simplification arises when two legs equally spaced from the robot COM (Assumption D.2) are controlled so as to be locked in parallel,  $\theta_1(t) \equiv \theta_2(t)$ ,

$$\varepsilon_n := \frac{\dot{\phi}}{\dot{\theta}_1} = -\frac{2I_l + m_{r2}(\frac{\rho_1}{2})^2}{I_b + 2I_l + 2m_l\ell_1 + m_{r2}\frac{\rho_1}{2}}, \quad (68)$$

$$m_{r2} := \frac{m_b(2m_l)}{m_b + (2m_l)},$$

i.e. the configuration dependence goes away. With all six legs included, the effectiveness for RHex is only  $\varepsilon_n = 0.035$ , though it is almost twice a naïve estimate of  $\frac{6I_l}{I_b} = 0.018$  (see Table 4.2).

To verify the inertial effects of the legs, the robot performed a single jump (as in Chapter 3) and the legs were sent to a given position, but in one case they were controlled to recirculate completely, while in the other they were not. Thus between the two tests the leg angles  $\theta$  differ by exactly  $360^\circ$ . This resulted in a difference in body pitch of  $14^\circ$  (median taken across 5 jumps of each type), as shown in Fig. 4.13. Thus the measured effectiveness is  $\varepsilon_m = 14/360 = 0.039$ , quite close to what the model predicts, and critically,

*Result C.5.* The legs act as inertial tails and, when locked in phase, can produce a body rotation of  $\varepsilon_n$  (68) for each complete rotation they execute during flight (Fig. 4.13).

## 4.4 Appendix to Chapter 4

### 4.4.1 Kinematic Constraints

The base constraint (8) may be expanded as,

$$\mathbf{x}_{c_k} = \pi_{c_k}(\mathbf{g}_{c_k w}(\mathbf{q})) = \pi_{c_k}(\mathbf{g}_{c_k s_k}(\mathbf{q}) \cdot \mathbf{g}_{s_k w}(\mathbf{x})),$$

where,

$$\begin{aligned}\mathbf{g}_{c_k s_k}(\mathbf{q}) &:= \mathbf{g}_{c_k f_k}(\mathbf{q}) \cdot \mathbf{g}_{f_k s_k}(\theta), \\ \mathbf{g}_{s_k w}(\mathbf{x}) &:= \mathbf{g}_{s_k p} \cdot \mathbf{g}_{p w}(\mathbf{x}),\end{aligned}$$

however note that while  $\mathbf{g}_{c_k f_k}$  depends on  $\mathbf{q}$ , the projection  $\pi_{c_k}(\mathbf{g}_{c_k f_k})$  does not vary over time (i.e. it may be thought of as being parameterized by the initial value,  $\mathbf{q}_a(0)$ , but not a time varying function of  $\mathbf{q}$ ). This frictional restriction is much clearer when expressed as a velocity constraint,  $\mathbf{B}_{c_k}^T \mathbf{V}_{c_k f_k}^s \equiv 0$ , which is one reason most multi-fingered manipulation texts often skip the base constraint and directly apply a velocity or force constraint (including refs. [13, 119, 120, 134, 137, 162]).

The velocity constraint equation (11) is proven in twist coordinates by using the following identities (see [134, p. 59] for proof of (69) and Section 4.4.6, below, for a proof of (70)),

$$\mathbf{V}_{ac}^s = \mathbf{V}_{ab}^s + \mathbf{Ad}_{g_{ab}} \mathbf{V}_{bc}^s, \quad (69)$$

$$\mathbf{V}_{ab}^s = -\mathbf{V}_{ba}^b, \quad (70)$$

[134, Prop. 2.14, Lemma 2.16], and the friction constraint,

$$\mathbf{B}_{c_k}^T \mathbf{V}_{c_k f_k}^s \equiv 0, \quad (71)$$

[134, Eqn. 5.9] (ensuring no motion in the constrained directions) and so,

$$0 = \frac{d}{dt} \mathbf{a}_k \circ \mathbf{q}_a = \mathbf{B}_{c_k}^T \dot{\mathbf{g}}_{c_k w} \cdot \mathbf{g}_{c_k w}^{-1} \cdot \mathbf{g}_{c_k w} \Rightarrow 0 = \mathbf{B}_{c_k}^T \mathbf{V}_{c_k w}^s$$

$$\begin{aligned}
&= \mathbf{B}_{c_k}^T (\mathbf{V}_{c_k s_k}^s + \mathbf{Ad}_{g_{c_k s_k}} \mathbf{V}_{s_k w}^s), \\
\mathbf{V}_{c_k s_k}^s &= \mathbf{V}_{c_k f_k}^s + \mathbf{Ad}_{g_{c_k f_k}} \mathbf{V}_{f_k s_k}^s = -\mathbf{V}_{f_k c_k}^b - \mathbf{Ad}_{g_{c_k f_k}} \mathbf{V}_{s_k f_k}^b, \\
\mathbf{V}_{s_k w}^s &= \mathbf{V}_{s_k p}^s + \mathbf{Ad}_{g_{s_k p}} \mathbf{V}_{pw}^s = 0 - \mathbf{Ad}_{g_{s_k p}} \mathbf{V}_{wp}^b, \\
0 &= \mathbf{B}_{c_k}^T (-\mathbf{Ad}_{g_{c_k f_k}} \mathbf{V}_{s_k f_k}^b - \mathbf{Ad}_{g_{c_k s_k}} \mathbf{Ad}_{g_{s_k p}} \mathbf{V}_{wp}^b) \\
&= -\mathbf{B}_{c_k}^T \mathbf{Ad}_{g_{c_k f_k}}(\mathbf{q}) \mathbf{J}_{s_k f_k}^b(\theta) \dot{\theta} - \mathbf{B}_{c_k}^T \mathbf{Ad}_{g_{c_k p}}(\mathbf{q}) \mathbf{R}_{wp}^T \dot{\mathbf{x}}.
\end{aligned}$$

An alternate proof of (11) is given here using a homogeneous representations of velocity,  $\hat{\mathbf{V}} := (\mathbf{V})^\wedge$ , by using the following identities (in addition to (70), proven below),

$$\begin{aligned}
\hat{\mathbf{V}}_{ab}^s &:= \dot{\mathbf{g}}_{ab} \mathbf{g}_{ab}^{-1}, \\
(\mathbf{Ad}_{g_{ab}} \mathbf{V}_{bc}^s)^\wedge &= \mathbf{g}_{ab} \hat{\mathbf{V}}_{bc}^s \mathbf{g}_{ab}^{-1},
\end{aligned}$$

[134, Eqn. 2.53, Lemma 2.13] (and indeed all of [134, Section 2.4]), and the friction constraint (71) so,

$$\begin{aligned}
0 &= \frac{d}{dt} \mathbf{a}_k \circ \mathbf{q}_a \\
&= \mathbf{B}_{c_k}^T (\dot{\mathbf{g}}_{c_k f_k} \mathbf{g}_{f_k s_k} \mathbf{g}_{s_k w} + \mathbf{g}_{c_k f_k} \dot{\mathbf{g}}_{f_k s_k} \mathbf{g}_{s_k w} + \mathbf{g}_{c_k f_k} \mathbf{g}_{f_k s_k} \dot{\mathbf{g}}_{s_k p} \mathbf{g}_{pw}^\vee) \\
&= \mathbf{B}_{c_k}^T \left( (\dot{\mathbf{g}}_{c_k f_k} \mathbf{g}_{c_k f_k}^{-1} + \mathbf{g}_{c_k f_k} \dot{\mathbf{g}}_{f_k s_k} \mathbf{g}_{f_k s_k}^{-1} \mathbf{g}_{c_k f_k}^{-1} + \mathbf{g}_{c_k p} \dot{\mathbf{g}}_{pw} \mathbf{g}_{pw}^{-1} \mathbf{g}_{c_k p}^{-1}) \mathbf{g}_{c_k w} \right)^\vee \\
\Rightarrow 0 &= \mathbf{B}_{c_k}^T (\mathbf{V}_{c_k f_k}^s + \mathbf{Ad}_{g_{c_k f_k}} \mathbf{V}_{f_k s_k}^s + \mathbf{Ad}_{g_{c_k p}} \mathbf{V}_{pw}^s) \\
&= 0 - \mathbf{B}_{c_k}^T \mathbf{Ad}_{g_{c_k f_k}} \mathbf{J}_{s_k f_k}^b \dot{\theta} - \mathbf{B}_{c_k}^T \mathbf{Ad}_{g_{c_k p}} \mathbf{R}_{wp}^T \dot{\mathbf{x}} = \mathbf{A}_k(\mathbf{q}) \dot{\mathbf{q}}.
\end{aligned}$$

#### 4.4.2 Grasp Map and Hand Jacobian

The definition of the grasp map (13) is often given in terms of body velocity,  $\mathbf{V}_{po}^b$ , but computation of the dynamics is easiest in some local coordinates,  $\dot{\mathbf{x}}$ . Here we have also defined a grasp map in terms of the more relevant body velocity  $\mathbf{V}_{op}^b$ . These various versions of the grasp map are, of course, equivalent as summarized here:

$$\mathbf{G}_s^T \mathbf{R}_{wp}^T \dot{\mathbf{x}} = \mathbf{G}_s^T \mathbf{V}_{wp}^b = \mathbf{G}_s^T \mathbf{V}_{op}^b = \mathbf{G}^T \mathbf{V}_{po}^b.$$

For further notes on this see [134, Eqn. 6.18] as opposed to [134, Eqn. 5.15], discussion on [134, pp. 279, 283], and paragraph surrounding [162, Eqn. 28.1].

As for the hand Jacobian, note that the contact wrenches (or twists) at one toe have no direct effect on joints on a different leg (hence the block diagonal structure of  $\mathbf{J}_h$ ). The indirect effects are captured by the closed-loop constraint (11,12). That the legs can be decoupled in this way is less obvious than in the multi-finger manipulation case, where each finger is rigidly attached to a fixed inertial frame. This decoupling comes from Newton’s third law of motion, that every action has an equal and opposite reaction, and thus we may calculate the joint torques equally well by adding up the effects on either side of the joint.

### 4.4.3 Rolling Contact

As noted in Sec. 4.1.6, the fact that RHex’s legs are not simple sticks does not change any of the analysis thus far, it simply makes the  $\mathbf{G}_s$  and  $\mathbf{J}_h$  matrices more complicated. The free motion of the hip at any given moment under rolling contact is identical to the motion of an equivalent stick leg connecting the hip to the contact point.

To prove this, consider a point on the circumference of a circle as it rolls — it follows a cycloid path. If we first assume that the world frame  $W$  is attached to the ground at the toe when the robot is standing ( $\theta = 0$ ), with the  $z$  axis pointing into the ground, then the hip location is  $(x_c, z_c) := \pi \mathbf{g}_{ws}(0) = (0, -2\rho_h)$  (where  $\rho_h := \rho_1/2$  is the leg radius) then the position of the hip as a function of the motor angle  $\theta$  is,

$$x_c = \rho_h \theta + \rho_h \sin(\theta), \quad z_c = -\rho_h - \rho_h \cos(\theta).$$

Note that the definition of  $\theta$  used in this chapter has the leg in contact on the rounded half of the leg when  $\theta < 0$ , i.e. the leg is on the rounded half before mid-stance, and on the toe afterwards (as opposed to other robots whose half-circle legs are used in the opposite direction [74]).

Now consider a virtual leg extending from the hip to the contact point. Let the angle that this virtual leg makes with vertical be  $\vartheta$  and the leg length be  $\rho_l$ . The hip position relative to the true

world frame at that moment,  $(x_f, z_f) := \pi \mathbf{g}_{ws}(\vartheta)$ , for a fixed leg of length  $\rho_l$  and angle  $\vartheta$  is,

$$x_f = \rho_l \sin(\vartheta), \quad z_f = -\rho_l \cos(\vartheta).$$

First note that the triangle consisting of the center of the leg, the hip, and the contact point must be isosceles, as two of the sides are length  $\rho_h$ , and the third length  $\rho_l$ . The angle at the center of the circle must then be  $\pi - \theta$  as the supplementary angle is  $\theta$ . Therefore by noting that the equal angles in that triangle are  $\vartheta$ , we find that  $\vartheta = \theta/2$ .

Now the infinitesimal direction of free motion for each case (i.e. the tangent of the trajectory),

$$\begin{aligned} \frac{\partial x_c}{\partial \theta} &= \rho_h + \rho_h \cos(\theta), & \frac{\partial z_c}{\partial \theta} &= \rho_h \sin(\theta), \\ \frac{\partial x_f}{\partial \vartheta} &= \rho_l \cos(\vartheta), & \frac{\partial z_f}{\partial \vartheta} &= \rho_l \sin(\vartheta), \\ \frac{\partial z_c}{\partial x_c} &= \frac{\sin(\theta)}{1 + \cos(\theta)}, & \frac{\partial z_f}{\partial x_f} &= \frac{\sin(\vartheta)}{\cos(\vartheta)}, \end{aligned}$$

can be compared using the double angle identity to find,

$$\frac{\partial z_c}{\partial x_c} = \frac{2 \sin(\vartheta) \cos(\vartheta)}{1 + 2 \cos^2(\vartheta) - 1} = \frac{\sin(\vartheta)}{\cos(\vartheta)} = \frac{\partial z_f}{\partial x_f}.$$

Therefore the twist direction is the same whether you follow the full cycloid curve, or at each instant follow a virtual leg. This property is much more general than just for half circle legs, as shown in [134, Chapter 5.6].

#### 4.4.4 Dynamics

The generalized mass matrix,  $\overline{\mathbf{M}}$ , is derived by summing the contribution of each link,

$$\begin{aligned} T &= \frac{1}{2} m_b \|\mathbf{v}_{wp}^b\|^2 + \frac{1}{2} I_b \|\boldsymbol{\omega}_{wp}^b\|^2 + \sum_{i=1}^n \left( \frac{1}{2} m_{l_i} \|\mathbf{v}_{wl_i}^b\|^2 + \frac{1}{2} I_{l_i} \|\boldsymbol{\omega}_{wl_i}^b\|^2 \right) \\ &= \frac{1}{2} (\mathbf{V}_{wp}^b)^T \mathbf{M}_b \mathbf{V}_{wp}^b + \sum_{i=1}^n \frac{1}{2} (\mathbf{V}_{wl_i}^b)^T \mathbf{M}_{l_i} \mathbf{V}_{wl_i}^b, \\ \mathbf{V}_{wl_i}^b &= \mathbf{Ad}_{g_{pl_i}^{-1}} \mathbf{V}_{wp}^b + \mathbf{V}_{pl_i}^b, \end{aligned}$$

$$\begin{aligned}
T &= \frac{1}{2}(\mathbf{V}_{wp}^b)^T \mathbf{M}_b \mathbf{V}_{wp}^b + \sum_{i=1}^n \frac{1}{2} (\mathbf{Ad}_{g_{pl_i}^{-1}} \mathbf{V}_{wp}^b + \mathbf{V}_{pl_i}^b)^T \mathbf{M}_{l_i} (\mathbf{Ad}_{g_{pl_i}^{-1}} \mathbf{V}_{wp}^b + \mathbf{V}_{pl_i}^b) \\
&= \frac{1}{2}(\mathbf{V}_{wp}^b)^T \mathbf{M}_b \mathbf{V}_{wp}^b + \sum_{i=1}^n \left( \frac{1}{2} (\mathbf{V}_{pl_i}^b)^T \mathbf{M}_{l_i} \mathbf{V}_{pl_i}^b \right. \\
&\quad \left. + (\mathbf{V}_{pl_i}^b)^T \mathbf{M}_{l_i} \mathbf{Ad}_{g_{pl_i}^{-1}} \mathbf{V}_{wp}^b + \frac{1}{2} (\mathbf{V}_{wp}^b)^T \mathbf{Ad}_{g_{pl_i}^{-1}}^T \mathbf{M}_{l_i} \mathbf{Ad}_{g_{pl_i}^{-1}} \mathbf{V}_{wp}^b \right),
\end{aligned}$$

where both  $\mathbf{Ad}_{g_{pl_i}^{-1}}$  and  $\mathbf{J}_{l_i}$  both depend only on  $\theta$ . Substituting  $\mathbf{V}_{wp}^b = \mathbf{R}_{wp}^T \dot{\mathbf{x}}$  results in the inertia tensor given in (26).

The accelerations and constraint forces may be solved for as follows (33),

$$\begin{aligned}
\bar{\mathbf{M}}(\theta, \phi) \ddot{\mathbf{q}} + \bar{\mathbf{C}}(\theta, \phi, \dot{\mathbf{q}}) \dot{\mathbf{q}} + \bar{\mathbf{N}}(\theta, \phi) + \mathbf{A}^T(\theta, \phi) \boldsymbol{\lambda} &= \Upsilon(\tau) \\
\begin{bmatrix} \bar{\mathbf{M}} & \mathbf{A}^T & \bar{\mathbf{C}} \\ \mathbf{A} & 0 & \dot{\mathbf{A}} \end{bmatrix} \begin{bmatrix} \ddot{\mathbf{q}} \\ \boldsymbol{\lambda} \\ \dot{\mathbf{q}} \end{bmatrix} &= \begin{bmatrix} \Upsilon - \bar{\mathbf{N}} \\ 0 \end{bmatrix} \\
\begin{bmatrix} \bar{\mathbf{M}} & \mathbf{A}^T \\ \mathbf{A} & 0 \end{bmatrix} \begin{bmatrix} \ddot{\mathbf{q}} \\ \boldsymbol{\lambda} \end{bmatrix} &= \begin{bmatrix} \Upsilon - \bar{\mathbf{N}} \\ 0 \end{bmatrix} - \begin{bmatrix} \bar{\mathbf{C}} \\ \dot{\mathbf{A}} \end{bmatrix} \dot{\mathbf{q}} \\
\begin{bmatrix} \ddot{\mathbf{q}} \\ \boldsymbol{\lambda} \end{bmatrix} &= \begin{bmatrix} \bar{\mathbf{M}} & \mathbf{A}^T \\ \mathbf{A} & 0 \end{bmatrix}^{-1} \begin{bmatrix} \Upsilon - \bar{\mathbf{N}} \\ 0 \end{bmatrix} - \begin{bmatrix} \bar{\mathbf{M}} & \mathbf{A}^T \\ \mathbf{A} & 0 \end{bmatrix}^{-1} \begin{bmatrix} \bar{\mathbf{C}} \\ \dot{\mathbf{A}} \end{bmatrix} \dot{\mathbf{q}}.
\end{aligned}$$

Some dimensional analysis — the dynamics provides  $q$  equations, and the constraint equation provides  $c$ . Total, there are  $2q + c$  unknowns, so in non-singular configurations we can solve for the  $q + c$  unknowns  $\ddot{\mathbf{q}}$  and  $\boldsymbol{\lambda}$  in terms of the  $q$  remaining variables,  $\dot{\mathbf{q}}$ , as shown above. Note that this does not require  $\bar{\mathbf{M}}$  be invertible, which is not the case with massless legs, or require  $\mathbf{J}_h$  be invertible (as with [134, Eqn. 6.22]), which never is the case with “simple” legs like on RHex. Instead this method solves for both the system accelerations and constraint forces at the same time by inverting a block matrix that includes  $\bar{\mathbf{M}}$  and  $\mathbf{A}$  that in general is non-singular so long as  $\text{rank}(\bar{\mathbf{M}}) + \text{rank}(\mathbf{A}) \geq q + c$ , or  $\text{rank}(\bar{\mathbf{M}}) \geq e = q - c$  and the constraints are non-singular (this is equivalent to the requirement that the mass matrix of the reduced dynamics,  $\tilde{\mathbf{M}}$ , to be defined in the next section, be full rank).

Now putting the whole system together we arrive at the differential equation (and splitting up the rows of  $\mathbf{D}$  and  $\mathbf{E}$  as suggested by the subscript),

$$\begin{aligned} \frac{d}{dt} \begin{bmatrix} \dot{\mathbf{q}} \\ \mathbf{q} \end{bmatrix} &= \begin{bmatrix} -\mathbf{D}_{\dot{q}} & 0 \\ \mathbf{I}_{\mathbf{d}_q} & 0 \end{bmatrix} \begin{bmatrix} \dot{\mathbf{q}} \\ \mathbf{q} \end{bmatrix} + \begin{bmatrix} \mathbf{E}_{\ddot{q}} \\ 0 \end{bmatrix}, \\ \lambda &= -\mathbf{D}_{\lambda} \dot{\mathbf{q}} + \mathbf{E}_{\lambda}. \end{aligned} \quad (72)$$

As used in [134, Eqn. 6.23], and [162, Eqn. 28.20], the dynamics may re-written in twist coordinates (though only after we have derived them in local coordinates), where (33) becomes,

$$\begin{aligned} \widehat{\mathbf{M}}(\theta) \dot{\mathbf{v}} + \widehat{\mathbf{C}}(\theta, \mathbf{v}) \mathbf{v} + \widehat{\mathbf{N}}(\theta, \phi) + \begin{bmatrix} -\mathbf{J}_h \\ \mathbf{G}_s \end{bmatrix} \lambda &= \Upsilon(\tau), \\ \mathbf{v} &:= \begin{bmatrix} \dot{\theta} \\ \mathbf{V}_{op}^b \end{bmatrix}, \end{aligned} \quad (73)$$

where  $\widehat{\mathbf{M}}$  is the combined body inertia tensor as given in (25), while  $\widehat{\mathbf{C}}$ , and  $\widehat{\mathbf{N}}$  have been suitably rotated by  $\mathbf{R}_{wp}$ . However the lower line of (72) must reflect  $\dot{\mathbf{x}} = \mathbf{R}_{wp} \mathbf{V}_{op}^b$ .

If  $\overline{\mathbf{M}}$  is invertible, the Lagrange multipliers may be solved for first and then used to calculate  $\ddot{\mathbf{q}}$ ,

$$\begin{aligned} \lambda &= (\mathbf{A} \overline{\mathbf{M}}^{-1} \mathbf{A}^T)^{-1} \left( \mathbf{A} \overline{\mathbf{M}}^{-1} (\Upsilon - \overline{\mathbf{C}} \dot{\mathbf{q}} - \overline{\mathbf{N}}) + \dot{\mathbf{A}} \dot{\mathbf{q}} \right), \\ \ddot{\mathbf{q}} &= \overline{\mathbf{M}}^{-1} (\Upsilon - \overline{\mathbf{C}} \dot{\mathbf{q}} - \overline{\mathbf{N}} - \mathbf{A}^T \lambda), \end{aligned}$$

[134, Eqn. 6.5, 6.6].

#### 4.4.5 Reduced Dynamics

The reduced dynamics can be found by using the Lagrangian written in the reduced coordinates,

$$\begin{aligned} \tilde{T}(\mathbf{y}, \dot{\mathbf{y}}) &:= \frac{1}{2} \dot{\mathbf{y}}^T \mathbf{H}^T(\mathbf{h}(\mathbf{y})) \overline{\mathbf{M}}(\mathbf{h}(\mathbf{y})) \mathbf{H}(\mathbf{h}(\mathbf{y})) \dot{\mathbf{y}} = \frac{1}{2} \dot{\mathbf{y}}^T \tilde{\mathbf{M}} \dot{\mathbf{y}}, \\ \tilde{V}(\mathbf{y}) &:= V(\mathbf{h}(\mathbf{y})), \\ \tilde{L}(\mathbf{y}, \dot{\mathbf{y}}) &= \frac{1}{2} \dot{\mathbf{y}}^T \tilde{\mathbf{M}}(\mathbf{h}(\mathbf{y})) \dot{\mathbf{y}} - \tilde{V}(\mathbf{h}(\mathbf{y})), \end{aligned}$$

and following along as above, or by noting that  $\mathbf{H}^T \mathbf{A}^T = 0$  and working from (32),

$$\begin{aligned}
\bar{\mathbf{M}}(\theta)\ddot{\mathbf{q}} + \bar{\mathbf{C}}(\theta, \dot{\theta})\dot{\mathbf{q}} + \bar{\mathbf{N}}(\theta, \phi) + \mathbf{A}^T(\theta, \phi)\lambda &= \Upsilon \\
\mathbf{H}^T\bar{\mathbf{M}}\dot{\mathbf{q}} + \mathbf{H}^T\bar{\mathbf{C}}\dot{\mathbf{q}} + \mathbf{H}^T\bar{\mathbf{N}} + \mathbf{H}^T\mathbf{A}^T\lambda &= \mathbf{H}^T\Upsilon \\
\mathbf{H}^T\bar{\mathbf{M}}(\mathbf{H}\ddot{\mathbf{y}} + \dot{\mathbf{H}}\dot{\mathbf{y}}) + \mathbf{H}^T\bar{\mathbf{C}}\mathbf{H}\dot{\mathbf{y}} + \mathbf{H}^T\bar{\mathbf{N}} + 0 &= \mathbf{H}^T\Upsilon \\
\tilde{\mathbf{M}}\ddot{\mathbf{y}} + \tilde{\mathbf{C}}\dot{\mathbf{y}} + \tilde{\mathbf{N}} &= \tilde{\Upsilon},
\end{aligned}$$

leading to (35) and summarized as,

$$\frac{d}{dt} \begin{bmatrix} \dot{\mathbf{y}} \\ \mathbf{q} \end{bmatrix} = \begin{bmatrix} -\tilde{\mathbf{D}}(\mathbf{q}, \dot{\mathbf{y}}) & 0 \\ \mathbf{H}(\mathbf{q}) & 0 \end{bmatrix} \begin{bmatrix} \dot{\mathbf{y}} \\ \mathbf{q} \end{bmatrix} + \begin{bmatrix} \tilde{\mathbf{E}}(\mathbf{q}) \\ 0 \end{bmatrix}. \quad (74)$$

To recover the Lagrange multipliers, using the pseudoinverse  $\mathbf{A}^*\mathbf{A}^T = \mathbf{Id}_c$  as chosen in (40),

$$\begin{aligned}
\lambda &= \mathbf{A}^*(\Upsilon - \bar{\mathbf{M}}\ddot{\mathbf{q}} - \bar{\mathbf{C}}\dot{\mathbf{q}} - \bar{\mathbf{N}}) \\
&= \mathbf{A}^*(\Upsilon - (\bar{\mathbf{M}}\mathbf{H})\ddot{\mathbf{y}} - (\bar{\mathbf{M}}\dot{\mathbf{H}} + \bar{\mathbf{C}}\mathbf{H})\dot{\mathbf{y}} - \bar{\mathbf{N}}) \\
&= \mathbf{A}^*(\mathbf{Id}_q - \bar{\mathbf{M}}\mathbf{H}(\mathbf{H}^T\bar{\mathbf{M}}\mathbf{H})^{-1}\mathbf{H}^T)(\Upsilon - (\bar{\mathbf{M}}\dot{\mathbf{H}} + \bar{\mathbf{C}}\mathbf{H})\dot{\mathbf{y}} - \bar{\mathbf{N}}) \\
&= \mathbf{A}^*(\Upsilon - (\bar{\mathbf{M}}\dot{\mathbf{H}} + \bar{\mathbf{C}}\mathbf{H})\dot{\mathbf{y}} - \bar{\mathbf{N}}).
\end{aligned}$$

Note that the other term in (40) has an interesting (though here unused) interpretation, as  $(\bar{\mathbf{M}}\mathbf{H})^*\mathbf{A}^T = \mathbf{0}$  implies that when  $\dot{\mathbf{q}}^T \in (\bar{\mathbf{M}}\mathbf{H})^*$ ,  $\mathbf{A}\mathbf{q} = \mathbf{0}$ , i.e. its rows are the state velocities that imparts no contact force whatsoever. Furthermore since  $(\bar{\mathbf{M}}\mathbf{H})^*(\bar{\mathbf{M}}\mathbf{H}) = \mathbf{Id}_c$ , such velocities also impart unit compliment momentum in the reduced system, i.e.  $\mathbf{H}^T\bar{\mathbf{M}}\dot{\mathbf{q}}$  is a unit basis vector.

#### 4.4.6 Proofs of Lemmas

The proof of [134, Lemma 2.16],

$$\begin{aligned}
\mathbf{V}_{ab}^b &= -\mathbf{V}_{ba}^s, \\
\mathbf{V}_{ab}^b &= -\mathbf{Ad}_{g_{ba}} \mathbf{V}_{ba}^b,
\end{aligned}$$

uses the following properties of rigid transformations and skew symmetric matrices,

$$\begin{aligned}
\mathbf{R}_{ab} &= \mathbf{R}_{ba}^{-1} = \mathbf{R}_{ba}^T, \\
\mathbf{R}^T(\mathbf{p})^\wedge \mathbf{R} &= (\mathbf{R}^T \mathbf{p})^\wedge, \quad (\mathbf{p})^\wedge \mathbf{R} = \mathbf{R}(\mathbf{R}^T \mathbf{p})^\wedge, \\
\dot{\mathbf{R}}\mathbf{R}^T &= -(\dot{\mathbf{R}}\mathbf{R}^T)^T, \\
\mathbf{R}(\mathbf{S})^\vee &= (\mathbf{R}\mathbf{S}\mathbf{R}^T)^\vee, \\
(\mathbf{p})^\wedge \mathbf{q} &= -(\mathbf{q})^\wedge \mathbf{p}, \\
\mathbf{g}_{ab}^{-1} &= (-\mathbf{R}_{ab}^T \mathbf{p}_{ab}, \mathbf{R}_{ab}^T) = (\mathbf{p}_{ba}, \mathbf{R}_{ba}) = \mathbf{g}_{ba},
\end{aligned}$$

[134, Sec. 2.2.1, 2.4] and the definitions

$$\begin{aligned}
\mathbf{V}_{ab}^s &= \begin{bmatrix} -\dot{\mathbf{R}}_{ab} \mathbf{R}_{ab}^T \mathbf{p}_{ab} + \dot{\mathbf{p}}_{ab} \\ (\dot{\mathbf{R}}_{ab} \mathbf{R}_{ab}^T)^\vee \end{bmatrix}, \\
\mathbf{V}_{ab}^b &= \begin{bmatrix} \mathbf{R}_{ab}^T \dot{\mathbf{p}}_{ab} \\ (\mathbf{R}_{ab}^T \dot{\mathbf{R}}_{ab})^\vee \end{bmatrix}, \\
\mathbf{Ad}_{g_{ab}} &= \begin{bmatrix} \mathbf{R}_{ab} & (\mathbf{p}_{ab})^\wedge \mathbf{R}_{ab} \\ 0 & \mathbf{R}_{ab} \end{bmatrix}, \\
\mathbf{V}_{ab}^s &= \mathbf{Ad}_{g_{ab}} \mathbf{V}_{ab}^b,
\end{aligned}$$

[134, Eqn. 2.58–2.61] and so the second part of the Lemma is proven as,

$$\begin{aligned}
-\mathbf{Ad}_{g_{ba}} \mathbf{V}_{ba}^b &= - \begin{bmatrix} \mathbf{R}_{ba} & (\mathbf{p}_{ba})^\wedge \mathbf{R}_{ba} \\ 0 & \mathbf{R}_{ba} \end{bmatrix} \begin{bmatrix} \mathbf{R}_{ba}^T \dot{\mathbf{p}}_{ba} \\ (\mathbf{R}_{ba}^T \dot{\mathbf{R}}_{ba})^\vee \end{bmatrix} \\
&= - \begin{bmatrix} \mathbf{R}_{ba} \mathbf{R}_{ba}^T \dot{\mathbf{p}}_{ba} + (\mathbf{p}_{ba})^\wedge \mathbf{R}_{ba} (\mathbf{R}_{ba}^T \dot{\mathbf{R}}_{ba})^\vee \\ \mathbf{R}_{ba} (\mathbf{R}_{ba}^T \dot{\mathbf{R}}_{ba})^\vee \end{bmatrix} \\
&= - \begin{bmatrix} \dot{\mathbf{p}}_{ba} + \mathbf{R}_{ba} (\mathbf{R}_{ba}^T \mathbf{p}_{ba})^\wedge (\mathbf{R}_{ba}^T \dot{\mathbf{R}}_{ba})^\vee \\ (\mathbf{R}_{ba} (\mathbf{R}_{ba}^T \dot{\mathbf{R}}_{ba}) \mathbf{R}_{ba}^T)^\vee \end{bmatrix} \\
&= - \begin{bmatrix} \dot{\mathbf{p}}_{ba} - \dot{\mathbf{R}}_{ba} \mathbf{R}_{ba}^T \mathbf{p}_{ba} \\ (\dot{\mathbf{R}}_{ba} \mathbf{R}_{ba}^T)^\vee \end{bmatrix} \\
&= - \begin{bmatrix} (-\dot{\mathbf{R}}_{ab}^T \mathbf{p}_{ab} - \mathbf{R}_{ab}^T \dot{\mathbf{p}}_{ab}) - \dot{\mathbf{R}}_{ab}^T \mathbf{R}_{ab} (-\mathbf{R}_{ab}^T \mathbf{p}_{ab}) \\ (\dot{\mathbf{R}}_{ab}^T \mathbf{R}_{ab})^\vee \end{bmatrix} \\
&= \begin{bmatrix} \mathbf{R}_{ab}^T \dot{\mathbf{p}}_{ba} \\ (\mathbf{R}_{ab}^T \dot{\mathbf{R}}_{ab})^\vee \end{bmatrix} \\
&= \mathbf{V}_{ab}^b,
\end{aligned}$$

and thus the first part is also proven by combining this with the definition of  $\mathbf{Ad}_{g_{ba}}$ ,

$$\mathbf{V}_{ba}^s = \mathbf{Ad}_{g_{ba}} \mathbf{V}_{ba}^b = -\mathbf{V}_{ab}^b.$$

#### 4.4.7 Values for RHex

Based on the specification of Section 4.2.1.

From Section 4.1.3, the point contacts with friction at the toes implies a projection  $\pi_{c_k} := \pi$  down to the linear components,  $x$  and  $z$ , which thus leads to a planar wrench basis of,

$$\mathbf{B}_{c_k} := \begin{bmatrix} 1 & 0 \\ 0 & 1 \\ 0 & 0 \end{bmatrix}, \quad k \in 1, 2, \quad (75)$$

corresponding to tangential and normal forces in the contact frame. The corresponding friction cone (7) is (where recall that  $\mathcal{C}_k$  is defined with the  $\mathbf{z}$  axis pointing into the ground),

$$\mathbf{U}_k \lambda_{c_k} := \begin{bmatrix} \pm 1 & \mu_k \\ 0 & -1 \end{bmatrix} \begin{bmatrix} \lambda_{kt} \\ \lambda_{kn} \end{bmatrix} \geq 0, \quad k \in 1, 2, \quad (76)$$

where the sign of the coefficient on the tangent components is selected to be the opposite of the sign of  $\lambda_t$ , or alternatively both signs may be included in separate rows, and  $\mu_k$  is the usual static friction coefficient.

When the body contacts the ground, the sliding contact implies a projection  $\pi_{c_k} := \pi_z$  down to only the normal component,  $z$ , and thus has a wrench basis of,

$$\mathbf{B}_{b_k} := \begin{bmatrix} 0 \\ 1 \\ 0 \end{bmatrix}, \quad k \in 3, 4, \quad (77)$$

and the friction cone is,

$$\mathbf{U}_k \lambda_{c_k} := \begin{bmatrix} -1 \end{bmatrix} \begin{bmatrix} \lambda_{kn} \end{bmatrix} \geq 0, \quad k \in 3, 4. \quad (78)$$

The combined  $\mathbf{U}$  for all  $k$  contacts is then defined as (7),

$$\mathbf{U}\boldsymbol{\lambda} := \begin{bmatrix} \mathbf{U}_1 & 0 & 0 \\ 0 & \ddots & 0 \\ 0 & 0 & \mathbf{U}_k \end{bmatrix} \begin{bmatrix} \lambda_{c_1} \\ \vdots \\ \lambda_{c_k} \end{bmatrix} \geq 0. \quad (79)$$

From Section 4.1.4, the active components  $\mathbf{a}_k$  of the base kinematic constraint are shown in (41)–(43), which combine to form  $\mathbf{a}$  in each contact mode,

$$\mathbf{a} := \begin{bmatrix} \mathbf{a}_1 \\ \vdots \\ \mathbf{a}_k \end{bmatrix}. \quad (80)$$

From Section 4.1.5, the component of the self-manipulation grasp map for each toe contact ( $0 \leq \theta_k - \phi < \pi, k \in 1, 2$ ) is thus,

$$\mathbf{G}_{s,k} = \begin{bmatrix} -\cos \phi & \sin \phi \\ -\sin \phi & -\cos \phi \\ \ell_k \sin \phi - \rho_k \cos(\theta_k - \phi) & \ell_k \cos \phi - \rho_k \sin(\theta_k - \phi) \end{bmatrix}, \quad (81)$$

while the component of the grasp map for rolling contact ( $-\pi < \theta_k - \phi < 0, k \in 1, 2$ ) is,

$$\mathbf{G}_{s,k} = \begin{bmatrix} -\cos \phi & \sin \phi \\ -\sin \phi & -\cos \phi \\ \ell_k \sin \phi - \frac{\rho_k}{2} (1 + \cos(\theta_k - \phi)) & \ell_k \cos \phi - \frac{\rho_k}{2} \sin(\theta_k - \phi) \end{bmatrix}. \quad (82)$$

The component of the grasp map for each body contact  $k \in 3, 4$  is thus,

$$\mathbf{G}_{s,k} = \begin{bmatrix} \sin \phi \\ -\cos \phi \\ \ell_k \cos \phi \end{bmatrix}. \quad (83)$$

A complete grasp map is then the concatenation of all active components (14),

$$\mathbf{G}_s := [ \mathbf{G}_{s,1} \quad \dots \quad \mathbf{G}_{s,k} ]. \quad (84)$$



The hand Jacobian for legs in toe contact ( $0 < \theta_k - \phi < \pi, k \in 1, 2$ ) is thus,

$$\mathbf{J}_{h,k} = \begin{bmatrix} -\rho_k \cos(\theta_k - \phi) \\ -\rho_k \sin(\theta_k - \phi) \end{bmatrix}, \quad (85)$$

while the hand Jacobian for rolling contact ( $-\pi < \theta_k - \phi < 0, k \in 1, 2$ ),

$$\mathbf{J}_{h,k} = \begin{bmatrix} -\frac{\rho_k}{2} (1 + \cos(\theta_k - \phi)) \\ -\frac{\rho_k}{2} \sin(\theta_k - \phi) \end{bmatrix}, \quad (86)$$

and the hand Jacobian is zero for  $k \in 3, 4$ . A complete hand Jacobian is then a block diagonal of all active components,

$$\mathbf{J}_h := \begin{bmatrix} \mathbf{J}_{h,1} & 0 & 0 \\ 0 & \ddots & 0 \\ 0 & 0 & \mathbf{J}_{h,k} \end{bmatrix}. \quad (87)$$

The combined velocity constraint matrix  $\mathbf{A}$  for each contact mode is defined from these components (17). For example the combined constraint  $\mathbf{A}$  in the mode shown in Fig. 4.2 (front leg rolling, rear leg toe contact, no body contact) is,

$$\mathbf{A} = [-\mathbf{J}_h \quad \mathbf{G}_s^T \mathbf{R}_{pw}^T] = \begin{bmatrix} \frac{\rho_1}{2} (1 + \cos(\theta_1 - \phi)) & 0 & -1 & 0 & \ell_1 \sin \phi - \frac{\rho_1}{2} (1 + \cos(\theta_1 - \phi)) \\ \frac{\rho_1}{2} \sin(\theta_1 - \phi) & 0 & 0 & -1 & \ell_1 \cos \phi - \frac{\rho_1}{2} \sin(\theta_1 - \phi) \\ 0 & \rho_2 \cos(\theta_2 - \phi) & -1 & 0 & -\ell_2 \sin \phi - \rho_2 \cos(\theta_2 - \phi) \\ 0 & \rho_2 \sin(\theta_2 - \phi) & 0 & -1 & -\ell_2 \cos \phi - \rho_2 \sin(\theta_2 - \phi) \end{bmatrix}.$$

From Section 4.1.7 and 4.1.8, see examples worked out in Section 4.3.

From Section 4.1.9, the combined mass matrix (26) and Coriolis matrix (30) are shown in Fig. 4.14. Recall that these are the same in every contact state.

However when assuming massless legs,  $\overline{\mathbf{M}}$  is much simpler,

$$\bar{\mathbf{M}}_{massless} = \begin{bmatrix} 0 & 0 & 0 & 0 & 0 \\ 0 & 0 & 0 & 0 & 0 \\ 0 & 0 & m_b & 0 & 0 \\ 0 & 0 & 0 & m_b & 0 \\ 0 & 0 & 0 & 0 & I_b \end{bmatrix}, \quad (88)$$

and  $\bar{\mathbf{C}}_{massless}$  is all zeros.

The potential energy is (recall that  $z$  points “down”),

$$V = -m_b g z, \quad (89)$$

and thus the nonlinear forces (gravity) are,

$$\bar{\mathbf{N}} = \begin{bmatrix} 0 \\ 0 \\ 0 \\ -m_b g \\ 0 \end{bmatrix}, \quad (90)$$

while the body wrench due to gravity is (recall that the body wrench is the negative of the object wrench),

$$\mathbf{F}_g = -\mathbf{R}_{wp}^T \bar{\mathbf{N}}_o = \begin{bmatrix} -m_b g \sin \phi \\ m_b g \cos \phi \\ 0 \end{bmatrix}. \quad (91)$$

The applied force is,

$$\Upsilon = \begin{bmatrix} \tau_1 \\ \tau_2 \\ 0 \\ 0 \\ 0 \end{bmatrix}. \quad (92)$$

From Section 4.1.10, the constituent matrices are different in each contact mode and parameterization of the closed-loop parameter, but can be derived from (75)–(92).

## Chapter 5

# Impulses and Hybrid Systems

Simple models of complex robot-world interactions are key to understanding and generalizing observed behaviors [52] and reasoning about the composition of their constituents to generate new ones. Many of these simplifications are known to be only coarse approximations to the true physical processes, but still have significant value. Beyond their clarity, generalizability, and analytical tractability, they can provide qualitatively correct predictions for the behavior of real physical systems, such as the simulated leaping behavior depicted in Figure 5.1 that recreates the empirical results of Chapter 3 at a coarse level<sup>1</sup>. In this chapter we will combine several commonly-used simplifications into a consistent mathematical model suitable for analysis.

While the primary goal of this thesis is not numerical analysis, simulation does provide a useful way to visualize key features of the model and the utility of some of the simplifying assumptions. Numerical results obtained through a custom Mathematica<sup>2</sup> simulation will be used to illustrate key concepts, as in Figure 5.1. Of course, the relevance of the modeling choices proposed can only be established by the breadth of physical phenomena they usefully approximate, regardless of the simplification and ease of analysis they afford.

---

<sup>1</sup>For this simulation the middle and rear legs are used with a maximum current limit of 20A, a pseudo-impulse magnitude of  $\delta_t = 0.03$  (hand selected to give the qualitatively best overall results), relative leg timing of  $t_2 = 0.01$  (i.e. the middle legs are started 0.01s before the rear legs), and once a leg has lifted off the ground it is slowly rotated upwards out of the way. Remaining model parameters are as listed in Sections 4.2 and 4.4.7.

<sup>2</sup>Wolfram Mathematica 9, <http://www.wolfram.com/mathematica/>. Numerical integration uses the `NDSolve` command, event detection uses the `WhenEvent` command.

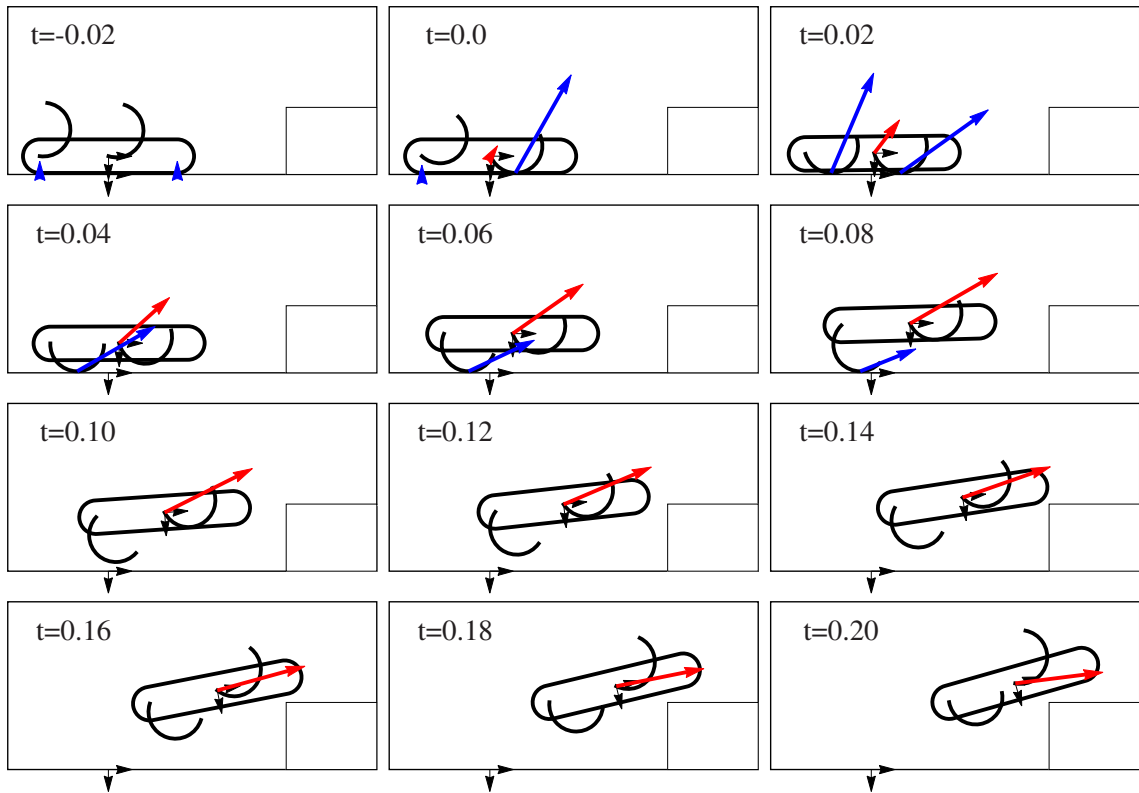


Figure 5.1: Keyframes from RHex simulation leaping onto a 20cm ledge. Blue arrows show contact forces (relative scale  $10N = 1cm$ ) while the red arrow shows body velocity (relative scale  $10cm/s = 1cm$ ).

$\mathbf{A} : T\mathcal{Q} \rightarrow T\mathcal{C}$	Velocity constraint function (5.1.1)
$\mathbf{A}^\dagger : T^*\mathcal{Q} \rightarrow T^*\mathcal{C}$	Force constraint function (2)
$\mathcal{D} = \coprod_{J \in \mathcal{J}} D_J$	Hybrid system domains (Def. 5.1)
$\mathcal{F} : \mathcal{D} \rightarrow T\mathcal{D}, F_J = \mathcal{F} _{D_J}$	Vector field (Def. 5.1)
$\mathcal{G} = \coprod_{(I,J) \in \Gamma} G_{I,J}, G_{I,J} \subset D_I$	Guard set (Def. 5.1)
$\mathcal{H} := (\mathcal{J}, \Gamma, \mathcal{D}, \mathcal{F}, \mathcal{G}, \mathcal{R})$	Hybrid dynamical system (Def. 5.1)
$i, j, k \in K \subseteq \mathcal{K}$	Contact constraints (5.1)
$I, J, K \in \mathcal{J} \subset \mathbb{N}$	Discrete states and their indexing set (5.1)
$\mathcal{J} \subset \mathbb{N}$	Discrete indexing set (Def. 5.1)
$\overline{\mathbf{M}} : T^2\mathcal{Q} \rightarrow T^*\mathcal{Q}$	Inertia tensor (5.1.1)
$\overline{\mathbf{M}}^\dagger : T^*\mathcal{Q} \rightarrow T^2\mathcal{Q}$	Constrained inverse inertia tensor (2)
$\mathbf{P}_{\mathbf{q}} \in T^*\mathcal{Q}, \mathbf{P}_\lambda, \mathbf{P}_\delta \in T^*\mathcal{C}$	Impulses (5.1.2, 10, 39)
$\mathbf{q} \in \mathcal{Q} := \Theta \times SE(d)$	Continuous state (5.1)
$\mathbf{T}\mathbf{q} \in T\mathcal{Q}$	Continuous state and velocity (5.1)
$\mathcal{R} : \mathcal{G} \rightarrow \mathcal{D}, R_{I,J} = \mathcal{R} _{G_{I,J}}$	Reset map (Def. 5.1)
$\mathbf{U} : T^*\mathcal{C} \rightarrow \mathbb{R}^k$	Unilateral constraint cone (5.1)
$\Gamma \subset \mathcal{J} \times \mathcal{J}$	Set of discrete transitions (Def. 5.1)
$\delta_i \in \mathbb{R}^+$	Small time duration of impact (39)
$\Delta \dot{\mathbf{q}} \in T^2\mathcal{Q}$	Instantaneous change in velocity (5.1.2)
$\lambda \in T^*\mathcal{C}$	Lagrange multipliers (constraint forces) (5.1.1)
$\Lambda : T^2\mathcal{C} \rightarrow T^*\mathcal{C}$	Constrained contact inertia tensor (2)
$\preceq, \succeq, \equiv$	Trending negative/positive (Def. 5.4)

Table 5.1: Key symbols used throughout this chapter, in addition to Table 4.1, with section, equation, or definition of introduction marked.

## 5.1 Dynamics

The continuous Lagrangian dynamics of self-manipulation is specified in Chapter 4 using the notation and terminology of [134], and we continue to work within that framework here. However the impulsive dynamics (instantaneous changes in velocity when a new contact is added) were not specified in either, and so we will briefly describe them here. In addition this section will make explicit how the massless leg and frictional assumptions made in Chapter 4 affect both the continuous time and impulsive dynamics, leading to a formulation that is different but, as we will show, equivalent to the usual formulation when there are no massless links. Finally this section introduces a new pseudo-impulse that eliminates certain Zeno executions and related chattering behavior.

The notation used in this chapter was chosen to be consistent with Chapter 4 (in particular

Table 4.1 and agreeing where possible with [134]) or will be defined as it is used and summarized in Table 5.1. The base component of the state is denoted,  $\mathbf{q}$ , while the full state is,  $\mathbf{Tq} := (\dot{\mathbf{q}}, \mathbf{q})$ , and this state completely describes the motion of interest, as,

*Assumption 5.1 (Rigid Bodies).* The robot is made up of a finite number of rigid bodies and therefore its configuration can be described by some set of coordinates  $\mathbf{q}$ .

We are concerned with sets of constraints  $I, J, K$  whose individual elements  $i, j, k$ , comprise the possible contact constraints (Chapter 4.1.3, [134, Sec. 5.2.1]), both in the *normal* (non-penetrating — algebraically the span of the  $i^{\text{th}}$  row of the array  $\mathbf{A}_k$  which is the tangent map arising from the  $i^{\text{th}}$  constraint) or *tangential* (non-sliding — algebraically, the orthogonal complement of that same  $i^{\text{th}}$  row) directions (denoted with a subscript  $n$  or  $t$ , respectively). It is well established that the motion of mutually constrained rigid bodies can be effectively modeled using polynomial maps [175], hence imposing contact constraints arising from their interaction with the piecewise polynomial representations of the environment (commonly adopted by the sensory community [104]) leads to,

*Assumption 5.2 (Semialgebraic).* The set of free configurations can be represented as a semialgebraic set.

With respect to the strata of this model of space, the persistence of contact is merely a further assumption,

*Assumption 5.3 (Persistent Contact).* The robot is in contact with the world at some finite number of points  $K \subset \mathcal{K}$ , and that contact in general persists for some non-zero amount of time.

The impact problem can be summarized as determining which constraints to add or remove from the active set. The active set continues to constrain the system so long as the unilateral constraint cone (Section 4.1.3) is positive,  $\mathbf{U}(\lambda) \geq 0$ , where  $\lambda \in T^*\mathcal{C}$  is the vector of Lagrange multipliers (constraint forces, Section 4.1.9). Included in  $\mathbf{U}$  is both the non-attachment condition that normal direction forces are positive as well as the friction cone that relates the magnitude of the normal and tangential components.

### 5.1.1 Massless Considerations

Massless appendages will be allowed here only in a limited form,

*Assumption 5.4* (Massless Limbs). The rank deficiencies of the inertia tensor  $\bar{\mathbf{M}}$  (Section 4.1.9) must be “corrected” by constraints sufficient to guarantee that any remaining allowed physical movement excites some associated kinetic energy.

This condition admits its most physically straightforward expression via the requirement that the inertia tensor is nonsingular when written with respect to generalized coordinates (i.e., any local chart arising from an implicit function solution to the constraint equation (Section 4.1.4). However, for purposes of this chapter, we find it more useful to work with the Lagrange-d’Alembert formulation of the constrained dynamics (Section 4.1.9) hence, we translate that natural assumption into more formal algebraic terms governing the relationship between the lifted (velocity) constraints,  $\mathbf{A}$  (Section 4.1.5), and the overall inertia tensor  $\bar{\mathbf{M}}$  as follows,

**Lemma 5.1.** *The matrix  $\begin{bmatrix} \bar{\mathbf{M}} & \mathbf{A}^T \\ \mathbf{A} & \mathbf{0} \end{bmatrix}$  (as used in Section 4.1.9) is invertible if and only if the inertia tensor expressed in generalized coordinates,  $\tilde{\mathbf{M}}$  (Section 4.1.10), is invertible (Assumption A.4 of Section 4.1.11).*

as shown in [85].

One common set of circumstances that satisfy this requirement arises when only the robot’s most distal link (the lower leg, foot, or in the case of RHex, the entire leg) is massless and the motion of its most distal point is completely constrained when it is on the ground. Although the rank requirement is not limited to this setting, it represents the immediate motivation for our present inquiry<sup>3</sup>.

Consider a parametrized family of singular semi-Riemannian metrics,

$$\bar{\mathbf{M}}_{\epsilon}(\mathbf{q}) : \mathcal{Q} \times [0, \bar{\epsilon}] \rightarrow \mathbb{R}^{q \times q} \tag{1}$$

---

<sup>3</sup> Of course, any such massless links or limbs must then be removed from consideration as mechanical degrees-of-freedom: since they are massless, when unconstrained, the associated joints can be considered to have arbitrary configuration. Alternately, they may be governed by other dynamics that evolve at a much faster timescale than the massive body segments.

such that  $\overline{\mathbf{M}}_0(\mathbf{q}) := \overline{\mathbf{M}}$  is the (possibly) degenerate inertia tensor for the system (Section 4.1.9) and may be singular, while  $\varepsilon$  assigns a small mass and inertia to any putatively massless links such that  $\overline{\mathbf{M}}_\varepsilon(\mathbf{q})$  is full-rank for all  $\varepsilon > 0$  (for our present purposes, it is sufficient to use a generic limiting model such as  $\overline{\mathbf{M}}_\varepsilon := \overline{\mathbf{M}}_0 + \varepsilon \mathbf{I} \mathbf{d}_q$  rather than some more specific physically motivated one). The dynamics of the system can be expressed using the inverse of the following block matrix containing  $\overline{\mathbf{M}}_\varepsilon$ ,

$$\begin{bmatrix} \overline{\mathbf{M}}^\dagger & \mathbf{A}^{\dagger T} \\ \mathbf{A}^\dagger & \Lambda \end{bmatrix} := \lim_{\varepsilon \rightarrow 0} \left( \begin{bmatrix} \overline{\mathbf{M}}_\varepsilon & \mathbf{A}^T \\ \mathbf{A} & 0 \end{bmatrix} \right)^{-1} = \left( \lim_{\varepsilon \rightarrow 0} \begin{bmatrix} \overline{\mathbf{M}}_\varepsilon & \mathbf{A}^T \\ \mathbf{A} & 0 \end{bmatrix} \right)^{-1} = \begin{bmatrix} \overline{\mathbf{M}}_0 & \mathbf{A}^T \\ \mathbf{A} & 0 \end{bmatrix}^{-1} \quad (2)$$

where  $\overline{\mathbf{M}}_\varepsilon, \overline{\mathbf{M}}^\dagger, \Lambda$  are symmetric positive semi-definite matrices ( $\Lambda$  is positive-definite). According to the assumptions yielding Lemma 5.1, this  $\varepsilon$ -parametrized curve always takes its image in  $GL(n)$  (the group of invertible matrices over  $\mathbb{R}^n$ ) within which matrix inversion is a continuous operation, hence the limit commutes with the inverse operation, and  $\overline{\mathbf{M}}_\varepsilon^\dagger$  is a well defined smooth curve defined over all  $\varepsilon \in [0, \bar{\varepsilon}]$ .

The dynamics in this massless case will rely heavily on  $\mathbf{A}^\dagger : T^*Q \rightarrow T^*C$  that maps forces in configuration coordinates to forces in contact coordinates<sup>4</sup>.

With this notation, the continuous-time dynamics of Section 4.1.9 can be expressed as

$$\ddot{\mathbf{q}} = \overline{\mathbf{M}}^\dagger (\Upsilon - \overline{\mathbf{C}}\dot{\mathbf{q}} - \overline{\mathbf{N}}) - \mathbf{A}^{\dagger T} \dot{\mathbf{A}}\dot{\mathbf{q}} \quad (3)$$

$$\lambda = \mathbf{A}^\dagger (\Upsilon - \overline{\mathbf{C}}\dot{\mathbf{q}} - \overline{\mathbf{N}}) - \Lambda \dot{\mathbf{A}}\dot{\mathbf{q}} \quad (4)$$

where  $\Upsilon$  is the applied forces,  $\overline{\mathbf{C}}$  is the centripetal and Coriolis forces, and  $\overline{\mathbf{N}}$  is the nonlinear and gravitational forces.

When  $\overline{\mathbf{M}}_\varepsilon$  is invertible (and, possibly, even for  $\varepsilon = 0$ ), it is easy to verify the equivalences,

---

<sup>4</sup>Note that (40) of Section 4.1.10 used the notation  $\mathbf{A}^*$  while in this chapter we will use  $\mathbf{A}^\dagger$  to signify the slight difference in definition used here, and to avoid confusion with the pullback of  $\mathbf{A}$ , usually noted as  $\mathbf{A}^*$ , but which happens to be  $\mathbf{A}^{\dagger T}$ .

$$\bar{\mathbf{M}}^\dagger = \bar{\mathbf{M}}^{-1} - \bar{\mathbf{M}}^{-1} \mathbf{A}^T (\mathbf{A} \bar{\mathbf{M}}^{-1} \mathbf{A}^T)^{-1} \mathbf{A} \bar{\mathbf{M}}^{-1} \quad (5)$$

$$\mathbf{A}^\dagger T = \bar{\mathbf{M}}^{-1} \mathbf{A}^T (\mathbf{A} \bar{\mathbf{M}}^{-1} \mathbf{A}^T)^{-1} \quad (6)$$

$$\Lambda = -(\mathbf{A} \bar{\mathbf{M}}^{-1} \mathbf{A}^T)^{-1} \quad (7)$$

as shown in Section 5.3.1.

**Lemma 5.2.** *When  $\bar{\mathbf{M}}_0 = \bar{\mathbf{M}}$  is invertible, the dynamics (3) and (4) are equivalent to the more common expression (as stated e.g. in the last equations of Section 4.4.4, or [134, Eqn. 6.5, 6.6]),*

$$\ddot{\mathbf{q}} = \bar{\mathbf{M}}^{-1} (\Upsilon - \bar{\mathbf{C}}\dot{\mathbf{q}} - \bar{\mathbf{N}} - \mathbf{A}^T \lambda), \quad (8)$$

$$\lambda = (\mathbf{A} \bar{\mathbf{M}}^{-1} \mathbf{A}^T)^{-1} (\mathbf{A} \bar{\mathbf{M}}^{-1} (\Upsilon - \bar{\mathbf{C}}\dot{\mathbf{q}} - \bar{\mathbf{N}}) + \dot{\mathbf{A}}\dot{\mathbf{q}}). \quad (9)$$

The claim follows directly from substituting (5)–(7), the explicit solution to (2) when  $\bar{\mathbf{M}}$  is invertible, into (3)–(4), as worked out in Section 5.3.3.

In order to avoid infinite cycling of adding and removing a contact point in a finite amount of time (Zeno), an upper bound on all accelerations (even for massless limbs) must be assumed. Without such a bound, a massless leg that has just separated could accelerate instantly to re-impact the ground.

Though there are no truly massless limbs, computing the dynamics using (3)–(4) is numerically more stable than inverting  $\bar{\mathbf{M}}_\varepsilon$  in the presence of large disparities in limb segment masses [72, Sec. 4.3]. Figure 5.2 shows the condition number for the RHex model<sup>5</sup> (ratio of largest to smallest singular values) for both  $\bar{\mathbf{M}}_\varepsilon$  and the combined matrix inverted in (2). In this case the leg mass and inertia are scaled with  $\varepsilon$  (i.e.  $m_l = \varepsilon$ ,  $I_l = 0.007\varepsilon$ ). At the actual value of  $m_l$  reported in Table 4.2, the condition number of  $\bar{\mathbf{M}}_\varepsilon$  is more than an order of magnitude larger than that of the matrix in (2) (4483 vs. 269).

<sup>5</sup>Here calculated at a “typical” position, with both legs resting on the ground ( $\theta_1 = -1.75$ ,  $\theta_2 = -1.9$ ).

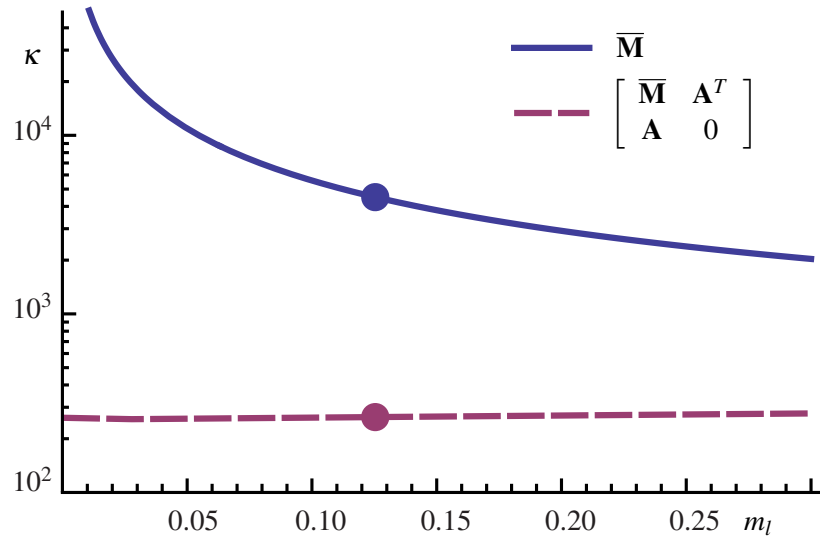


Figure 5.2: Condition number  $\kappa$  over various values of the leg mass  $m_l = \varepsilon$ , with the actual value of  $m_l = 0.126\text{kg}$  marked.

### 5.1.2 Impact Map

At impact into contact mode  $J$ , any incoming constraint velocity  $\mathbf{A}_J \dot{\mathbf{q}}$  must be eliminated. Here, we assume a Newtonian impact law, that is,

*Assumption 5.5* (Plastic Impact). Impacts occur instantaneously and their effect is described by an algebraic equation. Furthermore for the plastic impacts of this chapter, that relationship takes the form of a mass-weighted projection into the constrained domain.

Thus consider  $\Delta \dot{\mathbf{q}} := \dot{\mathbf{q}}^+ - \dot{\mathbf{q}}^-$  be the instantaneous change in velocity,  $\Delta \dot{\mathbf{q}} = -(1 + \varepsilon) \mathbf{A}_J^{\dagger T} \mathbf{A}_J \dot{\mathbf{q}}^-$  (recall that  $\mathbf{A}^{\dagger T} : TC \rightarrow TQ$  maps contact velocities to configuration velocities). The coefficient of restitution,  $\varepsilon$ , is defined in the usual way, however throughout this thesis plastic impact ( $\varepsilon = 0$ ) is assumed. The *body impulse* in configuration coordinates is  $\mathbf{P}_q := -\bar{\mathbf{M}} \Delta \dot{\mathbf{q}}$ . The *contact impulse* (i.e. the impulse at the contact points that induces the desired change in velocity to agree with the new constraint set  $J$ ) is,

$$\mathbf{P}_{\lambda, J} := \mathbf{A}_J^{\dagger} \mathbf{P}_q = \mathbf{A}_J^{\dagger} \bar{\mathbf{M}} \mathbf{A}_J^{\dagger T} \mathbf{A}_J \dot{\mathbf{q}}^- = -\Lambda_J \mathbf{A}_J \dot{\mathbf{q}}^- \quad (10)$$

where recall that  $\mathbf{A}_J$ ,  $\mathbf{A}_J^\dagger$ ,  $\bar{\mathbf{M}}$ , and  $\Lambda_J$  are parameterized by the state  $\mathbf{q}$  (which does not change during impact, i.e.  $\mathbf{q}^+ = \mathbf{q}^-$ ), and the impulses,  $\mathbf{P}_{\lambda,J}$  and  $\mathbf{P}_{\mathbf{q}}$ , are parameterized by both the state and the incoming velocity,  $\dot{\mathbf{q}}^-$ .

**Lemma 5.3.** *When  $\bar{\mathbf{M}}$  is invertible, contact impulse (10) into contact mode  $J$  is equivalent to the non-degenerate plastic impact law,*

$$\mathbf{P}_\lambda = (\mathbf{A}_J \bar{\mathbf{M}}^{-1} \mathbf{A}_J^T)^{-1} \mathbf{A}_J \dot{\mathbf{q}}^- \quad (11)$$

as listed e.g. in [35, Eqn. 3].

As with the proof of Lemma 5.2, the result may be seen by substituting (6) or (7), the explicit solution to (2) when  $\bar{\mathbf{M}}$  is invertible, into (10), as worked out in Section 5.3.4.

### 5.1.3 Complementarity

We now introduce and reformulate for the massless setting the classical complementarity problem for forces and impulses at the contact points. A general statement of the complementarity problem (c.f. [42, 80]) is to find some indexed array of variables,  $\mathbf{x}$  and  $\mathbf{y}$ , such that

$$\mathbf{x} \geq 0, \quad \mathbf{y} \geq 0, \quad \mathbf{x}^T \mathbf{y} = 0, \quad (12)$$

(where for a vector  $\mathbf{x}$ ,  $\mathbf{x} \geq 0 \Rightarrow \mathbf{x}_i \geq 0 \forall i$ ) subject to some problem constraints — in the linear complementarity problem,  $\mathbf{y} := \mathbf{A}\mathbf{x} + \mathbf{c}$ . Solutions to this problem produce a natural partition on the index set  $\mathcal{K}$ , where let  $J = \{j \in \mathcal{K} : x_j > 0\}$  and  $J^c = \{j \in \mathcal{K} : x_j = 0\}$ . Here we will use physical laws to determine the variables  $\mathbf{x}$  and  $\mathbf{y}$  based on the outgoing bipartition  $(J, J^c)$  and the incoming state,  $\mathbf{T}\mathbf{q}^- = (\mathbf{q}^-, \dot{\mathbf{q}}^-)$ . Therefore the complementarity problem is reduced to only finding the unknown partition  $(J, J^c)$ . Given two functions that map partition  $J \in 2^{\mathcal{K}}$  and state  $\mathbf{T}\mathbf{q} \in T\mathcal{Q}$  into a Euclidian space with dimension equal to the size of the index set  $\mathcal{K}$ ,  $Y, Z : 2^{\mathcal{K}} \times T\mathcal{Q} \rightarrow \mathbb{R}^{|\mathcal{K}|}$ , we will assume the existence of a complementarity function  $CP$ ,

$$CP_{Y,Z} : TQ \rightarrow 2^{\mathcal{K}}, \quad (13)$$

$$CP_{Y,Z}(\mathbf{Tq}^-) = J, \quad (14)$$

with the properties that,

$$Y_j(J, \mathbf{Tq}^-) > 0, \quad Z_j(J, \mathbf{Tq}^-) = 0, \quad \forall j \in J, \quad (15)$$

$$Y_k(J, \mathbf{Tq}^-) = 0, \quad Z_k(J, \mathbf{Tq}^-) \geq 0, \quad \forall k \notin J. \quad (16)$$

where the equality constraints are often written as  $Y_k(J, \mathbf{Tq}^-)Z_j(J, \mathbf{Tq}^-) = 0$  [19, Eqn. 9], [112, Eqn. 2.10b]. Existence and uniqueness of a solution  $J$  will in the most general cases have to be an additional assumption (see Assumption 5.6 and 5.7, below), although for the specific complementarity problems in this section (i.e. based on the relationship of the specific functions  $Y$  and  $Z$  used in these cases), in the absence of friction, existence and uniqueness has been proven in e.g. [172, Ex. 3.3].

There are two complementarity conditions that are often considered in rigid body dynamics: force–acceleration (there cannot be both a continuous time contact force and a separation acceleration at the same contact point) and impulse–velocity (there cannot be both an impact-induced contact impulse and a separation velocity at the same contact point), see Section 1.2.3 for motivation and related work. With possibly massless limbs, the concept of a separation velocity or acceleration is poorly defined as once it has lifted off the ground the joints in question must be dropped from the state. Theorems 5.5–5.6 re-work both notions of complementarity to be compatible with massless limbs and prove that they agree with the traditional statements when the separation velocity or acceleration is well defined.

In the complementarity problems, the following definition simplifies the statements about the invariance of high order contact that seem to arise unavoidably (as stated in [172, Sec. 3], [71, Sec. 1], formalizing the concepts represented in e.g. [48, Fig. 11.4], [162, Sec. 27.2])

**Definition 5.4.** Given a smooth function  $h : M \rightarrow \mathbb{R}$ , a point  $x \in M$ , and a smooth vector field  $F : M \rightarrow TM$ , we say that  $h$  is *trending negative* with respect to the vector field  $F$  at  $x$ , denoted  $h(x) \preceq_F 0$ , (or  $h(x) \preceq 0$  if the context specifies  $F$ ), if,

$$(h(x) < 0) \vee \left( (h(x) = 0) \wedge \left( \exists m > 0 : (\mathcal{L}_F^m h)(x) < 0 \wedge \forall \ell < m : (\mathcal{L}_F^\ell h)(x) = 0 \right) \right) \quad (17)$$

(here  $\mathcal{L}_F h : M \rightarrow \mathbb{R}$  is the Lie derivative of  $h$  with respect to the vector field  $F$ , c.f. [105, Ch. 9]). Similarly, we say that  $h$  is *trending positive* at  $x$ , denoted  $h(x) \succeq 0$ , when  $-h(x) \preceq 0$ . Finally, we say that  $h$  is *trending zero* at  $x$ , denoted  $h(x) \equiv 0$ , when  $\forall \ell \in \mathbb{N} : (\mathcal{L}_F^\ell h)(x) = 0$ .

That is,  $h(x) \preceq 0$  if and only if the following vector,

$$[h(x), (\mathcal{L}_F h)(x), (\mathcal{L}_F^2 h)(x), \dots] \quad (18)$$

is lexicographically smaller than zero [12, Def. 3.5]. Note that the closure of  $\{x : h(x) \preceq 0\}$  is simply  $\{x : h(x) \leq 0\}$  (as  $\{x : h(x) < 0\} \subset \{x : h(x) \preceq 0\} \subset \{x : h(x) \leq 0\}$  for any vector field), and similarly the closure of the set  $\{x : h(x) \succeq 0\}$  is simply  $\{x : h(x) \geq 0\}$ .

### Force–Acceleration Complementarity

For continuous time contact forces, with  $\mathbf{P} = 0$ , when one or more contact constraints violate the unilateral constraint cone<sup>6</sup>  $\mathbf{U}$ , some constraint will lift off and must be removed from the active constraint set. This sets up a complementarity problem between the unilateral constraint cone,  $\mathbf{U}_k(\lambda)$ , if the contact is kept, and the separation acceleration  $\frac{d}{dt} \mathbf{A}_k \dot{\mathbf{q}} = \mathbf{A}_k \ddot{\mathbf{q}} + \dot{\mathbf{A}}_k \dot{\mathbf{q}}$  if it is removed (recall that as an active constraint the state velocity is initially  $\mathbf{A}_k \dot{\mathbf{q}} = 0$ ). For transition from state  $I$  to  $J$ , consider contact force (29) both in  $J$  but also in the alternative state  $K = J \cup \{k\}$  where contact  $k$  is maintained,

$$\mathbf{U}_j(\lambda_j) \succeq 0, \mathbf{A}_j \ddot{\mathbf{q}} + \dot{\mathbf{A}}_j \dot{\mathbf{q}} = 0, \quad \forall j \in I \cap J, \quad (19)$$

$$\mathbf{U}_k(\lambda_k) = 0, \mathbf{U}_k(\lambda_k) \preceq 0, \quad \forall k \in I \setminus J, \quad (20)$$

where the equality constraints are maintained by the dynamics on the active constraint set. Note that  $\forall j \notin I, \mathbf{U}_j(\lambda_j) = 0$  by definition and so these constraints do not need to be checked.

<sup>6</sup>Recall that  $\mathbf{U}$  in the normal direction is  $-1$  according to the frame conventions of Chapter 4.

**Theorem 5.5.** *The non-penetrating acceleration condition at a contact  $k$  after liftoff into state  $J$ ,  $\mathbf{A}_k \ddot{\mathbf{q}} + \dot{\mathbf{A}}_k \dot{\mathbf{q}} \geq 0$  (when such an acceleration is well defined), is equivalent to a trending negative contact force  $\mathbf{U}_k(\lambda_K) \preceq 0$  in state  $K := J \cup \{k\}$ , i.e. (19)–(20) are equivalent to the usual formulation,*

$$\mathbf{U}_j(\lambda_j) \succeq 0, \mathbf{A}_j \ddot{\mathbf{q}} + \dot{\mathbf{A}}_j \dot{\mathbf{q}} = 0, \quad \forall j \in I \cap J, \quad (21)$$

$$\mathbf{U}_k(\lambda_k) = 0, \mathbf{A}_k \ddot{\mathbf{q}} + \dot{\mathbf{A}}_k \dot{\mathbf{q}} \geq 0, \quad \forall k \in I \setminus J. \quad (22)$$

*Proof.* Let  $\mathbf{K}$  be the selector for the  $k$ th row, i.e.  $\mathbf{K} := [0, \dots, 0, 1]$ . Then,

$$\mathbf{A}_K = \begin{bmatrix} \mathbf{A}_J \\ \mathbf{A}_k \end{bmatrix}, \quad \mathbf{A}_k = \mathbf{K} \mathbf{A}_K \quad (23)$$

$$\mathbf{U}_k(\lambda_K) = -\mathbf{K} \left( \mathbf{A}_K^\dagger (\Upsilon - \bar{\mathbf{C}} \dot{\mathbf{q}} - \bar{\mathbf{N}}) - \Lambda_K \dot{\mathbf{A}}_K \dot{\mathbf{q}} \right) \quad (24)$$

$$= -\frac{\mathbf{A}_k \bar{\mathbf{M}}_J^\dagger}{\mathbf{A}_k \bar{\mathbf{M}}_J^\dagger \mathbf{A}_k} (\Upsilon - \bar{\mathbf{C}} \dot{\mathbf{q}} - \bar{\mathbf{N}}) - \frac{1}{\mathbf{A}_k \bar{\mathbf{M}}_J^\dagger \mathbf{A}_k^T} \begin{bmatrix} \mathbf{A}_k \mathbf{A}_J^{\dagger T} & -1 \end{bmatrix} \begin{bmatrix} \dot{\mathbf{A}}_J \\ \dot{\mathbf{A}}_k \end{bmatrix} \dot{\mathbf{q}} \quad (25)$$

$$= -\frac{\mathbf{A}_k \bar{\mathbf{M}}_J^\dagger (\Upsilon - \bar{\mathbf{C}} \dot{\mathbf{q}} - \bar{\mathbf{N}}) - \mathbf{A}_k \mathbf{A}_J^{\dagger T} \dot{\mathbf{A}}_J \dot{\mathbf{q}} + \dot{\mathbf{A}}_k \dot{\mathbf{q}}}{\mathbf{A}_k \bar{\mathbf{M}}_J^\dagger \mathbf{A}_k^T} \quad (26)$$

$$\mathbf{A}_k \ddot{\mathbf{q}} + \dot{\mathbf{A}}_k \dot{\mathbf{q}} = \mathbf{A}_k \left( \bar{\mathbf{M}}_J^\dagger (\Upsilon - \bar{\mathbf{C}} \dot{\mathbf{q}} - \bar{\mathbf{N}}) - \mathbf{A}_J^{\dagger T} \dot{\mathbf{A}}_J \dot{\mathbf{q}} \right) + \dot{\mathbf{A}}_k \dot{\mathbf{q}} \quad (27)$$

where the denominator in (26) is positive (see Section 5.3.2 for details on the substitution in (25)). Therefore a positive separation acceleration  $\mathbf{A}_k \ddot{\mathbf{q}} + \dot{\mathbf{A}}_k \dot{\mathbf{q}}$  implies a negative contact force  $\mathbf{U}_k(\lambda_K)$ , and vice-versa.  $\square$

Furthermore, with or without a full rank inertia tensor, we will make the following assumption, *Assumption 5.6* (Force/Acceleration Complementarity). The complementarity problem in (19)–(20) always has a unique solution for self-manipulation systems with frictional properties that follow Assumption 5.9, and that solution correctly captures the behavior of the physical system.

While there has been a long line of literature (c.f. [172, Ex. 3.3]) that proves that this is always true for plastic, frictionless contacts, no result has been found to cover the limited frictional conditions introduced in 5.1.5.

## Impulse–Velocity Complementarity

Impact at one contact location can cause another contact to break, as the contact impulse must obey the unilateral constraint cone  $\mathbf{U}_j(\mathbf{P}_{\lambda,J}) \geq 0 \forall j \in J$  – both that the impulse in the normal direction be positive (non-adhesive) and that the tangential impulse lie in the friction cone [35]. Any contact point that would have violated that requirement must be dropped from the active constraint set.

In addition the post-impact velocity must not allow the removed contact point to leave with a penetrating velocity (i.e. the impulse cannot result in a velocity “into” the surface). However with possibly massless legs a positive separation velocity is always achievable. As an alternative requirement that is based only on impulses<sup>7</sup>, consider the contact impulse (10),  $\mathbf{P}_{\lambda,J}$  (associated with the passage from contact  $I$  to contact  $J$ ), but also the contact impulse  $\mathbf{P}_{\lambda,K}, K := J \cup \{k\}$  (associated with the passage from contact  $I$  to alternative state  $K$  where contact  $k$  is maintained). These impulses, along with the exit velocity,  $\mathbf{A}_J \dot{\mathbf{q}}^+$ , must satisfy,

$$\mathbf{U}_j(\mathbf{P}_{\lambda,J}) \geq 0, \mathbf{A}_j \dot{\mathbf{q}}^+ = 0, \quad \forall j \in J, \quad (28)$$

$$\mathbf{U}_k(\mathbf{P}_{\lambda,J}) = 0, \mathbf{U}_k(\mathbf{P}_{\lambda,K}) < 0, \quad \forall k \in I \setminus J, \quad (29)$$

where the equality constraints are enforced by the impact law (10). Note that  $\forall j \notin I \cap J, \mathbf{U}_j(\mathbf{P}_{\lambda,J}) = 0$  by definition and so these constraints do not need to be checked.

**Theorem 5.6.** *The non-penetrating velocity condition at a contact  $k$  after impact into state  $J$ ,  $\mathbf{A}_k \dot{\mathbf{q}}^+ > 0$  (where such a velocity is well defined), is equivalent to a negative contact force  $\mathbf{U}_k(\mathbf{P}_{\lambda,K}) < 0$  at impact into state  $K := J \cup \{k\}$ , i.e. (28)–(29) are equivalent to the usual formulation,*

$$\mathbf{U}_j(\mathbf{P}_{\lambda,J}) \geq 0, \mathbf{A}_j \dot{\mathbf{q}}^+ = 0, \quad \forall j \in J, \quad (30)$$

$$\mathbf{U}_k(\mathbf{P}_{\lambda,J}) = 0, \mathbf{A}_k \dot{\mathbf{q}}^+ > 0, \quad \forall k \in I \setminus J. \quad (31)$$

*Proof.* For this proof, let  $\mathbf{K}$  be the selector for the  $k$ th row, i.e.  $\mathbf{K} := [0, \dots, 0, 1]$ . Then,

---

<sup>7</sup>Note that this formulation based only on impulses also simplifies the inclusion of the pseudo–impulse condition (40).

$$\mathbf{A}_K = \begin{bmatrix} \mathbf{A}_J \\ \mathbf{A}_k \end{bmatrix}, \quad \mathbf{A}_k = \mathbf{K}\mathbf{A}_K \quad (32)$$

$$\mathbf{U}_k(\mathbf{P}_{\lambda,K}) = \mathbf{K}\Lambda_K\mathbf{A}_K\dot{\mathbf{q}}^- \quad (33)$$

$$= \frac{1}{\mathbf{A}_k\overline{\mathbf{M}}_J^\dagger\mathbf{A}_k^T} \begin{bmatrix} \mathbf{A}_k\mathbf{A}_J^{\dagger T} & \mathbf{1} \end{bmatrix} \begin{bmatrix} \mathbf{A}_J \\ \mathbf{A}_k \end{bmatrix} \dot{\mathbf{q}}^- \quad (34)$$

$$= \frac{\mathbf{A}_k\mathbf{A}_J^{\dagger T}\mathbf{A}_J\dot{\mathbf{q}}^- - \mathbf{A}_k\dot{\mathbf{q}}^-}{\mathbf{A}_k\overline{\mathbf{M}}_J^\dagger\mathbf{A}_k^T}, \quad (35)$$

$$\mathbf{A}_k\dot{\mathbf{q}}^+ = \mathbf{A}_k\dot{\mathbf{q}}^- - \mathbf{A}_k\mathbf{A}_J^{\dagger T}\mathbf{A}_J\dot{\mathbf{q}}^- \quad (36)$$

$$= -\mathbf{U}_k(\mathbf{P}_{\lambda,K}) \left( \mathbf{A}_k\overline{\mathbf{M}}_J^\dagger\mathbf{A}_k^T \right) \quad (37)$$

where parenthetical term in the last line positive (see Section 5.3.2 for details on the substitution in (34)). Therefore a positive separation velocity  $\mathbf{A}_k\dot{\mathbf{q}}^+$  implies a negative impulse  $\mathbf{U}_k(\mathbf{P}_{\lambda,K})$ , and vice-versa.  $\square$

Furthermore, with or without a full rank inertia tensor, we will make the following assumption, *Assumption 5.7* (Impulse/Velocity Complementarity). The complementarity problem in (28)–(29) always has a unique solution for self-manipulation systems with frictional properties that follow Assumption 5.9, and that solution correctly captures the behavior of the physical system.

While there has been a long line of literature (c.f. [112, Eqn. 2.10b]) that proves that this is always true for plastic, frictionless contacts, no result has been found to cover the limited frictional conditions introduced in 5.1.5.

### 5.1.4 Pseudo-Impulse

In this section we define an additional impulse during impact which qualitatively improves results and eliminate some Zeno phenomena. This impulse may be thought of as a tuning parameter and while we give some physical motivation for its magnitude the inclusion of this term is motivated primarily by improving the qualitative behavior of the numerical simulation, e.g. by excluding chattering and Zeno phenomena, as well as the counterintuitive liftoff of a heavy rigid block struck by a small impulse (as discussed in Section 1.2.3). As an additional motivational example, consider

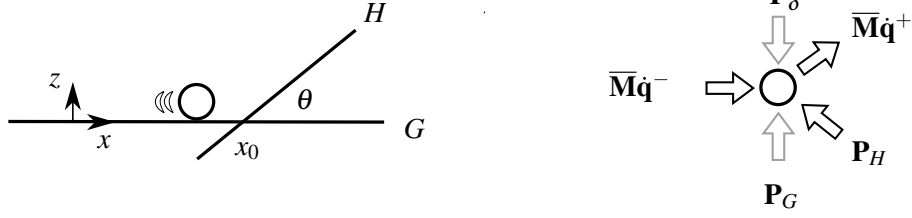


Figure 5.3: *Left:* A point sliding along ground  $G$  approaches hill  $H$ . *Right:* Free body diagram showing impulses at point of contact. Without  $\mathbf{P}_\delta$  no positive impulse from the ground  $\mathbf{P}_G$  is possible for any initial momentum  $\bar{\mathbf{M}}\dot{\mathbf{q}}^-$  and any hill slope  $\theta < 90^\circ$ .

a point sliding on the ground as in Figure 5.3, which hits a hill at some slope  $\theta$ . The contact impulse from the hill  $\mathbf{P}_H$  will cause the particle to break contact with the ground and leave with some velocity sliding up the hill. This is true for any initial velocity, no matter how small, and any  $\theta < 90^\circ$ . With a pseudo-impulse  $\mathbf{P}_\delta$  acting in the direction of gravity, there are initial conditions that result in the point coming to rest with impulses from both the ground and the hill (i.e. all impulses are positive and sum to zero in Figure 5.3). Therefore we will make the following new assumption about the physics of the system,

*Assumption 5.8 (Pseudo-Impulse).* The continuous time forces apply some small amount of work during the impact process.

Specifically, consider the *pseudo-impulse*,  $\mathbf{P}_\delta \in T^*\mathcal{C}$ , that the contact forces would impart on the system for some small time duration,  $\delta_t \in \mathbb{R}^+$ , during impact into state  $J$ ,

$$\bar{\mathbf{M}}\delta_{\mathbf{q}} := \lim_{\delta_t \rightarrow 0} \int_{\delta_t} \bar{\mathbf{M}}\ddot{\mathbf{q}} dt \approx (\Upsilon - \bar{\mathbf{C}}\dot{\mathbf{q}}^- - \bar{\mathbf{N}})\delta_t \quad (38)$$

$$\mathbf{P}_\delta := \mathbf{A}_J^\dagger \bar{\mathbf{M}}\delta_{\mathbf{q}} = \mathbf{A}_J^\dagger (\Upsilon - \bar{\mathbf{C}}\dot{\mathbf{q}}^- - \bar{\mathbf{N}})\delta_t \quad (39)$$

This small time  $\delta_t$  can be regarded as the finite duration of the (actually non-instantaneous) impact process [145]. In the simulations shown in this chapter a magnitude of  $\delta_t = 0.03s$  has been found to give the best results.

The introduction of this pseudo-impulse can be viewed as a *regularization* via the parameter  $\delta_t$  that precludes certain Zeno phenomena. It has the effect of *truncating* the execution when a con-

straint velocity drops below a threshold that scales with  $\delta_t$ . Though analogous to the truncation proposed in [138] for *elastic* impacts, we note that this pseudo-impulse as written only applies to *plastic* impacts, and the threshold is based on the magnitude of the continuous time forces.

This pseudo-impulse is not directly applied to the system (as in [145]), both because in this model impacts occur instantaneously and the velocity displacement  $\delta_{\mathbf{q}}$  would not be uniquely determined by (39) when  $\bar{\mathbf{M}}$  is singular. Instead the pseudo-impulse is used as an extra guard condition during impact,

$$\mathbf{U}(\mathbf{P}_\lambda + \mathbf{P}_\delta) > 0. \quad (40)$$

This is in addition to the usual condition  $\mathbf{U}(\mathbf{P}_\lambda) > 0$  since the pseudo-impulse should not break contacts that would otherwise persist. The formulation of the complementarity condition based only on impulses in (28)–(29) admits a consistent result even given this modification (using instead (30)–(31) would require considering both the impulsive and velocity implications of this pseudo-impulse).

### Pseudo-Impulse Examples

The inclusion of the pseudo-impulse at impact with contact  $j$  imposes an implicit bound on impact velocity which determines whether contact  $k$  will be maintained. This bound is independent of the impact velocity and it appears, anecdotally for now, that this bound truncates Zeno executions. Consider the rectangular rigid body in Figure 5.4 of width  $w$ , height  $h$ , mass  $m_b$ , and inertia  $I_b$  (where if a uniform distribution is assumed  $I_b = m_b(w^2 + h^2)/12$ ), as studied in e.g. [75, 113, 185]. As it is falling onto the ground if one corner is touching down<sup>8</sup> then the normal direction impulse at that corner when the other corner hits the ground is,

$$\mathbf{U}(\mathbf{P}_\lambda)_{1n} = \frac{\dot{z}(2I_b + m_b(w^2 - h^2)/2)}{w^2} \quad (41)$$

---

<sup>8</sup>In this example the contact points are assumed to resist sliding friction, although when they are both in contact with the ground one of the redundant tangential constraints is dropped. The phenomenon of interest occurs equally well with frictionless contact however the analysis is simpler in the frictional case as presented here.

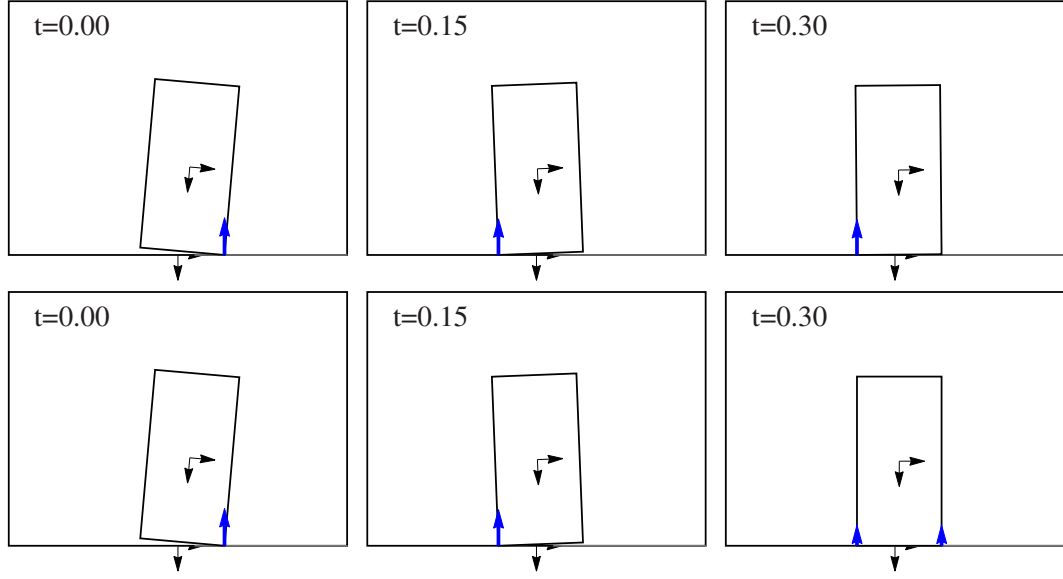


Figure 5.4: A rocking block (height  $h = 10\text{cm}$ , width  $w = 5\text{cm}$ , mass  $m = 5\text{kg}$ ) settling on the ground. *Top Row:* Without pseudo-impulse ( $\delta_t = 0$ ). *Bottom Row:* With pseudo-impulse ( $\delta_t = 0.03$ ). The execution is identical until the last frame.

(note that by convention a positive velocity  $\dot{z}$  is one that is towards the ground) and the required impulse will be negative if,

$$h^2 > w^2 + \frac{4I_b}{m_b} \Rightarrow \mathbf{U}(\mathbf{P}_\lambda)_{1n} < 0 \quad (42)$$

in which case the contact will be broken no matter how slow the block is moving. The system will exhibit Zeno behavior requiring infinite transitions in finite time as each impact removes some energy but does not immobilize the block, as can be seen in the upper row of Figure 5.5 which plots the vertical velocity as the system undergoes a Zeno execution.

Instead if the pseudo-impulse is considered,

$$\mathbf{U}(\mathbf{P}_\lambda + \mathbf{P}_\delta)_{1n} = \frac{\dot{z}(2I_b + m_b(w^2 - h^2)/2)}{w^2} + \frac{\delta_t m_b g}{2} \quad (43)$$

the contact will be broken if,

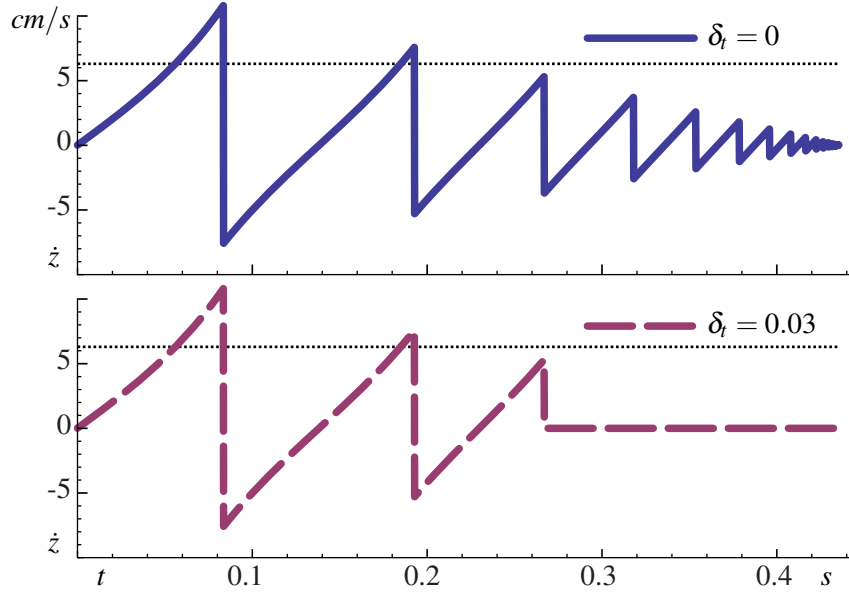


Figure 5.5: Vertical velocity of a settling block for evaluations with and without the pseudo-impulse. The execution is identical until the impact at  $t = 0.27\text{s}$ . The pseudo-impulse implicitly bounds the vertical velocity such that an impact at speeds lower than  $6.3\text{cm/s}$  will cause the block to come to rest, as indicated by the dotted line.

$$h^2 > w^2 + \frac{4I_b}{m_b} + \frac{\delta_t g w^2}{\dot{z}} \Rightarrow \mathbf{U}(\mathbf{P}_\lambda + \mathbf{P}_\delta)_{1n} < 0 \quad (44)$$

where as the speed goes to zero ( $\dot{z} \rightarrow 0$ ) the threshold on height that will allow the contact to persist will grow and eventually be met. This truncation of the Zeno execution can be seen in the lower row of Figure 5.5, where for the dimensions used the block will come to rest if the vertical speed at impact is less than  $6.3\text{cm/s}$ .

The pseudo-impulse is useful even in cases that are not formally Zeno, but simply involve impulsive transitions that are qualitatively undesirable. An example can be seen by running the RHex leaping simulation of Figure 5.1 with and without the pseudo-impulse term, as shown in Figure 5.6 which compares the state just before and after the rear leg touches down. At that instant the calculated impulse (10) is  $P_{1n} = -1.47\text{Ns}$  (in the normal direction on the front leg). Even though the leg motor is applying maximum torque trying to keep the leg on the ground the small negative

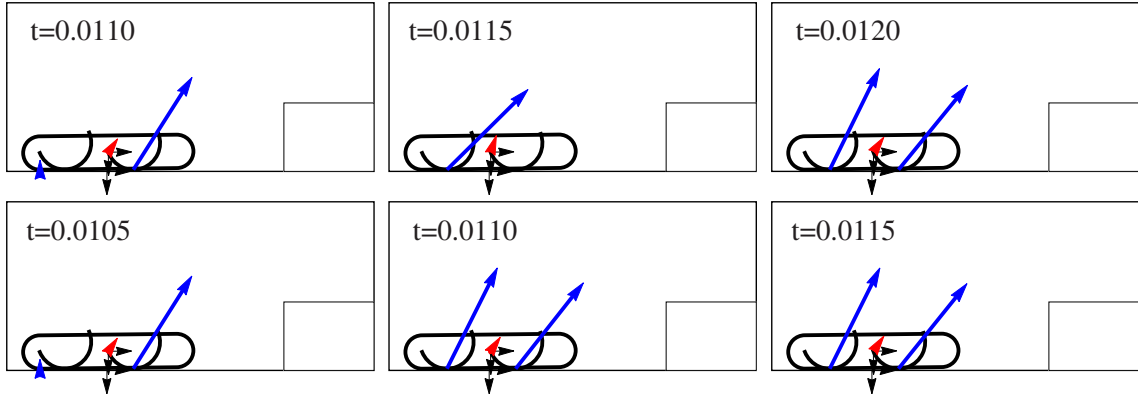


Figure 5.6: Keyframes around the impact of the second leg with the ground. *Top Row:* Without pseudo-impulse ( $\delta_t = 0$ ). *Bottom Row:* With pseudo-impulse ( $\delta_t = 0.03$ ). Note that there is a slight difference in touchdown time due to similar discrepancies around the time of the first leg touchdown.

impulse will cause the leg to separate, and then the motor torque will quickly accelerate the leg back to the ground (though recall that even massless legs are assumed to have finite acceleration, thus the leg may return quickly but not instantly). With the pseudo-impulse this is balanced out by  $P_{\delta,1n} = 7.91\text{Ns}$ , and the leg does not leave the ground (as would be the case on the real robot in this configuration to within modeling precision). If the induced impulse were much larger then the desired result may be for the front leg to lift off the ground, while a much smaller impulse would clearly not break the front leg's contact. The  $\delta_t$  term is in essence a tuning parameter that determines the threshold between a *quasi-static* regime (where contacts are maintained) and a *dynamic* regime (where impulses may break existing contacts).

Impulsively breaking contact at the wrong time is an even bigger problem when considering a full behavior and not just analyzing an individual impact event. As Figure 5.7 suggests, without a pseudo-impulse this impulsive liftoff can lead to chattering. In this case starting around  $t = 0.023$  the front leg lifts off but the continuous time forces return the leg to the ground after a short time. When the front leg impacts the ground, the rear leg then impulsively breaks contact, and a cyclic oscillation begins. This behavior is not quite a Zeno-execution, as the finite acceleration of the leg in the air results in only finitely many transitions in a finite time, however these transitions are still qualitatively undesirable.

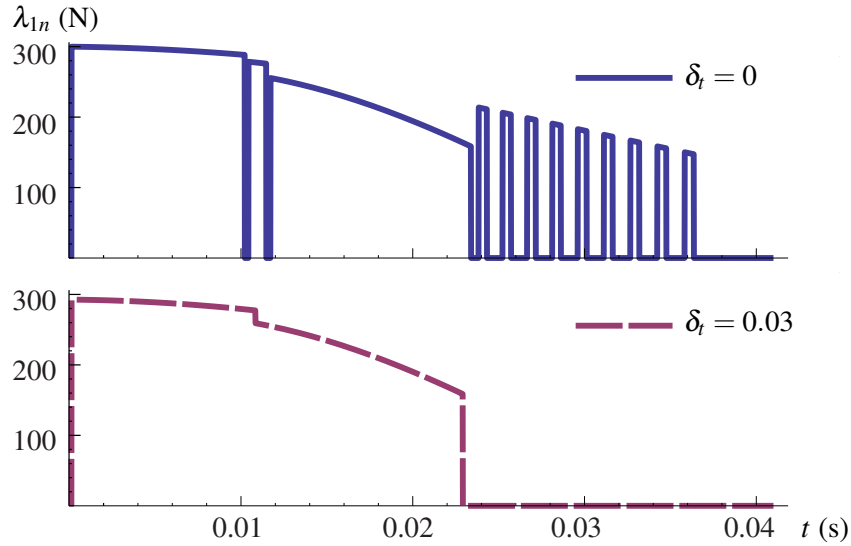


Figure 5.7: Comparison of the front leg normal direction ground reaction force for evaluations with and without the pseudo-impulse.

### 5.1.5 Friction

While this chapter is not focused on methods for modeling friction, including friction in some form is unavoidable. In continuous time, the frictional assumptions for the RHex model (Assumptions C.3 and C.4 of Section 4.2.3) (as show in Figure 5.1) are that the body has a low coefficient of friction and does not resist tangential forces while the leg’s rubber feet have a high coefficient of friction and therefore always do<sup>9</sup>. This *a priori* assumption about friction is certainly not a good model for every situation – consider what happens when RHex’s legs push against each other, as with the vertical leap described in Chapter 3. In order to model such a behavior the leg contact points must be allowed to transition to sliding contact when the contact forces reach the friction cone in the tangential direction,  $\mathbf{U}_k(\lambda) \geq 0$  (Section 4.1.3), though like the body contact points with a kinetic coefficient of friction  $\mu_k = 0$  (so that the jamming problems are again avoided). Adding this contact mode enables for example the simulation of the vertical leap shown in Figure 5.8 or the leap onto a ledge shown in Figure 5.9. The transition from sliding to sticking occurs when the tangential velocity drops to zero, i.e.  $\mathbf{A}_k \dot{\mathbf{q}} = 0$ , although care must be taken to avoid cycling between

<sup>9</sup>Nearly always in practice – in Figure 5.1 the frictional coefficient,  $\mu$ , was set to be the relatively large but finite values of 1.8 for the front leg and 2.5 for the rear.

stick and slip at zero velocity.

For the impact problem, in order to support the assumption of existence and uniqueness of a solution we will assume that,

*Assumption 5.9 (Friction).* All contact points with Coulomb friction are attached only to massless links. Contact points without friction are assumed to never resist sliding motion, and all contact points that are sliding have no kinetic coefficient of friction.

Therefore any conflict in impulses during impact can be resolved by simply removing that contact from the active set (see [167] for pathologies that arise when this assumption is relaxed). As a massless link, it can always rotate out of the way fast enough (as discussed above in Section. 5.1.3). The complementarity test of (28)–(29) is thus taken to include both the normal and tangential components of the friction cone.

## 5.2 Hybrid Dynamical System

The continuous time dynamics presented in Chapter 4 and the impulsive dynamics presented in this chapter can be combined to give a complete system description, as was done in the generation of Figures 5.1, 5.8, and 5.9. The code that generated those plots (as well as the analytical and numerical result from Chapter 4) is available online<sup>10</sup>. This section summarizes these modeling ideas as a hybrid system that the simulation code is an implementation of.

### 5.2.1 The General System

In the following definitions we make use of the natural (disjoint–union) topology on the hybrid state space; see [85] or [24, Section II] for more details.

**Definition 5.1.** A hybrid dynamical system, is a tuple  $\mathcal{H} := (\mathcal{J}, \Gamma, \mathcal{D}, \mathcal{F}, \mathcal{G}, \mathcal{R})$ , where:

- $\mathcal{J} = \{I, J, \dots, K\}$  is the finite set of *discrete states*;
- $\Gamma \subset \mathcal{J} \times \mathcal{J}$  is the set of *discrete transitions*, forming a directed graph structure over  $\mathcal{J}$ ;

---

<sup>10</sup><http://kodlab.seas.upenn.edu/Aaron/Code>

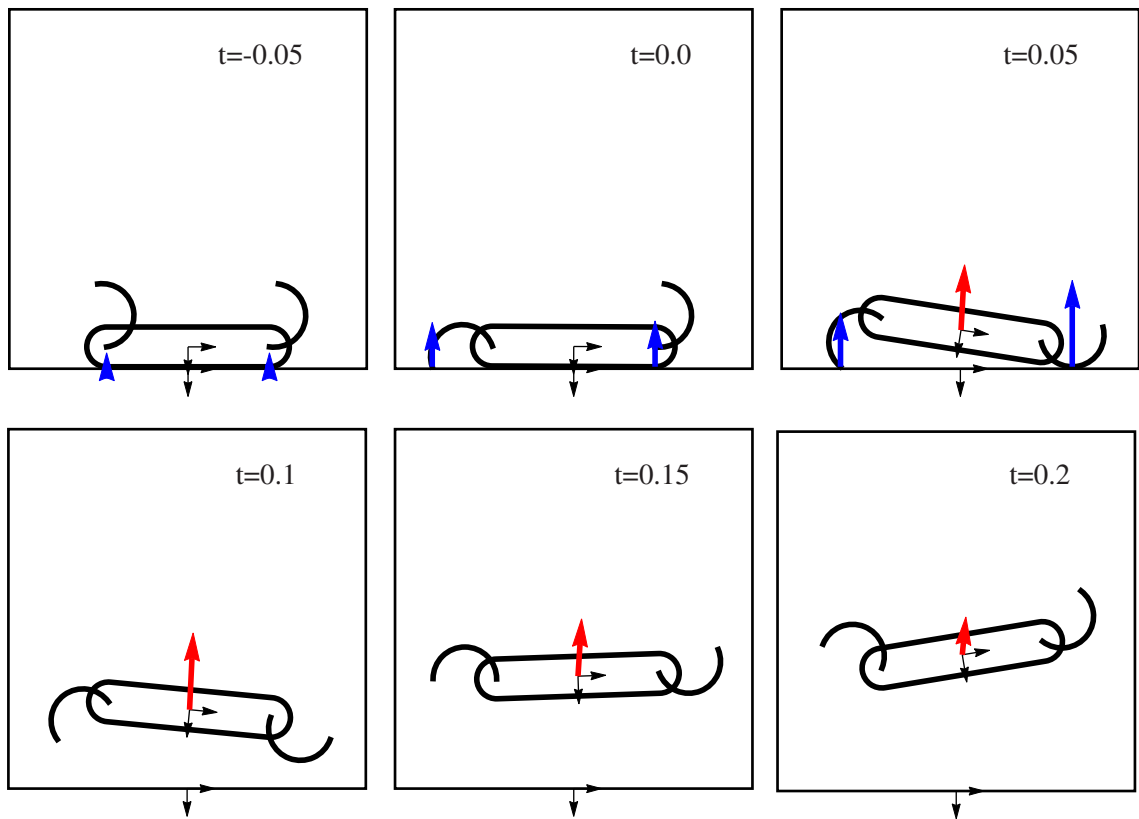


Figure 5.8: Keyframes from RHex simulation leaping vertically to a height of 37cm. Blue arrows show contact forces (relative scale  $10N = 1cm$ ) while the red arrow shows body velocity (relative scale  $10cm/s = 1cm$ ).

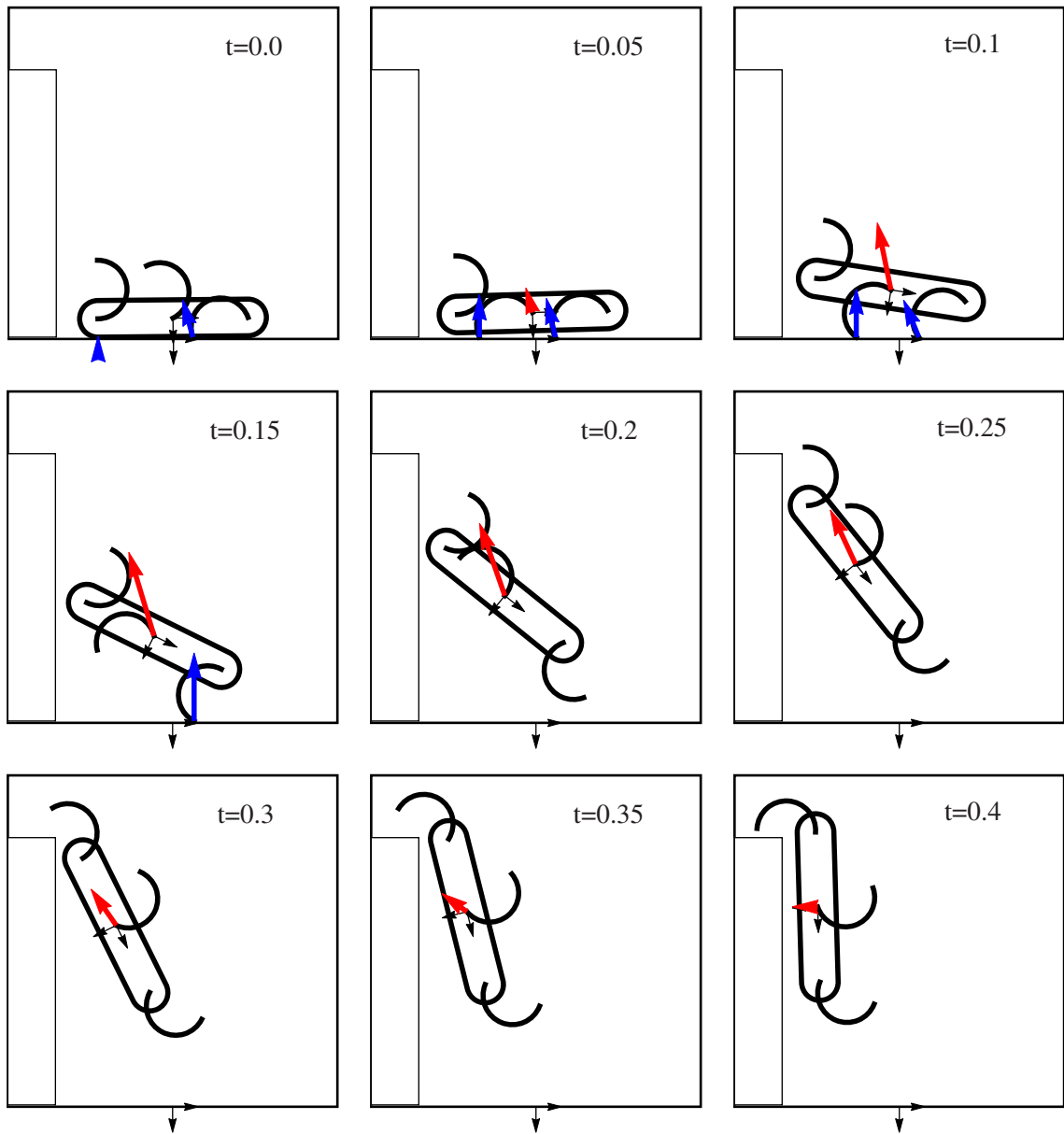


Figure 5.9: Keyframes from RHex simulation leaping onto a 73cm ledge. Blue arrows show contact forces (relative scale  $10N = 1cm$ ) while the red arrow shows body velocity (relative scale  $10cm/s = 1cm$ ).

- $\mathcal{D} = \coprod_{I \in \mathcal{J}} D_I$  is the collection of *domains*, where  $D_I$  is a smooth manifold with corners;
- $\mathcal{F} : \mathcal{D} \rightarrow T\mathcal{D}$  is a smooth hybrid map that restricts to a vector field  $F_I = \mathcal{F}|_{D_I}$  for each  $I \in \mathcal{J}$ ;
- $\mathcal{G} = \coprod_{(I,J) \in \Gamma} G_{I,J}$  is the set of *guards*, where  $G_{I,J} \subset D_I$  and  $G_{I,J} \cap G_{I,K} = \emptyset$  for  $(I,J), (I,K) \in \Gamma, J \neq K$ ;
- $\mathcal{R} : \mathcal{G} \rightarrow \mathcal{D}$  is a continuous map called the *reset* that restricts as  $R_{I,J} = \mathcal{R}|_{G_{I,J}} : G_{I,J} \rightarrow D_J$  for each  $(I,J) \in \Gamma$ .

Roughly speaking, an *execution* of a hybrid dynamical system is determined from an initial condition in  $\mathcal{D}$  by following the continuous-time dynamics determined by the vector field  $\mathcal{F}$  until the trajectory reaches the guard  $\mathcal{G}$ , at which point the reset map  $\mathcal{R}$  is applied to obtain a new initial condition. This notion, and Definition 5.1, are formalized in [85].

## 5.2.2 The Self-Manipulation System

This section will define the self-manipulation system (Chapter 4 and by the analogy of that chapter, equivalently a manipulation system [134]), where individual contact modes are built from the set of possible contact constraints  $\mathcal{K} = \mathcal{K}_n \cup \mathcal{K}_t$ . Here,  $\mathcal{K}_n$  denotes the set of *normal penetration* contacts, where each  $i \in \mathcal{K}_n$  specifies a holonomic constraint of the form  $\{(\dot{\mathbf{q}}, \mathbf{q}) \in T\mathcal{Q} : \mathbf{a}_i(\mathbf{q}) = 0\}$  where  $\mathbf{a}_i \in C^r(\mathcal{Q}, \mathbb{R})$ , and  $\mathcal{K}_t$  denotes the set of *tangent non-sliding* contacts, where each  $i \in \mathcal{K}_t$  specifies a nonholonomic constraint of the form  $\{(\dot{\mathbf{q}}, \mathbf{q}) \in T\mathcal{Q} : \mathbf{A}_i(\mathbf{q})\dot{\mathbf{q}} = 0\}$  where  $\mathbf{A}_i \in C^r(\mathcal{Q}, T^*\mathcal{Q})$ . We note that there is an assignment  $\alpha : \mathcal{K}_t \rightarrow \mathcal{K}_n$  of tangent contacts to normal contacts since it is not physically permissible for  $i \in \mathcal{K}_t$  to be active without some associated  $\alpha(i) \in \mathcal{K}_n$  to be simultaneously active as well.

**Definition 5.2.** The self-manipulation hybrid system is defined as follows,

### Indexing Set

The set of all physically permissible combinations of contact constraints is given by

$$\mathcal{J} = \{I \in 2^{\mathcal{K}} \mid \forall i \in I \cap \mathcal{K}_t : \alpha(i) \in I\}. \quad (45)$$

As mentioned above, it is not physically permissible to have  $I \in \mathcal{J}$  such that  $\exists i \in I \cap \mathcal{K}_t : \alpha(i) \notin I$ .

### Edges

The set of edges is any pair of distinct domains,

$$\Gamma = \{(I, J) \in \mathcal{J} \times \mathcal{J}\} \quad (46)$$

where specific problems may allow for further restrictions where, e.g., the guard (defined below) is the null set.

### Domains

The domain associated with a contact state  $I \in \mathcal{J}$  is the subset of the ambient tangent bundle  $T\mathcal{Q}$  that satisfies the normal penetration and tangent non-sliding constraints,

$$D_I = \{(\dot{\mathbf{q}}, \mathbf{q}) \in (T\mathcal{Q}) : \mathbf{a}_{I \cap \mathcal{K}_n}(\mathbf{q}) = 0, \mathbf{A}_I \dot{\mathbf{q}} = 0, \mathbf{a}_i(\mathbf{q}) \geq 0 \forall i \in \mathcal{K}_n \setminus I\}. \quad (47)$$

Recall that  $\mathcal{Q} := \Theta \times SE(d)$  is the joint space combined with the position space of the body.

### Flows

The vector field on each domain consists of the self-manipulation dynamics for  $\dot{\mathbf{q}}$  (as in (3) and Section 4.1.9) and trivial dynamics on  $\mathbf{q}$  (as  $\dot{\mathbf{q}}$  is a part of the state),

$$F_I(\dot{\mathbf{q}}, \mathbf{q}) = \left( \overline{\mathbf{M}}^\dagger (\Upsilon - \overline{\mathbf{C}}\dot{\mathbf{q}} - \overline{\mathbf{N}}) - \mathbf{A}_I^{\dagger T} \dot{\mathbf{A}}_I \dot{\mathbf{q}}, \quad \dot{\mathbf{q}} \right). \quad (48)$$

The control input  $\tau \in T^*\Theta$  that appears in  $\Upsilon$  is prescribed by a smooth function of state  $\tau \in C^r(T\mathcal{Q}, T^*\mathcal{Q})$  (for example a fixed-voltage motor model  $\tau_i = \kappa_P \kappa_G (1 - \kappa_G \dot{\theta}_i)$  Section 4.3.3sec:pronkdtakeoff).

## Guards

The guards are easiest to define in unison and then the subsequent state can be calculated afterwards,

$$G_I = \{(\dot{\mathbf{q}}, \mathbf{q}) \in D_I : (\exists k \in \mathcal{K}_n \setminus I, \mathbf{a}_k(\mathbf{q}) = 0 \wedge \mathbf{a}_k(\mathbf{q}) \preceq 0) \quad (49)$$

$$\vee (\exists k \in \mathcal{K}_t \setminus I, \mathbf{A}_k \dot{\mathbf{q}} = 0) \quad (50)$$

$$\vee (\exists k \in I, \mathbf{U}_k(\lambda_k) \preceq 0)\}. \quad (51)$$

The subsequent state  $J$  is determined by adding or subtracting contacts from  $I$  according to which of the conditions (49)–(51) are active, and subsequently removing any contacts that would violate the complementarity conditions (19)–(20) or (28)–(29). As the frictional assumptions guarantee a unique solution any algorithm that reaches that solution may be used.

For purposes of analysis, it will be necessary to explicitly define the individual guards, and formally the execution will check if the state is in any of the guards separately. This definition, as well as a guarantee that the separate guards are disjoint, is included in [85].

## Reset Maps

With the definition of impact maps given above, the reset map is,

$$R_{I,J}(\dot{\mathbf{q}}, \mathbf{q}) = [\dot{\mathbf{q}} - \Delta_{\dot{\mathbf{q}}}, \mathbf{q}] = [(\dot{\mathbf{q}} - \mathbf{A}_J^{\dagger T} \mathbf{A}_J \dot{\mathbf{q}}), \mathbf{q}] \quad (52)$$

Note that for takeoff events, the prior velocity will already agree with the new constraint set and therefore the impact map will have no effect.

## 5.3 Appendix to Chapter 5

### 5.3.1 Linear Algebra

For additional notes on the Schur complement and block matrix inverse, see e.g. [40, 81]. Given a block matrix  $M$  defined as,

$$M := \begin{bmatrix} A & B \\ C & D \end{bmatrix} \quad (53)$$

when submatrices  $A$  or  $D$  are nonsingular, then the Schur complement of  $A$  or  $D$  in  $M$  is,

$$S_A := D - CA^{-1}B \quad (54)$$

$$S_D := A - BD^{-1}C \quad (55)$$

which is sometimes written as  $(M|A)$  or  $(M|D)$ , respectively.

If  $M$  is also nonsingular, the inverse of  $M$  is,

$$\begin{bmatrix} A & B \\ C & D \end{bmatrix}^{-1} = \begin{bmatrix} A^{-1} + A^{-1}BS_A^{-1}CA^{-1} & -A^{-1}BS_A^{-1} \\ -S_A^{-1}CA^{-1} & S_A^{-1} \end{bmatrix} \quad (56)$$

$$= \begin{bmatrix} S_D^{-1} & -A^{-1}BS_A^{-1} \\ -D^{-1}CS_D^{-1} & S_A^{-1} \end{bmatrix} \quad (57)$$

Furthermore if  $M$  is positive-definite, then  $M^{-1}$  is as well, as is the leading submatrix  $A$ . Since  $\det M = (\det A)(\det S_A)$ , clearly the Schur complement must also be positive definite.

### 5.3.2 Matrices Used in Proofs

A common matrix inverse that will come up is,

$$\mathbf{A}_K = \begin{bmatrix} \mathbf{A}_J \\ \mathbf{A}_k \end{bmatrix} \quad (58)$$

$$\begin{bmatrix} \begin{bmatrix} \overline{\mathbf{M}} & \mathbf{A}_J^T \\ \mathbf{A}_J & \mathbf{0}_{J \times J} \\ \mathbf{A}_k & \mathbf{0}_{1 \times J} \end{bmatrix} & \begin{bmatrix} \mathbf{A}_k^T \\ \mathbf{0}_{J \times 1} \\ 0 \end{bmatrix} \end{bmatrix}^{-1} = \quad (59)$$

$$\begin{bmatrix} \begin{bmatrix} \overline{\mathbf{M}}_J^\dagger & \mathbf{A}_J^{\dagger T} \\ \mathbf{A}_J^\dagger & \Lambda_J \end{bmatrix} + \begin{bmatrix} \overline{\mathbf{M}}_J^\dagger & \mathbf{A}_J^{\dagger T} \\ \mathbf{A}_J^\dagger & \Lambda_J \end{bmatrix} \begin{bmatrix} \mathbf{A}_k^T \\ \mathbf{0} \end{bmatrix} S_A^{-1} \begin{bmatrix} \mathbf{A}_k & \mathbf{0} \end{bmatrix} \begin{bmatrix} \overline{\mathbf{M}}_J^\dagger & \mathbf{A}_J^{\dagger T} \\ \mathbf{A}_J^\dagger & \Lambda_J \end{bmatrix} & - \begin{bmatrix} \overline{\mathbf{M}}_J^\dagger & \mathbf{A}_J^{\dagger T} \\ \mathbf{A}_J^\dagger & \Lambda_J \end{bmatrix} \begin{bmatrix} \mathbf{A}_k^T \\ \mathbf{0} \end{bmatrix} S_A^{-1} \\ & - S_A^{-1} \begin{bmatrix} \mathbf{A}_k & \mathbf{0} \end{bmatrix} \begin{bmatrix} \overline{\mathbf{M}}_J^\dagger & \mathbf{A}_J^{\dagger T} \\ \mathbf{A}_J^\dagger & \Lambda_J \end{bmatrix} & S_A^{-1} \end{bmatrix}$$

$$\begin{aligned}
&= \left[ \begin{array}{cc} \left[ \begin{array}{cc} \overline{\mathbf{M}}_J^\dagger & \mathbf{A}_J^{\dagger T} \\ \mathbf{A}_J^\dagger & \Lambda_J \end{array} \right] + \left[ \begin{array}{cc} \overline{\mathbf{M}}_J^\dagger \mathbf{A}_k^T \\ \mathbf{A}_J^\dagger \mathbf{A}_k^T \end{array} \right] S_A^{-1} \left[ \begin{array}{cc} \mathbf{A}_k \overline{\mathbf{M}}_J^\dagger & \mathbf{A}_k \mathbf{A}_J^{\dagger T} \end{array} \right] & - \left[ \begin{array}{c} \overline{\mathbf{M}}_J^\dagger \mathbf{A}_k^T \\ \mathbf{A}_J^\dagger \mathbf{A}_k^T \end{array} \right] S_A^{-1} \\ - S_A^{-1} \left[ \begin{array}{cc} \mathbf{A}_k \overline{\mathbf{M}}_J^\dagger & \mathbf{A}_k \mathbf{A}_J^{\dagger T} \end{array} \right] & S_A^{-1} \end{array} \right] \\
&= \left[ \begin{array}{ccc} \overline{\mathbf{M}}_J^\dagger + \overline{\mathbf{M}}_J^\dagger \mathbf{A}_k^T S_A^{-1} \mathbf{A}_k \overline{\mathbf{M}}_J^\dagger & \mathbf{A}_J^{\dagger T} + \overline{\mathbf{M}}_J^\dagger \mathbf{A}_k^T S_A^{-1} \mathbf{A}_k \mathbf{A}_J^{\dagger T} & -\overline{\mathbf{M}}_J^\dagger \mathbf{A}_k^T S_A^{-1} \\ \mathbf{A}_J^\dagger + \mathbf{A}_J^\dagger \mathbf{A}_k^T S_A^{-1} \mathbf{A}_k \overline{\mathbf{M}}_J^\dagger & \Lambda_J + \mathbf{A}_J^\dagger \mathbf{A}_k^T S_A^{-1} \mathbf{A}_k \mathbf{A}_J^{\dagger T} & -\mathbf{A}_J^\dagger \mathbf{A}_k^T S_A^{-1} \\ -S_A^{-1} \mathbf{A}_k \overline{\mathbf{M}}_J^\dagger & -S_A^{-1} \mathbf{A}_k \mathbf{A}_J^{\dagger T} & S_A^{-1} \end{array} \right] \quad (60)
\end{aligned}$$

$$S_A = 0 - \left[ \begin{array}{cc} \mathbf{A}_k & \mathbf{0} \end{array} \right] \left[ \begin{array}{cc} \overline{\mathbf{M}}_J^\dagger & \mathbf{A}_J^{\dagger T} \\ \mathbf{A}_J^\dagger & \Lambda_J \end{array} \right] \left[ \begin{array}{c} \mathbf{A}_k^T \\ \mathbf{0} \end{array} \right] = -\mathbf{A}_k \overline{\mathbf{M}}_J^\dagger \mathbf{A}_k^T \quad (61)$$

This allows us to express  $\mathbf{A}_K^\dagger$ ,  $\overline{\mathbf{M}}_K^\dagger$ , and  $\Lambda_K$  in terms of  $\mathbf{A}_J^\dagger$ ,  $\overline{\mathbf{M}}_J^\dagger$ , and  $\Lambda_J$  together with the added constraint  $\mathbf{A}_k$ ,

$$\mathbf{A}_{K,k}^\dagger := \left[ \mathbf{A}_K^\dagger \right]_k = -S_A^{-1} \mathbf{A}_k \overline{\mathbf{M}}_J^\dagger = \frac{\mathbf{A}_k \overline{\mathbf{M}}_J^\dagger}{\mathbf{A}_k \overline{\mathbf{M}}_J^\dagger \mathbf{A}_k^T} \quad (62)$$

$$\mathbf{A}_{K,J}^\dagger := \left[ \mathbf{A}_K^\dagger \right]_J = \mathbf{A}_J^\dagger (\mathbf{Id} - \mathbf{A}_k^T \mathbf{A}_{K,k}^\dagger) \quad (63)$$

$$\overline{\mathbf{M}}_K^\dagger = \overline{\mathbf{M}}_J^\dagger (\mathbf{Id} - \mathbf{A}_k^T \mathbf{A}_{K,k}^\dagger) \quad (64)$$

$$\Lambda_{K,k} := [\Lambda_K]_k = \left[ \begin{array}{cc} -S_A^{-1} \mathbf{A}_k \mathbf{A}_J^{\dagger T} & S_A^{-1} \end{array} \right] \quad (65)$$

$$\Lambda_{K,J} := [\Lambda_K]_J = \left[ \begin{array}{cc} \Lambda_J & \mathbf{0} \end{array} \right] - \mathbf{A}_J^\dagger \mathbf{A}_k^T \Lambda_{K,k} \quad (66)$$

### 5.3.3 Proof of Lemma 5.2

*Proof.* Recall that  $\lim_{\varepsilon \rightarrow 0} \overline{\mathbf{M}}_\varepsilon = \overline{\mathbf{M}}$  and that  $\overline{\mathbf{M}}_\varepsilon$  is invertible for all  $\varepsilon \in (0, \bar{\varepsilon})$ , for some  $\bar{\varepsilon} > 0$ . For all  $\varepsilon \geq 0$ , define  $\overline{\mathbf{M}}_\varepsilon^\dagger$ ,  $\mathbf{A}_\varepsilon^\dagger$ , and  $\Lambda_\varepsilon$  by replacing  $\overline{\mathbf{M}}$  with  $\overline{\mathbf{M}}_\varepsilon$  in (2). Using (5)–(7) we can rewrite the dynamics,

$$\lambda = \mathbf{A}^\dagger (\Upsilon - \overline{\mathbf{C}}\dot{\mathbf{q}} - \overline{\mathbf{N}}) - \Lambda \dot{\mathbf{A}}\dot{\mathbf{q}} \quad (67)$$

$$= \lim_{\varepsilon \rightarrow 0} \mathbf{A}_\varepsilon^\dagger (\Upsilon - \overline{\mathbf{C}}\dot{\mathbf{q}} - \overline{\mathbf{N}}) - \Lambda_\varepsilon \dot{\mathbf{A}}\dot{\mathbf{q}} \quad (68)$$

$$= \lim_{\varepsilon \rightarrow 0} \left( (\mathbf{A} \overline{\mathbf{M}}_\varepsilon^{-1} \mathbf{A}^T)^{-1} \mathbf{A} \overline{\mathbf{M}}_\varepsilon^{-1} \right) (\Upsilon - \overline{\mathbf{C}}\dot{\mathbf{q}} - \overline{\mathbf{N}}) + (\mathbf{A} \overline{\mathbf{M}}_\varepsilon^{-1} \mathbf{A}^T)^{-1} \dot{\mathbf{A}}\dot{\mathbf{q}} \quad (69)$$

$$= \lim_{\varepsilon \rightarrow 0} (\mathbf{A} \overline{\mathbf{M}}_\varepsilon^{-1} \mathbf{A}^T)^{-1} \left( \mathbf{A} \overline{\mathbf{M}}_\varepsilon^{-1} (\Upsilon - \overline{\mathbf{C}}\dot{\mathbf{q}} - \overline{\mathbf{N}}) + \dot{\mathbf{A}}\dot{\mathbf{q}} \right) \quad (70)$$

$$\ddot{\mathbf{q}} = \overline{\mathbf{M}}^\dagger (\Upsilon - \overline{\mathbf{C}}\dot{\mathbf{q}} - \overline{\mathbf{N}}) - \mathbf{A}^{\dagger T} \dot{\mathbf{A}}\dot{\mathbf{q}} \quad (71)$$

$$= \lim_{\varepsilon \rightarrow 0} \overline{\mathbf{M}}_\varepsilon^\dagger (\Upsilon - \overline{\mathbf{C}}\dot{\mathbf{q}} - \overline{\mathbf{N}}) - \mathbf{A}_\varepsilon^{\dagger T} \dot{\mathbf{A}}\dot{\mathbf{q}} \quad (72)$$

$$= \lim_{\varepsilon \rightarrow 0} \left( \overline{\mathbf{M}}_\varepsilon^{-1} - \overline{\mathbf{M}}_\varepsilon^{-1} \mathbf{A}^T (\mathbf{A} \overline{\mathbf{M}}_\varepsilon^{-1} \mathbf{A}^T)^{-1} \mathbf{A} \overline{\mathbf{M}}_\varepsilon^{-1} \right) (\boldsymbol{\Upsilon} - \overline{\mathbf{C}} \dot{\mathbf{q}} - \overline{\mathbf{N}}) - \overline{\mathbf{M}}_\varepsilon^{-1} \mathbf{A}^T (\mathbf{A} \overline{\mathbf{M}}_\varepsilon^{-1} \mathbf{A}^T)^{-1} \dot{\mathbf{A}} \dot{\mathbf{q}} \quad (73)$$

$$= \lim_{\varepsilon \rightarrow 0} \overline{\mathbf{M}}_\varepsilon^{-1} \left( \boldsymbol{\Upsilon} - \overline{\mathbf{C}} \dot{\mathbf{q}} - \overline{\mathbf{N}} - \mathbf{A}^T \left( (\mathbf{A} \overline{\mathbf{M}}_\varepsilon^{-1} \mathbf{A}^T)^{-1} (\mathbf{A} \overline{\mathbf{M}}_\varepsilon^{-1} (\boldsymbol{\Upsilon} - \overline{\mathbf{C}} \dot{\mathbf{q}} - \overline{\mathbf{N}}) + \dot{\mathbf{A}} \dot{\mathbf{q}}) \right) \right) \quad (74)$$

$$= \lim_{\varepsilon \rightarrow 0} \overline{\mathbf{M}}_\varepsilon^{-1} (\boldsymbol{\Upsilon} - \overline{\mathbf{C}} \dot{\mathbf{q}} - \overline{\mathbf{N}} - \mathbf{A}^T \boldsymbol{\lambda}) \quad (75)$$

where (70) and (75) are identically equal to the desired formulation of (8) and (9) when  $\overline{\mathbf{M}}_0$  is non-singular.  $\square$

### 5.3.4 Proof of Lemma 5.3

*Proof.* Recall that  $\lim_{\varepsilon \rightarrow 0} \overline{\mathbf{M}}_\varepsilon = \overline{\mathbf{M}}$  and that  $\overline{\mathbf{M}}_\varepsilon$  is invertible for all  $\varepsilon \in (0, \bar{\varepsilon})$ , for some  $\bar{\varepsilon} > 0$ . For all  $\varepsilon \geq 0$ , define  $\overline{\mathbf{M}}_\varepsilon^\dagger$ ,  $\mathbf{A}_\varepsilon^\dagger$ , and  $\Lambda_\varepsilon$  by replacing  $\overline{\mathbf{M}}$  with  $\overline{\mathbf{M}}_\varepsilon$  in (2). Then using equation (6) we can rewrite the impulse (where all constraints  $\mathbf{A}$  are taken to be for the target contact mode  $J$ ),

$$\mathbf{P}_\lambda = \mathbf{A}^\dagger \overline{\mathbf{M}} \mathbf{A}^{\dagger T} \mathbf{A} \dot{\mathbf{q}}^- = \lim_{\varepsilon \rightarrow 0} \mathbf{A}_\varepsilon^\dagger \overline{\mathbf{M}}_\varepsilon \mathbf{A}_\varepsilon^{\dagger T} \mathbf{A} \dot{\mathbf{q}}^- \quad (76)$$

$$= \lim_{\varepsilon \rightarrow 0} \left( (\mathbf{A} \overline{\mathbf{M}}_\varepsilon^{-1} \mathbf{A}^T)^{-1} \mathbf{A} \overline{\mathbf{M}}_\varepsilon^{-1} \right) \overline{\mathbf{M}}_\varepsilon \left( \overline{\mathbf{M}}_\varepsilon^{-1} \mathbf{A}^T (\mathbf{A} \overline{\mathbf{M}}_\varepsilon^{-1} \mathbf{A}^T)^{-1} \right) \mathbf{A} \dot{\mathbf{q}}^- \quad (77)$$

$$= \lim_{\varepsilon \rightarrow 0} (\mathbf{A} \overline{\mathbf{M}}_\varepsilon^{-1} \mathbf{A}^T)^{-1} \mathbf{A} \dot{\mathbf{q}}^- \quad (78)$$

which is identically equal to (11) when  $\overline{\mathbf{M}}_0$  is non-singular.  $\square$

## Chapter 6

# Conclusion

Over the past few years the RHex robot has become much more capable and field-ready, due in part to significant hardware improvements of the X-RHex and XRL designs that have led to new levels of strength and robustness. High performance behaviors have expanded the navigable terrain, and new analytical tools have helped to distill design insight from these behaviors.

Chapter 2 presented a spectrum of motor sizing tasks, as well as documenting two specific case studies. In the first, a motor for an inertial tail is selected using an optimal gear ratio that is calculated analytically. With the tail the robot is capable of landing on its feet when dropped or when falling off of a ledge. Next the design process for selection of the motor for X-RHex reveals the importance of thermal considerations. A new metric, the heat coefficient, is used to compare the thermal performance of motors with differing morphologies.

In addition Chapter 2 introduced and documented empirically the performance of a software contact-event driven disturbance identification and recovery system, based on careful actuator modeling. Initial results demonstrate that our ground contact estimates successfully cue appropriate behavioral transitions, including effective reaction to the sudden and unexpected loss of a limb during locomotion followed by smooth, safe transition to a new, more stable gait. As a follow on to this work, these estimation techniques were used as a sensor for terrain classification [139]. This allows the robot to adapt gaits based upon terrain, such as when suddenly encountering a sandy rather than than expected hard surface [107]. Whereas the presented methods only estimate discrete leg contact,

the simple robot models presented in Chapter 4 should allow for estimation of the magnitudes of ground reaction forces as well [110].

Chapter 3 explored the space of legged transitions from complete rest to full flight as generated by combinatorial mixtures of various hybrid dynamical systems indexed by the cells of a “ground reaction complex”. The very regular adjacency relations implied by this topological space organize these sequential mixtures in a sufficiently simple manner as to allow the systematic (“grammatical”) generation of all possible leaps. This enumeration affords a number of new behaviors that significantly extend the range of terrains that the RHex robot can negotiate. Near term future extensions will focus on formal methods of design that exploit this analysis more systematically and effectively than the “hand-crafted” behaviors reported here. Moreover, we are interested in a broader range of dynamical transitions, particularly ones exploiting compliance, including the novel prospect of using the leg springs in extension introduced here.

Chapter 4 presented a formal framework for the generation of quasi-static and dynamic equations of motion for legged robots across multiple contact conditions. This framework matches as closely as possible the modeling decisions typically used for the analysis of multi-fingered hands, thereby highlighting the similarities and differences between the two classes of problems. The resulting systematic, unified and general methodology for modeling all contact conditions of a legged robot promotes analysis of a rich variety of behaviors for common scenarios that arise as legged robots leave the laboratory and enter the real world.

The utility of this methodology is demonstrated for platform, behavior, and controller design in the context of a specifically imagined episode in an autonomous mission of a RHex robot. The analysis of these behaviors recall from the manipulation literature the notion of a grasp map,  $\mathbf{G}$ , whose null space introduces a transparent account of internal and external forces, yielding a simple, general, and provably correct algorithm for standing still over unknown terrain with minimal power draw. Reducing the influence of the highly varied mechanics across the multiplicity of contact conditions to the appearance of one term promotes a straightforward comparison of the quality of exteroception across all quasi-statically reachable configurations, enabling the robot to act as an active laser wall/cliff detector. Formal reasoning about the intrinsic conflict between leg

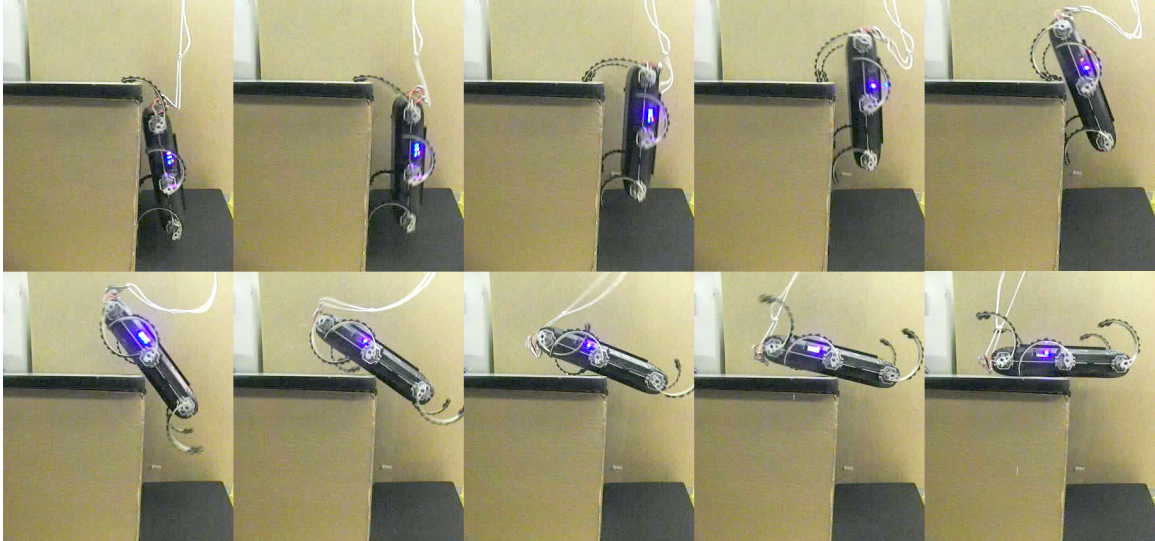


Figure 6.1: XRL scrambling onto a ledge. Frames taken every 100ms.

torques and liftoff speed sheds new light on the problem of how to leap forward most energetically without pitching. Finally, in each of these task settings, the formal nature of the results affords clear answers to morphological design questions such as the consequences of leg shape. Tracing back more systematically similar threads between the various design parameter values and the behavioral results they promote or constrain ought to be useful in future redesign of this and other legged robots.

Chapter 5 extends these idea to account for the impulsive dynamics necessary for transitioning between contact conditions while still ensuring compatibility with certain simplifying assumptions. The self-manipulation hybrid system presented here is not intended to produce the highest fidelity of numerical accuracy. Instead it is an analytically tractable system that is compatible with modeling assumptions, such as massless limbs, while still producing qualitatively correct results, such as the simulation of the various RHex leaps introduced in Chapter 3. Future work includes proving in general what is anecdotally appears true for the RHex model — the system is deterministic and non-blocking [82], truncates Zeno executions [1, 138], and has sufficient structure to arrive at the conclusions suggested in Chapter 3.

As dynamic robot behaviors become more capable and well understood, the need arises for a wide variety of equally capable and systematically applicable transitions between them. This thesis presented some behaviors that go beyond current levels of understanding, for example Figure 6.1,

the second stride in the leap-grab of Figure 3.1, intended to pull the robot up onto the ledge. That behavior involved a cyclic path through the ground reaction complex (the lower leg pushes three separate times), took full advantage of the leg compliance (in particular stretching the legs), and certainly involved subtle properties of friction. All of these represent challenges to the formal understanding of this behavior, but also great opportunities for future research. The analytical tools presented in this thesis only scratch the surface of what is needed to fully understand such behaviors, and to automate the distillation of design insight.

# Bibliography

- [1] A. Ames, H. Zheng, R. Gregg, and S. Sastry, “Is there life after zeno? taking executions past the breaking (zeno) point,” in *American Control Conference, 2006*, 2006, pp. 2652–2657.
- [2] R. L. Andersson, “Aggressive trajectory generator for a robot ping-pong player,” *Control Systems Magazine, IEEE*, vol. 9, no. 2, pp. 15–21, 1989.
- [3] M. Anitescu and F. A. Potra, “Formulating dynamic multi-rigid-body contact problems with friction as solvable linear complementarity problems,” *Nonlinear Dynamics*, vol. 14, no. 3, pp. 231–247, 1997.
- [4] M. Ankaralı and U. Saranlı, “Control of underactuated planar pronking through an embedded spring-mass hopper template,” *Autonomous Robots*, vol. 30, no. 2, pp. 217–231, 2011.
- [5] K. Arikawa and T. Mita, “Design of multi-dof jumping robot,” in *IEEE Int. Conf. Robotics and Automation*, vol. 4, 2002, pp. 3992–3997.
- [6] O. Arslan and U. Saranlı, “Reactive planning and control of planar spring-mass running on rough terrain,” *IEEE Trans. Robot.*, vol. 28, no. 3, Jun 2012.
- [7] R. Balasubramanian, A. Rizzi, and M. T. Mason, “Legless locomotion: A novel locomotion technique for legged robots,” *Int. J. Robotics Research*, vol. 27, no. 5, pp. 575 – 594, May 2008.
- [8] D. Baraff, “Coping with friction for non-penetrating rigid body simulation,” in *ACM SIG-GRAPH Computer Graphics*, vol. 25, no. 4. ACM, 1991, pp. 31–41.

- [9] E. Bayo and R. Ledesma, "Augmented lagrangian and mass-orthogonal projection methods for constrained multibody dynamics," *Nonlinear Dynamics*, vol. 9, no. 1-2, pp. 113–130, 1996.
- [10] B. Beigzadeh, M. N. Ahmadabadi, A. Meghdari, and A. Akbarimajd, "A dynamic object manipulation approach to dynamic biped locomotion," *Robotics and Autonomous Systems*, vol. 56, no. 7, pp. 570 – 582, 2008.
- [11] P. Ben-Tzvi, A. A. Goldenberg, and J. W. Zu, "Design and analysis of a hybrid mobile robot mechanism with compounded locomotion and manipulation capability," *Journal of Mechanical Design*, vol. 130, no. 7, p. 072302, 2008.
- [12] D. Bertsimas and J. Tsitsiklis, *Introduction to Linear Optimization*, 1st ed. Athena Scientific, 1997.
- [13] A. Bicchi and V. Kumar, "Robotic grasping and contact: A review," in *IEEE Int. Conf. Robotics and Automation*, vol. 1, 2000, pp. 348–353.
- [14] R. Blickhan and R. J. Full, "Similarity in multilegged locomotion: Bouncing like a monopode," *J. Comparative Physiology A: Sensory, Neural, and Behavioral Physiology*, vol. 173, no. 5, pp. 509–517, 1993.
- [15] R. Blickhan, "The spring-mass model for running and hopping," *Journal of biomechanics*, vol. 22, no. 11, pp. 1217–1227, 1989.
- [16] A. M. Bloch, *Nonholonomic mechanics and control*. New York: Springer, 2003.
- [17] J. Bongard, V. Zykov, and H. Lipson, "Resilient Machines Through continuous Self-Modeling," *Science*, vol. 314, pp. 1118–1121, 2006.
- [18] M. Branicky, "General hybrid dynamical systems: Modeling, analysis, and control," *Hybrid Systems III*, pp. 186–200, 1996.

- [19] B. Brogliato, A. Ten Dam, L. Paoli, F. Genot, and M. Abadie, “Numerical simulation of finite dimensional multibody nonsmooth mechanical systems,” *Applied Mechanics Reviews*, vol. 55, p. 107, 2002.
- [20] M. Buehler, D. E. Koditschek, and P. J. Kindlmann, “A family of robot control strategies for intermittent dynamical environments,” *IEEE Control. Syst. Mag.*, vol. 10, pp. 16–22, 1990.
- [21] ———, “Planning and control of robotic juggling and catching tasks,” *International Journal of Robotics Research*, vol. 13, no. 12, pp. 101–118, April 1994.
- [22] M. Buehler, D. Koditschek, and P. Kindlmann, *A simple juggling robot: Theory and experimentation*, ser. Lecture Notes in Control and Information Sciences, 1989, vol. 139, pp. 35–73.
- [23] M. Buehler, R. Playter, and M. Raibert, “Robots step outside,” in *Int. Symp. Adaptive Motion of Animals and Machines (AMAM)*, Ilmenau, Germany, 2005, pp. 1–4.
- [24] S. A. Burden, S. Revzen, and S. S. Sastry, “Model reduction near periodic orbits of hybrid dynamical systems,” *arXiv preprint arXiv:1308.4158*, 2013.
- [25] J. Burke, R. Murphy, M. Covert, and D. Riddle, “Moonlight in miami: Field study of human-robot interaction in the context of an urban search and rescue disaster response training exercise,” *Human–Computer Interaction*, vol. 19, no. 1-2, pp. 85–116, 2004.
- [26] R. R. Burridge, A. A. Rizzi, and D. E. Koditschek, “Toward a systems theory for the composition of dynamically dexterous robot behaviors,” in *Robotics Research, International Symposium on*, vol. 7, 1996, pp. 149–161.
- [27] ———, “Sequential composition of dynamically dexterous robot behaviors,” *Int. J. Robotics Research*, vol. 18, no. 6, pp. 534–555, 1999.
- [28] K. Byl and R. Tedrake, “Dynamically diverse legged locomotion for rough terrain,” in *Proceedings of the International Conference of Robotics and Automation*, video submission, May 2009.

- [29] ———, “Metastable walking machines,” *International Journal of Robotics Research*, 2009.
- [30] C. Cai and B. Roth, “On the spatial motion of a rigid body with point contact,” in *IEEE Int. Conf. Robotics and Automation*, vol. 4, 1987, pp. 686–695.
- [31] J. F. Canny and K. V. Goldberg, “A RISC approach to sensing and manipulation,” *Journal of Robotic Systems*, vol. 12, no. 6, 1995.
- [32] E. Chang-Siu, T. Libby, M. Tomizuka, and R. J. Full, “A lizard-inspired active tail enables rapid maneuvers and dynamic stabilization in a terrestrial robot,” in *Intelligent Robots and Systems*, San Fransisco, CA, USA, Sept. 2011.
- [33] A. Chatterjee, “On the realism of complementarity conditions in rigid body collisions,” *Non-linear Dynamics*, vol. 20, no. 2, pp. 159–168, 1999.
- [34] A. Chatterjee, R. Pratap, C. Reddy, and A. Ruina, “Persistent passive hopping and juggling is possible even with plastic collisions,” *The International Journal of Robotics Research*, vol. 21, no. 7, pp. 621–634, 2002.
- [35] A. Chatterjee and A. Ruina, “A new algebraic rigid-body collision law based on impulse space considerations,” *ASME Journal of Applied Mechanics*, vol. 65, pp. 939–951, 1998.
- [36] S. Chernova and M. Veloso, “An evolutionary approach to gait learning for four-legged robots,” in *In Proceedings of IROS’04*, September 2004.
- [37] C. Chevallereau, J. W. Grizzle, and C.-L. Shih, “Asymptotically stable walking of a five-link underactuated 3-d bipedal robot,” *IEEE Trans. Robot.*, vol. 25, no. 1, pp. 37–50, 2009.
- [38] S. Chitta, P. Vernaza, R. Geykhman, and D. D. Lee, “Proprioceptive localization for a quadrupedal robot on known terrain,” in *Proceedings of the International Conference on Robotics and Automation*, 2007.
- [39] Y.-C. Chou, W.-S. Yu, K.-J. Huang, and P.-C. Lin, “Bio-inspired step-climbing in a hexapod robot,” *Bioinspiration Biomimetics*, vol. 7, no. 3, p. 036008, Sep 2012.

- [40] R. W. Cottle, "Manifestations of the schur complement," *Linear Algebra and its Applications*, vol. 8, no. 3, pp. 189–211, 1974.
- [41] R. W. Cottle and Y.-Y. Chang, "Least-index resolution of degeneracy in linear complementarity problems with sufficient matrices," *SIAM Journal on Matrix Analysis and Applications*, vol. 13, no. 4, pp. 1131–1141, 1992.
- [42] R. Cottle, "On a problem in linear inequalities," *Journal of the London Mathematical Society*, vol. 1, no. 1, pp. 378–384, 1968.
- [43] N. J. Cowan, E. J. Ma, M. Cutkosky, and R. J. Full, "A biologically inspired passive antenna for steering control of a running robot," in *In International Symposium on Robotics Research*. Springer, 2003, pp. 541–550.
- [44] A. De, G. Lynch, A. M. Johnson, and D. Koditschek, "Motor sizing for legged robots using dynamic task specification," in *In Proceedings of IEEE International Conference on Technologies for Practical Robot Applications*, Boston, MA, USA, April 2011.
- [45] D. DeWitt and F. Incropera, *Fundamentals of heat and mass transfer*. Wiley New York, 1996.
- [46] D. Dunn-Rankin, E. Leal, and D. Walther, "Personal power systems," *Progress in Energy and Combustion Science*, vol. 31, no. 5–6, pp. 422–465, 2005.
- [47] P. E. Dupont and S. P. Yamajako, "Jamming and wedging in constrained rigid-body dynamics," in *Robotics and Automation, 1994. Proceedings., 1994 IEEE International Conference on*. IEEE, 1994, pp. 2349–2354.
- [48] R. Featherstone, *Rigid body dynamics algorithms*. New York: Springer, 2008.
- [49] C. Ferrell, "Failure recognition and fault tolerance of an autonomous robot," *Adaptive Behavior*, vol. 2, no. 4, pp. 375–398, 1994.

- [50] P. M. Frank, “Fault Diagnosis in Dynamic Systems Using Analytical and Knowledge-based Redundancy—A Survey and Some New Results,” *Automatica*, vol. 26, no. 3, pp. 459–474, 1990.
- [51] R. J. Full, *Concepts of efficiency and economy in land locomotion*. Cambridge University Press, 1991, pp. 97 – 131.
- [52] R. Full and D. Koditschek, “Templates and anchors: Neuromechanical hypotheses of legged locomotion on land,” vol. 202, no. 23, pp. 3325–3332, 1999.
- [53] N. Furukawa, A. Namiki, S. Taku, and M. Ishikawa, “Dynamic regrasping using a high-speed multifingered hand and a high-speed vision system,” in *Robotics and Automation. IEEE International Conference on*, 2006, pp. 181–187.
- [54] K. C. Galloway, “Passive variable compliance for dynamic legged robots,” Ph.D. dissertation, Mechanical Engineering, University of Pennsylvania, Philadelphia, PA, 2010.
- [55] K. C. Galloway, G. C. Haynes, B. D. Ilhan, A. M. Johnson, R. Knopf, G. Lynch, B. Plotnick, M. White, and D. E. Koditschek, “X-RHex: A highly mobile hexapedal robot for sensorimotor tasks,” Univ. of Pennsylvania, Tech. Rep., 2010.
- [56] G. Gilardi and I. Sharf, “Literature survey of contact dynamics modelling,” *Mechanism and machine theory*, vol. 37, no. 10, pp. 1213–1239, 2002.
- [57] D. I. Goldman, T. S. Chen, D. M. Dudek, and R. J. Full, “Dynamics of rapid vertical climbing in cockroaches reveals a template,” *Journal of Experimental Biology*, vol. 209, no. 15, pp. 2990–3000, 2006.
- [58] B. Goodwine and J. Burdick, “Motion planning for kinematic stratified systems with application to quasi-static legged locomotion and finger gaiting,” *IEEE Trans. Robot. Autom.*, vol. 18, no. 2, pp. 209–222, Apr 2002.
- [59] D. Goswami and P. Vadakkepat, “Planar bipedal jumping gaits with stable landing,” *IEEE Trans. Robot.*, vol. 25, no. 5, pp. 1030 –1046, Oct 2009.

- [60] P. Gregorio, M. Ahmadi, and M. Buehler, “Design, control, and energetics of an electrically actuated legged robot,” *IEEE Trans. Syst. Man Cybern.*, vol. 27, no. 4, pp. 626–634, 1997.
- [61] A. Hatcher, *Algebraic topology*. Cambridge University Press, 2002.
- [62] K. Hauser, T. Bretl, J. C. Latombe, and B. Wilcox, “Motion planning for a six-legged lunar robot,” in *Workshop on the Algorithmic Foundations of Robotics*, New York, NY, 2006.
- [63] G. C. Haynes, A. Khripin, G. Lynch, J. Amory, A. Saunders, A. A. Rizzi, and D. E. Koditschek, “Rapid pole climbing with a quadrupedal robot,” in *Proceedings of the IEEE International Conference on Robotics and Automation*, May 2009, pp. 2767–2772.
- [64] G. C. Haynes and D. E. Koditschek, “On the comparative analysis of locomotory systems with vertical travel,” in *Int. Symp. Experimental Robotics*, Delhi, India, Dec. 2010.
- [65] G. C. Haynes, J. Pusey, R. Knopf, A. M. Johnson, and D. E. Koditschek, “Laboratory on legs: an architecture for adjustable morphology with legged robots,” in *Unmanned Systems Technology XIV*, vol. 8387, no. 1. SPIE, 2012, p. 83870W.
- [66] G. C. Haynes and A. A. Rizzi, “Gait regulation and feedback on a robotic climbing hexapod,” in *Proc. Robotics: Science and Systems*, Philadelphia, USA, Aug. 2006.
- [67] ———, “Gaits and gait transitions for legged robots,” in *IEEE Int. Conf. Robotics and Automation*, Orlando, FL, USA, May 2006, pp. 1117–22.
- [68] G. C. Haynes, F. R. Cohen, and D. E. Koditschek, “Gait transitions for quasi-static hexapedal locomotion on level ground,” in *Robotics Research*, ser. Springer Tracts in Advanced Robotics, C. Pradalier, R. Siegwart, and G. Hirzinger, Eds. Springer Berlin Heidelberg, 2011, vol. 70, pp. 105–121.
- [69] G. C. Haynes, “Gait regulation control techniques for robust legged locomotion,” Ph.D. dissertation, Robotics Institute, Carnegie Mellon Univ., Pittsburgh, PA, May 2008.

- [70] G. Haynes, A. Rizzi, and D. Koditschek, “Multistable phase regulation for robust steady and transitional legged gaits,” *The International Journal of Robotics Research*, vol. 31, no. 14, pp. 1712–1738, 2012.
- [71] W. Heemels, J. M. Schumacher, and S. Weiland, “Linear complementarity systems,” *SIAM journal on applied mathematics*, pp. 1234–1269, 2000.
- [72] P. Holmes, R. J. Full, D. E. Koditschek, and J. Guckenheimer, “The dynamics of legged locomotion: Models, analyses, and challenges,” *SIAM Review*, vol. 48, no. 2, pp. 207–304, 2006.
- [73] J. Hong, G. Lafferriere, B. Mishra, and X. Tan, “Fine manipulation with multifinger hands,” in *The IEEE International Conference on Robotics and Automation*, May 1990, pp. 1568–1573 vol.3.
- [74] A. Hoover, S. Burden, X.-Y. Fu, S. Sastry, and R. Fearing, “Bio-inspired design and dynamic maneuverability of a minimally actuated six-legged robot,” in *IEEE Int. Conf. Biomedical Robotics and Biomechatronics*, Sept. 2010, pp. 869–876.
- [75] G. W. Housner, “The behavior of inverted pendulum structures during earthquakes,” *Bulletin of the seismological society of America*, vol. 53, no. 2, pp. 403–417, 1963.
- [76] W. H. Huang and M. T. Mason, “Experiments in impulsive manipulation,” in *Robotics and Automation, 1998. Proceedings. 1998 IEEE International Conference on*, vol. 2. IEEE, 1998, pp. 1077–1082.
- [77] I. W. Hunter, J. M. Hollerbach, and J. Ballantyne, “A comparative analysis of actuator technologies for robotics,” *Robotics Review*, vol. 2, pp. 299–342, 1992.
- [78] Y. Hurmuzlu and D. B. Marghitu, “Rigid body collisions of planar kinematic chains with multiple contact points,” *The International Journal of Robotics Research*, vol. 13, no. 1, pp. 82–92, 1994.

- [79] H. Hwang, K. Lynch, and Y. Youm, “Locomotion via impact switching between decoupling vector fields,” in *IEEE/RSJ Int. Conf. Intelligent Robots and Systems*, 2006, pp. 5243–5248.
- [80] A. W. Ingleton, “A problem in linear inequalities,” *Proceedings of the London Mathematical Society*, vol. 3, no. 1, pp. 519–536, 1966.
- [81] S. E. Jo, S.-W. Kim, and T. J. Park, “Equally constrained affine projection algorithm,” in *Signals, Systems and Computers. Conference Record of the Thirty-Eighth Asilomar Conference on*, vol. 1, 2004, pp. 955–959.
- [82] K. H. Johansson, M. Egerstedt, J. Lygeros, and S. Sastry, “On the regularization of Zeno hybrid automata,” *Systems & Control Letters*, vol. 38, no. 3, pp. 141–150, 1999.
- [83] A. M. Johnson and S. Axinn, “The morality of autonomous robots,” *Journal of Military Ethics*, vol. 12, no. 2, pp. 129–141, 2013.
- [84] ———, “Acting vs. being moral: The limits of technological moral actors,” in *Proceedings of the 2014 IEEE Intl. Symposium on Ethics in Engineering, Science, and Technology*, May 2014, to appear.
- [85] A. M. Johnson, S. A. Burden, and D. E. Koditschek, “A hybrid systems model for simple manipulation and self-manipulation systems,” 2014, in prep.
- [86] A. M. Johnson, M. T. Hale, G. C. Haynes, and D. E. Koditschek, “Autonomous legged hill and stairwell ascent,” in *IEEE Int. Workshop Safety, Security, and Rescue Robotics*, Nov. 2011, pp. 134–142.
- [87] A. M. Johnson, G. C. Haynes, and D. E. Koditschek, “Disturbance detection, identification, and recovery by gait transition in legged robots,” in *IEEE/RSJ Int. Conf. Intelligent Robots and Systems*, Taipei, Taiwan, Oct. 2010.
- [88] ———, “Standing self-manipulation for a legged robot,” in *IEEE/RSJ Int. Conf. Intelligent Robots and Systems*, Algarve, Portugal, Oct. 2012, pp. 272–279.

- [89] A. M. Johnson and D. E. Koditschek, “Parametric jumping dataset on the RHex robot,” Univ. of Pennsylvania, Tech. Rep., 2012.
- [90] —, “Legged self-manipulation,” *IEEE Access*, vol. 1, pp. 310–334, May 2013.
- [91] —, “Toward a vocabulary of legged leaping,” in *IEEE Int. Conf. Robotics and Automation*, May 2013, pp. 2553–2560.
- [92] A. M. Johnson, T. Libby, E. Chang-Siu, M. Tomizuka, R. J. Full, and D. E. Koditschek, “Tail assisted dynamic self righting,” in *Int. Conf. Climbing and Walking Robots*, July 2012, pp. 611–620.
- [93] —, “Tail assisted dynamic self righting: Full derivations,” University of Pennsylvania, Tech. Rep., 2012.
- [94] U. Kafader, *The Selection of High-Precision Microdrives*. Maxon Academy, 2006.
- [95] S. Kajita, T. Yamaura, and A. Kobayashi, “Dynamic walking control of a biped robot along a potential energy conserving orbit,” *Robotics and Automation, IEEE Transactions on*, vol. 8, no. 4, pp. 431–438, 1992.
- [96] J. Keller, “Impact with friction,” *Journal of applied Mechanics*, vol. 53, no. 1, pp. 1–5, 1986.
- [97] J. Kerr and B. Roth, “Analysis of multifingered hands,” *Int. J. Robotics Research*, vol. 4, no. 4, pp. 3–17, 1986.
- [98] N. Kohl and P. Stone, “Machine learning for fast quadrupedal locomotion,” in *In Proceedings of the National Conference on Artificial Intelligence*, July 2004.
- [99] H. Komsuoglu, “Dynamic legged mobility—an overview,” in *Proceedings of International Joint Robotics Conference and Workshop*, 2009.
- [100] H. Komsuoglu, D. McMordie, U. Saranlı, N. Moore, M. Buehler, and D. E. Koditschek, “Proprioception based behavioral advances in a hexapod robot,” in *IEEE Int. Conf. Robotics and Automation*, vol. 4, 2001, pp. 3650–3655.

- [101] S. Koos, A. Cully, and J.-B. Mouret, “Fast damage recovery in robotics with the t-resilience algorithm,” *The International Journal of Robotics Research*, vol. 32, no. 14, pp. 1700–1723, 2013.
- [102] X. Koutsoukos, J. Kurien, and F. Zhao, “Estimation of distributed hybrid systems using particle filtering methods,” in *In Hybrid Systems: Computation and Control (HSCC 2003)*. Springer Verlag Lecture Notes on Computer Science. Springer, 2003, pp. 298–313.
- [103] M. Kovač, M. Schlegel, J. Zufferey, and D. Floreano, “Steerable miniature jumping robot,” *Autonomous Robots*, vol. 28, no. 3, pp. 295–306, 2010.
- [104] J.-F. Lalonde, N. Vandapel, and M. Hebert, “Data structures for efficient dynamic processing in 3-d,” *International Journal of Robotics Research*, vol. 26, no. 8, pp. 777–796, 2007.
- [105] J. Lee, *Introduction to smooth manifolds*. Springer–Verlag, 2012.
- [106] U. Lerner and B. Moses, “Monitoring a complex physical system using a hybrid dynamic bayes net,” in *In UAI*. UAI, 2002.
- [107] C. Li, P. B. Umbanhowar, H. Komsuoglu, D. E. Koditschek, and D. I. Goldman, “Sensitive dependence of the motion of a legged robot on granular media,” *Proceedings of the National Academy of Sciences*, vol. 106, no. 9, pp. 3029–3034, 2009.
- [108] T. Libby, T. Y. Moore, E. Chang-Siu, D. Li, D. J. Cohen, A. Jusufi, and R. J. Full, “Tail-assisted pitch control in lizards, robots and dinosaurs,” *Nature*, vol. 481, no. 7380, pp. 181–184, 2012.
- [109] P.-C. Lin, H. Komsuoglu, and D. E. Koditschek, “A leg configuration sensory system for dynamical body state estimates in a hexapod robot,” in *Proceedings of International Conference on Robotics and Automation*, Taipei, Taiwan, September 2003, pp. 1391–1396.
- [110] C.-S. Liu and H. Peng, “Inverse-Dynamics Based State and Disturbance Observers for Linear Time-Invariant Systems,” *Journal of Dynamic Systems, Measurement, and Control*, vol. 124, pp. 375–381, 2002.

- [111] Y. Liu and G. Liu, “Mobile manipulation using tracks of a tracked mobile robot,” in *Intelligent Robots and Systems, IEEE/RSJ International Conference on*, Oct. 2009, pp. 948–953.
- [112] P. Lötstedt, “Mechanical systems of rigid bodies subject to unilateral constraints,” *SIAM Journal on Applied Mathematics*, vol. 42, no. 2, pp. 281–296, 1982.
- [113] J. Lygeros, K. H. Johansson, S. N. Simic, J. Zhang, and S. S. Sastry, “Dynamical properties of hybrid automata,” *IEEE Transactions on Automatic Control*, vol. 48, no. 1, pp. 2–17, 2003.
- [114] G. A. Lynch, J. E. Clark, P.-C. Lin, and D. E. Koditschek, “A bioinspired dynamical vertical climbing robot,” *The International Journal of Robotics Research*, vol. 31, no. 8, pp. 974–996, 2012.
- [115] K. Lynch, “Nonprehensile robotic manipulation: Controlability and planning,” Ph.D. dissertation, Robotics Institute, Carnegie Mellon University, Pittsburgh, PA, March 1996.
- [116] J. D. Madden, “Mobile robots: Motor challenges and materials solutions,” *Science*, vol. 318, no. 5853, pp. 1094–1097, Nov 2007.
- [117] M. Mani, “A quick overview on rotatory Brush and Brushless DC Motors,” Motion Control Department, Ingenia, Barcelona, Spain, Tech. Rep., 2006.
- [118] M. T. Mason, “Kicking the sensing habit,” *AI Magazine*, vol. 14, no. 1, pp. 58–59, 1993.
- [119] ———, *Mechanics of Robotic Manipulation*. Cambridge, MA: MIT Press, Aug. 2001.
- [120] M. T. Mason and J. J. Kenneth Salisbury, *Robot Hands and the Mechanics of Manipulation*. Cambridge, MA: MIT Press, 1985.
- [121] M. T. Mason, D. Pai, D. Rus, J. Howell, L. R. Taylor, and M. Erdmann, “Experiments with desktop mobile manipulators,” in *International Symposium on Experimental Robotics*, 1999.
- [122] M. T. Mason, D. Pai, D. Rus, L. R. Taylor, and M. Erdmann, “A mobile manipulator,” in *IEEE International Conference on Robotics and Automation (ICRA '99)*, vol. 3, May 1999, pp. 2322–2327.

- [123] M. T. Mason and Y. Wang, "On the inconsistency of rigid-body frictional planar mechanics," in *Robotics and Automation, 1988. Proceedings., 1988 IEEE International Conference on.* IEEE, 1988, pp. 524–528.
- [124] Maxon Motors, *Maxon Catalog, Key Information*, 2009–2010.
- [125] T. McGeer, "Passive dynamic walking," *Int. J. Robotics Research*, vol. 9, no. 2, pp. 62–82, Apr. 1990.
- [126] S. Mcilraith, G. Biswas, D. Clancy, and V. Gupta, "Hybrid systems diagnosis," in *In Proceedings of Hybrid Systems: Computation and Control, Lecture Notes in Computer Science.* Springer, 2000, pp. 282–295.
- [127] D. McMordie, "Towards pronking with a hexapod robot," Master's thesis, McGill Univ., 2002.
- [128] D. McMordie and M. Buehler, "Towards pronking with a hexapod robot," in *Int. Conf. Climbing and Walking Robots*, Karlsruhe, Germany, Sept. 2001, pp. 659–666.
- [129] D. McMordie, C. Prahacs, and M. Buehler, "Towards a dynamic actuator model for a hexapod robot," in *IEEE International Conference on Robotics and Automation*, Sept. 2003, pp. 1386–1390 vol.1.
- [130] B. Mirtich and J. Canny, "Impulse-based simulation of rigid bodies," in *Proceedings of the 1995 symposium on Interactive 3D graphics.* ACM, 1995.
- [131] D. J. Montana, "The kinematics of contact and grasp," *Int. J. Robotics Research*, vol. 7, no. 3, pp. 17–32, 1988.
- [132] E. Z. Moore, D. Campbell, F. Grimminger, and M. Buehler, "Reliable stair climbing in the simple hexapod 'RHex'," in *Proceedings of the IEEE International Conference on Robotics and Automation*, vol. 3, 2002, pp. 2222–2227.
- [133] E. Z. Moore, "Leg design and stair climbing control for the RHex robotic hexapod," Ph.D. dissertation, McGill University, 2002.

- [134] R. M. Murray, Z. Li, and S. S. Sastry, *A Mathematical Introduction to Robotic Manipulation*. Boca Raton, FL: CRC Press, 1994.
- [135] J. Nelder and R. Mead, “A simplex method for function minimization,” *The Computer Journal*, vol. 7, no. 4, pp. 308–313, 1965.
- [136] A. Nordmark, H. Dankowicz, and A. Champneys, “Discontinuity-induced bifurcations in systems with impacts and friction: Discontinuities in the impact law,” *International Journal of Non-Linear Mechanics*, vol. 44, no. 10, pp. 1011 – 1023, 2009.
- [137] A. M. Okamura, N. Smaby, and M. R. Cutkosky, “An overview of dexterous manipulation,” in *IEEE Int. Conf. Robotics and Automation*, vol. 1, 2000, pp. 255–262.
- [138] Y. Or and A. Ames, “Stability and completion of zeno equilibria in lagrangian hybrid systems,” *IEEE Transactions on Automatic Control*, vol. 56, no. 6, pp. 1322 –1336, June 2011.
- [139] C. Ordonez, J. Shill, A. Johnson, J. Clark, and E. Collins, “Terrain identification for RHex-type robots,” in *SPIE Defense, Security, and Sensing*. International Society for Optics and Photonics, 2013, pp. 87 410Q–87 410Q.
- [140] D. K. Pai, R. A. Barman, and S. K. Ralph, “Platonic beasts: Spherically symmetric multilimbed robots,” *Autonomous Robots*, vol. 2, no. 3, pp. 191–201, 1995.
- [141] P. Painlevé, *Leçons sur le frottement*. Paris: Hermann, 1895.
- [142] O. Pettersson, “Execution monitoring in robotics: A survey,” *Robotics and Autonomous Systems*, vol. 53, pp. 73–88, 2005.
- [143] D. Pongas, M. Mistry, and S. Schaal, “A robust quadruped walking gait for traversing rough terrain,” in *Proceedings of the International Conference on Robotics and Automation*, 2007.
- [144] I. Poulakakis, J. A. Smith, and M. Buehler, “Experimentally validated bounding models for the Scout II quadrupedal robot,” in *ICRA*, 2004, pp. 2595–2600.

- [145] D. D. Quinn, “Finite duration impacts with external forces,” *Journal of applied mechanics*, vol. 72, no. 5, pp. 778–784, 2005.
- [146] M. H. Raibert, *Legged Robots that Balance*. Cambridge, MA, USA: MIT Press, 1986.
- [147] E. Rimon and J. W. Burdick, “Mobility of bodies in contact. I. A 2nd-order mobility index for multiple-finger grasps,” *IEEE Trans. Robot. Autom.*, vol. 14, no. 5, pp. 696–708, 1998.
- [148] P. Ringegni, M. Actis, and A. Patanella, “An experimental technique for determining mass inertial properties of irregular shape bodies and mechanical assemblies,” *Measurement*, vol. 29, no. 1, pp. 63 – 75, 2001.
- [149] M. Ruggiu, “On the lagrangian and cartesian stiffness matrices of parallel mechanisms with elastic joints,” *Advanced Robotics*, vol. 26, no. 1–2, pp. 137–153, 2012.
- [150] M. Sampath, R. Sengupta, S. Lafortune, K. Sinnamohideen, and D. C. Teneketzis, “Failure diagnosis using discrete-event models,” *Transactions on Control Systems Technology*, vol. 4, no. 2, March 1996.
- [151] N. Sankar, V. Kumar, and X. Yun, “Velocity and acceleration analysis of contact between three-dimensional rigid bodies,” *J. Applied Mechanics*, vol. 63, no. 4, pp. 974–984, 1996.
- [152] U. Saranlı, A. Rizzi, and D. Koditschek, “Model-based dynamic self-righting maneuvers for a hexapedal robot,” *Int. J. Robotics Research*, vol. 23, no. 9, pp. 903–918, 2004.
- [153] ———, “Model-based dynamic self-righting maneuvers for a hexapedal robot,” *The International Journal of Robotics Research*, vol. 23, no. 9, p. 903, 2004.
- [154] U. Saranlı, M. Buehler, and D. E. Koditschek, “RHex: A Simple and Highly Mobile Hexapod Robot,” *Int. J. Robotics Research*, vol. 20, no. 7, pp. 616–631, 2001.
- [155] E. Sayginer, T. Akbey, Y. Yazicioglu, and A. Saranlı, “Task oriented kinematic analysis for a legged robot with half-circular leg morphology,” in *IEEE Int. Conf. Robotics and Automation*, May 2009, pp. 4088 –4093.

- [156] S. Schaal and C. G. Atkeson, "Open loop stable control strategies for robot juggling," in *Robotics and Automation, 1993. Proceedings., 1993 IEEE International Conference on.* IEEE, 1993, pp. 913–918.
- [157] V. Seghete and T. Murphey, "Variational solutions to simultaneous collisions between multiple rigid bodies," in *Robotics and Automation (ICRA), 2010 IEEE International Conference on.* IEEE, 2010, pp. 2731–2738.
- [158] T. Senoo, Y. Tanno, and M. Ishikawa, "Jumping patterns analysis for 1-dof two-legged robot," in *Control Automation Robotics Vision, 11th Int. Conf.*, 2010, pp. 603–608.
- [159] L. Sentis, J. Park, and O. Khatib, "Compliant control of multicontact and center-of-mass behaviors in humanoid robots," *IEEE Trans. Robot.*, vol. 26, no. 3, pp. 483–501, 2010.
- [160] A. Shapiro, E. Rimon, and J. W. Burdick, "Passive force closure and its computation in compliant-rigid grasps," in *IEEE/RSJ Int. Conf. Intelligent Robots and Systems*, 2001, pp. 1769–1775.
- [161] N. Shiraishi, Y. Kawaida, Y. Kitamura, S. Nakaura, and M. Sampei, "Vertical jumping control of an acrobat robot with consideration of input timing," in *SICE Conf.*, vol. 4, 2002, pp. 2531–2536.
- [162] B. Siciliano and O. Khatib, *Handbook of Robotics*. New York: Springer, 2008.
- [163] M. Sobotka and M. Buss, "Locomotion studies for a 5dof gymnastic robot," in *IEEE/RSJ Int. Conf. Intelligent Robots and Systems*, 2005, pp. 3275–3280.
- [164] J. Sousa, V. Matos, and C. Peixoto dos Santos, "A bio-inspired postural control for a quadruped robot: An attractor-based dynamics," in *IEEE/RSJ Int. Conf. Intelligent Robots and Systems*, Oct. 2010, pp. 5329–5334.
- [165] M. A. Spenko, G. C. Haynes, A. Saunders, A. A. Rizzi, M. Cutkosky, R. J. Full, and D. E. Koditschek, "Biologically inspired climbing with a hexapedal robot," *J. Field Robotics*, vol. 25, no. 4-5, pp. 223–242, 2008.

- [166] S. Srinivasa, C. R. Baker, E. Sacks, G. Reshko, M. T. Mason, and M. Erdmann, "Experiments with nonholonomic manipulation," in *Proceedings of the IEEE International Conference on Robotics and Automation (ICRA)*, vol. 2. IEEE, May 2002, pp. 2042 – 2047.
- [167] D. E. Stewart, "Rigid-body dynamics with friction and impact," *SIAM Review*, vol. 42, no. 1, pp. 3–39, 2000.
- [168] D. E. Stewart and J. C. Trinkle, "An implicit time-stepping scheme for rigid body dynamics with inelastic collisions and coulomb friction," *International Journal for Numerical Methods in Engineering*, vol. 39, no. 15, pp. 2673–2691, 1996.
- [169] R. Tedrake, I. Manchester, M. Tobenkin, and J. Roberts, "Lqr-trees: Feedback motion planning via sums-of-squares verification," *Int. J. Robotics Research*, vol. 29, no. 8, pp. 1038–1052, 2010.
- [170] J. C. Trinkle, J.-S. Pang, S. Sudarsky, and G. Lo, "On dynamic multi-rigid-body contact problems with coulomb friction," *ZAMM-Journal of Applied Mathematics and Mechanics/Zeitschrift für Angewandte Mathematik und Mechanik*, vol. 77, no. 4, pp. 267–279, 1997.
- [171] S. Trujillo and M. Cutkosky, "Thermally constrained motor operation for a climbing robot," in *IEEE International Conference on Robotics and Automation*. IEEE, May 2009, pp. 2362–2367.
- [172] A. J. van der Schaft and J. Schumacher, "Complementarity modeling of hybrid systems," *Automatic Control, IEEE Transactions on*, vol. 43, no. 4, pp. 483–490, 1998.
- [173] P. Vernaza, M. Likhachev, S. Bhattacharya, S. Chitta, A. Kushleyev, and D. D. Lee, "Search-based planning for a legged robot over rough terrain," in *Proceedings of the International Conference on Robotics and Automation*, 2009.
- [174] R. Voyles and A. Larson, "Terminatorbot: a novel robot with dual-use mechanism for locomotion and manipulation," *Mechatronics, IEEE/ASME Transactions on*, vol. 10, no. 1, pp. 17 –25, Feb. 2005.

- [175] C. W. Wampler and A. J. Sommese, *Applying Numerical Algebraic Geometry to Kinematics*. Springer London, Jan 2013, pp. 125–159.
- [176] Y.-T. Wang and V. Kumar, “Simulation of mechanical systems with multiple frictional contacts,” *Journal of Mechanical Design*, vol. 116, no. 2, pp. 571–580, 1994.
- [177] Y. Wang and M. Mason, “Modeling impact dynamics for robotic operations,” in *Robotics and Automation. Proceedings. 1987 IEEE International Conference on*, vol. 4. IEEE, 1987, pp. 678–685.
- [178] Y. Wei and B. Goodwine, “Stratified motion planning on nonsmooth domains with robotic applications,” *IEEE Trans. Robot. Autom.*, vol. 20, no. 1, pp. 128–132, 2004.
- [179] J. D. Weingarten, R. E. Groff, and D. E. Koditschek, “A framework for the coordination of legged robot gaits,” in *IEEE Int. Conf. Robotics and Automation*, 2004, pp. 679–686.
- [180] J. D. Weingarten, D. E. Koditschek, H. Komsuoğlu, and C. Massey, “Robotics as the delivery vehicle: A contextualized, social, self paced, engineering education for life-long learners,” in *Robotics Science and Systems Workshop on “Research in Robots for Education”*, 2007.
- [181] J. D. Weingarten, G. A. D. Lopes, M. Buehler, R. E. Groff, and D. E. Koditschek, “Automated gait adaptation for legged robots,” in *Proceedings of the International Conference on Robotics and Automation*, vol. 3, April 2004, pp. 2153–2158.
- [182] E. R. Westervelt, J. W. Grizzle, and D. E. Koditschek, “Hybrid zero dynamics of planar biped walkers,” *IEEE Trans. Autom. Control*, vol. 48, no. 1, pp. 42–56, 2003.
- [183] T.-Y. Wu, T. J. Yeh, and B.-H. Hsu, “Trajectory planning of a one-legged robot performing a stable hop,” *Int. J. Robotics Research*, vol. 30, no. 8, pp. 1072–1091, Jul 2011.
- [184] J.-M. Yang, “Two-phase discontinuous gaits for quadruped walking machines with a failed leg,” *Robotics and Autonomous Systems*, vol. 56, no. 9, pp. 728 – 737, 2008.

- [185] C. Yilmaz, M. Gharib, and Y. Hurmuzlu, “Solving frictionless rocking block problem with multiple impacts,” *Proceedings of the Royal Society A: Mathematical, Physical and Engineering Science*, vol. 465, no. 2111, pp. 3323–3339, 2009.
- [186] M. Yim, “Why study statically stable locomotion?” available online: <http://robotics.stanford.edu/users/mark/loco-loco.html>.
- [187] M. Yim, J. Reich, and A. A. Berlin, “Two approaches to distributed manipulation,” in *Distributed Manipulation*, K. Böhringer and H. Choset, Eds. Springer, 2000, pp. 237–261.
- [188] V. Zykov, J. Bongard, and H. Lipson, “Evolving dynamic gaits on a physical robot,” in *Late Breaking Papers at the 2004 Genetic and Evolutionary Computation Conference*, M. Keijzer, Ed., Seattle, Washington, USA, 26 Jul. 2004.